Fatigue of Ti-6Al-4V thin parts made by electron beam melting

Théo Persenot

N°d'ordre NNT : 2018LYSEI117

THESE de DOCTORAT DE L'UNIVERSITE DE LYON
opérée au sein de
L'Institut National des Sciences Appliquées de Lyon

Ecole Doctorale N° EDA 034
Matériaux de Lyon

Spécialité de doctorat : Matériaux

Soutenue publiquement le 11/12/2018, par :
Théo Persenot

Fatigue of Ti-6Al-4V thin parts made by Electron Beam Melting

Devant le jury composé de :

Nicolas SAINTIER	Professeur	ENSAM	Rapporteur
Véronique AUBIN	Professeur	Centrale Supelec	Rapporteur
Eric CHARKALUK	Directeur de recherche	Ec. Polytechnique	Examinateur
Jean-Yves BUFFIERE	Professeur	INSA Lyon	Directeur de thèse
Rémy DENDIEVEL	Professeur	Grenoble INP	Directeur de thèse
Guilhem MARTIN	Maitre de conférences	Grenoble INP	Examinateur
Philippe EMILE	Ingénieur	AIRBUS	Invité

Département FEDORA – INSA Lyon - Ecoles Doctorales – Quinquennal 2016-2020

SIGLE	ECOLE DOCTORALE	NOM ET COORDONNEES DU RESPONSABLE
CHIMIE	**CHIMIE DE LYON** http://www.edchimie-lyon.fr Sec. : Renée EL MELHEM Bât. Blaise PASCAL, 3e étage secretariat@edchimie-lyon.fr INSA : R. GOURDON	M. Stéphane DANIELE Institut de recherches sur la catalyse et l'environnement de Lyon IRCELYON-UMR 5256 Équipe CDFA 2 Avenue Albert EINSTEIN 69 626 Villeurbanne CEDEX directeur@edchimie-lyon.fr
E.E.A.	**ÉLECTRONIQUE, ÉLECTROTECHNIQUE, AUTOMATIQUE** http://edeea.ec-lyon.fr Sec. : M.C. HAVGOUDOUKIAN ecole-doctorale.eea@ec-lyon.fr	M. Gérard SCORLETTI École Centrale de Lyon 36 Avenue Guy DE COLLONGUE 69 134 Écully Tél : 04.72.18.60.97 Fax 04.78.43.37.17 gerard.scorletti@ec-lyon.fr
E2M2	**ÉVOLUTION, ÉCOSYSTÈME, MICROBIOLOGIE, MODÉLISATION** http://e2m2.universite-lyon.fr Sec. : Sylvie ROBERJOT Bât. Atrium, UCB Lyon 1 Tél : 04.72.44.83.62 INSA : H. CHARLES secretariat.e2m2@univ-lyon1.fr	M. Philippe NORMAND UMR 5557 Lab. d'Ecologie Microbienne Université Claude Bernard Lyon 1 Bâtiment Mendel 43, boulevard du 11 Novembre 1918 69 622 Villeurbanne CEDEX philippe.normand@univ-lyon1.fr
EDISS	**INTERDISCIPLINAIRE SCIENCES-SANTÉ** http://www.ediss-lyon.fr Sec. : Sylvie ROBERJOT Bât. Atrium, UCB Lyon 1 Tél : 04.72.44.83.62 INSA : M. LAGARDE secretariat.ediss@univ-lyon1.fr	Mme Emmanuelle CANET-SOULAS INSERM U1060, CarMeN lab, Univ. Lyon 1 Bâtiment IMBL 11 Avenue Jean CAPELLE INSA de Lyon 69 621 Villeurbanne Tél : 04.72.68.49.09 Fax : 04.72.68.49.16 emmanuelle.canet@univ-lyon1.fr
INFOMATHS	**INFORMATIQUE ET MATHÉMATIQUES** http://edinfomaths.universite-lyon.fr Sec. : Renée EL MELHEM Bât. Blaise PASCAL, 3e étage Tél : 04.72.43.80.46 Fax : 04.72.43.16.87 infomaths@univ-lyon1.fr	M. Luca ZAMBONI Bât. Braconnier 43 Boulevard du 11 novembre 1918 69 622 Villeurbanne CEDEX Tél : 04.26.23.45.52 zamboni@maths.univ-lyon1.fr
Matériaux	**MATÉRIAUX DE LYON** http://ed34.universite-lyon.fr Sec. : Marion COMBE Tél : 04.72.43.71.70 Fax : 04.72.43.87.12 Bât. Direction ed.materiaux@insa-lyon.fr	M. Jean-Yves BUFFIÈRE INSA de Lyon MATEIS - Bât. Saint-Exupéry 7 Avenue Jean CAPELLE 69 621 Villeurbanne CEDEX Tél : 04.72.43.71.70 Fax : 04.72.43.85.28 jean-yves.buffiere@insa-lyon.fr
MEGA	**MÉCANIQUE, ÉNERGÉTIQUE, GÉNIE CIVIL, ACOUSTIQUE** http://edmega.universite-lyon.fr Sec. : Marion COMBE Tél : 04.72.43.71.70 Fax : 04.72.43.87.12 Bât. Direction mega@insa-lyon.fr	M. Jocelyn BONJOUR INSA de Lyon Laboratoire CETHIL Bâtiment Sadi-Carnot 9, rue de la Physique 69 621 Villeurbanne CEDEX jocelyn.bonjour@insa-lyon.fr
ScSo	**ScSo*** http://ed483.univ-lyon2.fr Sec. : Viviane POLSINELLI Brigitte DUBOIS INSA : J.Y. TOUSSAINT Tél : 04.78.69.72.76 viviane.polsinelli@univ-lyon2.fr	M. Christian MONTES Université Lyon 2 86 Rue Pasteur 69 365 Lyon CEDEX 07 christian.montes@univ-lyon2.fr

*ScSo : Histoire, Géographie, Aménagement, Urbanisme, Archéologie, Science politique, Sociologie, Anthropologie

Remerciements

Un camarade d'entraînement m'a un jour décrit le cross-country de la manière suivante : "Au départ, tu sprintes à fond. Ensuite, tu cours vite toute la course, à chaque côte, tu accélères et, à la fin, tu sprintes encore". Je pense que cette description correspond bien à ce que représente une thèse : un effort long, constant mais intense. Néanmoins, pas une seule fois pendant ces trois ans ne me suis-je levé en considérant la journée de travail à venir comme une obligation et c'est en grande partie dû aux personnes que j'ai cotoyées au sein du laboratoire et en dehors. J'ai essayé dans les quelques paragraphes qui suivent de rendre justice à toutes ces personnes et la longueur de ces remerciements est à peine à la hauteur de la reconnaissance que je leur porte.

Je tiens tout d'abord à remercier mes deux co-directeurs de thèse Jean-Yves Buffière et Rémy Dendievel ainsi que mes deux encadrants Eric Maire et Guilhem Martin pour leur accompagnement quotidien. Ils m'ont fourni la parfaite combinaison d'autonomie et de support dont j'avais besoin pour mener à bien ce projet. Je pense sincèrement qu'avoir été encadré par cette équipe a été une chance incroyable et je souhaite à tout doctorant d'être suivi par la même équipe. Les réunions ont toujours été remplies de bonne humeur, de bon humour tout en restant efficaces et c'était un plaisir à chaque fois. Merci Jean-Yves pour tes conseils, pour m'avoir poussé à chercher plus au fond des choses, pour ton encadrement humain et bienveillant et enfin pour m'avoir fait découvrir la montagne derrière le mythe de l'Alpe d'Huez. Merci Rémy pour ton esprit de synthèse et ton impressionnante capacité à extraire la "substantifique moelle" de mon discours parfois confus et pour les discussions téléphoniques qui ont eu plusieurs fois raison de la batterie des fixes grenoblois. Merci Eric pour ton suivi et ta présence, pour tes remarques toujours pertinentes et surtout tes idées qui ont grandement contribué à faire avancer ce projet. Enfin, merci Guilhem pour ton encadrement et surtout ton implication de tous les instants, pour cette énergie qui a permis de rentabiliser à 100% tous mes passages à Grenoble, pour ta réactivité exceptionnelle en toute circonstance et ton encadrement attentif.

Je tiens également à remercier les rapporteurs Véronique Aubin et Nicolas Saintier d'avoir accepté de relire ce manuscrit dans son intégralité. Un grand merci à Eric Charkaluk pour sa présence en tant que président du jury de ma soutenance. Pouvoir présenter le résultat de ces trois années de travail devant une des personnes qui m'a donné le goût de la recherche est un énorme privilège dont j'ai conscience.

Mes remerciements vont également à tous les autres membres du projet FA^{2}SCINAE : Frédéric Vignat, François Villeneuve et Franck Pourroy de G-SCOP, Claude Archambeau et Philippe Emile d'Airbus ainsi que Benjamin Vayre de Polyshape. Une émulation

certaine a toujours émané des réunions réalisées ensemble et je vous remercie de m'avoir accueilli les bras ouverts au sein de ce projet. Je vous suis également reconnaissant d'avoir réussi à supporter mes présentations surchargées en diapos mais surtout je vous remercie pour les liens qui ont pu se tisser au cours de ces trois années.

Au cours de ces douze derniers mois, deux post-docs sont venus renforcer les "forces vives" du projet FA^{2}SCINAE : Alexis Burr puis Pierre-Thomas Doutre. Notre collaboration sur l'étude des "lattices" a été très enrichissante de par l'émulation qu'elle a générée. Une mention particulière à Alexis grâce à qui la recherche de fissures s'est transformée à une chasse au trésor.

Ce voyage n'aurait jamais eu lieu si mon stage de fin d'études ne s'était pas agréablement déroulé et je remercie donc Fabien Szmytka pour m'avoir transmis sa passion et pour m'avoir conseillé avec clairvoyance de me lancer dans l'aventure lyonnaise.

Cette thèse a aussi été l'occasion pour moi de co-encadrer deux projets de fin d'études. Ces premières expériences de management très distinctes l'une de l'autre m'ont été très bénéfiques en particulier d'un point de vue humain et je tiens donc à en remercier Alexandre Mathurin et Nadia Jmal.

L'utilisation de moyens expérimentaux implique avant toute chose leur apprentissage. Je remercie donc Sophie Cazottes et Sylvain Dancette à Lyon ainsi que Pierre Lhuissier à Grenoble d'avoir donné de leur temps pour m'accompagner et me former sur différentes techniques de caractérisation et d'essais. Mes remerciements les plus sincères vont aux deux J. qui faisaient et font tourner la tomographie à MATEIS : Jérôme Adrien et Joël Lachambre. Les centaines d'heures passées au sous-sol de Jules Verne n'auraient pas été envisageables sans leur aide et leur curiosité et leur implication ont grandement contribué à améliorer la qualité de mon travail.

De manière plus générale, l'ambiance au sein de l'équipe MetAl restera gravée en moi. Elle a permis d'innombrables discussions plus ou moins professionnelles dans des cadres plus ou moins formels mais toujours enrichissantes et intéressantes. Par risque d'oublier quelqu'un, je ne citerai personne mais sachez que je rêve de retrouver une telle ambiance de travail au cours de mes futures pérégrinations. Il m'est cependant impossible de ne pas remercier sincÃlrement Frida sur qui repose tout le fonctionnement de l'équipe.

La majeure partie de mon temps passé éveillé pendant ces trois années s'est fait au côté d'un groupe de doctorants avec qui des amitiés durables se sont créés. Merci aux "vieux" pour leur intégration et leur accueil : Sébastien, puits de connaissance intarissable, pour tes conversations parfois interminables mais toujours profitables, William pour ta verve piquante et hilarante cachée sous une réserve confondante, Juan pour ton humour et ton caractère déterminé, Josselin pour ton rire communicatif et ton attention aux détails (ta connaissance encyclopédique des classiques de la souris la plus célèbre du monde m'étonnera toujours), Morgane Ma. pour ta persévérance, ta motivation et ta grande gentillesse, Aléthéa pour tes excuses trop nombreuses, ta joie exhaltante et ton sens de l'organisation inégalable, Sam parce que tu as montré que les grandes épopées cyclistes étaient encore d'actualité aujourd'hui, Yasin pour ton amour téméraire des défis (la découverte des spécialités belges à tes côtés est mémorable), Mélanie pour ton intérêt profond et sincère envers les autres, Thibaut pour ton sourire carnassier et ton inventivité débordante, Marta pour ton énergie, ta constante bonne humeur et ta générosité incom-

parable, Malgo pour ton goût de l'aventure, Erik pour ta classe de dandy et pour avoir amené l'hospitalité transalpine à Lyon, Titi et Claire pour l'organisation du week-end des doctorants (j'ai appris grâce à vous qu'une course ne se fait pas forcément en épinglant un dossard), Nico pour m'avoir fait léviter et voler à de multiples reprises et Fanfan pour avoir été le cœur de la vie extraprofessionnelle du laboratoire (tes talents de DJ nous manquent terriblement).

Merci aux "plus jeunes" d'avoir repris le flambeau et de continuer à dynamiser les relations extra-professionnelles et les activités sportives de l'équipe : Gabriel pour ton humour incisif, ta confiance les skis aux pieds et aussi parce que tu seras à jamais le premier des nouveaux, François pour avoir supporté mes élucubrations quotidiennes pendant les deux ans passés ensemble dans le même bureau, Julie pilier auto-proclamé de nos soirées dès son arrivée et étendard du bon esprit dijonnais et grenoblois à la fois, Alexis pour tes connaissances musicales inégalables et son appréciation de la victoire comme de la défaite, Amin pour ta force et ta motivation à toute épreuve, Alexandre pour ta persévérance qui se transforme parfois en témérité et ton appétit sans fin, Arnaud pour m'avoir transmis ton amour du vélo et pour nos discussions endiablées, Marion (et Mathieu) pour ta détermination, ton caractère mais aussi pour l'oeil attentif avec lequel tu regardes les autres, Lucile pour les footings partagés et ta modestie sans limite, Flore pour le court temps passé au sein de l'équipe mais suffisant pour découvrir ton enthousiasme contagieux, Quentin pour la force tranquille dont tu fais preuve, Qinqin pour ton sourire en toute circonstance et merci et bon courage aux nouveaux que je n'ai cotoyés que quelques semaines (Arnaud, Thibaut, Manon et Maxime). Vous êtes entre de bonnes mains.

Enfin, il m'est impossible d'oublier ceux qui ont partagé mon quotidien pendant ces trois années, les thésards qui ont entamé et terminé cette aventure en même temps que moi ou presque. Les évènements organisés et passés ensemble durant cette période n'ont fait que cimenter les fondations d'amitiés nées pour durer. Oriane, merci entre autres pour toutes les séances de cinéma partagées malgré la qualité parfois aléatoires des films visionnés, pour ton esprit de compétition parfois excessif mais toujours positif et pour les discussions libératrices à la fin de longues journées. Justine, merci pour ton sourire à pleines dents et tes yeux pétillants, pour tes expressions bien d'ici, pour les centaines de kilomètres partagés assis sur une selle ou à patiner les skis aux pieds et pour ta résilience incommensurable qui demeure un exemple à mes yeux. Morgane Mo., merci pour le moments passés ensemble au labo ou en conférence, pour ton énergie et ta curiosité débordantes. Gwen, merci pour m'avoir fait découvrir une certaine spécialité montpelliéraine, pour ton rire chantant, pour ta fougue et ta renversante envie de gagner "par tous les moyens" et pour ton caractère entier qui a pimenté les journées et égayé les soirées. Zack, merci pour ta soif de connaissances, ta voix renversante et ton intégration confondante au sein de l'équipe. Aurélien, merci pour toutes les soirées organisées, pour tous les souvenirs emmagasinés grâce à tes talents de photographe, pour toutes les descentes passées à essayer sans succès de m'accrocher à ta roue ou à tes skis et pour toutes les heures passées à planer grâce à tes découvertes musicales. Victor, merci pour cette première année où j'ai pu partager un bureau avec toi et tes cheveux, pour m'avoir fait découvrir la joie de se réveiller à 23h un vendredi soir pour aller bosser, pour ces trois années ponctuées d'épopées (les rails du tram à vélo, la vvmobile, ...) et de fous rires, pour tes expérimentations culinaires et pour

tes expressions québecoises. Merci à vous d'avoir été vous-mêmes et de le rester le plus longtemps possible !

D'autres personnes ont également eu à me supporter pendant ce temps. Merci donc à Matthieu, Bastien, Florent et Sylvain d'avoir répondu à mes invitations de dernière minute et de m'avoir initié au quizz anglais. Merci à mes amis de prépa (Victor, Antoine, Lætitia, Laure, Nicolas, Mélanie, Louise, Jocelyn, Bertrand, et tous les autres) et d'école (Charles et Mathilde, Gaël, Yannick et Caro, David, Antoine, Josua et Sarah, Guillaume, Aurélien, Victor, Axel, Poulp', Zim', Antonin et tous ceux que j'oublie de citer) de m'avoir rappelé mon statut d'étudiant et de m'avoir soutenu à votre manière durant trois ans. Un merci tout particulier à Antoine, David, Josua et Aurélien d'avoir pris part à une partie ou à toutes les randonnées/épopées libératrices réalisées et à la *dream team* pour les parenthèses enchantées qu'ont représentées les escapades corses, romaines, strabourgeoises, ... Merci à Camille pour notre discussion ininterrompue.

Enfin, je tiens à remercier toute ma famille et plus particulièrement ma mère, mon père et ma belle-mère qui m'ont donné la possibilité de faire cette thèse grâce à l'éducation qu'ils m'ont prodiguée. Les retours en région parisienne ont toujours été des moments chargés mais reposants. Merci également à mon frère Simon pour son soutien indéfectible et les moments de détente passés ensemble. Merci à mes grand-parents pour leur soutien et à Papi Daniel pour l'intérêt porté à mon travail.

Merci à toutes ces personnes, je ne regrette pas un instant la décision prise de partir dans cette aventure et le fait de l'avoir passée à vos côtés y est pour beaucoup. Infiniment merci.

Contents

French summary - Résumé en français

Cette partie est un résumé étendu de la thèse en français. Le contexte de la thèse, les principaux résultats ainsi que les perspectives que l'on peut en tirer y sont présentés. Cela reste néanmoins un simple aperçu du manuscrit complet. Pour accéder à l'entièreté des résultats et du raisonnement scientifique, le lecteur est prié de se référer au reste du manuscrit rédigé en anglais.

Introduction

Dans le contexte industriel actuel, la réduction des dépenses énergétiques est un enjeu crucial. Pour les indutries du transport (aéronautique, automobile, ferroviaire, ...), d'importantes économies peuvent être réalisées grâce à des réductions de masse. Dans cette optique, les structures poreuses telles que les structures cellulaires sont très prometteuses. Néanmoins, l'élaboration de telles structures métalliques par des moyens de fabrication conventionnels demeure extrêmement complexe. Avec l'émergence de techniques de fabrication additive sur lit de poudre telles que la fusion par faisceau laser (SLM) ou par faisceau d'électrons (EBM), la production de structures cellulaires est devenue beaucoup plus aisée et se développe de manière significative. En effet, ces procédés de fabrication couche par couche accordent une liberté géométrique inenvisageable pour des procédés conventionnels.

Cependant, il est nécessaire de connaître de manière fiable les propriétés mécaniques de ces structures avant d'envisager leur intégration dans des pièces industrielles. Plus précisément, leur résistance à la fatigue en traction revêt un intérêt tout particulier pour l'industrie aéronautique. Par ailleurs, les procédés de fabrication additive sont connus pour générer des défauts internes mais surtout d'importantes rugosités de surface qui sont susceptibles d'impacter négativement les propriétés mécaniques. Il est donc nécessaire d'étudier en détails cet impact mais également comment il peut être limité.

L'objectif de ce travail de thèse est donc de déterminer les mécanismes qui gouvernent le comportement en fatigue de structures cellulaires. Cette étude s'est focalisée sur une unique technique d'élaboration (la technique EBM ou fusion par faisceau d'électrons) et un unique matériau (l'alliage de titane Ti-6Al-4V). Pour cela, l'élément unitaire constitutif de ces structures a été considéré : la poutre unitaire. Elle a été dans un premier temps caractérisée à l'état brut de fabrication et les propriétés mécaniques correspon-

dantes (statique et fatigue) ont été déterminées. Leur potentielle amélioration par le biais de post-traitements a ensuite été étudiée. Le but de cette étape n'a pas été d'atteindre des performances comparables ou meilleures que celles obtenues par des moyens de fabrication conventionnels mais plutôt d'atteindre la meilleure résistance en fatigue possible par des techniques applicables à des pièces complexes telles que les structures cellulaires. Enfin, en se basant sur les mécanismes de rupture identifiés, une méthode permettant de prédire la résistance en fatigue d'un échantillon directement à partir de sa caractérisation par des contrôles non-destructifs a été recherchée. Des recommandations quant à la fabrication de structures cellulaires et à l'application des post-traitements sont donc attendues à la suite de ce travail.

Chapitre 1 : Caractérisation du matériau brut de fabrication et influences de post-traitements

Avant d'utiliser des structures cellulaires élaborées par fabrication additive, il est au préalable nécessaire de caractériser le matériau qui les compose dans son état brut de fabrication. La fine géométrie des éprouvettes (échantillons avec une zone utile cylindrique de 10 mm de long et de 2 mm de diamétre) a été définie afin d'être représentative d'une poutre unitaire d'une structure cellulaire. Trois orientations de fabrication différentes ont été considérées (cylindres verticaux, penchés à 45° et horizontaux) de manière à obtenir des conditions de fabrication semblables à celles des poutres au sein de ces structures. L'élaboration des éprouvettes a été réalisée par une machine ARCAM A1 à partir d'une poudre Ti-6Al-4V ELI (faibles proportions d'éléments intersticiels). La stratégie de fusion standard recommandée par ARCAM pour de telles géométries a été employée.

La microscopie optique a été utilisée pour observer leur microstructure tandis que la caractérisation géométrique et l'observation des défauts (internes et surfaciques) a été principalement réalisée par tomographie aux rayons X de laboratoire.

Une fine microstructure $\alpha + \beta$ lamellaire similaire à celle rapportée dans la littérature a été observée.

L'analyse des volumes issus de la tomographie a montré que les éprouvettes fabriquées sont toujours plus fines que la géométrie définie en CAO. Ce phénomène a été relié à la stratégie de fusion conservative définie par ARCAM. La comparaison des éprouvettes a quant à elle mis en lumière la très bonne reproductibilité du procédé de fabrication.

La tomographie a également permis d'identifier les défauts inhérents à la fabrication additive sur lit de poudre :

- les défauts internes au sein desquels les *pores de gaz* sphériques principalement issus de l'atomisation de la poudre peuvent être distingués des *défauts de fusion* non sphériques et causés par le procédé EBM.

- les défauts surfaciques composés de particules de poudre collées à la surface et de défauts d'empilement en "pile d'assiettes" qui peuvent amener à la formation de défauts semblables à des entailles.

Ces derniers sont responsables de l'importante rugosité de surface mesurée pour toutes les éprouvettes et ces résultats sont cohérents avec ceux de la littérature.

Un impact de l'orientation de fabrication sur la géométrie des échantillons ainsi que sur les défauts de surface a été observé et relié aux conditions d'évacuation thermique qui varient pour chaque orientation. En effet, la diffusion thermique dans la poudre non fondue étant moins efficace que dans une couche fondue, des excès de fusion ont lieu sur les surfaces suspendues, comme la face inférieure des échantillons horizontaux. Sur ces dernières, de larges protubérances ont été observées et la section de coupe de ces échantillons était semblable à une goutte d'eau. De plus, un lien entre la densité de défauts d'empilement et d'entailles et le nombre de couches nécessaire à la fabrication d'un échantillon a été établi. Par conséquent, les échantillons verticaux présentaient une plus grande densité de défauts de ce type.

Pour les trois orientations de fabrication, des distribution spatiales hétérogènes des défauts internes ont été obtenues : la densité de défauts internes est plus importante au sein d'un anneau sub-surfacique. Cet anneau se superpose parfaitement avec celui généré par les irrégularités de surface. La présence de ces deux anneaux semble être causée par la stratégie de fusion utilisée et potentiellement par une densité d'énergie plus faible utilisée lors de la fusion des contours.

Une fois le matériau brut de fabrication caractérisé, plusieurs post-traitements ont été étudiés afin de réduire les populations de défauts internes et surfaciques. Seuls ceux pouvant être applicables à des structures cellulaires ont été envisagés. Par conséquent, les opérations de polissage mécanique tels que l'usinage ont été proscrites.

La Compression Isostatique à Chaud (CIC) (2 h à 920°C et 100 MPa suivies d'un refroidissement lent) a provoqué la fermeture ou la diminution de la taille des défauts internes de manière à ce qu'aucun ne soit détectable par tomographie (taille de voxel = 2.5 μm) après post-traitement. Un grossissement de la microstructure a aussi été observé (augmentation de la taille des lattes de ~1 à ~3-4 μm). Des effets similaires sont rapportés dans la littérature.

Deux post-traitements différents ont été considérés pour améliorer l'état de surface des échantillons : l'attaque chimique et le grenaillage ultrasonique.

L'attaque chimique (HF + HNO$_3$ + H$_2$O) améliore l'état de surface des échantillons par dissolution. Les observations par tomographie ont montré que toutes les poudres collées à la surface sont dissoutes rapidement et que les défauts d'empilement en "pile d'assiettes" ainsi que ceux en forme d'entailles sont impactés de manière positive. Leur profondeur est significativement réduite tandis que le rayon de courbure à leur racine est sensiblement augmenté de telle sorte que seuls les défauts les plus profonds conservent un aspect d'entaille. Une amélioration conséquente de la rugosité de la surface est alors mesurée. De plus et malgré quelques légères variations liées aux états de surface, ce post-traitement a un impact similaire quelque soit l'orientation de fabrication. Par conséquent, l'influence de l'orientation de fabrication sur les défauts de surface (densité, orientation et aspect morphologique des défauts) est conservée après traitement. Un inconvénient de celui-ci est la perte de matière non négligeable. Par conséquent, des défauts internes (*pores de gaz* et *défauts de fusion*) sont amenés proche de ou à la surface de l'échantillon.

Le grenaillage ultrasonique a une influence à la fois sur la surface et sur la couche sub-surfacique des échantillons bruts de fabrication. Les impacts des billes d'aciers écrasent les pics de la surface et les replient sur les creux (vallées) voisins. Les défauts de sur-

face sont par conséquent "remplis" par déformation plastique. L'état de surface obtenu est alors sensiblement similaire à celui d'échantillons usinés. L'anneau sub-surfacique au sein duquel la densité de défauts internes était plus forte à l'état brut de fabrication a également été impacté par le traitement puisqu'après grenaillage, il n'est plus détecté sur les images tomographiques. Néanmoins, des défauts internes formant un nouvel anneau sont détectés sous la surface. La comparaison des images tomographiques avant et après grenaillage a permis de déterminer leur origine. Ce sont des défauts d'entailles qui ont été seulement partiellement "remplis" au cours du traitement. La déformation plastique par le grenaillage affecte aussi la microstructure jusqu'à une profondeur d'environ ∼100 μm sous la surface. Jusqu'à ∼15-20 μm environ, toutes les lattes α ont été sévèrement comprimées ; elles présentent des épaisseurs sub-microniques et sont toutes alignées avec leur axe principal parallèle à la surface. Des mesures de nano-identation ont montré que cette déformation de la microstructure induit un durcissement de la surface. Des mesures complémentaires de contraintes résiduelles par diffraction des rayons X ont également indiqué que ce post-traitement induisait d'importantes contraintes de compression jusqu'à environ ∼250 μm de profondeur.

Chapitre 2 : Propriétés de traction et facteurs d'abaissement

Il a été montré dans le chapitre précédent qu'à l'état brut de fabrication, les éprouvettes EBM diffèrent sensiblement d'éprouvettes usinées, notamment par leur état de surface, et que les divers post-traitements étudiés les affectaient de manière significative. Des essais de traction ont donc été réalisés sur des échantillons brut de fabrication et des échantillons post-traités. Afin de déterminer l'impact de chaque condition, les résultats obtenus ont été comparés à ceux rapportés dans la littérature pour des échantillons usinés. Cette étude a été restreinte au cas des échantillons verticaux et le grenaillage ultrasonique n'a pas été pris en considération.

A cause des importantes variations de section au sein de la zone utile des échantillons bruts de fabrication ou attaqués chimiquement, la mesure de la contrainte n'est pas directe. Trois approches simples (section CAO, section moyenne et section minimale) ont été considérées. La section moyenne déterminée à partir des images tomographiques s'est avérée être la section la plus appropriée pour le calcul des contraintes ; elle a donc été utilisée comme base de calcul des contraintes dans le reste de cette étude.

Les résultats des essais de traction ont montré que la surface brute de fabrication des échantillons affectait de manière négative leurs propriétés mécaniques de traction (limite d'élasticité ($Rp_{0,2}$), résistance maximale à la traction (Rm) et allongement à rupture (A%)). Ceci a été relié à la présence des défauts d'entailles à la surface qui agissent comme concentrateurs de contraintes. Après attaque chimique, les propriétés de résistance ($Rp_{0,2}$ et Rm) sont semblables à celles des échantillons usinés grâce à l'impact positif de ce post-traitement sur les défauts surfaciques. Une amélioration de la ductilité est aussi observée. Neanmoins, à cause de la présence résiduelle de certains sites de concentration de contraintes à la surface, la ductilité demeure limitée par rapport aux valeurs standards rapportées dans la littérature pour des échantillons usinés. Une relation linéaire a pu être établie entre la rugosité des échantillons et leur allongement à rupture.

Une amélioration de la ductilité a également été observé pour les échantillons ayant subis un traitement CIC. Cette amélioration a été attribuée à la fois à la fermeture des défauts internes induite par le traitement et à son impact sur la microstructure. Concernant ce dernier, la CIC induit une diminution de la densité de dislocations et un grossissement de la microstructure, tout deux pouvant impacter positivement la ductilité. Par ailleurs, une légère diminution de $Rp_{0,2}$ et Rm a été observée. Enfin, la combinaison de ces deux post-traitements (attaque chimique et CIC) n'a pas conduit à une amélioration supplémentaire des propriétés mécaniques de ces éprouvettes.

Malgré les améliorations obtenues grâce aux post-traitements, les propriétés rapportées pour des éprouvettes usinées n'ont donc pas été égalées. Par conséquent, des facteurs d'abaissement ont été suggérés afin de tenir compte des pertes de propriétés causées par un état brut de fabrication ou post-traité. De tels facteurs pourraient ensuite être utilisés pour déduire les propriétés de traction de structures cellulaires brutes de fabrication ou post-traitées à partir de simulation numériques réalisées sur des géométries parfaites.

Chapitre 3 : Propriétés de fatigue et influence des défauts

Une fois le matériau caractérisé et les propriétés de traction déterminées, les propriétés en fatigue des poutres unitaires fabriquées par EBM ont été étudiées. En se basant sur les résultats du chapitre précédent, pour chaque éprouvette, la section moyenne au sein de sa zone utile a été utilisée pour calculer les niveaux de contrainte. Les essais de fatigue ont été réalisés à contrainte constante à une fréquence f = 10 Hz. Les conditions d'essai (sollicitation uniaxiale de traction, ratio R=0.1) ont été choisie de manière à remplir les exigences aéronautiques.

Les essais de fatigue ont dans un premier temps été réalisés sur les éprouvettes brutes de fabrication élaborées dans les trois orientations. La comparaison des résultats de ces essais (limite de fatigue à 10^7 cycles $\sigma_f = 140$ MPa pour des éprouvettes verticales) avec ceux obtenus par ARCAM pour des échantillons usinés (limite de fatigue à 10^7 cycles $\sigma_f = 400$ MPa) montrent une importante diminution des propriétés en fatigue. Cette diminution a pu être reliée à la présence des défauts surfaciques. En effet, l'observation des faciès de rupture au Microscope Électronique à Balayage (MEB) a montré que, dans tous les cas, la fissure reponsable de la rupture avait amorcé depuis la surface. Une fois couplée avec la comparaison des images tomographiques avant et après rupture, le défaut critique ainsi que sa morphologie ont pu être déterminés. Dans tous les cas, c'est un défaut d'entaille ou un défaut d'empilement en "pile d'assiettes" qui a été responsable de la rupture. L'impact négatif de ces défauts sur les propriétés de fatigue des éprouvettes a pu être pris en compte en utilisant les diagrammes de *Kitagawa-Takahashi*. Les diagrammes classiques pour des durées de vie longues ($> 5.10^5$ cycles) ainsi que des approches modifiées afin de considérer des durées de vie plus courtes ont été appliquées avec succès.

Les résultats des essais de fatigue ont également montré que l'orientation de fabrication affecte les propriétés en fatigue des éprouvettes brutes de fabrication. Cela a été attribué à l'influence de l'orientation de fabrication sur la densité, la taille et l'orientation des défauts surfaciques et notamment les défauts d'entailles à partir desquels la fissure amenant à la rupture est la plus suspectible d'amorcer. Par conséquent, les moins bonnes et les

meilleures performances en fatigue ont respectivement été obtenues pour les échantillons verticaux et horizontaux (durée de vie moyenne à 290 MPa = 55 000 et 250 000 cycles).

Enfin, il a été démontré que les mesures de rugosité ne sont pas significativement impactées par les défauts d'entailles (fins et profonds) responsable pour l'amorçage des fissures de fatigue. Cela signifie qu'aucune corrélation directe ne peut être établie entre les mesures de rugosité et les résultats des essais de fatigue. Par conséquent, la rugosité ne semble pas être le bon critère pour prédire la performance en fatigue d'éprouvettes brutes de fabrication élaborées par fabrication additive.

En ce qui concerne les structures cellulaires, le dimensionnement et la conception de structures résistantes à la fatigue ne peuvent définitivement pas être basés sur les propriétés en fatigue d'éprouvettes massives usinées. Une telle approche amènerait à des conclusions érronées et non-conservatives comme l'ont montré les résultats de fatigue précédents. En terme de fabrication, l'impact de l'orientation de fabrication a montré qu'il serait judicieux de construire les structures cellulaires de manière à ce que la quantité de poutres verticales soit la plus faible possible et inversement pour les poutres horizontales.

La résistance à la fatigue réduite des poutres unitaires brutes de fabrication a confirmé la nécessité de les améliorer par des post-traitements. Dans ce sens, l'influence de l'attaque chimique et du grenaillage ultrasonique a été étudiée. Leur combinaison respective avec un traitement CIC a aussi été considérée.

Bien qu'elles demeurent inférieures à celles rapportées pour des éprouvettes usinées, une amélioration significative des performances en fatigue a été observée grâce à l'importante réduction de la criticité des défauts d'entailles induite par l'attaque chimique (limite de fatigue à 10^7 cycles $\sigma_f = 220$ MPa pour des éprouvettes verticales après attaque chimique). Par ailleurs, comme il avait été observé dans le chapitre 1 que l'impact de l'orientation de fabrication sur ces défauts persistait après attaque chimique, la même tendance a été obtenue pour les résultats des essais de fatigue. Pour toutes les éprouvettes verticales ainsi que pour la plupart de celles fabriquées à 45°, la rupture de fatigue a été provoquée par la partie restante d'un défaut d'entaille. Dans le cas contraire, des défauts d'empilement en "pile d'assiettes" ou des défauts internes devenus surfaciques à cause de l'attaque chimique ont été identifiés comme sites d'amorçage des fissures. Par conséquent, si des durées d'attaque plus longues permettait d'obtenir une suppression complète de tous les défauts en forme d'entailles, la résistance à la fatigue des éprouvettes verticales - et potentiellement celle des éprouvettes à 45° - pourrait connaître une amélioration supplémentaire.

Après grenaillage, les résultats de fatigue obtenus sont semblables à ceux rapportés pour des éprouvettes usinées (limite de fatigue à 10^7 cycles $\sigma_f = 400$ MPa pour des éprouvettes verticales (orientation la moins résistante) après grenaillage). La fissure provoquant la rupture amorce systématiquement à partir d'un défaut sub-surfacique. L'observation des images tomographiques avant et après grenaillage montre que ce defaut correspond à chaque fois à la racine d'un défaut d'entaille résultant d'un "remplissage" incomplet qui l'a transformé en un défaut sub-surfacique réduit. Cependant, l'observation des faciès de rupture par MEB a montré que le "remplissage" provoqué par le grenaillage n'induit aucune cohésion de la matière. Cela signifie que la taille réelle du défaut est proche de sa taille à l'état brut de fabrication. Cette taille a donc grandement été sous-estimée sur les images tomographiques et, par conséquent, cette technique de caractérisation n'est pas

fiable pour déterminer la santé matière d'une éprouvette après grenaillage. Par ailleurs, cette importante taille de défaut implique également que l'amélioration de la résistance en fatigue induite par le grenaillage n'est pas causée par le "remplissage" des défauts mais plutôt par les importantes contraintes résiduelles de compression mesurées à la surface.

L'impact de la CIC sur les performances en fatigue semble dépendre de l'état de surface des échantillons. D'un côté, aucune amélioration n'a été observée lorsque ce traitement a été appliqué à des éprouvettes brutes de fabrication. D'un autre côté, quand la CIC est appliquée avant une attaque chimique ou du grenaillage, la résistance en fatigue est améliorée de manière significative (par exemple, limite de fatigue à 10^7 cycles $\sigma_f = 290$ MPa pour des éprouvettes verticales après CIC + attaque chimique). Et ceci malgré l'absence de sites d'amorçage internes. Cet effet bénéfique de la CIC a été attribué au grossissement de la microstructure. En effet, il a été montré dans la littérature que cela améliorait la résistance à la propagation des fissures de l'alliage Ti-6Al-4V élaboré par EBM.

Les trois post-traitements (CIC + attaque chimique + grenaillage) ont été combinés dans une tentative d'obtention d'éprouvettes vierges de défauts. Des tests supplémentaires sont nécessaires pour atteindre cet objectif mais une amélioration de la résistance en fatigue a déjà été obtenue (+50 MPa pour un durée de vie donnée).

Chapitre 4 : Detection des défauts critiques and prediction de la résistance en fatigue

Le chapitre précédent a montré que la résistance en fatigue des éprouvettes est profondément liée à la présence de défauts surfaciques et plus précisément à la présence de défauts en forme d'entailles. Une méthode pour les détecter automatiquement et pour évaluer leur criticité à partir d'une technique de contrôle non destructif (tomographie aux rayons X) a donc été développée.

La méthode d'identification des défauts critiques proposée repose exclusivement sur l'utilisation des images des éprouvettes obtenues par tomographie de laboratoire aux rayons X. Tous les défauts en forme d'entailles sont distingués des autres défauts surfaciques grâce à leur empreinte géométrique distinctive : une importante variation locale de la hauteur de la surface. Plusieurs opérations de traitement d'images ont été nécessaires pour obtenir pour chaque éprouvette une carte de sa surface sur laquelle apparaissent les variations locales de la hauteur de la surface. Une fois correctement seuillées, seules les défauts en forme d'entailles sont visibles sur ces cartes. Les mesures des aires projetées de tous les défauts détectés ont ensuite été réalisées à partir des images tomographiques. Ces mesures ont alors été utilisées pour déterminer la criticité de ces défauts en utilisant le paramètre de Murakami $\sqrt{aire}$. Enfin, les défauts ont été reportés sur des diagrammes de *Kitagawa-Takahashi* à partir desquels la résistance en fatigue d'un échantillon peut être déterminée à partir de sa distribution de défauts.

Cette méthode a été appliquée avec succès aux éprouvettes ayant subies une attaque chimique. Pour la grande majorité des éprouvettes ayant rompues au cours des essais de fatigue, le défaut responsable de la rupture est demeuré visible sur la carte de surface après seuillage. Cela signifie qu'il a correctement été identifié par la méthode comme l'un des défauts les plus critiques. De plus, les diagrammes classiques de *Kitagawa-Takahashi* permettent de correctement prédire la rupture par fatigue ou la durée de vie infinie ($>3.10^6$

cycles) de la plupart des éprouvettes. Par ailleurs, dans le cas des éprouvettes horizontales ou de celles fabriquées à 45°, des diagrammes adaptés au durée de vie finies ont permis de prédire avec succès la durée de vie des éprouvettes rompues.

Cependant, dans la plupart des cas, le défaut provoquant la rupture de l'éprouvette n'a pas été identifié comme le plus critique par la méthode dans la mesure où ce n'est pas le défaut avec la plus grande aire projetée. Une tendance a néanmoins été observée : le défaut responsable de la rupture possède toujours une racine aigüe. Le faible rayon de courbure correspondant augmente la propension du défaut à amorcer une fissure, ce qui semble donc impacter sa criticité. Ce paramètre n'a pas été pris en compte dans le calcul de criticité et cela tendrait à expliquer pourquoi le défaut critique n'est pas correctement identifié. La prise en compte de ce critère pourrait donc améliorer l'efficacité de la méthode.

Par ailleurs, il a été observé que l'attaque chimique n'affecte pas de manière homogène la racine de tous les défauts en forme d'entailles. Cela implique que les défauts les plus critiques à l'état brut de fabrication et après attaque chimique pourraient différer. Une analyse plus poussée est nécessaire pour établir un potentiel lien entre la forme du défaut à sa racine et l'efficacité de l'attaque chimique.

Cette méthode de détection a également été appliquée aux éprouvettes brutes de fabrication, mais avec un succès plus relatif. Les cartes de surface obtenues ont permis de visualiser avec une plus grande précision l'impact de l'orientation de fabrication sur l'état de surface et plus particulièrement sur la population de défauts surfaciques. Une bonne corrélation a pu alors être faite entre la quantité de défauts restants sur des cartes de surface seuillées obtenues pour des éprouvettes de différentes orientations et les résistances en fatigue des échantillons correspondants. Cela n'avait pas pu être fait par l'utilisation de paramètres géométriques simples tels que la rugosité de surface. Cependant, à cause de l'état de surface complexe et plus particulièrement à cause des poudres collées et des défauts non perpendiculairement orientés par rapport à l'axe du cylindre, pour de nombreux défauts, la méthode renvoie des valeurs de hauteur de la surface erronées. Cela rend pour le moment la méthode non applicable aux éprouvettes brutes de fabrication. Une solution pour remédier à cette limitation serait de supprimer les causes de ces erreurs de mesures, par exemple en post-traitant les images tomographiques. Appliquer un post-traitement qui reproduirait les premières minutes d'attaque chimique semble être une voie prometteuse.

Conclusion et perspectives

Cette thèse a permis d'avoir une meilleure compréhension de l'impact des défauts générés par la fabrication EBM sur les propriétés de fatigue de poutres unitaires à l'état brut de fabrication ou post-traitées. Ce travail a montré que les défauts en forme d'entailles ou leur partie restante étaient responsable de la rupture des éprouvettes et de la diminution de le résistance à la fatigue. Une méthode permettant de détecter automatiquement tous les defauts de ce type à partir d'images tomographiques a été proposée. À partir de cette méthode, ce travail de thèse a permis de prédire de manière conservative la résistance en fatigue de tout échantillon attaqué chimiquement simplement à partir de sa distribution de défauts détectés.

Dans la continuité de cette thèse, trois voies peuvent être envisagées :

- continuer à améliorer la résistance en fatigue de poutres unitaires ;
- améliorer la prédiction de la résistance et l'étendre à d'autres types d'éprouvettes;
- étendre les résultats de cette étude à l'échelle des structure cellulaires.

Une amélioration supplémentaire de la résistance en fatigue des éprouvettes peut se faire par le biais d'une optimisation des paramètres de fabrication ou des post-traitements et de leur combinaison. Concernant les paramètres de fabrication, l'analyse des défauts internes et surfaciques réalisée au cours de cette étude semble indiquer que les conditions de fusion du contour des échantillons peuvent être améliorées (plus grande densité de défauts internes dans cette zone). Un travail peut également être mené afin de limiter la présence de défauts en forme d'entaille à la surface des éprouvettes. Au niveau des post-traitements, la combinaison (CIC + attaque chimique + grenaillage) semble prometteuse pour obtenir des éprouvettes vierges de défauts. Un des paramètres clés est la durée de l'attaque chimique avant grenaillage afin d'empêcher le piégeage de la racine des entailles les plus profondes. Une simulation de l'étape d'attaque pourrait aider à optimiser cette durée. Une fois ces défauts supprimés, la résistance en fatigue de ces éprouvettes est supposée être grandement améliorée et dépasser celle des éprouvettes usinées grâce aux contraintes résiduelles de compression présentes à la surface des échantillons.

Afin d'améliorer la prédiction de la résistance en fatigue d'une éprouvette attaquée chimiquement, la méthode de détection doit être capable de définir le défaut amenant à la rupture comme le plus critique pour la fatigue. Comme montré dans le chapitre 4, prendre en compte le rayon de courbure à la racine du défaut semble primordial et doit être à la base d'une prochaine étude. L'amélioration de la méthode passe aussi par son adaptation à des surfaces complexes telles que celles des éprouvettes brutes de fabrication. La suppression des sources d'erreurs de mesure (poudres collées, ...) en simulant les premières minutes de l'attaque chimique semble être une piste à explorer. Enfin, une telle méthode pourrait également être utilisée pour déterminer les défauts susceptibles d'être piégés durant le grenaillage.

Concernant le transfert des résultats acquis sur les poutres unitaires à des structures cellulaires, les premiers résultats obtenus sont présentés ci-après. Tout d'abord, une géométrie d'éprouvette pertinente a été définie. La cellule unitaire choisie est un "octet-truss" dont les poutres subissent uniquement des efforts de traction et de compression (sollicitations cohérentes avec les essais de fatigue réalisés sur les poutres unitaires). Le nombre de cellules au sein d'une éprouvette (4 cellules superposées) a été délibérément réduit afin de pouvoir observer plus facilement les mécanismes de rupture. Afin de s'assurer que la rupture aura bien lieu au sein de la structure cellulaire, un gradient de porosité a été intégré (poutres coniques dans les cellules aux extrémités de la structure). De la même manière, des congés ont été ajoutés aux nœuds afin de localiser les contraintes dans les poutres. Les résultats de la thèse ont ensuite été utilisés afin de déterminer l'orientation de fabrication optimale (aucune poutre verticale).

Les premiers essais de fatigue ont confirmé le bon choix d'éprouvette puisque la rupture a toujours lieu au centre de ces dernières. Un scénario de rupture a pu être établi. Dans un premier temps, plusieurs poutres internes rompent successivement jusqu'à ce qu'une

poutre externe rompe à son tour. Des ruptures de poutres en cascade ont alors lieu ce qui amène à la rupture complète de l'éprouvette. La rupture des poutres a toujours lieu à une de ses extrémités, proche d'un congé, au niveau des concentrations de contraintes observées sur les simulations par éléments finis. Cette rupture progressive a permis de distinguer deux phases dans la durée de vie d'une éprouvette. La durée de vie jusqu'à la rupture de la première poutre correspond à la phase d'*amorçage de la rupture* tandis que le reste de la durée de vie est appelé phase de *propagation de la rupture*. La durée relativement longue de la phase de propagation ($\sim 25\%$ de la durée de vie totale) peut s'avérer utile dans le cadre d'applications de détection de l'endommagement d'une pièce.

Un autre point a été de s'assurer de l'applicabilité des post-traitements à des structures cellulaires. La CIC et l'attaque chimique ont été appliquées avec succès aux éprouvettes cellulaires. L'attaque chimique a ainsi impacté de manière similaire toute la surface de l'éprouvette confirmant ainsi la bonne homogénéité de ce procédé. Par contre, l'effet du grenaillage n'est pas homogène. En effet, les billes d'acier utilisées ne sont pas suffisamment petites pour impacter les noeuds des cellules qui conservent donc une importante rugosité de surface. Des essais supplémentaires (réduction de la taille des billes) sont nécessaires pour améliorer ce point.

Une autre piste de travail est la mise en relation des résultats de fatigue de ces structures cellulaires avec ceux obtenus pour les poutres unitaires durant la thèse. Si les niveaux de contraintes dans les poutres des cellules s'avèrent être similaires à ceux des poutres unitaires, les résultats obtenus sur ces dernières pourraient alors être directement utilisés pour le dimensionnement de structures cellulaires intégrées dans des pièces industrielles. Cela permettrait à plus long terme de remplacer des pièces aéronautiques actuelles par des pièces hybrides contenant à la fois des parties massives et des structures cellulaires.

Introduction

Context

Nowadays, reducing the energy consumption is crucial for most of the industries. For transportation industries, it can be achieved through weight reduction. Through their combination of void and matter, lattice structures are extremely promising in this regard. However, until recently, it was very challenging to build such metallic lattice structures with conventional processes as multiple steps were required. With the emergence of powder-bed based additive manufacturing techniques such as selective laser melting (SLM) and electron beam melting (EBM), producing such structures is becoming easier. Indeed, their layer-by-layer manufacturing process enables a geometrical freedom unmatched by conventional techniques (Figure 1).
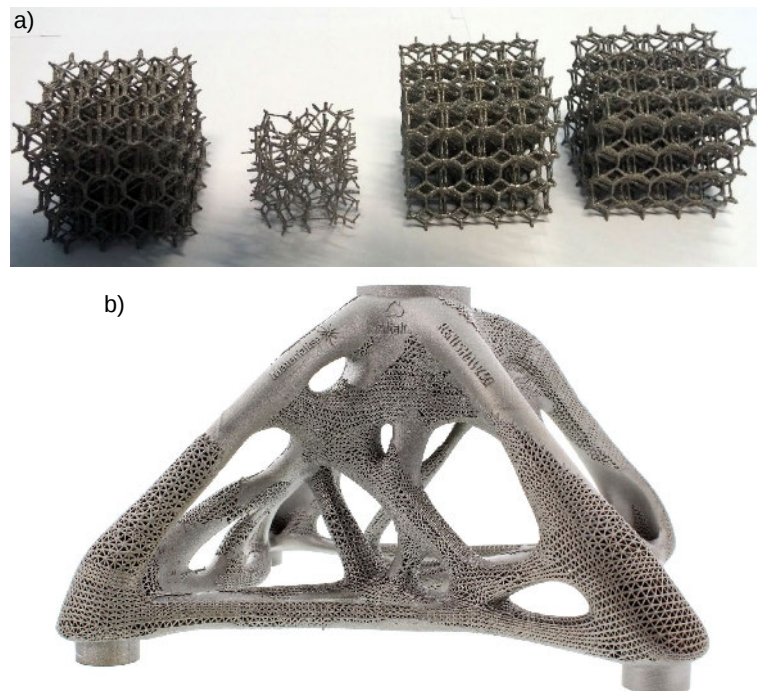

Figure 1: (a) Examples of manufactured lattice structures [SUA 15b]. (b) Example of a "spider" bracket integrating lattice structures[1].

---

[1]picture taken from https://resources.renishaw.com/gen/details/spider-bracket–78307

In order to integrate such structures in industrial parts, one needs however to determine reliable mechanical properties for the manufactured lattices. In aircraft industry, damage caused by cyclic mechanical loading is the main cause of parts failure. Determining both static and fatigue properties of lattice structures is therefore becoming a necessity. More precisely, the *tensile* fatigue properties are of interest for materials certification.

Besides, additive manufacturing is a process that generates internal defects as well as rough surfaces. Such features can have a significant detrimental impact on the mechanical properties. In the case of lattice structures, the important surface-to-volume ratio is likely to aggravate this detrimental impact. There is therefore a need to study in details how such defects affect the static and fatigue properties and how this impact can be limited.

This PhD work was undertaken in the frame of an ANR funded project , the FA^{2}SCINAE project[2]. It aims at investigating the fatigue properties of parts integrating lattice structures and obtained by additive layer manufacturing. It focuses on a specific technology (Electron Beam Melting) and a specific material (Titanium alloy Ti-6Al-4V which is extensively used in aeronautics). The objectives of the work and the organisation of this manuscript are detailed below.

PhD-objectives

Launched in November 2015, the final aim of the FA^{2}SCINAE project is to integrate lattice structures in re-designed aeronautical parts. The first step is the microstructural and mechanical characterization of lattices structures. Once fatigue mechanisms are identified, a second step is to try and improve the fatigue properties of such structures through the use of different post-treatments. From both steps, recommandations regarding the manufacturing and post-treatments processes can be drawn.

After this academic part of the project, the re-design of aeronautic parts, in a weight saving perspective, takes place. This re-design heavily relies on the recommandations previously drawn. Manufacturing and testing of the re-designed parts are the last two steps of the project.

The present PhD-work is part of the academic study. The aim of this PhD thesis is thus to understand the mechanisms that govern the fatigue behavior of such lattice structures. In this regard, the unitary element of these structures is considered: the strut. First, as-built thin struts are characterized and their resulting static and fatigue properties are determined. Second, the potential improvement of those properties through several post-treatments is studied. The main goal here is not to compete with the fatigue resistance of traditionally manufactured samples but rather to achieve the best fatigue properties by means that can later be applied to lattice structures. Finally, a method enabling to predict the fatigue resistance of struts directly from their characterization by non-destructive means is sought. This third axis of research is based on the results of the fatigues tests and on their detailed analysis. At the end of this work, recommandations regarding the manufacturing and post-treatment of lattices structures are expected.

---

[2]Project FA2SCINAE-ANR-15-CE08-0038-03 entitled "Fabrication Additive et FAtigue de Structures Cellulaires Intégrées en AEronautique". Project initiator: SIMAP (Grenoble INP). Partners: G-SCOP (Grenoble INP), MATEIS (INSA Lyon), Poly-Shape and AIOP (AIRBUS Operation SAS)

PhD-manuscript outline

This current PhD-manuscript is composed of 4 chapters organized in the following manner:

- **Chapter 1** is focused on the material characterization of Ti-6Al-4V samples manufactured by EBM. A literature survey of the microstructure of EBM sample is given. The thin struts samples built in this study are characterized in the as-built conditions. Based on those results, several post-treatments are reviewed to improve both the internal and surface conditions. The most promising ones (Hot Isostatic Pressing, Chemical Etching and Ultrasonic Shot Peening) are applied and their respective impact studied.

- **Chapter 2** considers the tensile properties of thin struts in as-built and post-treated conditions. An appropriate way to measure the tensile stresses in such samples is first discussed. This approach is then used to compare the struts tensile properties with those of machined samples reported in the literature. Causes for the potential discrepancies are suggested based on the results from **Chapter 1**.

- **Chapter 3** presents the results from fatigue tests performed on thin struts. In as-built conditions, the defects responsible for fatigue failure are identified. Their impact on the fatigue properties is then analyzed. Tools such as classical and modified *Kitagawa-Takahashi* diagrams are proposed to predict this impact. Post-treated samples are also tested. The impacts of the post-treatments on fatigue properties are analyzed in light of their impact on the AM defects which were discussed in **Chapter 1**. All post-treatments are also combined in an attempt to achieve defect-free samples.

- **Chapter 4** proposes a method for the prediction of the fatigue resistance of EBM samples. The successive image processing operations of the tomographic images mandatory for the detection of all potentially harmful defects are first detailed. A methodology is proposed to determine the criticality of the detected defects. The efficiency of this method is first assessed on chemically etched samples. Its application to as-built samples is also discussed.

This manuscript ends with a conclusion which summarizes the major results obtained during this study. Different perspectives are suggested, with an emphasis on the application of these results to lattice structures. To this aim, the following questions are to be answered:

- Is the study of the fatigue mechanisms of a single strut sufficient to understand those of a complete structure or is there a structural effect ?
- Can the post-treatments be efficiently applied to lattice structures ?

© 2018 – Théo PERSENOT – MATEIS *laboratory*

<div align="right">

Chapter 1

</div>

<div align="center">

Material characterization

</div>

Contents

1.1 Microstructure of Ti-6Al-4V

The Ti-6Al-4V alloy presents a good combination of high strength at relatively low temperature, light weight and high corrosion resistance. This makes it very attractive for the aerospace industry. Its additional great biocompatibility explains why it is also widely used in the biomedical industry. Examples of applications in the aerospace industry are, amongst others, aircraft structural parts or rotating parts in turbines. For obvious reasons

(weight saving, complex shapes, ...), those domains of applications can benefit from additive manufacturing. This explains why Ti-6Al-4V is the most additively manufactured metallic material and why this study is focused on it.

1.1.1 Chemical composition and microstructure of Ti-6Al-4V

The chemical compositions of the Ti-6Al-4V and Ti-6Al-4V ELI materials according to the ASTM F1108 [F11 14] and F136 [F13 13] standards are shown in Table 1.1. ELI stands for "Extra Low Interstitials" meaning that the Ti-6Al-4V ELI material contains reduced levels of carbon, iron, oxygen and nitrogen. Such a chemical composition is reported to provide improved ductility and better fracture toughness, [WEL 93]. That is the reason why it will be used in this study.

Table 1.1: Chemical composition of the Ti-6Al-4V and Ti-6Al-4V ELI materials according to respectively the ASTM F1108 and F136 standards.

Elements	Al	V	C	Fe	O	N	H	Ti
Ti-6Al-4V (wt%)	5.5-6.75	3.5-4.5	< 0.1	< 0.3	< 0.2	< 0.05	< 0.01	Bal.
Ti-6Al-4V ELI (wt%)	5.5-6.5	3.5-4.5	< 0.08	< 0.25	< 0.13	< 0.05	< 0.01	Bal.

This alloy is an $\alpha + \beta$ alloy because of the presence of aluminium (α stabilizer) and vanadium (β stabilizer). Figure 1.1 shows a schematic pseudo-binary phase diagram of such alloys for a varying percentage by weight of V. For Ti-6Al-4V (whose composition is represented by the red dashed line), an $\alpha + \beta$ alloy is obtained at room temperature [LÜT 98].
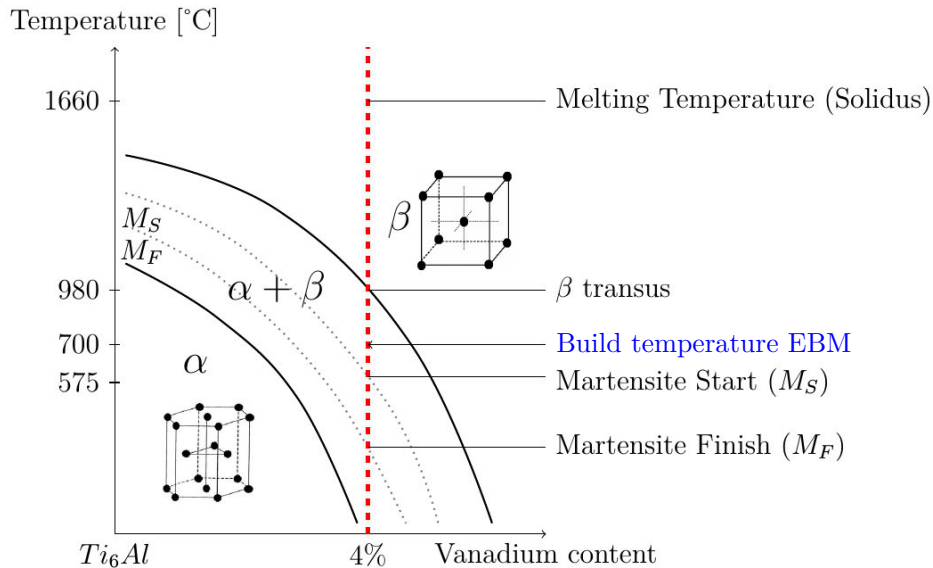
Figure 1.1: Schematic pseudo-binary phase diagram of the Ti-6Al-4V alloy. The red dashed line represents the composition of the Ti-6Al-4V alloy. The melting temperature, β transus, build temperature for EBM as well as the martensite start M_s and finish M_f temperatures are given. Adapted from [SUA 15a].

For high cooling rates ($> 400°C/s$), the martensitic α' phase can be formed between the martensite start M_s ($575°C$) and the martensite finish M_f temperatures leading to an $\alpha + \alpha'$ microstructure [AHM 98].

The microstructure of Ti-6Al-4V depends on the process route used during manufacturing. The traditional manufacturing processes are composed of an homogeneisation step and a recrystallisation step with potentially a hot deformation step in between. An annealing treatment can be performed afterwards. Three types of microstructure can be obtained depending on the recrystallisation temperature and the following cooling rate: fully lamellar, bimodal microstructures or fully equiaxed [LÜT 98]. Examples of such microstructures are respectively shown in Figure 1.2a, 1.2b and 1.2c.
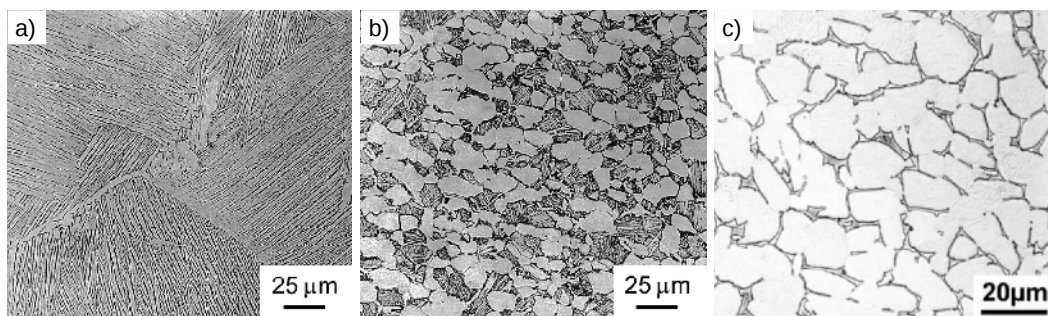
Figure 1.2: Examples of the three types of microstructures observed in Ti-6Al-4V alloys (optical micrographs): fully lamellar (a), bimodal (b) and fully equiaxed (c). The α and β phases are respectively represented in white and black. Adapted from [NAL 02] (a, b) and [LÜT 98] (c).

1.1.2 Ti-6Al-4V produced by EBM

1.1.2.1 Microstructure

During the EBM process, the build plate is maintained at about $\sim 730°C$. The rapid cooling from the melting temperature to this build temperature leads to a fully lamellar microstructure. The slow cooling from this temperature prevents the formation of α' martensitic phases (Figure 1.1). The microstructure consists in fine α laths (width of $\sim 1~\mu m$) with some residual β phase separating them, see e.g. [MUR 09], [SAF 12], [HRA 13], [JUE 14], [SUA 15b]. An example of microstructure is shown in Figure 1.3. Three types of α lamellae can be observed: the α phase that nucleated at the prior β grain boundaries (α_{GB}), the α laths that grew from the grain boundaries (α_P) and new α laths that nucleated at the interface of the α_P (α_W).

A strong anisotropy is reported between planes parallel and perpendicular to the building direction. Prior β grains (width of about 150-200 μm) elongated in the building direction are observed in the first ones whereas no anisotropry is observed on the perpendicular planes (Figure 1.3a and 1.3b respectively).

This columnar β grains have been related to the EBM process. Al-Bermani et al. [ALB 10] and Antonysamy et al. [ANT 13] have shown that, during manufacturing, the re-melting of the previous layers induces a thermal gradient. It provides the conditions
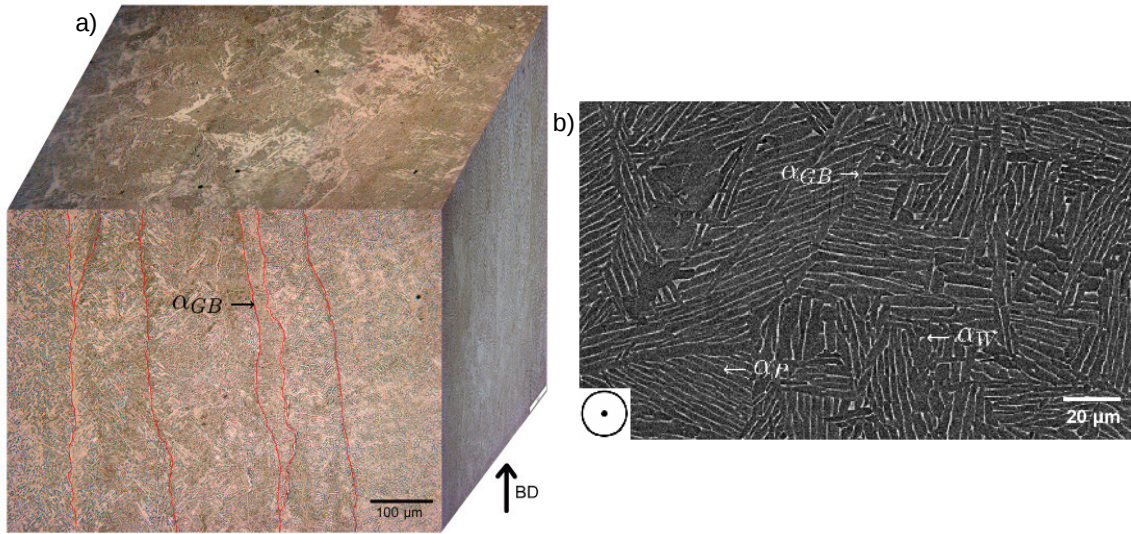
Figure 1.3: (a) 3D optical micrographs from a Ti-6Al-4V sample manufactured by EBM. The boundaries of the prior β grains are hightlighted in red. (b) SEM-BSE micrograph of a plane perpendicular to the build direction at a higher magnification. α_{GB}, α_P and α_W respectively indicate the α phase that nucleated at the prior β grain boundaries, the α laths grown from the grain boundaries and new α laths nucleated at the interface of the α_P. Adapted from [SUA 15b].

for an epitaxial growth of the β phase. Such columnar grains have been reported to grow through the entire build height, see e.g. [ANT 13].

The previous observations have been reported mostly for bulk samples. Antonysamy et al. compared the microstructure of vertical walls with varying thicknesses [ANT 13]. They generated Electron Bask Scattered (EBSD) orientation maps of both the α phase and the parent β phase. They showed that, for samples larger than 1.5 mm, β columnar grains start to grow at the center of the samples and that, for larger walls, such grains go through the entire height of the wall. However, on the sides of the walls, in the first 0.5 mm, the β grains are elongated on a tilted direction. This effect is also observed but less pronounced for the α laths.

Suard compared the microstructures obtained for thin struts (1 mm diameter) and for bulk samples [SUA 15b]. The only discrepancy that he reported concerned the width of the prior β grains which were thinner in struts (70-100 μm v.s. 150-200 μm). Contrary to the findings of Murr et al. [MUR 10] on thin struts, no martensitic α' phase was reported.

1.1.2.2 Porosity

Two types of porosity have been widely reported in the literature: spherical and non-spherical porosity. The spherical defects are *gas pores* containing argon. Tammas-Williams et al. showed that these pores were already present in the initial powder [TAM 15]. The other internal defects are *lack-of-fusion defects*. They are due to bad overlapping between layers [GON 15] or under-melting [HRA 17] which can be caused by unperfect process parameters or melting strategies. These latter defects are most of the time bigger than
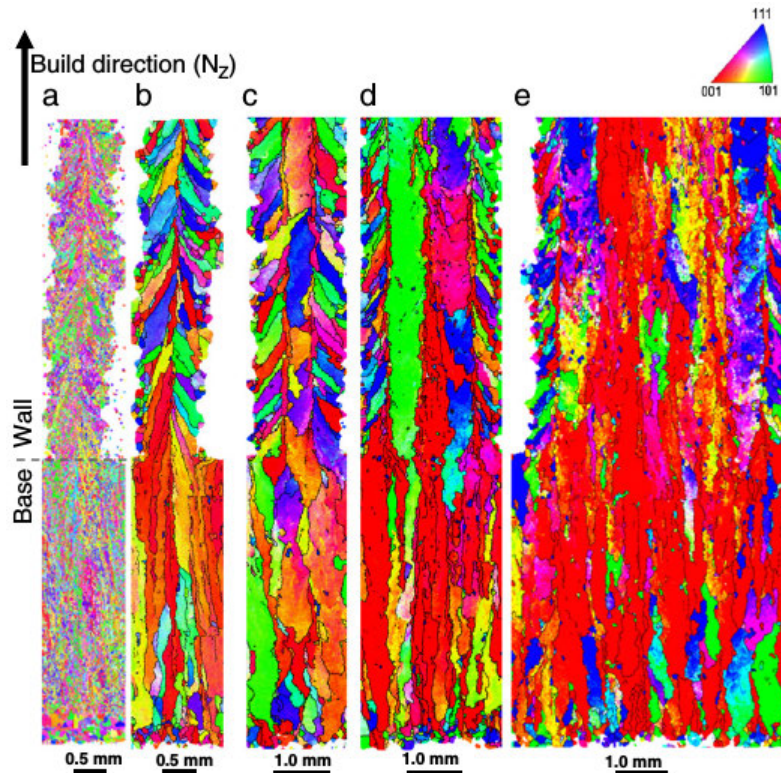
Figure 1.4: EBSD maps from XZ cross sections of vertical walls built on a continuous base. (a) Example of an original α phase map. (b-e) Examples of the reconstructed prior β grains for respectively 1 mm (b), 1.5 mm (c), 2.0 mm (d), and 5 mm wide walls (e). The black lines delineate boundaries (misorientation $> 15°$). The IPF orientation contrast is with respect to the build direction NZ. Adapted from [ANT 13].

the *gas pores*. Examples of pores detected by X-ray tomography are shown in Figure 1.5. Tammas-Williams et al. showed that the melting strategy greatly impacted both the density of defects and their spatial distribution [TAM 15]. For optimized process parameters, the pores volume fraction is extremely limited (always $< 0.1\%$) and very few *lack-of-fusion defects* are detected.

1.2 Experimental procedures

1.2.1 Samples manufacturing

The chemical composition of the initial powder batch is given in Table 1.2 (Ti-6Al-4V grade 23). The as-received Ti-6Al-4V ELI powders were loaded into the ARCAM A1-EBM machine operating at 60 kV accelerating voltage under a controlled pressure of He set to 2.10^{-3} mbar. For each layer, the build plate goes down 50 μm, a layer of powder is deposited and then slightly sintered with a defocused beam and finally selectively melted according to the input CAD geometry. The preheating temperature was maintained at about $\sim 730°C$ throughout the build. The standard "Melt" build theme recommended by
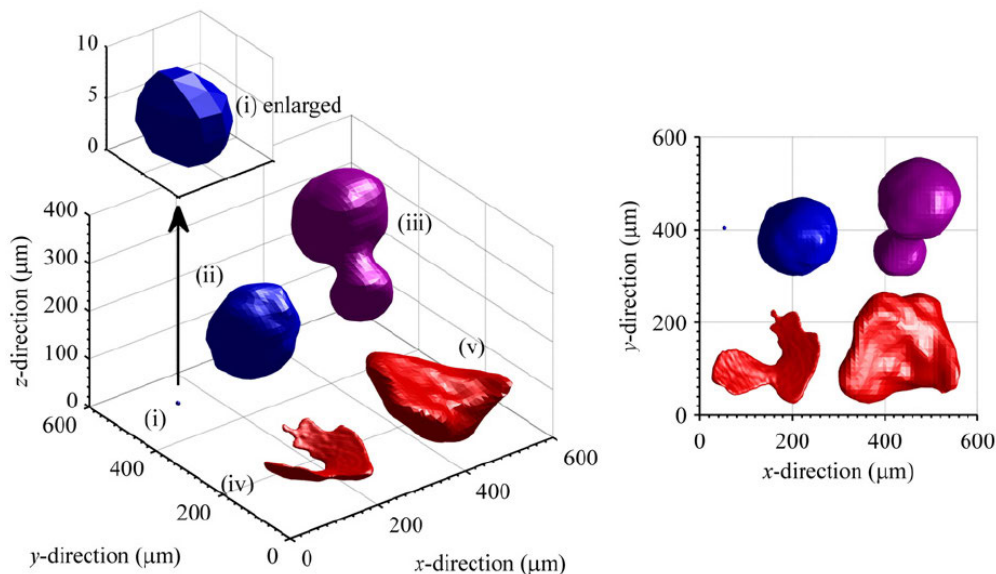
Figure 1.5: Examples of pore types observed in EBM samples: small (i) and large (ii) *gas pores* (blue), (iii) two *gas pores* joined together (turquoise) and small (iv) and large (v) *lack-of-fusion defects* (red). The build direction is shown by an arrow. An enlarged view of (i) is provided in the inset. Low and high resolution X-ray tomographic scans (voxel size = 10 and 2 μm respectively) have been used to respectively detect large (ii, iii and v) and small defects (i, iv). Adapted from [TAM 15].

ARCAM and defined in the EBM Control 3.2 software was used. The melting strategy is illustrated in Figure 1.6. It consists in scanning the area defined by the Computer Assisted Design (CAD) starting with the contours followed by hatching the inner part of the CAD input. During this latter step, the electron beam moves in a snake-like way with a line offset set to 0.1 mm and a line order set to 1. As shown in Figure 1.6, it means that the hatched lines are melted one after the other without skipping any line. The scanning direction is rotated by 90° after every layer.

Table 1.2: Chemical composition of the initial Ti-6Al-4V powder batch used for this investigation.

Elements	Al	V	C	Fe	O	N	H	Ti
wt%	6.47	3.93	0.01	0.22	0.09	0.01	0.001	Bal.

Cylindrical fatigue tensile specimens with a gauge length of 10 mm and a nominal diameter of 2 mm were produced. The small nominal diameter (2 mm) was chosen so as to be representative of a single strut of a lattice structure (large surface-to-volume ratio). These thin specimens were manufactured in three differents orientations: the tensile axis was either perpendicular (vertical sample), tilted at 45° or parallel (horizontal sample) to the build plate, see Figure 1.7.

Throughout this manuscript, the samples manufactured in these three orientations will be respectively referred to as 90° samples, 45° samples and 0° samples. These three orientations have been chosen because they can provide the most useful information on
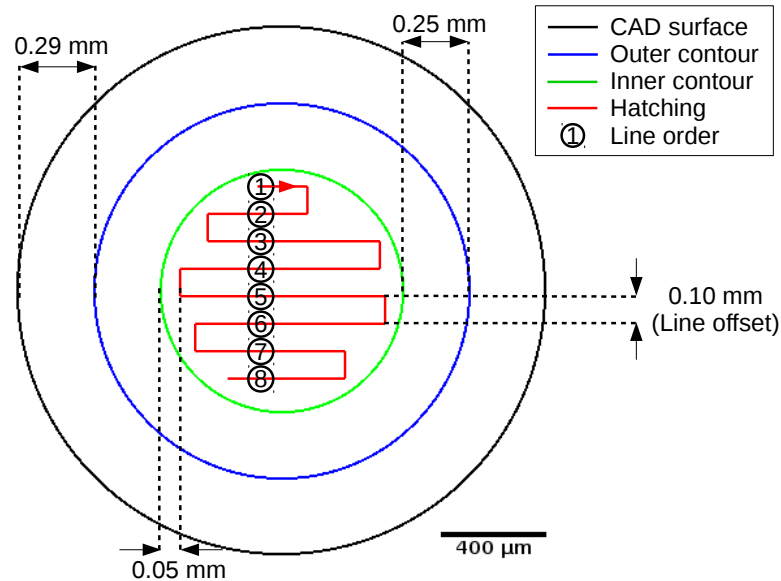
Figure 1.6: Illustration of the melting strategy for a 90° sample. Detailed melting strategy of one layer. The paths followed by the electron beam are represented by colored lines: blue for the outer contour, green for the inner contour and red for the hatching step. The black line represents the CAD surface input. The order in which the hatching lines are melted is indicated by the circles numbers.

the material and mechanical properties of struts in any lattice structure, regardless of its build orientation and unit cell. Indeed, as shown in Figure 1.8 [SUA 15a], for each of these three build orientations, a different thermal behavior occurs during manufacturing:

- From a thermal point of view, 90° samples are manufactured in optimized conditions. For every layer, the area to be melted stands on dense material which ensures a better thermal transfer and thus more controlled manufacturing conditions.

- The case of 0° samples is a special one as the bottom of the samples is directly manufactured on unmelted powder particles which provide a weaker and less controlled heat transfer. The most common way to resolve this situation is the use of removable manufacturing supports which mechanically support the build sample but also enable an effective thermal dissipation. In the case of lattice structures, such supports cannot be used as they would no longer be removable. In order to remain representative of lattice struts, the 0° samples were built without supports despite - and even because of - the special case it represents.

- The case of the 45° samples stands in between these two extreme situations: for each layer, most of the area to be melted stands over dense material and the rest is manufactured on unmelted powder particles. This peculiar situation occurs in parts with complex geometry such as lattice structures. As a result, those samples can be representative of oblique struts, i.e. with a tilted axis with respect to the building direction.
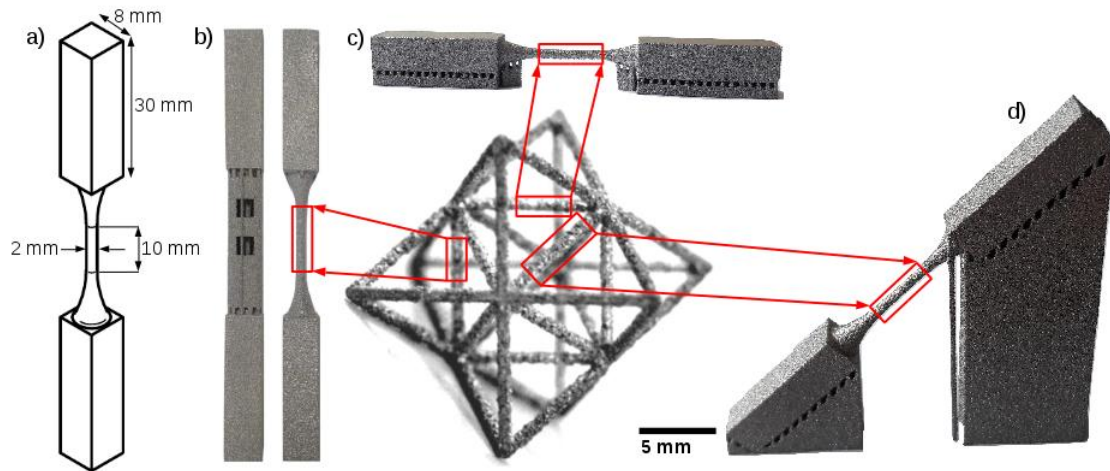
Figure 1.7: Geometry of the fatigue specimens representative of a single strut of any lattice structure (here, an octet truss). (a) 3D isometric view of the Computer Assisted Design (CAD) input. (b-d) Photographs of a lattice unit cell and of the fatigue specimens manufactured in three different orientations before removal of the manufacturing supports (b,c and d for 90°, 0° and 45° samples respectively).
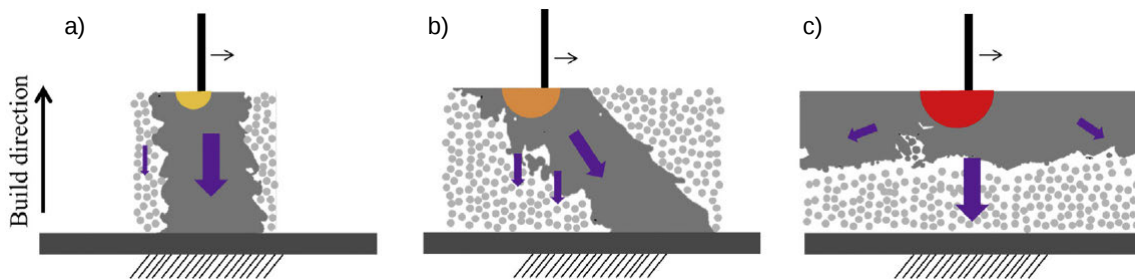
Figure 1.8: Schematic view of the thermal behavior during EBM process for three manufacturing orientations: vertical (a), tilted (b) and horizontal (c). Purple arrows indicate the thermal flux density and direction. The yellow-to-red semi-discs represented the melt pool and their color the efficiency of the thermal dissipation (from high (yellow) to low (red) efficiency). Adapted from Suard et al. [SUA 15a]

1.2.2 X-ray tomography

The full 3D characterization of the gauge length of the fatigue samples was obtained using laboratory X-ray tomography. The fatigue specimens were inspected in the as-built condition with a cone beam phoenix|x-ray V|tome|x laboratory tomograph using a 2.5 μm voxel size (spatial resolution of ~ 4 μm). In order to reduce as much as possible the distance between the sample and the X-ray source, the samples were positioned so that the cylinder axis was vertical in the chamber. This way, only 5 scans were required at different heights along the sample axis so that the whole gauge length could be visualized. The following scanning parameters were used: voltage V = 90 kV, current I = 240 μA, exposure time = 333 ms, 720 projections per scan. No filter was needed. The scanning time per sample (over its entire gauge length) was roughly 1 h. The reconstruction of the

3D images was performed using a standard filtered back projection method (phoenix datos x software). The reconstructed volumes were then post-treated and analyzed using Fiji software. The volume fraction of porosity was obtained through thresholding the 8 bits gray scale images. As the noise in the reconstructed images can generate some parasitic features during the thresholding step, features with a volume smaller than 8 voxels (cube of 2*2*2 voxels) were disregarded in the analysis. The samples were scanned in the as-built condition and after the different post-treatments that will be discussed later in this chapter.

Following the method initially suggested by Suard et al. [SUA 15a], the roughness was measured based on tomographic images. A series of profiles of the surface was extracted from a radial slice every 10° around the sample circumference (Figure 1.9). The 36 profiles obtained by this procedure for each sample were then used to compute several roughness measurements:

- the average roughness R_a which is the arithmetic average of the absolute values of the profile heights along the gauge length.
- the maximum roughness R_t which is the vertical distance between the highest and lowest points of the profile.
- the maximum profile valley depth R_v which is the distance between the lowest point (deepest valley) of the profile and the mean line along the gauge length.

More details about this method can be found in [SUA 15a] and [PER 18].

1.2.3 Profilometry

The roughness values obtained with the previous method have been compared to measurements performed with an INTRA2 Talysurf profilometer from Taylor Hobson based on the NF EN ISO 4288 standard [ISO 96]. Samples were attached to a table allowing micrometric displacements and roughness profiles were acquired along the gauge length using a conical diamond tip with a radius of 2 μm.

1.2.4 Microstructure characterization

Optical microscopy (OM) and Scanning Electron Microscopy (SEM) were used to characterize the microstructure. The SEM observations were performed using a SEM-FEG ZEISS ULTRA 55. Cross sections from as-built samples were mechanically grinded using SiC paper down to 2500 grit and polished with a solution consisting of 90% colloidal silica suspension and 10% H_2O_2. The resulting polished cross sections were observed with the backscattered electron detector to reveal microstructure details while the fracture surfaces were investigated using secondary electrons. For optical microscopy, the polished cross sections were then etched with the Kroll's reagent (93% H_2O, 6% HNO_3, 1% HF) in order to reveal the microstructure. The same protocol was used for the characterization of samples submitted to different post-processing operations which are discussed later in this chapter.
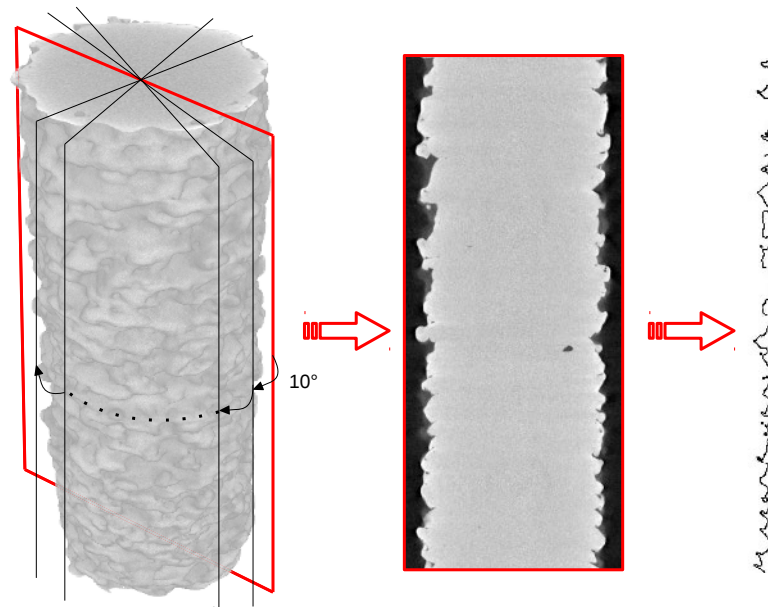
Figure 1.9: Schematic illustration of the methodology used to estimate the sample surface roughnesses based on the X-ray tomography scans. A surface profile is extracted from a radial slice every 10° around the sample circumference. The roughnesses (R_a, R_t and R_v) of the samples are then computed along these 36 profiles.

1.2.5   Residual stresses measurement

Surface residual stresses have been estimated by X-ray diffraction with the $\sin^2\Psi$ method using an AST X3000 diffractometer and the Ti-Kα radiation with an acceleration voltage of 28 kV. The method consists in focusing an X-ray beam at the sample surface and measuring the diffraction angle at which the X-rays are diffracted towards the dectectors. The interatomic distance measured from the diffraction angle can be used to evaluate the level of residual strain/stress at the sample surface.

In order to measure the stresses in a given direction, the $\sin^2\Psi$ method described in the standard NF EN 15305 [AFN 09] has been used. It consists in measuring the evolution of the diffraction angle when the incidence angle is varied (Figure 1.10). The diffraction peaks can then be used to measure the residual stresses.

If the diffraction peaks cannot be used to measure the residual stresses (limited number of counts, ...), average measurements by rotation can be performed. The sample is fixed on a plate set in rotation with the area to be analyzed centered on the axis of rotation. Thanks to the rotation (50 rounds per minute), the number of counts for this area is significantly increased and diffraction peaks with a good signal-to-noise ratio are obtained. The average residual stress is then computed on 360°. Both experimental setups (with or without the rotative plate) are shown in Figure 1.11.
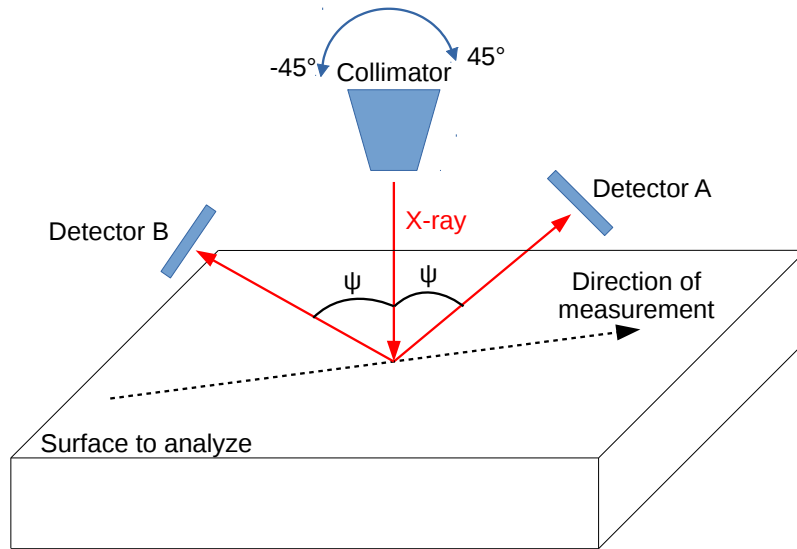
Figure 1.10: Schematic illustration of the $\sin^2\Psi$ method used to measure residual stresses in a given direction based on X-ray diffraction. The X-ray source is rotated so that the incidence angle varies between -45° and 45°. For each angular position, the diffraction angle is measured.
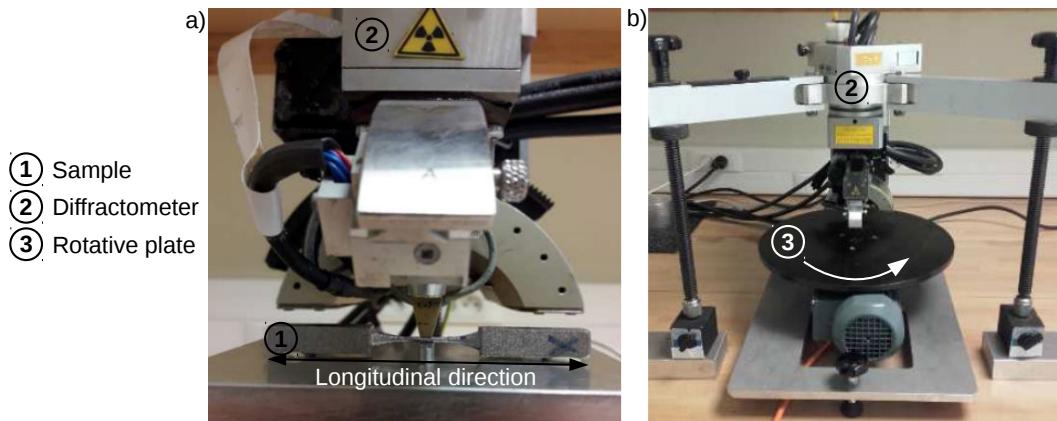
Figure 1.11: Pictures of the experimental setups used to measure residual stresses by X-ray diffraction. (a) Example of a measurement in the longitudinal direction. (b) Setup for the measurement of the average residual stress. The diffractometer is coupled with a rotative plate on which the sample is fixed.

1.3 As-built samples

1.3.1 Comparison to the CAD input

In order to assess the reliability of the EBM process, it is important to compare the geometry of the manufactured samples to the CAD input. The 3D rendering of the samples shown in Figure 1.12 shows the visual aspect of as-built samples fabricated in the three different orientations. Although the roughness of the samples surfaces appear

to be important for all surfaces except for the top surface of 0° samples, the cylindrical shape of the samples gauge length is rather well respected. Figure 1.12 also highlights the impact of the build orientation on the sample geometry. For instance, the cross sections of 45° and 90° samples are circular and agree well with the CAD input whereas the ones of 0° samples are not symmetrical (see the axial views in Figure 1.12d, 1.12e and 1.12f respectively). This water drop shape is only observed for the 0° samples meaning that this is a particular feature of this build orientation.
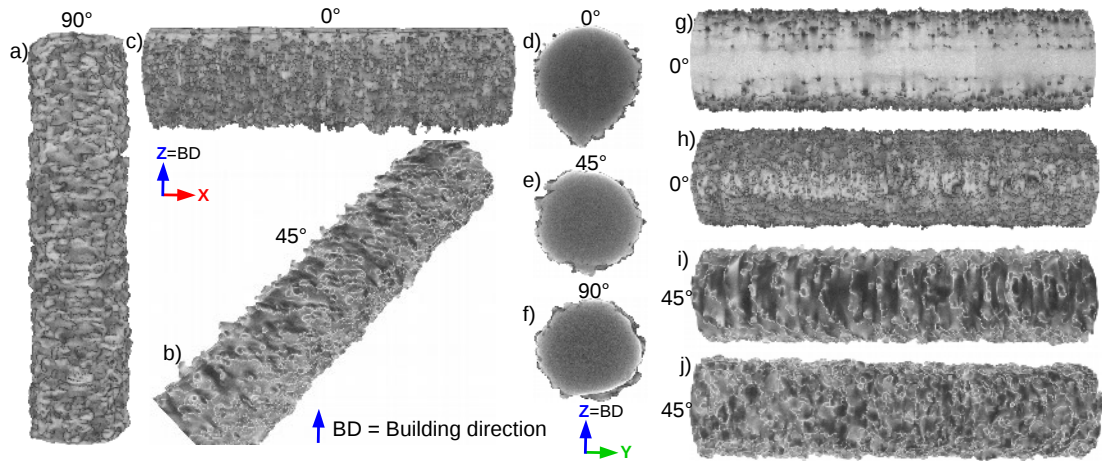
Figure 1.12: 3D rendering of as-built samples (2 mm diameter) manufactured in the three different orientations. Blue arrows indicate the building direction. (a-c) Side views of 90°, 45° and 0° samples respectively. (d-f) Axial views of 0°, 45° and 90° samples respectively. (g, h) Respectively upper and lower surface of a 0° sample. (i, j) Respectively upper and lower surface of a 45° sample.

The geometrical characteristics of as-built samples (diameter, cross section, ...) within the gauge length were compared with the CAD input (a 2 mm diameter circular cylinder with a 10 mm length). Thanks to their good spatial resolution ($\sim 4~\mu m$), the tomographic images can be used to analyze the as-built samples geometry. For all manufactured samples, the cross section of the sample was measured for all the slices within the gauge length, providing the cross section evolution along the gauge length, see Figure 1.13. For the three build orientations, the as-built samples are thinner than expected. This difference between the CAD and as-built sections is typical of the melting strategies developed by ARCAM for small parts and was already reported by Suard et al. [SUA 15a]. While 0° and 90° samples exhibit similar cross section values, the 45° samples seem to be even thinner: the average section of 0°, 45° and 90° samples are respectively 14%, 23% and 13% smaller than the CAD input.

These measurements were performed on several dozens of samples. The corresponding data were collected to compute several representative values such as the minimum, average and maximum diameter (respectively d_{min}, d_{aver} and d_{max}). They are reported in Table 1.3. These diameters were calculated from the samples cross sections which were considered like perfect discs. In order to measure the scatter within one sample, the ratio between d_{min} and d_{max} within a sample is also computed.
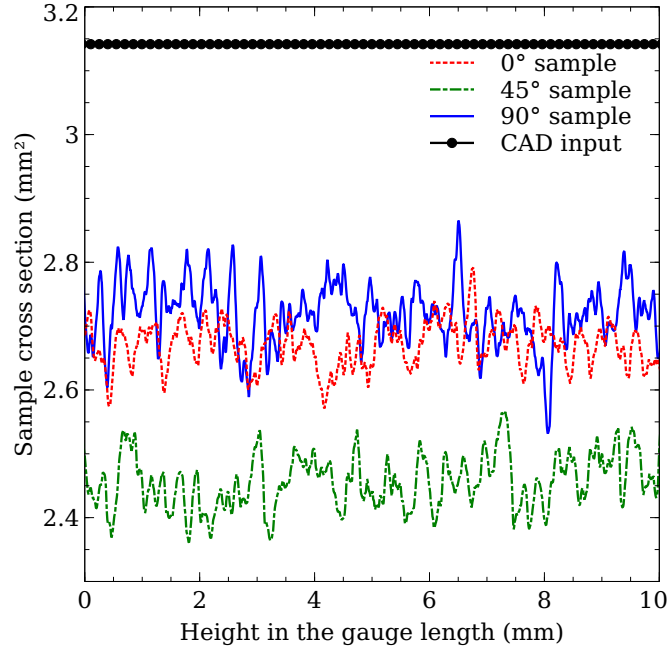
Figure 1.13: Example of the cross section variations along the gauge length for samples manufactured in the three orientations: 0° (dashed red line), 45° (dashed green line) and 90° (continuous blue line). The black dotted line at the top represents the corresponding CAD section.

Table 1.3: Effect of the build orientation on the as-built EBM samples geometry: minimum, average and maximum diameters, ratio between the maximum and the minimum diameter within one sample. The average values X and the standard deviations Y are reported as follows: X ± Y. For comparison, the nominal diameter is $d_{CAD} = 2\ mm$.

Build orientation	d_{min} (mm)	d_{aver} (mm)	d_{max} (mm)	d_{min}/d_{max}
0° samples	1.80 ± 0.03	1.84 ± 0.03	1.88 ± 0.04	0.955 ± 0.008
45° samples	1.71 ± 0.04	1.76 ± 0.03	1.82 ± 0.05	0.940 ± 0.011
90° samples	1.81 ± 0.05	1.87 ± 0.04	1.92 ± 0.04	0.945 ± 0.008

Beyond confirming the observations based on Figure 1.13, it is interesting to point out from Table 1.3 the very limited scatter of the representative values, meaning that the EBM process is extremely reliable for manufacturing similar samples. Another point worth mentioning is that within one sample the scatter of the section remains very limited: the worst value of the ratio d_{min}/d_{max} is 0.94 (obtained for the 45° samples).

1.3.2 Microstructure of as-built samples

An optical micrograph of the typical microstructure within an as-built sample is shown in Figure 1.14. The microstructure consists of fine α-laths (typical width of $\sim 1\ \mu m$) oriented in various directions which appear in white in Figure 1.14. Although some α colonies (group of parallel α laths belonging to the same variant of the Burgers relationship) can be seen occasionally (see for example detail A on Figure 1.14), most of the α laths are

individual ones. This suggests that the β phase transformation occurred at a very high cooling rate, see e.g. [ACK 09]. A continuous layer of α phase is also observed along some grain boundaries of the prior β grains (see detail B on Figure 1.14). Some residual β phase separating individual α laths appears in dark gray. The value of $\sim 1 \ \mu m$ measured for the lath width is consistent with the literature (Section 1.1.2.1). The microstructure is thinner than that obtained by traditional casting processes [KOB 03] and coarser than the ones generated by laser processing [FAC 10]. As a result of the high temperature processing (preheating of the powder bed at $\sim 730°C$), no martensitic α' phase was observed in the as-built samples.
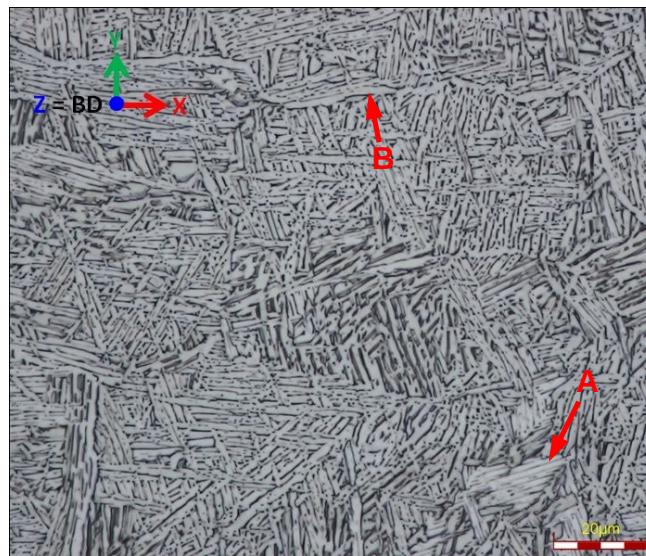
Figure 1.14: Optical micrographs showing the microstructure of a 90° EBM as-built sample in a XY plane (perpendicular to the building direction). The α-phase, in bright, exhibits a lath Widmanstätten morphology and the β-phase appears in dark. Detail A shows an α colony but most of the microstructure consists of individual laths. Detail B shows a continuous layer of α phase along the grain boundary of a prior β grain.

1.3.3 Characterization of defects produced by the EBM process

1.3.3.1 Porosity

The average pore volume fraction in as-built samples estimated from the 3D tomographic images is reported in Table 1.4 for each build orientation (several dozen of samples were analyzed). A very low value of internal porosity ($< 0.05\%$) was measured in the gauge volume of all the samples, confirming the possibility of making almost fully dense bulk samples using EBM.

For every sample, the pores detected within the gauge length were extracted and their geometry analyzed. The pore size distributions of samples built in the three different orientations are reported in Figure 1.15a. Similar distributions are obtained for every build orientation: the majority of the pores are small ones with 75% of them having an equivalent diameter $d_{eq} \leq 25 \ \mu m$.

Table 1.4: Effect of the build orientation on the as-built EBM samples porosity. The average values X and the standard deviations Y are reported as follows: X ± Y.

Build orientation	Internal Porosity (%)
0° samples	0.035 ± 0.005
45° samples	0.040 ± 0.007
90° samples	0.025 ± 0.004
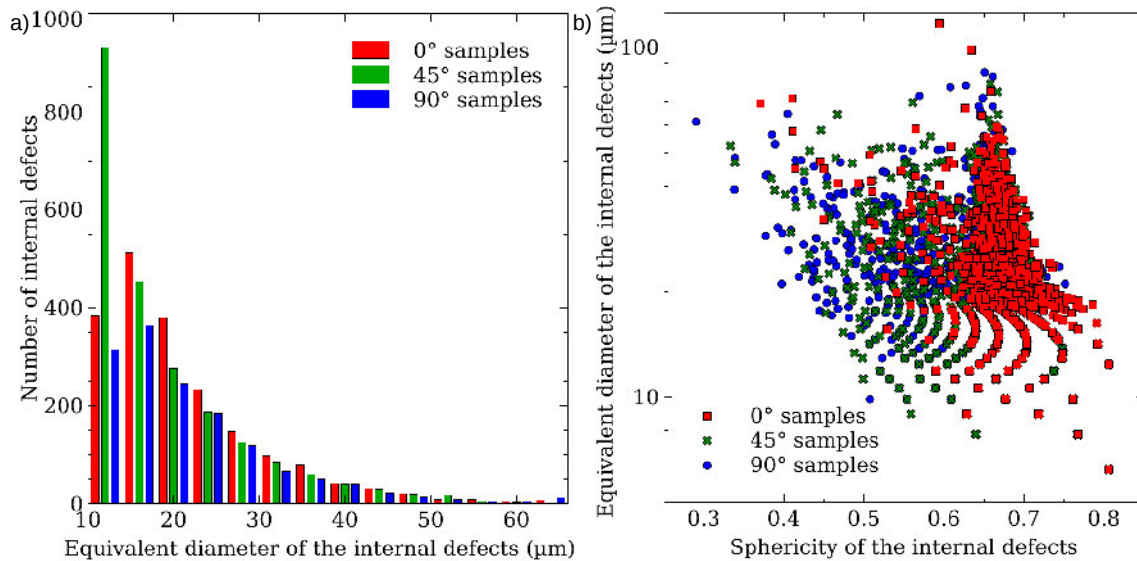
Figure 1.15: Exemples of pore distribution for samples manufactured in the three build orientation. (a) Pore size distributions. (b) Pore size plotted as a function of their sphericity.

Such distributions have already been reported in the literature and the authors always classify the pores into two different families :

- the *gas pores* which are spherical defects with a small diameter ($d \leq 25 \ \mu m$) for most of them;

- the *lack-of-fusion defects* which exhibit more complex shape and are often bigger than the *gas pores* (these defects always exhibit equivalent diameter d_{eq} larger than $50 \ \mu m$).

Tammas-Williams et al. [TAM 15] showed that most of the *gas pores* are already present in the initial powder particles which are produced by powder atomization. In this case, they contain argon gas. This means that such pores are not induced by the EBM process and that they cannot always be removed during the melting process. Consequently, a special attention must be paid to the powder used for manufacturing as its quality can impact the quality of the samples produced by the EBM machine. On the contrary, the *lack-of-fusion defects* are due to the EBM process since no such defects are visible in the initial powder particles. Very few internal *lack-of-fusion defects* are detected.

For all detected defects, their size was plotted with respect to their sphericity in Figure 1.15b. This graph shows that a majority of the pores have a sphericity larger than 0.6. This confirms the predominance of spherical *gas pores*: due to the limited spatial resolu-

tion ($\sim 4 \ \mu m$), the values of sphericity for internal defects with an equivalent diameter smaller than 25 μm are most likely underestimated. SEM-SE micrographs of internal pores confirm their spherical shape and therefore the underestimation of their sphericity by X-ray tomography (an example is shown in Figure 1.16). As a result, we will focus on bigger defects.

Given the distinct morphologies of *gas pores* and *lack-of-fusion defects*, it seems safe to assume that all internal defects with low values of sphericity are *lack-of-fusion defects*. First, the low number of points with such low values confirms that few *lack-of fusion defects* can be found in the samples. Second, although no clear tendency can be observed, it appears that the internal defects sphericity slightly decreases when the pores equivalent diameter increases which tends to confirm that the *lack-of-fusion defects* are on average bigger than the *gas pores*. This stands even more true when considering the fact that the equivalent diameter concept tends to underestimate the size of complex defects such as *lack-of-fusion defects*.
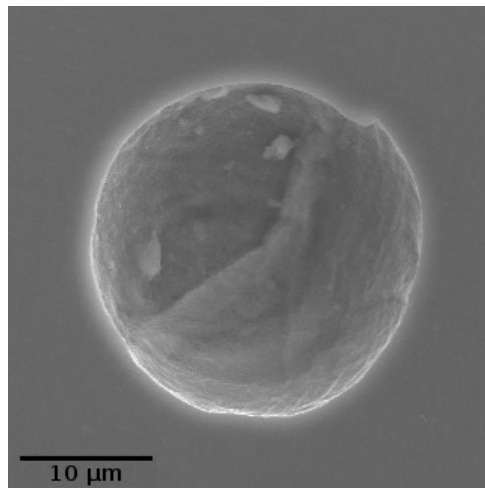
Figure 1.16: SEM-SE micrograph of a *gas pore* with a $\sim 25 \ \mu m$ diameter. The spherical shape of the *gas pore* is clearly visible.

Figure 1.17 shows cumulative projected views of all the internal defects detected in the sample gauge length for the three differents build orientations. A sub-surface circular region with a higher density of pores can be observed for the three orientations. Its width seems to vary with the build orientation, this region being thicker for 90° samples and thinner for 0° samples. In the central part of the latter, some horizontal patterning with a higher density of pores can also be identified. The impact of the build orientation on these pore spatial distributions will be discussed in details later on.

1.3.3.2 Surface irregularities and roughness measurements

The 3D rendering of the sample surfaces shown in Figure 1.12 illustrates the effect of the build orientation at a macroscopic scale (visual aspect of the sample surface). In the case of 0° (Figure 1.12b and 1.12d) and 45° samples (Figure 1.12c and Figure 1.12e), a
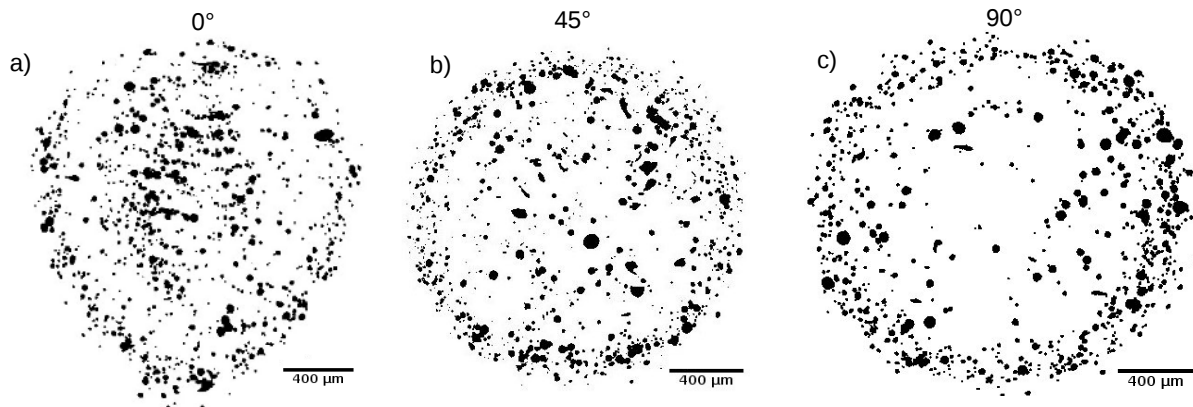
Figure 1.17: Projected views of all the internal pores within the gauge length of three samples (10mm) as detected by X-ray lab tomography (2.5 μm voxel size). (a) 0° sample, (b) 45° sample and (c) 90° sample. The corresponding volume fraction of pores are respectively 0.035%, 0.040% and 0.025% for the 0°, 45° and 90° samples.

clear difference between the upper and lower surfaces can be observed. In both cases, the upper surface is smoother than the lower one. This tendency is more pronounced for the horizontally manufactured samples: the upper surface of the 0° sample looks almost smooth while the successive manufacturing layers are visible on the 45° sample upper surface (Figure 1.12g and 1.12i respectively). As there is no upper nor lower surface for the gauge length of 90° samples, the surface state of those samples shows no evolution along their circumference (Figure 1.12f).

Table 1.5: Effect of the build orientation on the as-built EBM samples roughnesses: R_a, R_t and R_v. The average values X and the standard deviations Y are reported as follows: X ± Y. For R_a, the values for the upper and lower surfaces of the samples are also reported.

Material characterization	R_a (μm)			R_t (μm)	R_v (μm)
	Average	Upper surface	Lower surface		
0° samples	30.7 ± 1.5	11.0 ± 2.1	56.9 ± 7.7	494 ± 29	227 ± 39
45° samples	36.4 ± 1.5	32.4 ± 2.9	42.3 ± 6.3	356 ± 34	174 ± 11
90° samples	43.4 ± 2.1	N/A	N/A	379 ± 36	230 ± 27

The roughnesses values calculated for samples manufactured in the three different orientations are reported in Table 1.5. The lowest average roughness (R_a) is obtained for the horizontal samples (0°) whereas the vertical samples (90°) show the highest values (30.7 ± 1.5 μm and 43.4 ± 2.1 μm respectively). Regarding the maximum roughness (R_t), the lowest and highest values are obtained respectively for the 45° samples and 0° samples (356 ± 34 μm and 494 ± 29 μm respectively). And concerning the R_v values, 0° and 90° samples present similar values (227 ± 39 μm and 230 ± 27 μm respectively) while 45° samples show better results (174 ± 11 μm). The build orientation has clearly an impact on the surface roughness of as-built samples. Additional roughness measurements were performed on some 90° samples with a profilometer. Despite a slight underestima-

tion of the roughness by profilometry, a relatively good agreement is observed between the two different methods: the average value of R_a obtained by profilometry is 36.9 μm (*v.s.* 44.0 μm from tomographic images).

The R_a values of the upper and lower surfaces were computed for the 0° and 45° samples (Table 1.5). As expected, in both cases, values respectively lower and higher than the average ones are obtained. It is worth pointing out that for both build orientations, the roughness of the lower surfaces meets (45° samples) or exceeds (0° samples) the average value of 90° samples which show the highest average R_a value.

1.3.3.3 Surface defects
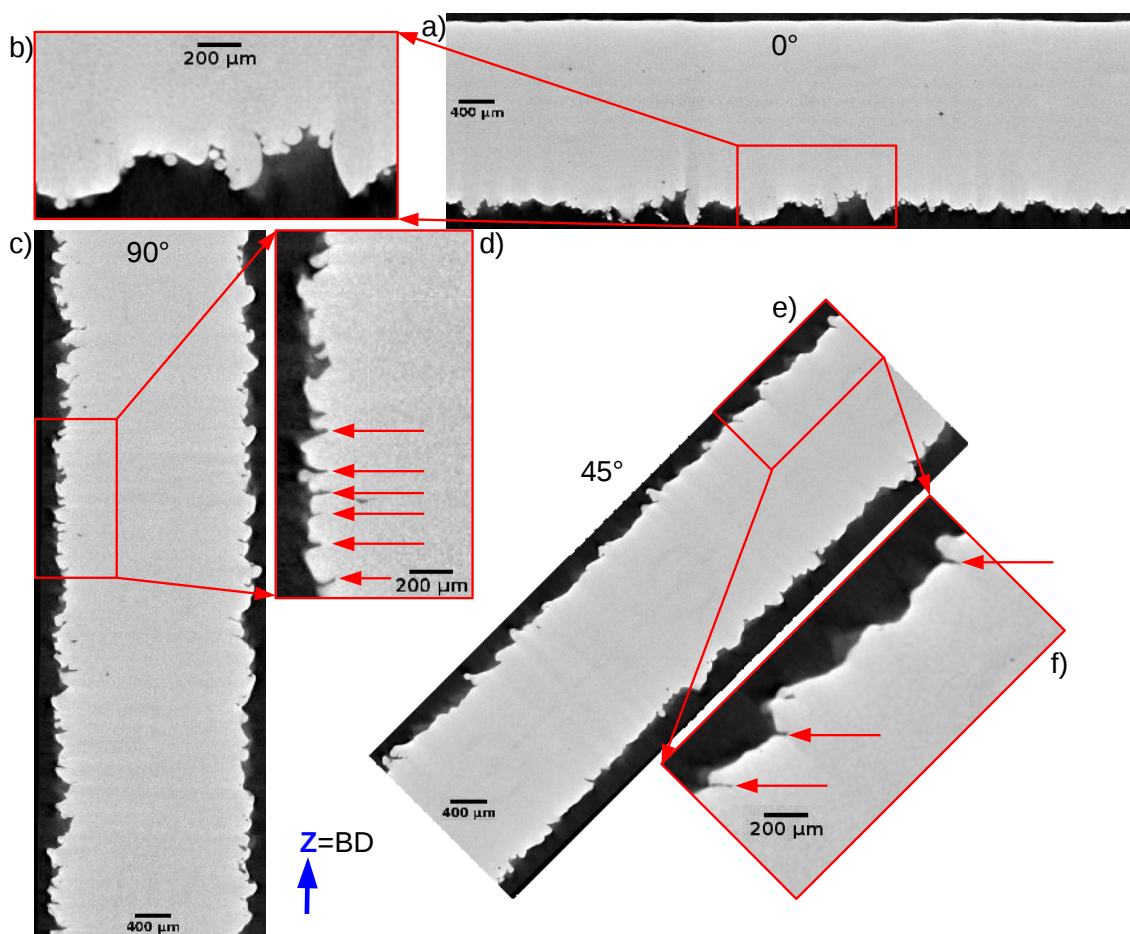
Figure 1.18: Impact of the build orientation on the surface of the samples gauge length. (a, c and e) Radial slices of samples manufactured respectively at 0°, 45° and 90°. (b, d and f) Magnification around surface defects. The slices are oriented in order to mimic the sample orientation in the build chamber, the building direction being vertical (blue arrow). Red arrows show notch-like defects.

The surface irregularities generated by the EBM process can be observed on radial tomographic slices as shown in Figure 1.18. Two different types of surface defects can be observed:

- unmelted powders stuck to the struts.

- the so-called "plate-pile" like stacking defects described in [KÖR 13], [SUA 15a] or [LHU 16] which are irregularities in the layer stacking.

The latter are observed in the 45° and 90° samples and they can sometimes lead to notch-like defects [PER 18]. A schematic illustration of the different types of defects observed in EBM as-built samples is shown in Figure 1.19. The notch-like defects (red arrows in Figure 1.18d and 1.18f) are always oriented perpendicularly to the building direction. There are fewer defects of this type in the 45° samples than in the 90° whereas hardly any can be observed in the 0° samples (for example, no notch-like defect can be found in the radial slice shown in Figure 1.18a).
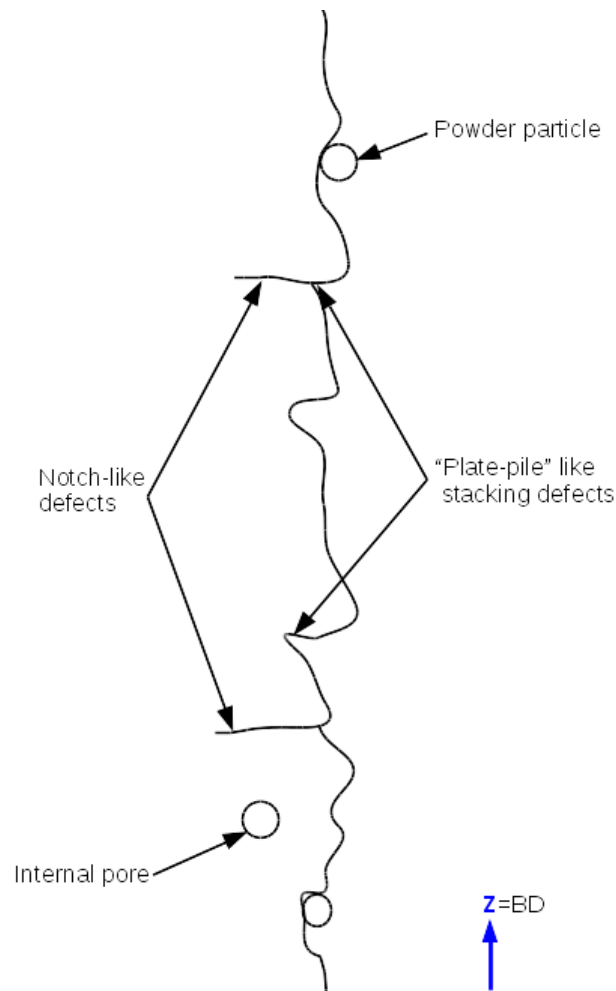
Figure 1.19: Schematic illustration of the defects that can be found in EBM as-built samples. The building direction is indicated by the blue arrow.

1.3.4   Effect of the manufacturing process on the material properties

1.3.4.1   Manufacturing process and comparison with the CAD input

As shown in Figure 1.13 and Table 1.3, all as-built samples are thinner than the CAD input and this difference cannot be neglected. This difference has been reported by other authors (see e.g. [SUA 15a], [CHA 16]) and linked to the standard melting strategy that ARCAM recommends for small parts. The tomographic images of the as-built samples have been used to better understand this link: a 2 mm diameter circle representing the CAD input was superimposed to the tomographic axial slices of the samples. For all samples, it appears on the axial slices that some surface peaks reach (or sometimes go slightly beyond) the CAD circle. In order to have an overview of this phenomenon, the cumulative projection (i.e. the mathematical union) of all the axial slices within a sample gauge length was computed from the binarized images. The resulting projection has been compared with the 2 mm diameter CAD circle and represented in Figure 1.20.
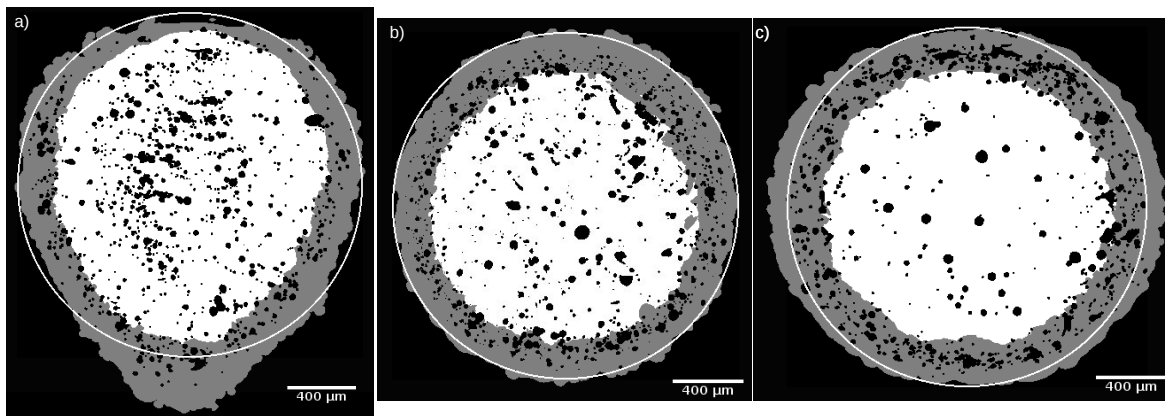
Figure 1.20: Comparison of the ring of surface irregularities and the one with a higher density of internal defects for all three build orientations: 0° (a), 45° (b) and 90° (c). The white and gray areas correspond respectively to the minimum projection (intersection) of every slices within the gauge length of a thresholded sample and the difference between the maximum projection (union) and the minimum projection of the same slices. The black spots represent all the detected pores within the gauge length of the sample. The white line indicates the edge of the CAD input.

It appears that the perimeter of this maximum projection (shown in gray in Figure 1.20) follows relatively well the CAD circle, particularly for 45° samples (Figure 1.20b). **This means that, for all manufacturing layers, the melted area remains almost perfectly inscribed inside the CAD input and that all the areas that best fit the CAD input are surface peaks.** The surface valleys, defects and stacking irregularities represent lack of material with respect to the CAD input. This means that the variations of the melt pool size and shape are correctly taken into account by ARCAM: even larger-than-expected melt pools never melt powder particles outside the area defined by the CAD input.

This conservative approach regarding the melted area produces in most cases smaller melted areas than the one indicated by the CAD input and therefore explains why the as-

built samples are always thinner than expected. This issue could be addressed relatively easily by modifying the CAD input. Thanks to the cross sections measurements performed (Figure 1.13), an adjustement factor can be determined between the CAD input and the average cross section obtained for each build orientation. By applying this homothetic factor to the CAD input, it is possible to obtain samples with the expected size. For future manufacturing, this homothetic factor should be used.

1.3.4.2 Effect of build orientation on samples geometry, roughness and defect density

Effect of build orientation on the geometry

Even though all samples remain thinner than the CAD input, discrepancies arise between the three build orientations with 45° samples being much thinner than the others (d_{aver}/d_{CAD} = 0.88, 0.92 and 0.94 respectively for the 45°, 0° and 90° samples, see Table 1.3). As this "downsizing" effect is caused by the surface irregularities, it is suspected that they can also partly account for the effect of build orientation on sample geometry.

In order to confirm this assumption, for all samples, the intersection of all axial slices within their gauge length have been added in Figure 1.20 (minimum projection in white). The difference between the minimum and maximum projections is a ring that represents the cumulated projection of all stacking irregularities (in gray in Figure 1.20). The results are presented in Figure 1.20 for three samples, one for each build orientation.

In the case of 0° samples, the bottom part of the ring of surface irregularities largely exceeds the CAD circle, see Figure 1.20a. As mentioned early on, no manufacturing supports have been added below their gauge length in order to represent the exact manufacturing conditions of lattice struts. Consequently, when manufacturing the first layer of the gauge area, the thermal energy induced by the melting process diffuse through unmelted powder (Figure 1.8). This relatively slow thermal diffusion enhances the melting pool depth and induces overmelting below the CAD area. It generates large protrusions on the lower surface which leads to important surface irregularities and the water drop shape of the cross section (Figure 1.12b and Figure 1.20a). This overmelting can explain why the cross section of 0° samples are rather close in size to the CAD input despite their unusual water drop shape.

For 90° and 45° samples, the CAD contour is relatively well followed by the cumulated projected view of all slices and similar widths of the ring of the surface irregularities are measured. The maximum projection on 90° samples seems to be slightly elongated along the left to right axis (Figure 1.20c). This may explain why 90° are thicker than 45° samples.

Effect of build orientation on defects density

Figure 1.18 shows the differences between the density of surface defects within the gauge length of the three types of samples. Hardly any "plate-pile" like stacking defects can be identified in the 0° samples whereas many can be observed in the 90° samples, 45° samples being somewhere between those two cases. These defects are caused by stacking irregularities and they form on planes parallel to the build plate. Therefore, **increasing**

the number of layers in a sample leads to more stacking defects. As the notch-like defects originate from the "plate-pile" like stacking defects, the same conclusion can be drawn for them.

Notch-like defects form on planes parallel to the build plate. Therefore, those defects appear horizontal and tilted at 45° in respectively 90° and 45° samples. On the contrary, the notch-like defects that could appear in 0° samples would be parallel to the cyclinder axis of the samples. This means that they would not look like notches on the radial views like the one presented in Figure 1.18 but rather like defects elongated in the z-axis direction.

Effect of build orientation on roughness

The impact of the build orientation on the density of "plate-pile" like stacking defects is reflected in the roughness measurements. The higher density of such defects observed for 90° samples also increases the probability of having severe defects. This explains why the vertically built samples exhibit overall the highest roughness values, see Table 1.5.

Table 1.5 also indicates that, for 0° samples, the roughness significantly varies between the upward and downward facing surfaces. On the one hand, the large protrusions caused by uncontrolled overmelting on the downward facing surface increase the surface roughness. On the other hand, the manufacturing of the upward facing surface is perfectly controlled as the thermal energy can diffuse through 2 mm of bulk material. This lead to extremely limited surface irregularities (Figure 1.20a) and a smooth surface that looks like the surface of a weld bead (Figure 1.12g).

It is interesting to note that this analysis can also be applied to 45° samples (Table 1.5) for which the heterogeneity of the surface state along the circumference is also visible but less pronounced, see Figure 1.12.

1.3.4.3 Effect of melting strategy on defects population and defects spatial distribution

Melting strategy

The standard "Melt" build theme chosen for the samples manufacturing is divided into two steps: contouring and hatching. First, the outer part of the cross section is fabricated by two paths of the electron beam: an outer contour followed by an inner contour. Then, the center part of the cross-section is melted by a hatching process with a snake-like pattern. In order to limit the *lack-of-fusion defects*, some overlapping occurs between the outer contour and the inner contour, between the inner contour and the hatching process and between each melt track of the hatching process. This melting strategy (and the corresponding offsets values) is illustrated for the 90° samples in Figure 1.6: the lines represent the trajectories of the the electron beam.

Effect of melting strategy on the defects population

For all build orientations, a sub-surface ring with a higher density density of internal defects is observed (Figure 1.17). When superimposed to the ring of surface irregularities, it appears that both rings perfectly superimpose one with each other (Figure 1.20) meaning

that they are likely to be caused by the same phenomenon. These rings of defects are suspected to be caused by the melting strategy.

Impact for 90° samples

For the sake of clarity, the impact of the melting strategy on the material defects will first be analyzed only for the 90° samples. For these samples which are built vertically, the cross section is a 2 mm diameter disc. As a result, the area melted by the hatching step is a disc and the one affected by the two contours is a circular ring. As the ring of defects is also circular (Figure 1.20c), it is therefore supposed that it is localized in the zone which has been melted only by the contours and that the melting parameters used for the contours can be invoked to explain this high density of both internal and surface defects.

Melting parameters (beam current, beam velocity, ...) leading to a reduced energy density (and thus a reduced melt pool depth) for the contours can explain the presence of such defects. A reduced melt pool depth or an increase of the beam velocity makes it harder for the *gas pores* present in the initial powder particles to escape and also increases the possibility to form lack-of-fusion defects. Such melting parameters could also be the reason for the presence of the multiple surface irregularities which lead to the ring of surface defects.

Impact for 45° and 0° samples

This analysis can be extended to the two other build orientations (Figure 1.20). The cross section of 45° samples is an ellipse (length = $2\sqrt{2}$ mm, width = 2 mm). This means that, for each manufactured layer, the area melted only by the contours is elliptical. When projected on the z axis, all these ellipses form a circular ring which matches the two rings of defects (surface defects and higher density of internal defects) that are shown in Figure 1.20b.

Regarding the 0° samples, the area melted only by the contours in each layer is defined by two rectangular areas, which creates a ring through the layers stacking, see Figure 1.21. Due to the width of the area melted only by the contours being constant for all layers, the thickness of the ring diminishes at the top of the sample which corresponds to what is observed in Figure 1.20a. However, the reverse water drop shape cannot be observed in Figure 1.21 as this shape is caused by uncontrolled overmelting.

Besides, contrary to other orientations, the spatial distribution of the pores in the center part of the 0° samples does not seem random. Some horizontal "lines" of pores can be distinguished in Figure 1.17a and Figure 1.20a. They are separated by approximately 100 μm which corresponds to 2 layer thicknesses. Between every layer, the hatching orientation is rotated by 90°. This means that for the 0° samples, the hatching direction is perpendicular to the cylinder axis for half of the manufacturing layers and that it is aligned with it for the other half. In the later case, the hatching lines go from one end of the sample to the other, which corresponds to a 90 mm length. It is not unlikely for the energy density to diminish for such long scanning lines because of problems of "scan length dependency" specific to the ARCAM A1 machine. This could explain the presence of such horizontal "lines" of pores every two layers.
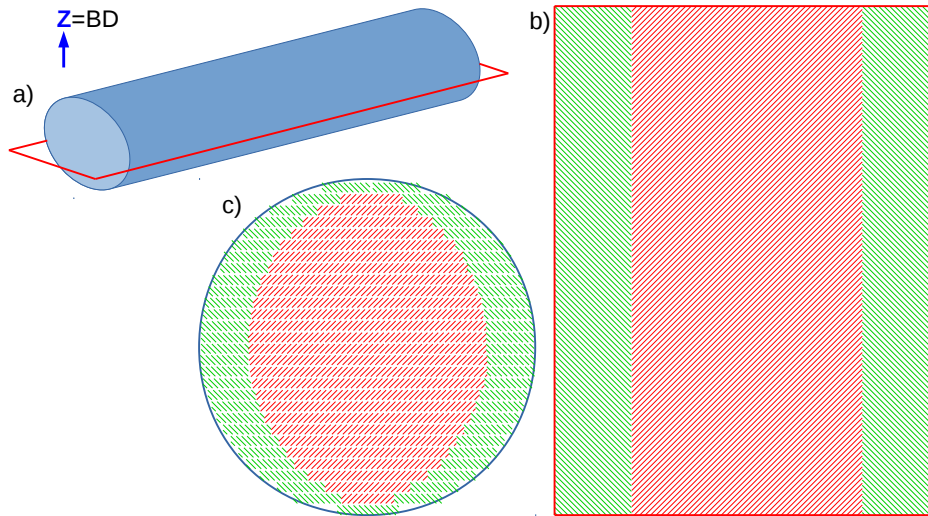
Figure 1.21: Illustration of the layers stacking for a 0° sample. (a) 3D schematic illustration of the sample. (b) Schematic illustration of the melting strategy of one layer. (c) Axial view of a sample gauge length showing the layers stacking. The areas melted by the hatching step and the ones only melted by the contours are respectively represented by red and green hatched rectangles.

Thus, **a direct link can be drawn between the melting strategy and the material defects** which can be summarized by the following idea: the contour zone may cause the appearance of a ring of defects, both internal and at the surface, because of a reduced energy density input. In order to confirm this correlation, some changes could be applied to the melting strategy. Some studies have looked into this, see e.g. [TAM 15], but different build parameters (higher layer thickness, ...) were used which makes it difficult to directly apply their results to the present case. The main idea here would be to shift the outer boundary of the hatching zone and see how this alters the defect distribution:

- removing the hatching step and melting the entire cross section with successive concentric contours.
- removing the contour step so that the hatching step melt the entire cross section.
- changing the offsets between the different steps in order to reduce or increase the width of the "hatch-free" zone.

This link between the melting strategy and the material defects also highlights the existing room for improvement in EBM manufacturing. Although the "optimized" parameters and strategy, i.e. the ones recommended by Arcam, were used in this study, it appears that it still leads to the presence of defects.

1.4   Post-treated samples

The previous section showed that as-built samples contain several types of defects which can be broadly divided in two families:

- the internal defects than can be tackled with Hot Isostatic Pressing.
- the surface defects and irregularities than can be tackled with surface treatments.

1.4.1   Internal defects closure: HIP treatment

1.4.1.1   Context (restricted to Additive Manufacturing)

Hot Isostatic Pressing, which will be refered to as HIP, has been widely used to remove internal defects and improve the mechanical properties of several metallic materials such as Al-based, Ni-based or Ti-based alloys [ATK 00]. A recent review [FRA 14] reports its effect on two Ni superalloys (IN625, IN718) and one Ti alloy (Ti-6Al-4V). For Ti alloys, the typical HIP thermomechanical process consisted of a temperature rise of 300°C/h followed by an annealing of 2 h at 920°C under a pressure of 100 MPa immediately followed by a natural furnace cooling (the temperature decreases below 150°C after 3 h). HIP has been used on additively manufactured samples by many authors who always reported a complete removal of the internal porosity. This was assessed through Archimede experiments [SVE 10], [WAU 15], microscopic observations (optical or scanning electron microscopy) [SVE 10], [KAS 15] on 2D cross sections or using X-ray tomography scans before and after HIP treatment [LEU 13], [KAS 15], [TAM 16b].

For example, Tammas-Williams [TAM 16b] used HIP on samples containing:

- typical pores population (*gas pores* and *lack-of-fusion defects*).
- voluntarily introduced important "tunnel defects" (vertical *lack-of-fusion defects* with a diameter of the order of 200 to 600 μm diameter and a vertical length of several millimeters (up to 10 mm)).

After the HIP treatment, the samples were scanned by X-ray tomography (voxel size = 10 μm). No *gas pores* or *lack-of-fusion defects* remained whereas some of the "tunnel defects" were still detected. The tomography scans showed that every remaining "tunnel defect" was in fact connected to the surface by ligaments. The authors also performed tomography scans at a higher resolution (voxel size = 2 μm) and obtained the same results. This means that all internal defects, regardless of their size, are closed or sufficiently shrunk by the HIP process that they become undetectable with the aforementioned voxel sizes.

The same research group performed heat treatments in the fully β domain on samples that underwent a HIP treatment [TAM 16a]. They showed that new pores were detected after such an annealing and that they were in fact caused by the regrowth of the argon *gas pores* detected prior to HIP. They concluded that, because of the difficult diffusion of argon in titanium, the HIP treatment only shrinks the *gas pores* sufficiently for them to be undetectable by X-ray microtomography, even with good laboratory tomography resolution (in this case, voxel size = 2 μm). No porosity regrowth was observed for the *lack-of-fusion defects*. Such defects are therefore completely closed by HIP.

Consequently, HIP is an efficient solution to greatly reduce the internal porosity but if heat treatments are applied afterwards, a special care must be paid to the porosity regrowth of *gas pores*.

HIP was also reported to have an impact on the microstructure of the treated samples. For Ti-6Al-4V additively manufactured samples, it leads to a coarsening of the α-phase lamellae, see for example [SVE 10] for samples produced by EBM and [LEU 13] for SLM.

1.4.1.2   Impact on internal defects

HIP was performed on several as-built samples whose geometry has been presented in Section 1.2.1. The classical HIP thermomechanical process (temperature rise of 300°C/h - annealing of 2 h at 920°C under a pressure of 100 MPa - furnace cooling) was used. The X-ray microtomography analysis revealed that after HIP, no remaining pores were detected, see e.g. Figure 1.22. Considering the voxel size used (2.5 μm), this means that **every internal pores, even the biggest ones, have disappeared or shrunk to a size smaller than the spatial resolution ($\sim$ 4 μm)**. However, no effect of the treatment was observed on the pores linked to the surface, as shown by Tammas-Williams et al. [TAM 16b].
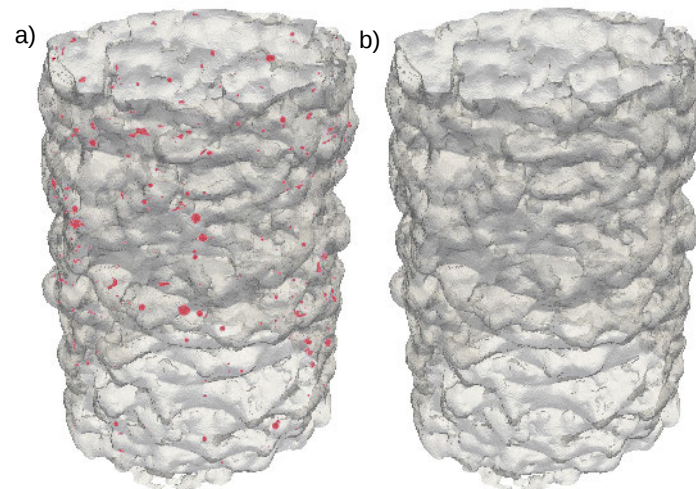
Figure 1.22: 3D renderings reconstructed from X-ray tomography scans of a 90° sample gauge length portion before (a) and after (b) HIP. The pores are shown in red. After HIP, there are no remaining pores that can be detected with a voxel size of 2.5 μm.

1.4.1.3   Microstructural change

Figure 1.23 illustrates the effect of HIP on the microstructure of a 90° sample. The size of the prior β grains is unaffected by the HIP operations because the HIP treatment was performed at a temperature below the β-transus ($\sim$ 990-1000°C), as already observed by [ATT 11], [FOR 16a]. However, **the HIP post-treatment leads to the coarsening of the alpha phase lamellae**, the α laths being wider ($\sim$ 3-4 μm, see Figure 1.23b) than in the as-built conditions ($\sim$ 1 μm, see Figure 1.23a).
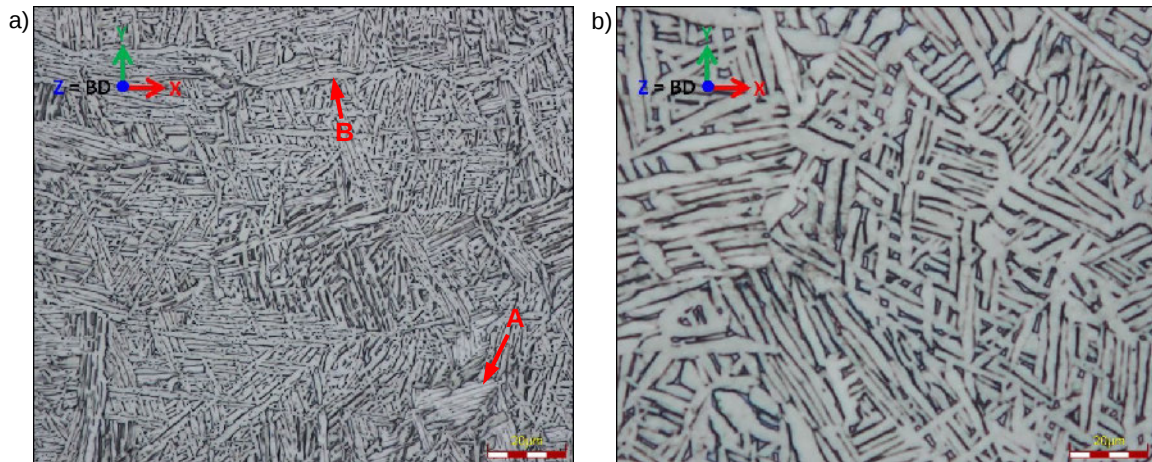
Figure 1.23: Optical micrographs taken in the XY plane showing the microstructure of an 90° EBM sample before (a) and after (b) HIP operations (2 h at 920°C - 100 MPa). The α-phase, in bright, exhibits a lath Widmanstätten morphology and the β-phase appears in dark. Detail A shows an α colony but most of the microstructure consists in individual laths. Detail B shows a continuous layer of α phase along the grain boundary of the prior β grain.

1.4.2 Surface post-treatments

1.4.2.1 Context

Different post-treatments can be applied to as-built samples in order to remove the surface defects. Surface machining is commonly used because of its high accuracy and efficiency. Nevertheless, the aim of this work is to identify solutions that can later on be applied to complex parts such as lattice structures for which machining operations seem unreasonable. Such post-treatments will not be considered in what follows. Instead, post-treatments that can be applied to complex geometries are briefly reviewed.

Several post-treatments have been investigated in the literature and can be classified according to the polishing techniques used:

- chemical etching.
- electrochemical polishing or etching.
- abrasive flow machining.
- shot peening.

Chemical etching

Chemical etching is based on chemical dissolution occuring at the sample surface where the contact with the chemical reagent occurs. In the case of Ti-alloys which have a good corrosion resistance, several reagents have been proposed in the literature for SLM and EBM made samples (see for example [PYK 12] for different chemical reagents). However, the combination of HF, HNO$_3$ and H$_2$O (with varying concentrations) was found to be the most efficient chemical solution. A combination of 10-30 vol% of nitric acid (HNO$_3$) and 1-3 vol% of hydrofluoric acid (HF) in distilled water is recommended by ASTM standards
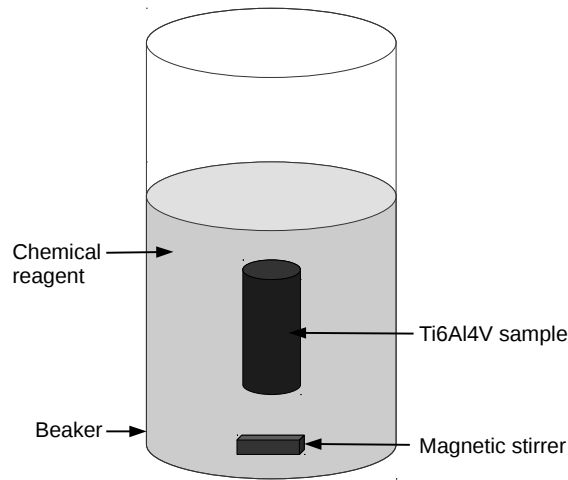
Figure 1.24: Schematic illustration of the chemical etching setup. The sample is dipped in a beaker filled with the chemical reagent. A stirrer is introduced in the beaker.

for the chemical reagent [B60 94]. The hydrofluoric acid (HF) is used in order to dissolve the TiO$_2$ oxydation layer that develops at the surface of Ti-alloys in contact with water. During this dissolution process, HF forms titanium fluorides and releases gaseous hydrogen. The latter can cause embrittlement of the surface layer of the Ti-alloys samples. The formation of free hydrogen can be minimized by a 10 to 1 ratio of HNO$_3$ to HF [LIU 04], [B60 94]. Otherwise, the TiO$_2$ oxydation layer prevents the chemical dissolution. Other acid-based chemical reagent have been studied (for example, Na$_2$S$_2$O$_8$, H$_2$SO$_4$ and HCl by Takeuchi et al. [TAK 03]) but the aim was mainly to *increase* the surface roughness of machined samples for osseointegration, i.e. the exact opposite of what is sought in the present study.

HF based etching treatments have been performed on bulk samples ([SUN 16]), single struts ([LHU 16]) or even lattice structures ([FOR 16b], [HOO 17], [PYK 12]) with promising results. The surface state is improved although it can never reach the quality (roughness) of machined samples. After a given duration and albeit the chemical reagent is still efficient, the surface state no longer improves [SUN 16], [LHU 16]. The evolution of the surface state of single struts during the chemical etching post-treatment has been analyzed by Lhuissier et al. [LHU 16] who interrupted the etching process at regular intervals in order to perform tomographic scans. Figure 1.25a, which is taken from [LHU 16], illustrates this evolution of the strut geometry.

According to Lhuissier et al., the chemical etching process of EBM Ti alloys is not homogeneous. Its efficiency is related to the local density of etchant near the surface, $\rho_{etchant} = V_{etchant}/V_{sphere}$ where $V_{etchant}$ is the volume of etchant inside a sphere of volume V_{sphere} [LHU 16]. The dissolution of metal during etching is thus larger on convex surfaces (Figure 1.25b) than on concave surfaces (Figure 1.25c). Stuck powder particles are first dissolved during the early stage of etching (Figure 1.25a); then the plate-pile like stacking defects start to be reduced. Once those ones are smoothed, the overall roughness is significantly improved, the etching process tends to be almost homogeneous and
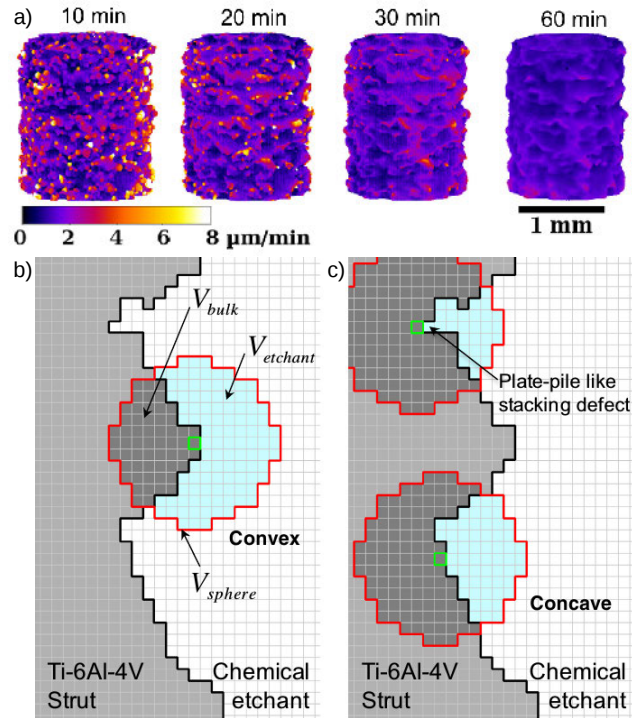
Figure 1.25: (a) 3D views of the vertical etched strut after 10, 20, 30 and 60 minutes of chemical etching (experimental results). The color code indicates the local etching rate (cold and warm colors respectively for small and high etching rates). (b, c) 2D schematic of the cellular automaton for a voxel located on a convex surface (b) and for voxels located on a concave surface and at the tip of a plate-pile like stacking defect (c). The pixels of interest are highlighted in green. Adapted from Lhuissier et al. [LHU 16].

the roughness does not evolve anymore. Thus, an optimized chemical duration between surface roughness and volume removal seems to exist.

Regarding the effect on lattice structures, thanks to the liquid environnement, all the sample surfaces can be etched whatever the geometrical complexity of the structure. Few studies have been published regarding this specific topic but the published results indicate that the chemical etching seems rather homogeneous and thus promising [FOR 16a], [HOO 17].

Electrochemical etching

A liquid environnement is also used in the case of electrochemical polishing with the same benefits. A schematic illustration of the process is shown in Figure 1.26. Here, oxydation-reduction reactions governed by an electrical current occur. The couple voltage-current is controlled so that the electropolishing conditions stay optimal. The sample plays the role of the anode (+) whereas a counter electrode (which can be made of platinum ([PYK 12]), copper ([YAN 16]) or titanium ([TAJ 08], [URL 17])) can be used for the cathode (-). Both are connected to a direct current source and dipped in a stirred electrolyte.

Many different electrolytes are reported in the literature, see for example a review on
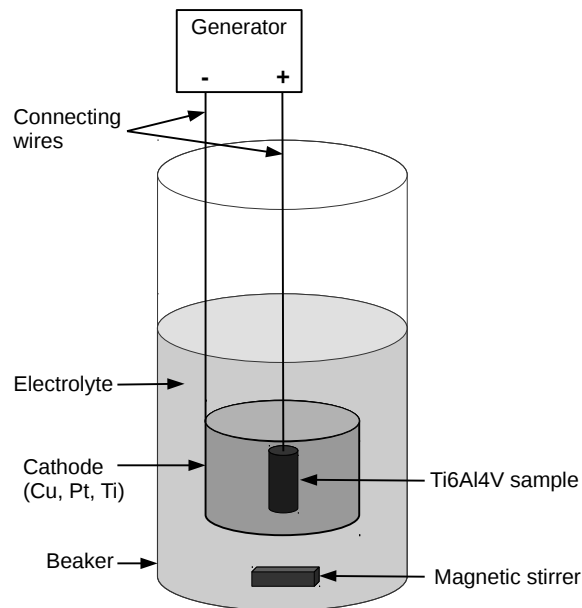
Figure 1.26: Schematic illustration of the electrochemical polishing setup. The sample and a counter electrode are dipped in a beaker filled with the electrolyte. They are connected to a generator, the sample and the counter electrode being respectively linked to the positive and negative poles. A stirrer is introduced in the beaker.

the existing patents by Kuhn [KUH 04]. Some are based on the similar ($HF+HNO_3$) combination than the chemical etching discussed previously. The electrolyte can be modified with sulfuric acid (H_2SO_4) used in addition or as a replacement of nitric acid [KUH 04] and with the use of acetic acid (CH_3COOH) instead of water ([PYK 12]). Others acid solutions have been used such as a combination of perchloric acid ($HClO_4$) and acetic acid ([URL 17]). Some alcoholic based electrolyte have also been tested: ethanol (C_2H_6O) and isopropyl alcohol (C_3H_8O) combined with zinc chloride ($ZnCl_2$) and aluminium chloride ($AlCl_3$) [TAJ 08], [YAN 16]. In each case, these solutions have been used for surface finishing or surface etching and show good results for plates or bulk samples.

However, the application to 3D parts such as lattice structures seems complicated. Indeed, one of the dominant factor in electropolishing is *the distance between the anode and the cathode.* The shorter the distance, the more efficient the electropolishing becomes. This means that maintaining this distance constant for all the samples surfaces is mandatory if a homogeneous surface state is sought. Within a lattice structure, this condition seems extremely difficult (if not impossible) to achieve.

A way to overcome this issue might be to combine both surface polishing techniques. Pyka et al. developed this sort of method for Ti-6Al-4V lattice structures produced by SLM [PYK 12]. Chemical etching was used to remove the first order of roughness and then the electrochemical polishing was used as a surface finishing process. The current density was then set to lower levels which limited the impact of the anode to cathode distance. A homogeneous surface state was reported. However, more results may be needed to fully assess its homogeneous effect.

Abrasive flow machining

Abrasive fow machining (AFM) is another post-treatment technique. Abrasive particles are dispersed in a paste or a liquid which is set in motion in order to make the particles polish the surface [KOH 88], [JAI 00], [UHL 13]. A schematic illustration of one AFM technique is presented in Figure 1.27. This technique is commonly used to polish relatively large internal channels but the use of liquid (water or chemical solutions) and the improvement of the experimental setups in recent years have made this technique available for thinner tubes and channels and even for bulk samples [MOH 18]. The chemical solution used for chemical etching (HF, HNO_3 and H_2O) is also used in this case and the abrasive particles (aluminium oxides, silicon carbides, ...) can enhance the surface state improvement. The weak point of this method is the uniaxial flow which is commonly used. This might generate an heterogeneous surface polishing and this is detrimental for complex structures [MOH 18].
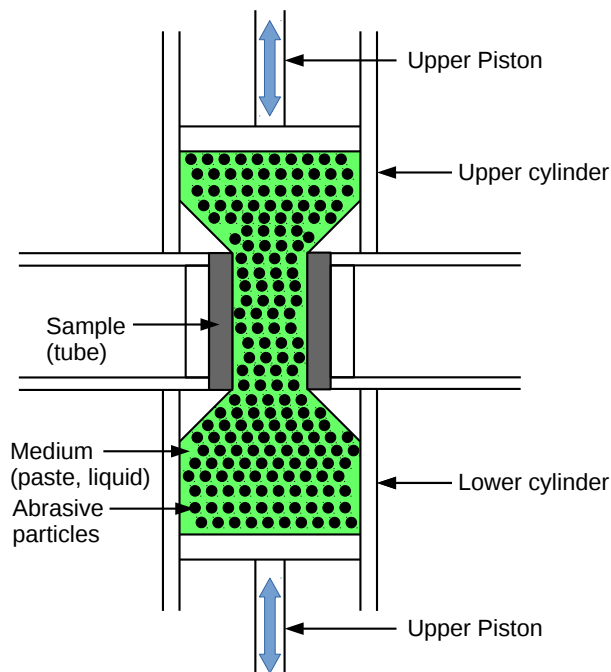
Figure 1.27: Schematic illustration of one abrasive flow machining setup. The hollow sample is fixed between two cylinders. They are filled together with the abrasive medium. The medium is then set in a back and forth motion by two pistons.

Shot peening

Last, some mechanical surface finishing techniques such as shot peening can still be of use. Only the principles of this technique are recalled here. For more details, see the recent review by Rakita et al. [RAK 13]. Shot peening consists in the projection at high velocity of a peening medium (for example steel balls or glass beads) against the surface of a sample to obtain plastic deformation [TOR 02]. The medium can be projected using conventional means (air blast systems or centrifugal blast wheels) or by advanced techniques such as wet peening or ultrasonic shot peening. In the latter case, a sonotrode is used to project

the medium. The same peening medium can be used for both conventional and ultrasonic shot peening.
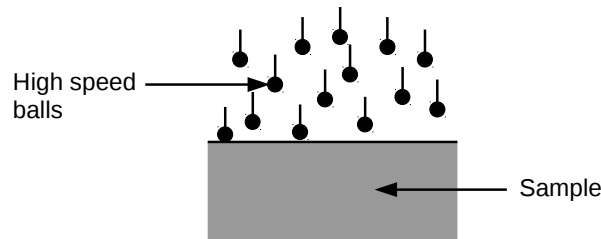
Figure 1.28: Schematic illustration of the shot peening process. A medium is projected at high speed against the surface of the sample.

The impacts physically deform the surface and smooth it. A surface state close to the one of machined samples can be obtained [BEN 17]. Watanabe et al. [WAT 02] report that a better surface roughness can be obtained with ultrasonic shot peening than with conventional shot peening. They relate it to both the lower shot velocity and the smooth surface of the polished peening medium of this process. Todaka et al. [TOD 04a] also compared air blast shot peening (ABSP) and ultrasonic shot peening (USP) and have shown that USP induced higher plastic strain values than ABSP. Other authors have reported that ABSP can have a detrimental effect on the surface state of machined samples as the first impacts slightly increase the surface roughness, see amongst others [DAI 04], [CHE 14].

Besides the roughness improvement, these techniques generate work hardening, introducing compressive residual stresses [KOB 98], [MEG 99] at the surface which can be beneficial in terms of mechanical properties, see for example [WAT 02]. The value of the compressive stresses at the surface can be increased if the process duration is increased (higher number of impacts) [KOB 98]. Regarding the depth of the plastically deformed layer, some authors report that it is only impacted by the size and kinetic energy of the shots for ultrasonic shot peening [DAI 07] whereas others report for conventional shot peening that increasing either the shot velocity or the treatment duration leads to a deeper layer of plastic deformation [ZIN 06].

At the microstructural level, the severe plastic deformations induced by the impacts of the shots also cause a fragmentation of the grains of the treated samples which lead to their refinement [TOD 04b]. In some cases, a nanostructured zone can be obtained at the surface below which submicron grains and then micro-sized grains can be observed as the depth increases [TAO 02]. The same authors report that the region affected by the plastic deformation goes deeper than the micro-sized grains. Considerable improvements of both the static and dynamic mechanical properties are reported when shot peening processes are applied [HOO 17], [WAT 02].

In order to apply it on complex structures, the main concern is about the homogeneity of the process. This implies that the entire surface of the samples must be reachable by the peening medium, even difficult to access areas such as the nodes of lattice structures. A small medium is thus needed and complex setups may be required.

To summarize, amongst the different techniques reported in the literature and briefly described here, two were used in this work and will be developed in what follows:

- chemical etching because this is the most promising technique in terms of homogeneity. Furthermore, the results obtained with this technique can be useful if electrochemical etching or abrasive flow machining were to be used in the future as the same chemical reagent can be used in the three processes.

- ultrasonic shot peening. First, the ultrasonic shot-peening is considered instead of the conventional shot peening process because of the better surface state it provides and because of the deeper plastically deformed layer. Its applicability to lattice structures still needs to be proven. Nevertheless, its positive effect on the surface state and the presence of compressive residual stresses are very promising.

1.4.2.2 Chemical etching

Experimental procedure

Chemical etching was used to decrease the surface defects of the as-built samples. Each specimen was dipped at room temperature in a fresh solution consisting of 12 mL HF (48%), 40 mL HNO_3 (70%) and 300 mL of distilled water (no stirring of the solution). The etching parameters (chemical concentrations and quantity of etchant) were determined based on the experimental procedure proposed by [LHU 16]. For long etching durations, the saturation of the etching solution is avoided by renewing it regularly. Lastly, the specimens were extensively rinsed under water immediately after being removed from the etchant in order to eliminate any trace of acid. This procedure was applied to samples manufactured in the three different orientations and the effect of the chemical etching duration was studied only on 90° samples as they have the most severe surface defects. An illustration of the effect of chemical etching on a 90° sample is shown in Figure 1.29.
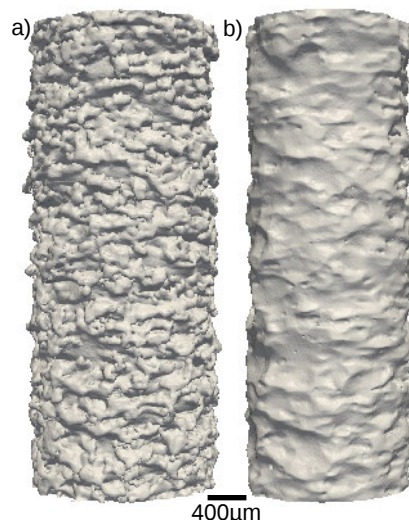
Figure 1.29: 3D renderings of a portion of gauge length of a 90° sample before (a) and after 30 min (b) of chemical etching. After 30 min of etching time, all powder particles stuck to the surface have been removed and the plate-pile like stacking defects have been slightly reduced.

Effect on the internal defects

It was shown previously that, regardless of the build orientation, a sub-surface ring with a higher density of internal defects was observed in every as-built sample (Figure 1.17). The effect of 30 minutes of chemical etching on this ring is shown in Figure 1.30 for a 90° sample. It shows that after 30 minutes of chemical etching, this sub-surface region has been almost completely erased, see Figure 1.30b. This also means that the remaining internal defects are now closer to the surface or they can even be turned into surface defects. Examples of gas pores turned into surface defects are pointed out by blue arrows in Figure 1.31.
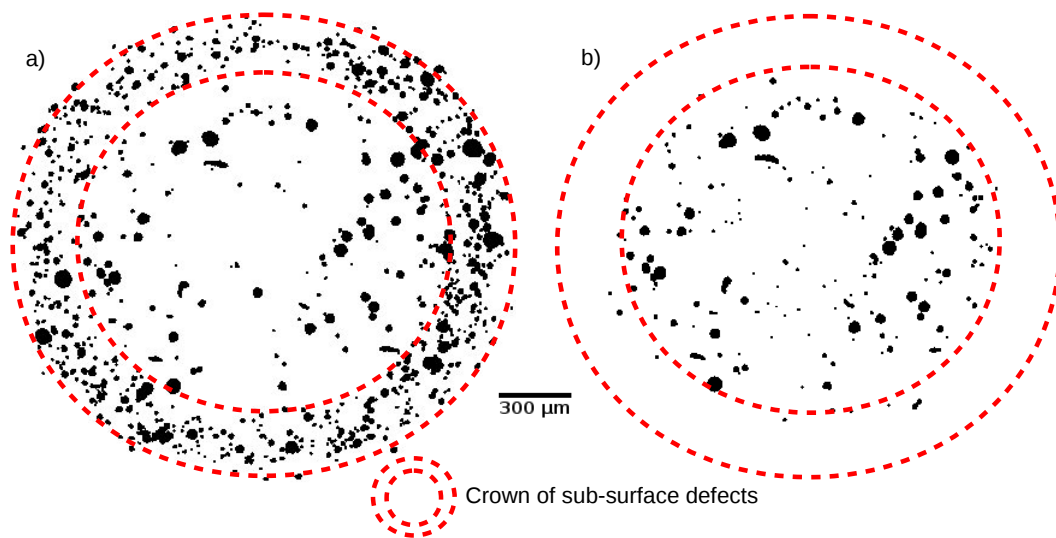
Figure 1.30: Projected views of all the internal pores within the gauge length of a 90° sample before (a) and after 30 min (b) of chemical etching. After 30 min of etching time, the sub-surface ring with a higher density of internal defects has been completely removed. The corresponding volume fraction pores are respectively 0.025% and 0.010%.

Effect of chemical etching duration

Based on the studies published by Sun et al. [SUN 16] and Lhuissier et al. [LHU 16], three different etching times were investigated (30, 45 and 60 minutes) with the purpose of identifying the duration at which the "plateau" region begins. To this end, the tomography scans before and after chemical etching have been compared. This "plateau" region is reached when the local density of etchant is almost constant along the entire surface which occurs after the removal of the powder particles stuck to the sample and the reduction of the plate-pile like stacking defects.

Figure 1.31 displays the effect of 30 and 60 minutes of chemical etching post-treatment on the surface defects. After 30 minutes, all the powder particles stuck to the struts are completely removed and the reduction of the plate-pile like stacking defects is in progress with some of them being already smoothed. However, the deepest notch-like defects remain (red arrows on Figure 1.31a). Regarding those defects, the part of the notch intersecting the sample surface is first dissolved while its root is not affected by the etchant. If the

etching process is prolonged, the depth of the notch-like defects decreases and the radius of curvature at the root of the defect increases making those defects rounder (red arrows in Figure 1.31b and d). Note that only a few notch-like defects with a sharp root persist after 1 h of etching. These observations show that a longer etching duration may be required in order to remove or at least sufficiently smooth the deepest notch-like defects. As a consequence, it seems that, **after 60 minutes, the "plateau" region is yet to be reached.**
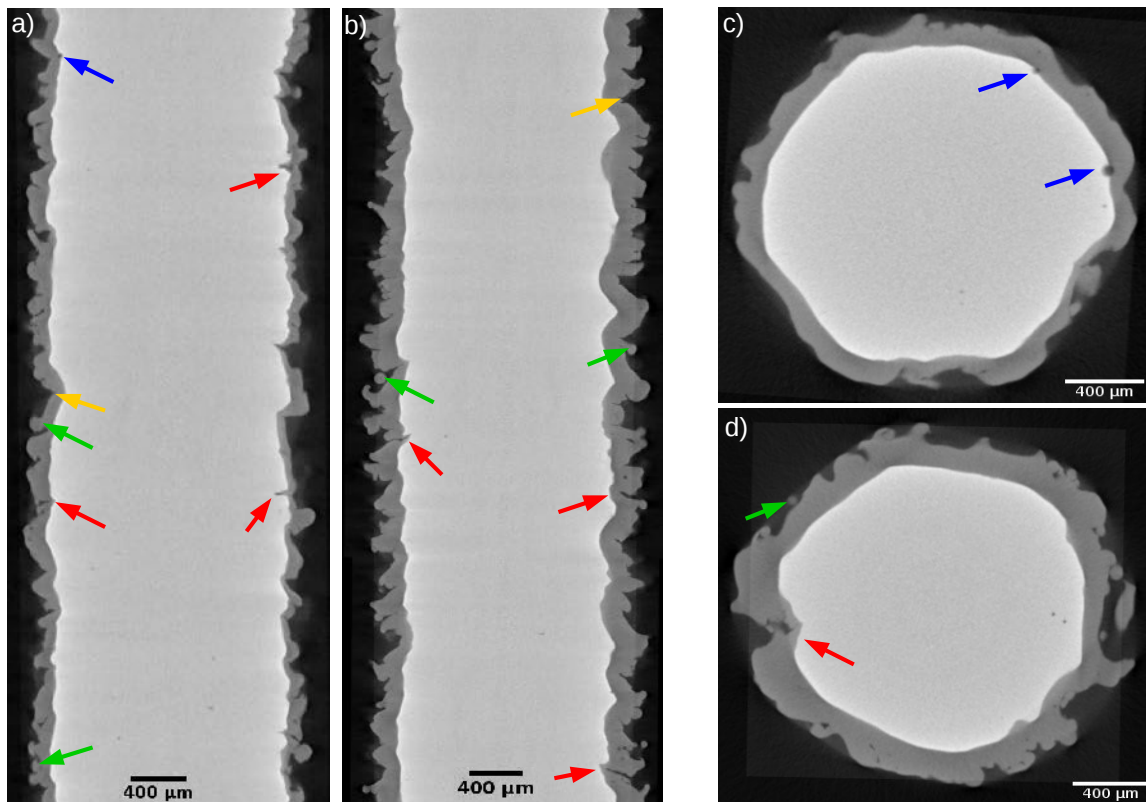
Figure 1.31: Effect of chemical etching on the surface of the gauge length of as-built specimens. Dark gray: sample cross section before etching; light gray: after etching. (a, b) Radial slices after respectively 30 min and 1 h of etching time. (c,d) Axial slices after respectively 30 min and 1 h of etching time. Green and orange arrows show respectively unmelted powder particules stuck to the surface and plate-pile like stacking defects, both in the as-built state. Red arrows point out notch-like defects. Blue arrows indicate sub-surface defects which became surface defects due to chemical etching.

Nevertheless, the analysis differs when the evolutions of the roughness and the average diameter of the strut are considered, see Figure 1.32. First, it is interesting to note that the etching mechanisms detailed above can be linked to the roughness and average diameter evolutions. Indeed, the roughness improvement predominantly takes place during the first 30 minutes and coincides with a fast decrease of the average diameter. This can be related to the dissolution of the powder particles which happens first in the etching process. Furthermore, they are often removed from the sample surface before their complete

dissolution which increases the rate of the diameter decrease. Next, both the roughness improvement and the average diameter variation slow down: all the powder particles are removed and the reduction of the plate-pile like stacking defects occurs.
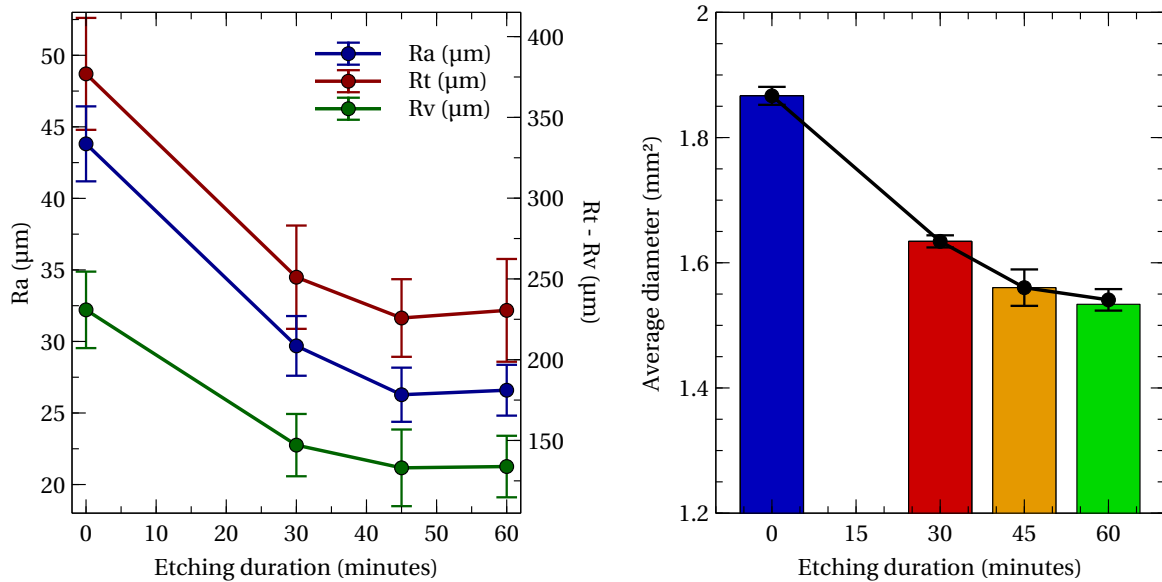
Figure 1.32: (a) Evolution of the roughnesses (R_a and R_t) with chemical etching duration. (b) Evolution of the volume in the sample's cylindrical zone with chemical etching duration. (Error bars represent the standard deviation of the measurements.)

In addition, the surface roughness is improved during the first 45 minutes of the etching process (both R_a, R_t and R_v are decreasing) but stops improving between 45 and 60 minutes of etching time. The roughness values remain more or less constant (R_a evolve from $26.3 \pm 1.9~\mu m$ to $26.6 \pm 1.8~\mu m$, R_t from $226 \pm 24~\mu m$ to $231 \pm 32~\mu m$ and R_v from $133 \pm 24~\mu m$ to $134 \pm 19~\mu m$). In the mean time, the average diameter is still decreasing, thus confirming that the reagent is still active and that no saturation occurs. These results seem to indicate that, from the roughness point of view, the "plateau" mentioned in the literature [LHU 16] and [SUN 16] is reached after 45 minutes.

When this analysis is compared to the previous observations based on the tomography scans analysis, it demonstrates that the roughness measurements are not the most suitable way to assess the efficiency of chemical etching. Even though chemical etching is still efficient at reducing the depth and increasing the radius of curvature at the root of the notch-like defects (Figure 1.31), it does not impact sufficiently the surface variations to have an important effect on the roughness measurements (Figure 1.32). Consequently, **if it is determined from roughnesses measurements, the etching duration necessary to reach the "plateau" region is underestimated leaving some critical notch-like defects at the surface.**

Chemical etching and build orientation

Effect on the geometry

The previous analysis on 90° samples showed that after 45 minutes of chemical etching, the surface roughness was no longer improving and that only the root of the deepest notch-like defects remained at the surface (Figure 1.31). As a result, and because the 90° samples exhibit the worst as-built surface state (Table 1.5), this etching duration of 45 minutes was considered sufficient and was applied to samples built in the three different orientations. The resulting surface states for the three build orientation are shown in Figure 1.33. The impact of the build orientation observed on the as-built conditions (Figure 1.12) remains on the chemically etched surfaces. For instance, the protrusions on the downward facing surface of 0° samples can still be observed (Figure 1.33c). However, contrary to what can be seen on the surface of 90° samples, all the remaining surface irregularities of 0° and 45° samples seem to be considerably smoother.
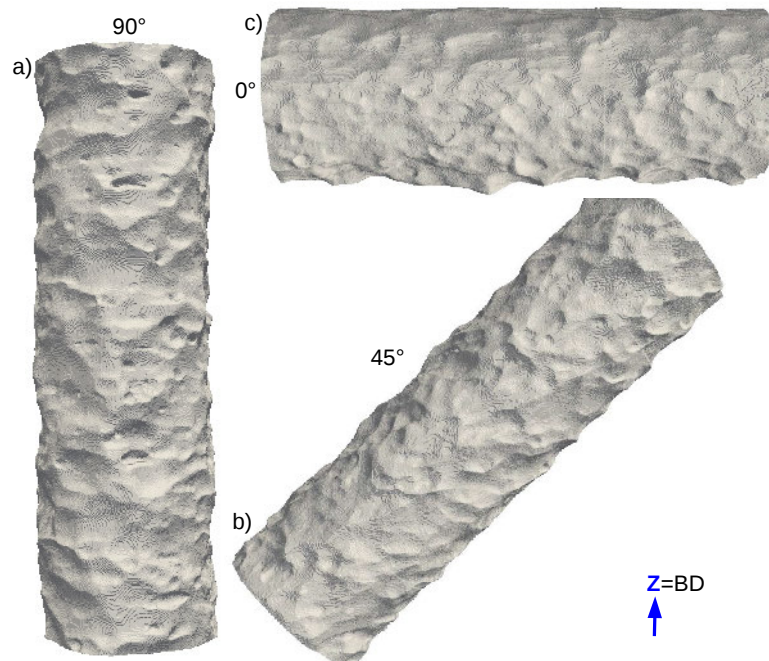
Figure 1.33: 3D renderings of a gauge length portion of 90° (a), 45° (b) and 0° samples (c) after 45 minutes of chemical etching.

The effect of chemical etching on the geometry and on the roughness values are respectively detailed in Table 1.6 and Table 1.7. Regarding the volume loss during chemical etching, 90° samples exhibit a higher loss of material ($30.9 \pm 2.7\%$) than the 0° and 45° samples ($27.2 \pm 1.1\%$ and $27.0 \pm 1.6\%$ reduction respectively). This can be linked to the surface state of the as-built samples. 90° samples are the roughest samples (Figure 1.5) which makes their contact surface with the chemical reagent larger. As the efficiency of the chemical etching is linked to this surface area, it is thus more efficient for 90° samples.

Another point to analyze is the effect of chemical etching on the macroscopic surface

variations. For this purpose, the parameter d_{max}-d_{min} has been measured (d_{min} and d_{max} are respectively calculated from the smallest and the largest cross section within the gauge length of the samples assuming them as perfect discs). A greater improvement of this parameter is obtained for 0° samples ($32.1 \pm 3.8\%$ improvement) whereas 45° and 90° samples share similar results ($25.5 \pm 5.8\%$ and $26.3 \pm 7.1\%$ improvement respectively). As explained by Lhuissier [LHU 16], the etching process is more efficient on convex surfaces (Figure 1.25). And because of the protrusions at the bottom surface of the 0° samples, more convex surfaces are found on these samples which can explain the better improvement of the section variations. This is confirmed by Figure 1.34b where it can be seen that the large protrusions on the downward facing surface of 0° samples are completely erased by the chemical etching process.

Table 1.6: Effect of chemical etching on the EBM samples geometry: volume, average diameter d_{aver} and maximum cross section variation d_{max}-d_{min}. The values in both as-built and chemically etched conditions as well as the corresponding improvements are reported. The average values X and the standard deviations Y are reported as follows: X $\pm$ Y.

Sample state	Volume (mm^3)	Volume loss (%)	d_{aver} (mm)	↘ (%)	d_{max}-d_{min} (μm)	↘ (%)
0° as-built	26.7 ± 0.7		1.84 ± 0.03		84 ± 12	
0° etched (45 min)	19.8 ± 0.4	27.2 ± 1.1	1.59 ± 0.02	14.7 ± 0.7	62 ± 7	32.1 ± 3.8
45° as-built	24.3 ± 0.3		1.76 ± 0.03		110 ± 20	
45° etched (45 min)	17.8 ± 0.4	27.0 ± 1.6	1.51 ± 0.02	14.6 ± 0.9	83 ± 16	25.5 ± 5.8
90° as-built	27.4 ± 0.4		1.87 ± 0.04		111 ± 25	
90° etched (45 min)	19.1 ± 0.7	30.9 ± 2.7	1.56 ± 0.03	16.9 ± 1.6	80 ± 10	26.3 ± 7.1

Effect on the roughness

If the R_a roughness values are now considered (Table 1.7), it appears that the ranking of the manufacturing orientations remains the same after chemical etching: $R_{a_{90°-CE}} > R_{a_{45°-CE}} > R_{a_{0°-CE}}$. The same observation can be made for the other roughness measurements (R_v and R_t). This means that, overall, this surface treatment is a rather homogeneous process between each orientation and that **the effect of the built orientation on the as-built surface is retained after chemical etching.**

Nevertheless, the comparison of the roughness values between the as-built state and after 45 minutes of chemical etching points out that larger improvements are generally obtained for higher roughness values (Table 1.7). For instance, the R_a value of 90° is reduced by 17.1 μm on average whereas the value for 0° samples is reduced by 14.3 μm. First, as explained for the volume loss, this is due to the size of the contact surface between the samples and the chemical reagent. Second, the efficiency of the chemical dissolution decreases over time (Figure 1.32). As a result, the better the initial surface state, the less it can be improved until the "plateau" region is reached. The overlay of tomographic slices before and after the chemical etching step is shown for the three build orientations in Figure 1.34. It demonstrates that, **for 0° samples, the surface state can hardly be further improved**: the entire surface, including the large protrusions in

Table 1.7: Effect of chemical etching on the EBM samples roughnesses: R_a, R_t and R_v. The values in both as-built and chemically etched conditions as well as the correspondings improvements are reported. The average values X and the standard deviations Y are reported as follows: X $\pm$ Y.

Sample state	Roughnesses					
	R_a (μm)	↘ (%)	R_t (μm)	↘ (%)	R_v (μm)	↘ (%)
0° as-built	30.7 $\pm$ 1.5		494 $\pm$ 29		227 $\pm$ 39	
0° etched (45 min)	16.1 $\pm$ 0.3	47.3 $\pm$ 2.1	243 $\pm$ 21	50.8 $\pm$ 1.7	125 $\pm$ 35	40.2 $\pm$ 8.3
45° as-built	36.4 $\pm$ 1.5		356 $\pm$ 34		174 $\pm$ 11	
45° etched (45 min)	19.4 $\pm$ 2.0	45.2 $\pm$ 3.2	177 $\pm$ 20	50.6 $\pm$ 5.7	101 $\pm$ 12	39.2 $\pm$ 8.7
90° as-built	43.4 $\pm$ 2.1		379 $\pm$ 36		230 $\pm$ 27	
90° etched (45 min)	26.3 $\pm$ 1.9	40.1 $\pm$ 4.7	226 $\pm$ 24	43.2 $\pm$ 8.6	133 $\pm$ 24	47.6 $\pm$ 7.0

the downward facing surface, has already been greatly smoothed (Figure 1.34a and 1.34b). **The conclusion is similar for 45° samples**: the protrusions have been dissolved, every notch-like defect has been smoothed and only surface irregularities persist (Figure 1.34c and 1.34d).

In contrast, **the roughness of the 90° samples can still be improved**: even after 60 minutes of post-treatment, the root of the deepest notch-like defects is yet to be smoothed and a pronounced wave pattern can still be clearly identified at the surface (Figure 1.31).
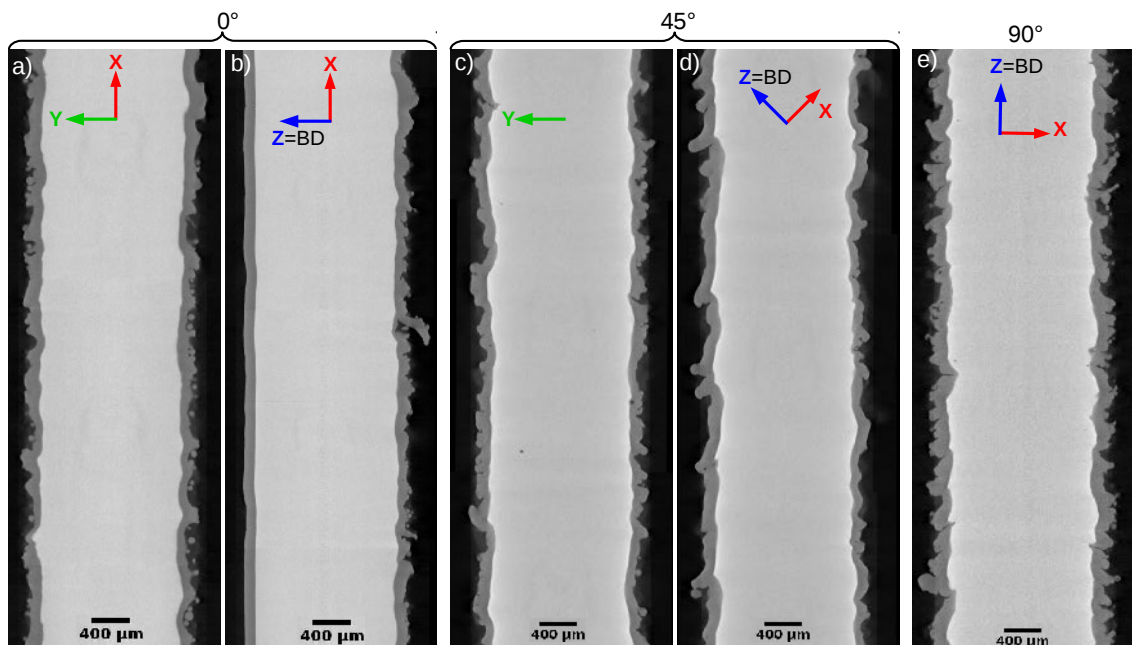

Figure 1.34: Effect of 45 minutes of chemical etching on the surface of the gauge length of as-built specimens built in the three different orientations. Dark gray: sample cross section before etching; light gray: after etching. Radial slices of samples manufactured respectively at 0° (a and b), 45° (c and d) and 90° (e). The building direction is indicated by blue arrows.

A closer analysis of the roughness improvements also shows heterogeneities between the three manufacturing orientations: 0° and 45° samples share similar roughness improvements which differ from the ones of 90° samples. For R_a and R_t measurements, 90° samples show smaller improvements than the 0° and 45° samples whereas they show greater improvements for R_v measurements.

As explained earlier, R_v values are mostly impacted by the valleys of the surface profiles. These valleys correspond to plate-pile like stacking defects or notch-like defects. It has been shown in the previous subsection that, thanks to the heterogeneity of the chemical etching process, the outer surface of the notch-like defects is first etched and the root remains intact which greatly reduces the depth of such defects. The 90° as-built samples present both a higher number of such surface defects (Figure 1.18) and the deepest ones (higher R_v in the as-built state, see Table 1.5 and 1.7). Consequently, their R_v values will be more affected by chemical etching, see Table 1.7.

Regarding R_a and R_t values, they are as much impacted by the valleys than the peaks of the roughness profiles. The R_v improvement values showed that the chemical etching effect on the valleys affected slightly less the roughness profiles of 0° and 45° samples than the ones of 90° samples. This means that the better improvement of the R_a and R_t values observed for 0° and 45° samples is most likely due to the reduction of the peaks height by chemical etching (Table 1.7). Those peaks, which are caused by protrusions at the surface, are more pronounced for the downward faces, see Figure 1.18 and greatly impact the R_t values. Furthermore, these defects are mainly convex and thus etched more efficiently. This can explain why the R_t values of 90° samples are less improved since such samples do not possess downward faces. The impact of such protrusions on the overall R_a value of a sample is limited: it only affects 3 to 5 profiles out of the 36 that were used for the roughness measurement [SUA 15a]. As a result, the discrepancies observed on the R_a values cannot be explained by the argument stated above.

The chemical etching process starts by dissolving the powder particles stuck to the surface which are present in approximately the same proportion at the surface of all the samples. This means that these powder particles affects evenly the roughness of all samples. The impact of the powder particles is therefore the same for all samples in *absolute* values but not *relative* ones: the smaller the R_a value, the higher the relative impact of the powder particles. This impact is thus more important for 0° samples and less for 90° samples. The same stands for the roughness improvement induced by the removal of those same powder particles and thus for the overall R_a improvements reported in Table 1.7. In order to confirm this assumption, roughness measurements should be done after a shorter etching time (e.g. 15 minutes), when only the powder particles have be dissolved.

1.4.2.3 Ultrasonic shot peening

Experimental procedure

The ultrasonic shot-peening process is presented in Figure 1.35a. It was performed using a SONATS equipment[1] acquired by SIMAP during my PhD. An ultrasonic wave is generated, transformed into a mechanical wave by a piezo-electric emitter which is then amplified in several steps until a sonotrode gives it the expected amplitude. The mechanical displacement of the sonotrode is then transmitted to the peening medium which is directly in contact with it.
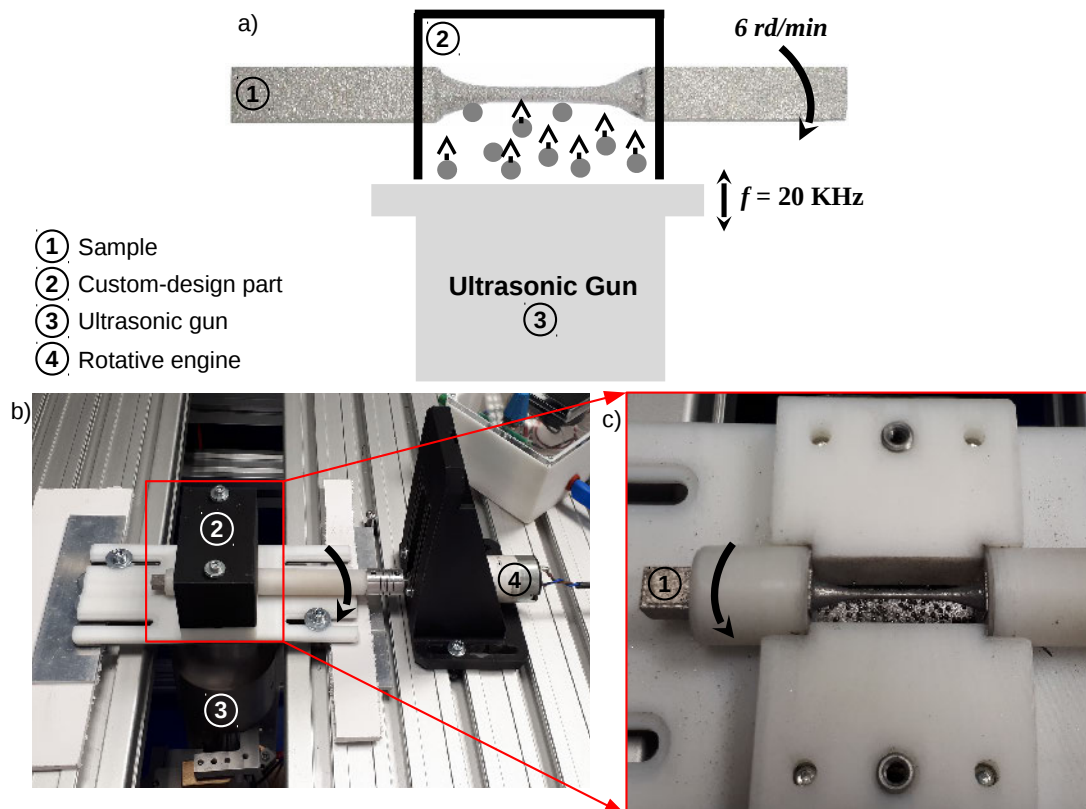
Figure 1.35: Schematic illustration (a) and pictures of the ultrasonic shot peening experimental setup (b, c). (b) Upper view of the setup. The sample stands on a white support part and is fixed in a white plastic cylinder connected to a rotative engine (in black). The black rectangular block closes the process zone. (c) Close-up view of the process zone. The center part of the sample is visible as well as steel balls standing on top of the sonotrode.

The sample is introduced in a custom-design part (in white in Figure 1.35b and 1.35c) whose top is closed (in black in Figure 1.35b). As a result, the area where the medium can interact with the sample is confined. An open view of this process area can be seen in Figure 1.35c. Each particle of the medium can bounce back on the walls of the confined zone and impact the sample several times with an energy high enough to

---

[1]Detailed information regarding the equipment can be found here: http://www.sonats-et.com/page_25-ultrasonic-shot-peening.html

plastically deform the surface of the sample. This increases the efficiency of the process as well as its homogeneity. The sample can rotate so that the surface facing the sonotrode (i.e. the area where the medium is the most efficient) changes over time; making the process more homogeneous for parts with rotational geometry such as the samples used in the present work.

In this work, a total weight of 0.5 g of 100C6 steel balls with a hardness of 60-66 HRC and a diameter of 1 mm was introduced in the custom-design enclosure. A vibration amplitude of 110 μm at a frequency of 20 kHz was applied to the sonotrode. The tensile specimen was rotated around its axis at a speed of 6 rounds per minute and treated for 2 h.

It has been shown in the previous sections that 90° samples exhibit more and deeper surface defects than the other build orientations both in the as-built state and after chemical etching. It was then chosen to apply ultrasonic shot peening only on 90° samples as they are the worst case scenario. An illustration of the effect of USP on the geometry of a 90° sample is shown in Figure 1.36.

Figure 1.36: 3D renderings reconstructed from X-ray tomography scans of a sample gauge length portion before (a) and after (b) USP. After the USP treatment, the sample presents a surface state close to the one obtained by machining.

Effect of USP on the geometry, roughness and surface defects

Effect on the sample geometry

When looking at Figure 1.36, the improvement of the surface state is rather impressive: after USP, the surface is very smooth and looks comparable to machined surfaces. This means that the plastic deformation induced by the impacts of the steel balls has enough energy to fold the peaks of the as-built state over the neighboring valleys and thus greatly smooth the surface. This efficiency of the process is confirmed by the 2D comparison of

the tomographic scans which were performed before and after USP. Figure 1.37 shows the overlay of slices from both scans. It appears that the valleys of the as-built state (notch-like or plate pile like stacking defects) are "filled" after USP whereas the peaks have been strongly deformed by the steel balls impacts.
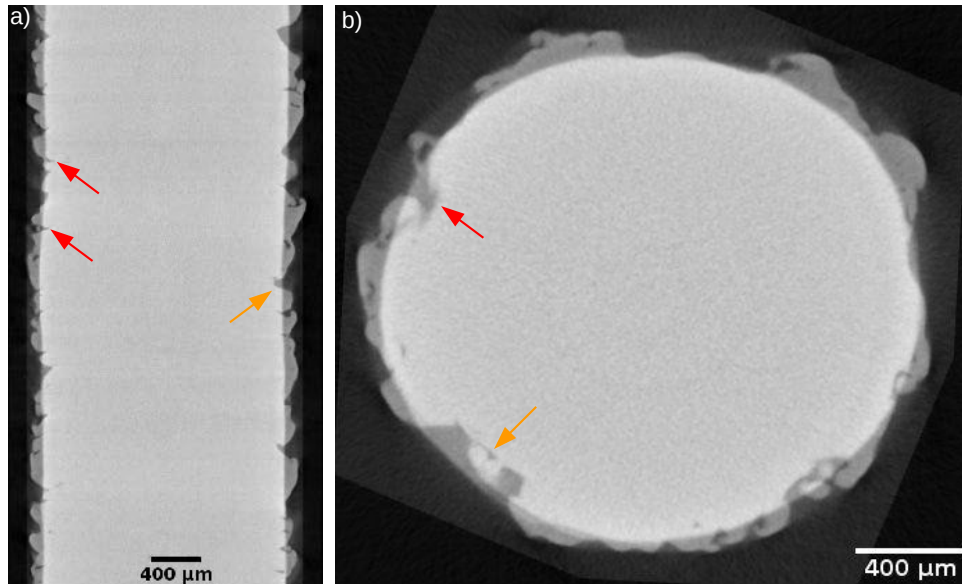
Figure 1.37: Effect of ultrasonic shot peening on the surface of the gauge length of as-built specimens (90° samples). Overlay of radial (a) and axial (b) slices. The dark gray areas show the peaks and valleys of the as-built state. Red and orange arrows respectively show notch-like defects and plate-pile like stacking defects.

In order to assess the post-treatment effect on the volume of the sample, the volume within the gauge length was measured from the tomography scans before and after USP. The obtained values are reported in Table 1.8 as well as several other geometrical parameters such as the average diameter or the roughness measurements. A $7.3 \pm 0.5\%$ volume loss is observed. This is confirmed by the cross section variations of one sample along its gauge length. They were computed from the tomography scans before and after USP and are plotted in Figure 1.38. In the as-built state, the cross section varies between approximately 2.8 and 3.1 mm^2 along the 10 mm gauge length whereas it varies between 2.6 and 2.68 mm^2 after USP. It is supposed that this volume loss may be caused by a limited removal of matter during USP: the impacts of steel balls at the sample surface could tear off small parts of the surface layer. Furthermore, this volume loss is rather limited when compared to the one induced by chemical etching, see Table 1.6. This is very interesting in terms of post-treatment efficiency as **the surface state and the geometry of the specimens are largely improved without a significant material loss.**

Regarding the geometry, Figure 1.38 also points out that the cross section variations are strongly reduced and smoothed by the shot peening process. This is further reflected by the improvement of the $d_{max} - d_{min}$ parameter (from 111 ± 25 μm to 38 ± 8 μm which corresponds to a $65.8 \pm 4.2\%$ improvement). However, this value is relatively large when compared to machined samples: classical geometrical tolerances for the nominal diameter

Table 1.8: Effect of ultrasonic shot peening on the EBM as-built samples properties: geometry (volume in the gauge length, ...) and roughness. The average values X and the standard deviations Y are reported as follows: X ± Y.

Sample state	Volume (mm³)	d_{aver} (mm)	d_{max}-d_{min} (µm)	Roughnesses		
				R_a (µm)	R_t (µm)	R_v (µm)
90° as-built	27.4 ± 0.4	1.87 ± 0.04	111 ± 25	43.4 ± 2.1	379 ± 36	230 ± 27
90° USP	25.4 ± 0.8	1.80 ± 0.03	38 ± 8	15.7 ± 2.1	130 ± 17	79 ± 8
Reduction (%)	7.3 ± 0.5	3.7 ± 0.3	65.8 ± 4.2	63.9 ± 1.4	65.7 ± 2.6	65.5 ± 2.1

of a small cylinder can be lower than 10 μm. A machining step consists in removing the surface layer of the sample in order to obtain a perfect cylinder. On the contrary, USP deforms the surface in order to smooth it. This means that **some defects of the as-built sample, typically a non constant average cross section, are kept after the USP post-treatment.**
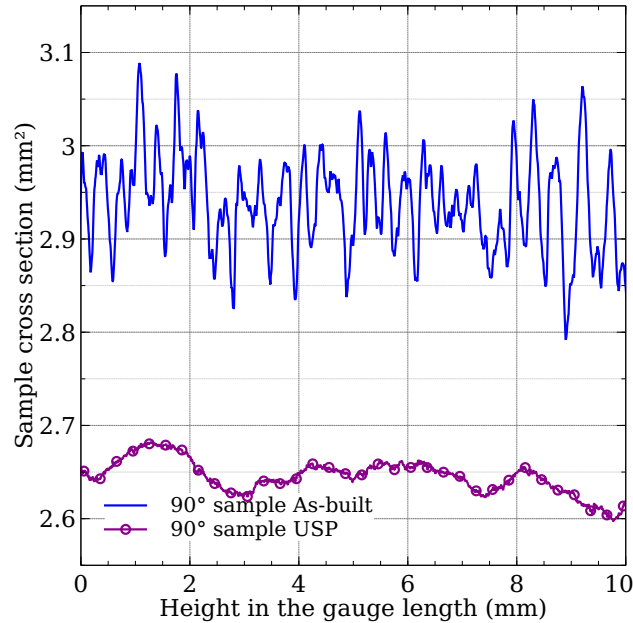
Figure 1.38: Example of variations of the cross section along the gauge length for one sample before (in blue) and after USP post-treatment (in purple). USP significantly reduces the cross section variations.

Effect on the roughness

Regarding the surface, the improvement observed on the 3D views (Figure 1.36) and 2D slices (Figure 1.37) leads to a large roughness reduction. The three roughness measurements (R_a, R_t and R_v) have been decreased by approximately 65 % (Table 1.8). Nevertheless, better roughness values were expected considering the surface aspect shown in Figure 1.36 and Figure 1.37. For instance, similar average R_a values are obtained for 90° USP treated and 0° chemically etched samples (R_a=15.7 and 16.1 μm respectively) whereas a clear improvement of the surface state can be observed, see Figure 1.34a and

1.34b and Figure 1.37a. Two surface profiles (one for each kind of samples) for which similar roughness values were obtained have been compared in Figure 1.39.
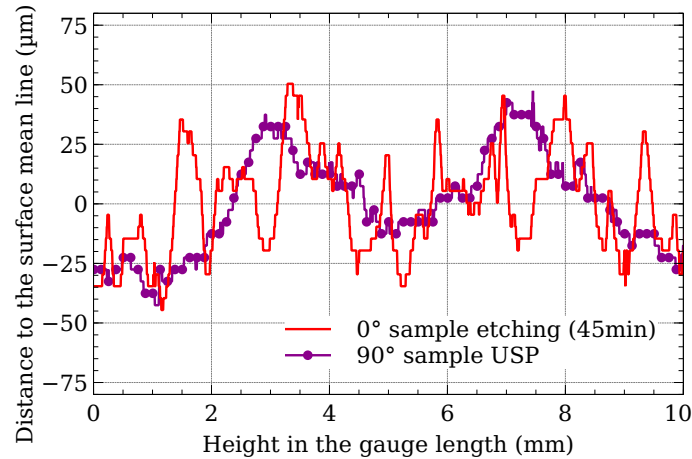
Figure 1.39: Comparison of two surface profiles which result in the same roughness measurements: one from a 90° USP treated sample (in purple) and one from a 0° chemically etched sample.

Some similarities can logically be found between the two profiles: both profiles share the same maximum and minimum distance to the surface mean line. However, Figure 1.39 clearly shows that the surface variations are smoother for the USP treated sample. This is the limit of the roughness measurements performed in this study: they do not reflect the high frequency of the surface variations. Additional roughness measurement on USP treated samples were made with the INTRA2 Taylor Hobson profilometer and lower roughness values were obtained (R_a value of $5.5 \pm 0.5 \ \mu m$). The difference between the values obtained by the two methods ($\sim 10 \ \mu m$) is of the same order of magnitude than the one obtained for as-built samples (~ 7-$8 \ \mu m$).

Effect on the defects

It has been shown previously that a sub-surface ring with a higher density of internal defects is observed in every as-built sample. The effect of USP on the ring of one sample is presented in Figure 1.40. As expected, no change can be observed on the center part of the projection. However, all the pores within the ring are no longer detected after the USP process. This means that, when the surface peaks are folded over the neighboring surface valleys, they are submitted to compressive stresses that also affect the internal defects. Those defects are progressively closed until they become small enough to be undetectable by X-ray tomography when using a voxel size of $2.5 \ \mu m$.

A closer observation of the projection of every internal defect detected after USP shows however that **"new" internal pores are detected** (one example is circled in red in Figure 1.40). These defects are always located near the surface of the USP treated samples and are likely to be originated from as-built surface defects.

Overall, USP has a huge effect on the surface and sub-surface defects detected in as-built samples (Figure 1.20). The only remaining defects seem thus to be the internal defects in the bulk which can be removed by HIP.

Figure 1.40: Projected views of all the internal pores detected by X-ray lab tomography ($2.5\mu m$ voxel size) within the gauge length of one sample before (a) and after (b) USP post-treatment.

HIP+USP

With the objective of obtaining defect-free samples, some samples were first submitted to HIP prior to USP. This treatment can also be used to determine the origin of the "new" internal defects detected after USP. The samples were tomographically scanned after each post-treatment. As observed previously, after HIP and prior to USP, no internal defect was detected. Figure 1.41 shows the projected views of all internal defects detected within the gauge length of a 90° sample after both post-treatments (HIP+USP). For every sample observed, such a sub-surface ring of internal defects can be observed. This confirms the hypothesis previously made: these internal voids were not present after HIP and were thus induced by USP which turned surface defects into internal ones. These defects exhibit complex shapes which demonstrate that they are not *gas pores*.

Some of these "new" internal defects are selected and the corresponding as-built surfaces are submitted to a thorough examination. An example of comparison of the as-built and USP states of one sample is shown in Figure 1.42. It can be seen that the remaining defect after USP can be perfectly superimposed with the tip of the notch-like defect observed at the same location in the as-built state (Figure 1.42). This proves that this is the same defect observed before and after USP and that **the "new" internal defects detected after USP originated from notch-like defects.** As explained previously, during the shot peening process, the peaks of the plate-pile like stacking defects are folded over the neighboring valleys. If a deep notch-like defect is located at the root of a valley, the tip of the notch can be too deep for it to be fully "filled" during USP. As a result, the tips of the deepest defects were "trapped" and internal defects were thus generated (no remaining link with the surface can be detected with a voxel size of 2.5 μm).

Tomographic scans at a higher spatial resolution (voxel size = 1 μm) were performed in order to assess the internal nature of these defects. The comparison of the scans performed with both resolutions is reported in Figure 1.43. Thanks to the increased resolution, the exact morphology of the defect is detected and it also brings additional information close to the sample surface. For example, a "sheet-like" defect which corresponds to a flattened
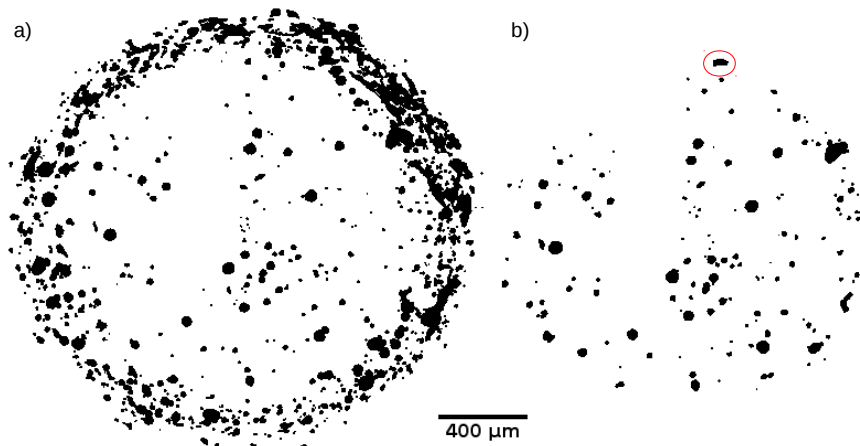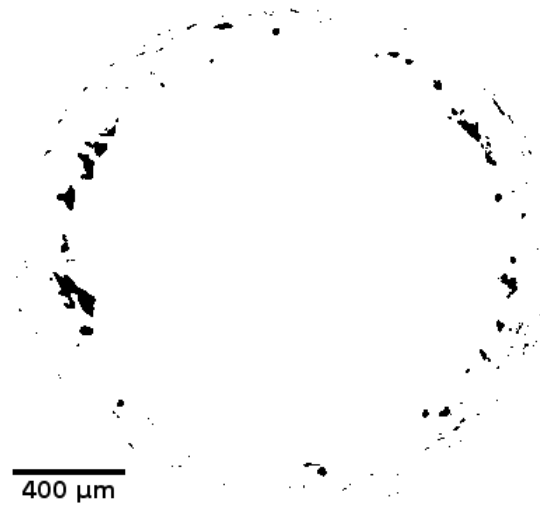
Figure 1.41: Projected views of all the internal defects detected by X-ray lab tomography (2.5 μm voxel size) within the gauge length of a sample that underwent successively HIP and USP. A clear ring of internal defects can be observed at the periphery.
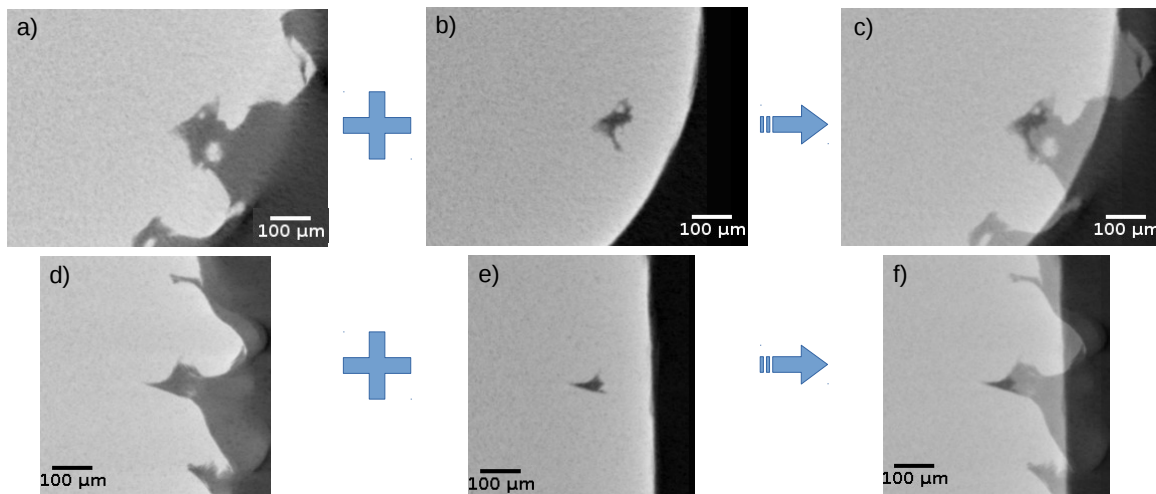
Figure 1.42: Effect of USP on notch-like defects at the surface of as-built specimens. (a, b and c) Axial slices representing respectively the notch in the as-built state, the corresponding internal defect after USP and the overlay of both states. (d, e and f) Radial slices representing respectively the notch in the as-built state, the corresponding internal defect after USP and the overlay of both states.

protrusion can be distinguished as pointed out by the red arrows in Figure 1.43b and 1.43d. Nevertheless, despite the enhanced spatial resolution, no connection between the internal defect and the surface can be found. This confirms the internal nature of this defect after the USP treatment or at least indicates that, if this defect is in fact linked to the surface, the thickness of the path joining both of them is thinner than 2 μm.
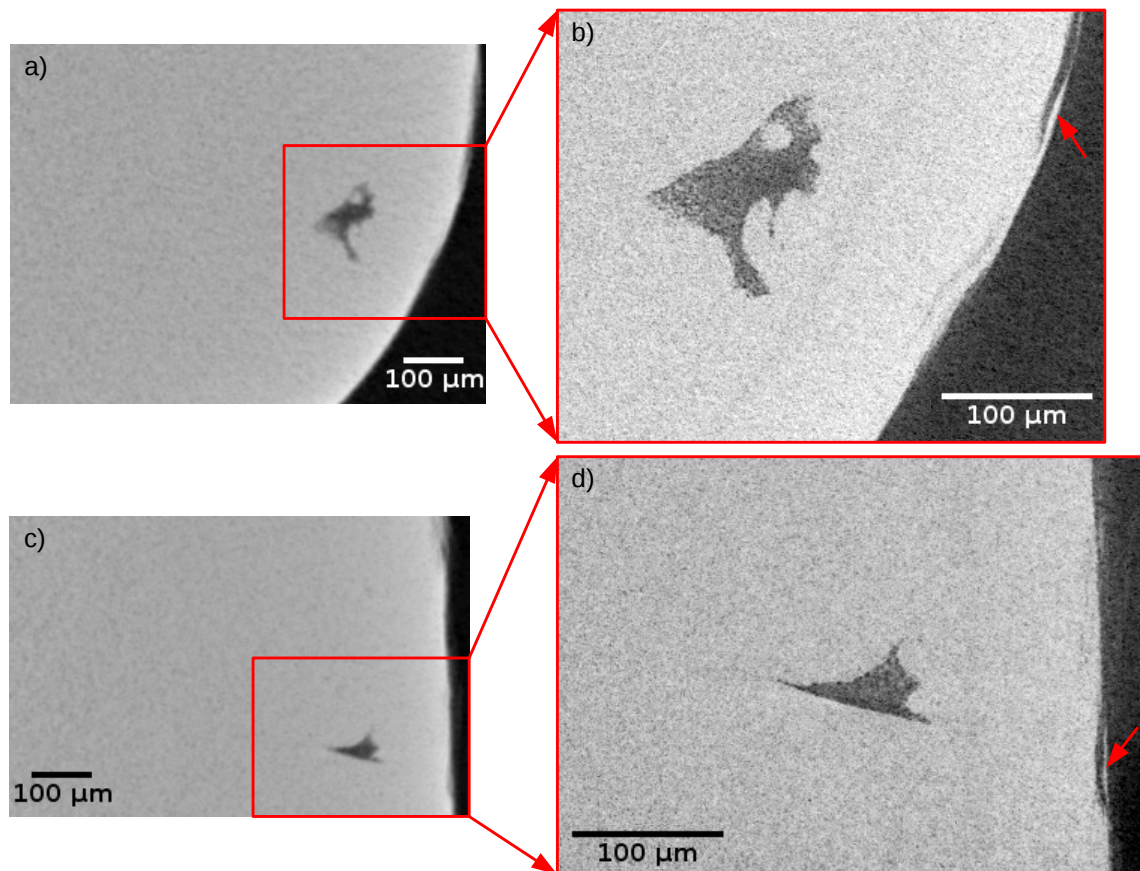
Figure 1.43: Impact of the tomography spatial resolution on the geometrical aspect of the defects. (a, b) Axial slices representing the detected defect using a voxel size of 2.5 μm and 1 μm respectively. (c, d) Radial slices representing the detected defect using a voxel size of 2.5 μm and 1 μm respectively. No gain of information appears despite the resolution improvement.

Plastically deformed surface layer: microstructure and mechanical characterization

Modification of the sub-surface microstructure

As mentioned earlier, several authors have reported that the impacts of the peening media on the sample surface induce plastic deformation which can deeply affect the microstructure and the mechanical properties (hardness and residual stresses) of the surface layer. SEM observations were performed on USP treated samples in order to investigate its impact on the microstructure of EBM made samples.

Figure 1.44 shows a low magnification SEM micrograph of the microstructure in the vicinity of the surface. The micrograph was obtained using a Back Scattered Detector (BSD). Although the proportions of α and β phases remain the same as in the as-built conditions, the microstructure near the surface differs significantly from the as-built one (Figure 1.14). Within a ~ 100 μm thick layer, the fine (~ 1 μm) α-laths have been plastically deformed (Figure 1.44).
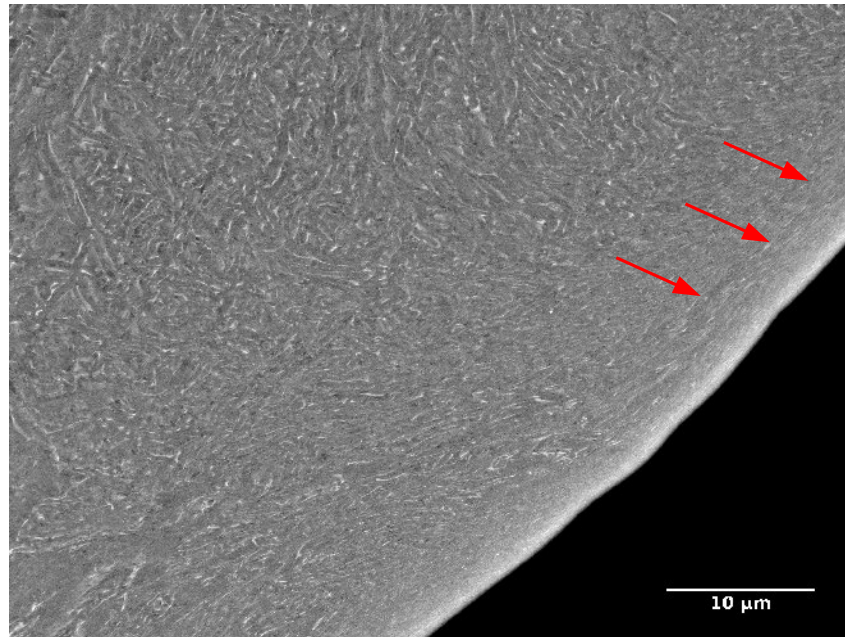
Figure 1.44: SEM-BSE micrographs showing the microstructure of an as-built 90° EBM sample after USP treatment. The α and β phases are respectively shown in dark and bright.

Over the first 10 to 20 μm underneath the surface, the laths have been severely plastically deformed so that they are elongated parallel to the surface. This phenomenon can clearly be seen in the right part of Figure 1.44 (red arrows) where the bright β-phase which separates the α-laths seems to "flow" parallel to the surface. The higher magnification micrographs taken 5 μm and 10 μm below the surface (Figure 1.45a and 1.45b respectively) show that sub-micron distances are obtained between these β rods. This means that **the plastic deformation leads to a refinement of the microstructure.** Note that the deformation of the α phase is so important that the laths can no longer be observed.

Between 20 and 100 μm from the surface, the plastic deformation of the microstructure is less important since α-laths can still be observed, see for example Figure 1.45c which is taken 30 μm from the surface. Further away from the surface, the microstructure is rather similar to the one in the center part, see comparison between Figure 1.45d and Figure 1.45e. This means that this is approximatively the limit of the plastically deformed surface layer.

Furthermore, the thickness of this layer of "aligned" laths seems to vary around the periphery of the sample. As shown in Figure 1.46a for a HIP and USP treated sample, the same observation can be made for the complete surface layer where the microstructure is plastically affected. Those variations of the thickness affected by plastic deformation are supposed to be linked to the as-built surface state. This is schematically illustrated in Figure 1.46. During USP, the surface peaks are deformed and they "fill" the valleys with severely deformed material. This leads to large deformed areas whereas the areas corresponding to peaks in the as-built state are crushed and generate a thinner deformed layer.

5 µm from the surface

a)

10 µm from the surface

b)

30 µm from the surface

c) **5µm**

100 µm from the surface

d)

Center of the cross section

e)
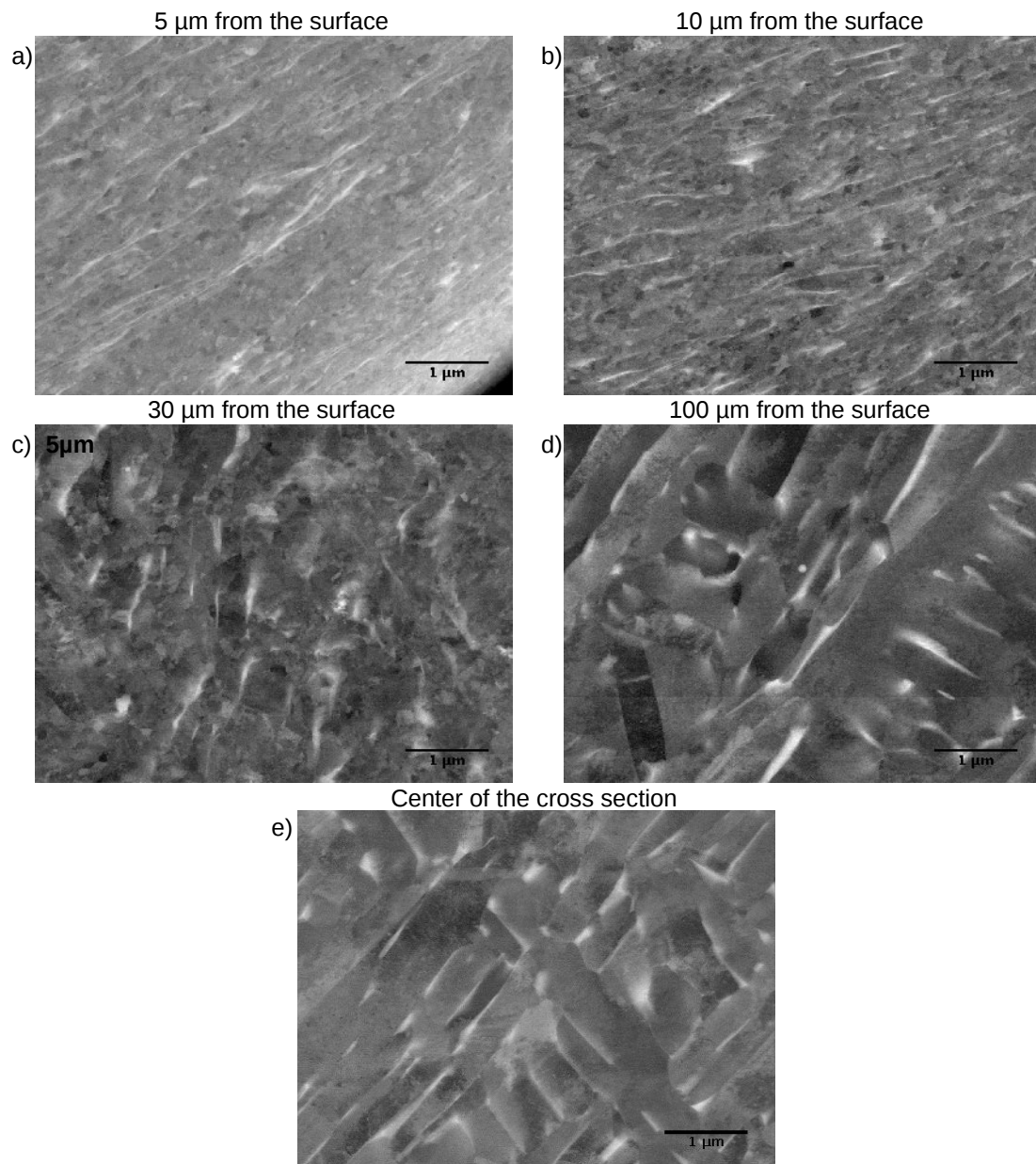
Figure 1.45: Evolution of the microstructure after USP from the surface to the center of the sample. SEM-BSE micrographs at higher resolution showing the microstructure of an as-built 90° EBM sample after USP treatment: 5 μm (a), 10 μm (b), 30 μm (c), 100 μm from the surface (d) and at the center of the cross section (e).

Sub-surface hardening: nano-indentation measurements

Nano-indentation tests were performed on polished cross sections of USP treated samples using an UNHT3 tester with a Berkovich tip. The applied load was set to $F = 10\ mN$, the depth of the indents to $d = 300\ nm$ and a distance $g = 6\ \mu m$ was therefore set between each indent in order to prevent any interaction between each measurement. For each indent, the resulting indentation hardness was measured depending on the area of
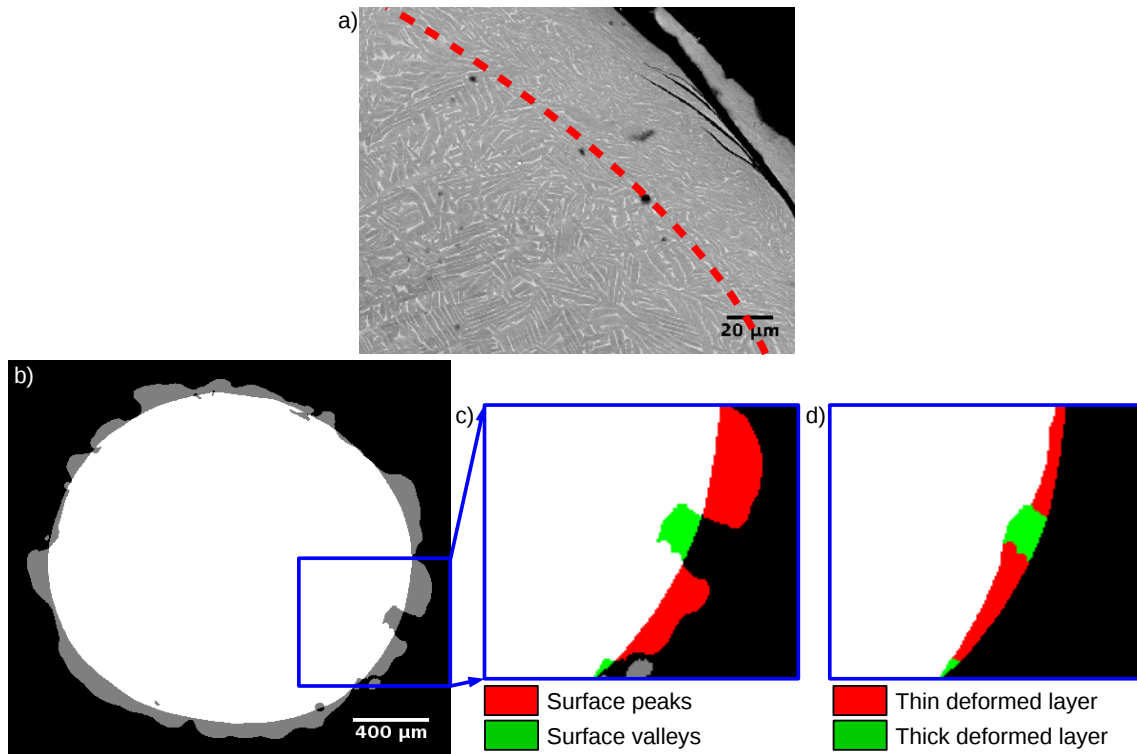
Figure 1.46: Origin of the uneven layer of deformed microstructure. (a) SEM-BSE micrograph of a HIP and USP treated sample showing the uneven layer. (b) Overlay of axial slices before and after USP. The intersection of both slices appears in white and its complementary part in gray. (c) Detailed view of a surface valley "filled" by USP (in green) and the surrounding peaks (in red). (d) Schematic illustration of the resulting deformed layer. Surface valleys lead to thick deformed layers (in green) whereas deformed peaks lead to thinner ones (in red).

the indent, $area_{ind}$ ($HITHardness = F/area_{ind}$). In order to determine the effect of microstructure deformation on hardness, 3 series of 30 indents were performed: one at the surface, one 15 μm from the surface where the microstructure is severely deformed and another 250 μm from the surface where the microstructure has been affected by USP (Figure 1.47). The resulting hardness values are reported as boxplots in Figure 1.48.

It can be seen that the results obtained from indents performed at the extreme surface are extremely scattered. It is highly possible that these indents were performed so close to the surface that the mounting resin affected the nano-indentation measurements. This could explain such a scatter and, consequently, these results will not be taken into consideration. The results from the other two series of indents show that USP affects the hardness near the surface: the average hardness value obtained 15 μm from the surface is ~ 0.3 GPa higher than the one obtained 250 μm from the surface.

This improvement is rather limited when compared to the ones reported in the literature. For instance, Tsuji et al. [TSU 09] reported a 20% increase of the hardness at the surface for a Ti-6Al-4V grade 5 alloy which has a similar chemical composition. The first reason could be linked to our nano-indentation measurements. They were performed
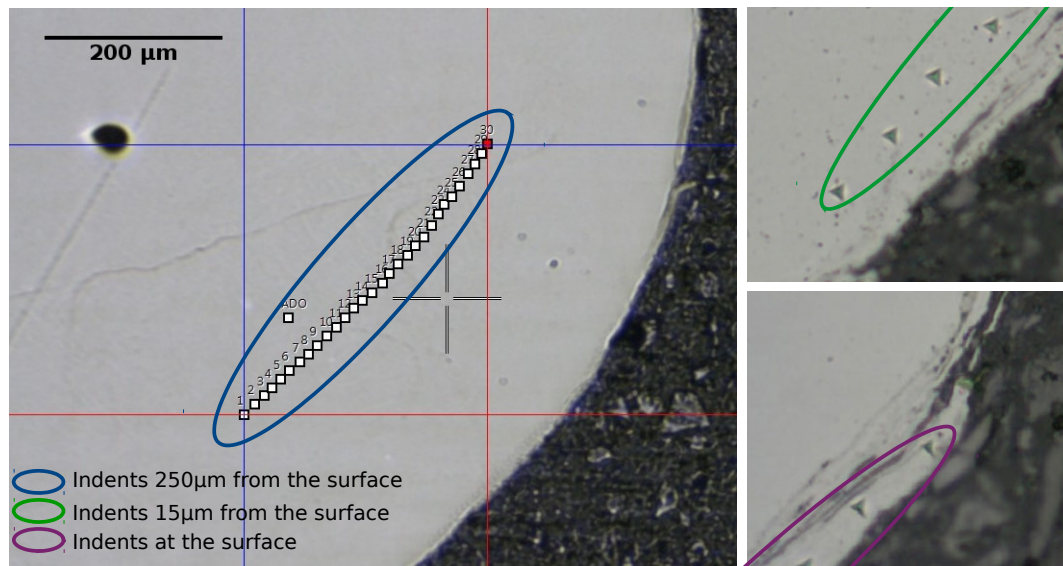
Figure 1.47: Optical micrographs showing the location of the three series of indents. (a) Low magnification micrograph showing the internal series 250 μm from the surface (blue ellipse). (b, c) Higher magnification micrographs showing portions of the series of indents taken respectively 15 μm from the surface (green ellipse) and at the surface (purple ellipse). The distance between the indents is 6 μm.
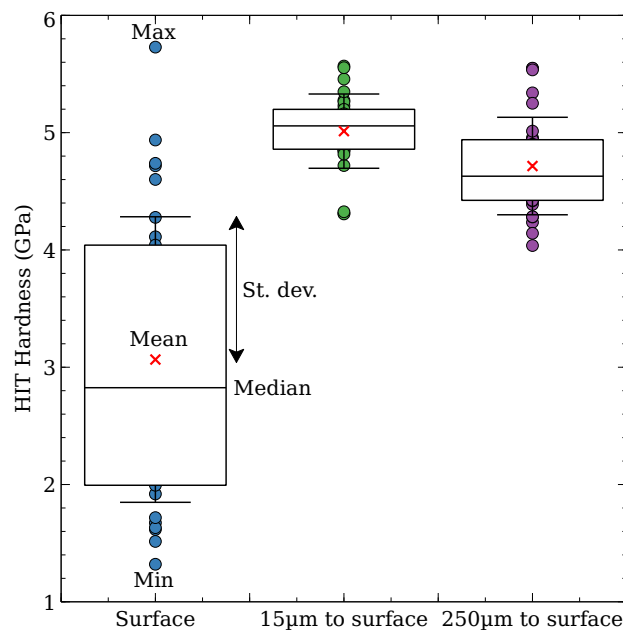
Figure 1.48: Boxplot of the HIT hardness results from the nano-indentation. The values from the indents are represented by dots (blue, green and purple for the indents respectively at the surface, 15 μm and 250 μm from it). For each series of indents, a boxplot indicates the mean (red cross) and median values (black line), the bottom and top quartile at the extremities of the box. The ends of the whiskers are separated from the mean value by one standard deviation.

15 μm from the surface which corresponds to the limit of the severely plastically deformed layer. Higher hardness values may be obtained for indents slightly closer to the surface.

Besides, the samples used by Tsuji et al. sustained first a solution treatment (955°C in an argon atmosphere for 1 h) before water quenching and were then aged (538°C in vacuum for 4 h) before cooling in an argon atmosphere. The resulting microstructure significantly differs from ours: a bimodal microstructure with roughly 20% in volume of primary-α and 80% of transformed-β (martensitic α'-phase). The latter causes a strengthening effect [MEY 08] and increases the work-hardening capability of Ti-6Al-4V alloys. A recent study by De Formanoir et al. showed that the high work-hardening of $\alpha + \alpha'$ Ti-6Al-4V resulted from a difference in yield strength between the two phases [FOR 19]. This justifies the high work-hardening of the surface layer reported in [TSU 09].

For the lamellar microstructure of our study, the proportion of β-phase is much more limited ($< 10\%$) and is not transformed in martensitic α'-phase. The cause for the surface hardening is therefore different. It is supposed that **the hardening resulting from USP is mainly caused by the refinement of the microstructure observed at the surface.**

Residual stresses: measurements by X-ray diffraction

Another beneficial effect of ultrasonic shoot peening is the compressive residual stresses generated at the surface layer of the treated samples. They can greatly improve the crack initiation resistance and thus the fatigue properties.

All the residual stresses measurements were performed by SONATS. Measurements were performed on chemically etched samples in order to determine if any residual stresses are induced by the EBM process. X-ray diffraction cannot be successfully applied if the surface roughness of the samples exceeds the minimum penetration depth of the X-ray beam. Consequently, a smoother surface, such as the one obtained after chemical etching, is required. Additional measurements were performed on both USP treated and HIP treated samples in order to determine their respective impact on the residual stresses distributions. Measurements were performed along the longitudinal and transverse direction with respect to the sample cylinder axis and an average stress measurement by rotation has also been performed. The results are presented in Table 1.9.

Table 1.9: Effect of ultrasonic shot peening on the residual stresses of as-built EBM samples. The residual stresses are measured in the longitudinal $\sigma_{res,long}$ and transverse $\sigma_{res,trans}$ directions. The average values obtained by rotation $\sigma_{res,rot}$ are also reported. The uncertainty of the measurements is estimated at $\pm$ 60 MPa. The average values X and the standard deviations Y are reported as follows: X $\pm$ Y.

Sample state	Surface residual stresses (MPa)		
	$\sigma_{res,long}$	$\sigma_{res,trans}$	$\sigma_{res,rot}$
90° etching	153 $\pm$ 7	-4 $\pm$ 15	-12 $\pm$ 5
90° HIP+etching	-53 $\pm$ 16	53 $\pm$ 24	-1 $\pm$ 6
90° USP	-737 $\pm$ 40	-589 $\pm$ 48	-325 $\pm$ 12
90° HIP+USP	-615 $\pm$ 14	-429 $\pm$ 23	-374 $\pm$ 9

First, the results show the presence of tensile residual stresses in the longitudinal direction of chemically etched samples ($\sim$ 150 MPa). Higher values of tensile residual stresses have been reported in the literature for SLM made samples, see for e.g. [VIL 11], [LEU 13]. However, this is not the case for EBM samples for which the manufactured samples are usually considered free of residual stresses thanks to the heated build plate, see for e.g. [HRA 17]. Here, given the uncertainty of measurement ($\sim$ 60 MPa), the stress levels are rather limited and their potential detrimental impact on the tensile mechanical properties is likely to be negligible.

Second, the well-known stress relieving effect of HIP is confirmed by these measurements. Considering the uncertainty of measurements (estimated at $\pm$ 60 MPa), the results suggest that no residual stresses are detected after HIP.

Finally, whether applied to as-built or HIP treated samples, **USP induces significant compressive residual stresses** which greatly exceed the tensile ones induced by the EBM process. The comparison of the three different measurements (longitudinal, transverse and average by rotation) indicates that these residual stresses appear to be heterogeneously distributed. The average value measured by rotation is only half as important as the one measured in the longitudinal direction (-325 $\pm$ 12 MPa *v.s.* -737 $\pm$ 40 MPa for USP samples) with the value for the transverse direction standing in between. These values fall in agreement with the results from the literature, see amongst others [JIA 07], [LIU 09] and [CHE 14].

Additional in-depth measurements have been performed on two samples (an USP treated sample and a HIP+USP treated sample) with the rotation method. The measurements have been performed down to a 350 μm depth. The resulting curves are shown in Figure 1.49.
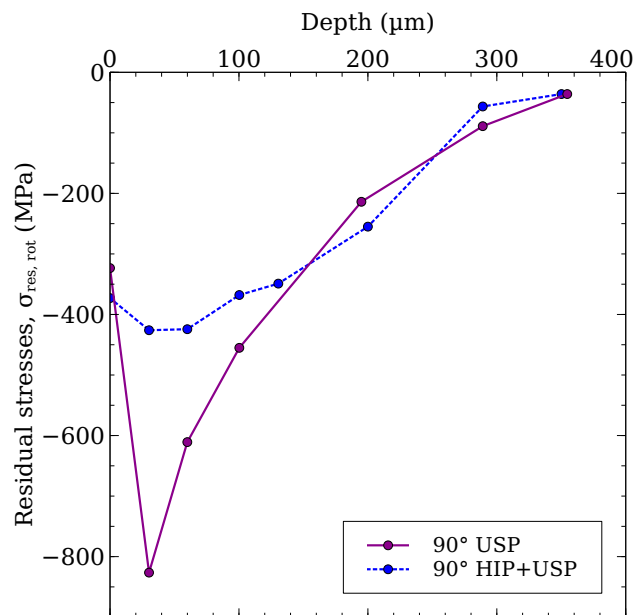

Figure 1.49: Evolution of the residual stresses as a function of depth for an USP treated sample (continuous purple line) and a HIP+USP treated sample (dashed blue line).

For both samples, the compressive residual stresses increase in the first 30 μm and then decrease until they become unsignificant at a 350 μm depth. At 200 μm from the surface, the compressive residual stresses remain important (over 200 MPa for both samples). Given the uncertainty of measurement, it can be assumed that USP induces compressive residual stresses on a sub-surface layer with a $\sim$ 250 μm thickness. Note that this layer is much thicker than the layer with a severely deformed microstructure (Figure 1.46a). The main difference between the curves obtained for the USP sample and for the HIP+USP sample occurs at the maximum peak of compressive residual stresses. On the one hand, for the USP sample, the residual stresses measured at a 30 μm depth are 2.5 times more important than the ones measured at the surface. On the other hand, for the HIP+USP sample, the residual stresses remain almost constant within the first 60 μm. This is most likely due to the difference between the residual stresses of as-built samples and HIP treated samples. Besides, the residual stresses profile obtained for the USP treated sample is quite similar to profiles reported in the literature for USP treated Ti-6Al-4V samples, see for e.g. [JIA 07], [LIU 09].

1.5 Conclusion

Before using additively manufactured lattice structures, it is necessary to characterize their as-built material conditions. In addition, conventional machining techniques cannot be used to improve their surface state. Therefore, other post-treatments must be used and their impact on the material properties must be determined. These were the goals of the work presented in this chapter. Both as-built and post-treated single struts were characterized and the main conclusions can be drawn as follows:

- In the as-built conditions, the geometry, microstructure and the defects have been characterized:
    - The manufactured samples are always thinner than the CAD input.
    - A fine and lamellar $\alpha + \beta$ microstructure is observed.
    - Internal (*lack-of-fusion* and *gas pores*) and surface defects (sintered or not fully melted powder particles, "plate-pile" like stacking defects and notch-like defects) have been detected by X-ray tomography. The latter lead to high roughness values.
    - Because of thermal aspects, the build orientation affects the sample geometry and the surface defects distribution.
        * Because of a poor thermal diffusion, a severe overmelting occurs at the downward facing surface of 0° samples. This leads to large protrusions and a cross section shaped like a water drop.
        * The density of "plate-pile" like stacking and notch-like defects is linked to the number of layers necessary to build a sample. As a result, the larger density of such defects is obtained for 90° samples.
    - For all build orientations, the spatial distribution of internal defects is heterogeneous: a sub-surface ring with a higher density of internal defects is observed. This ring can be perfectly superimposed to the ring generated by the surface

irregularities. Both rings have been linked to the melting strategy: they are most likely caused by a reduced energy density used for melting the contours.

- Hot Isostatic Pressing (HIP) affects both the internal defects and the microstructure:
    - After HIP, no remaining pores are detected by X-ray tomography (voxel size $= 2.5 \ \mu m$).
    - A coarsening of the microstructure is observed, the thickness of the α-laths being increased from ~ 1 to $\sim 3\text{-}4 \ \mu m$.
- Chemical etching improves the surface of EBM samples and the mechanisms of dissolution have been identified based on tomographic images:
    - Regardless of the build orientation, a significant improvement of the surface roughness is obtained. However, the impact of the build orientation on the surface defects (surface defects density, orientation and shape) remains.
    - All powder particles stuck to the strut are quickly dissolved by the chemical reagent.
    - The "plate-pile" like stacking defects and notch-like defects are positively impacted. Their depth is reduced and the radius of curvature at their root significantly increased.
    - Because of the volume loss, internal defects (*lack-of-fusion defects* and *gas pores*) can turn into surface defects.
- Ultrasonic shot-peening (USP) improves the surface state and has also an impact on the sub-surface layer:
    - After USP, no remaining surface defects are detected by X-ray tomography (voxel size $= 2.5 \ \mu m$). A surface state similar to the one of machined samples is obtained.
    - The sub-surface ring with a higher density of internal defects is also removed by USP.
    - "New" internal defects are however detected just underneath the surface. They have been identified as notch-like defects which are not fully "filled" by USP.
    - Near the surface, the microstructure is severely plastically deformed. All α-laths are oriented with their major axis aligned parallel with the surface. The thickness of the ring with a deformed microstructure is of the order of $100 \ \mu m$. The plastic deformation of the microstructure leads to a surface hardening.
    - Important compressive residual stresses are measured near the surface after USP.

1.6   Graphical summary
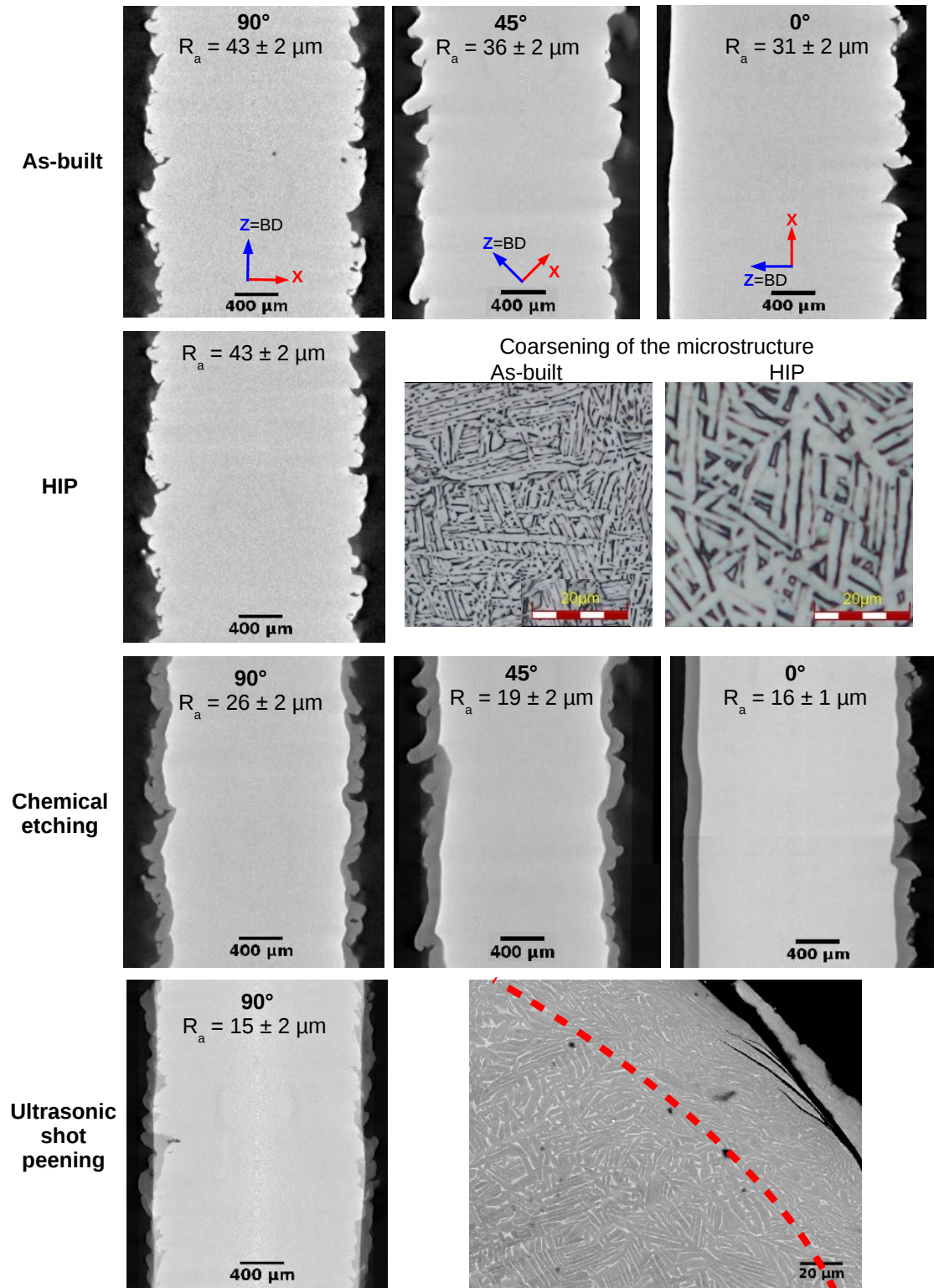
Tensile properties of single struts: effect of chemical etching and HIP

Contents

2.1   Context

In order to determine the tensile properties of thin struts manufactured by EBM, tensile tests were performed. It has been shown in the previous chapter that the worst surface state (roughnesses, density and criticality of surface defects, ...) is obtained for 90° samples. It was therefore chosen to carry out the tensile tests only on samples built in this orientation. The results obtained on these samples can later be safely applied to other build orientations. The specimens were tested in their as-built conditions and after different post-treatments that were detailed in the previous chapter (HIP, chemical etching and the combination of HIP followed by chemical etching) so that the effect of these post-treatments on the static mechanical behavior could be evaluated. Ultrasonic shot-peening was not considered in this study. [1]

---

[1] The results and the analysis presented in this Chapter have already been published in [PER 18].

2.2   Mechanical testing: experimental procedure

Tensile tests were performed on the cylindrical specimens whose geometry is detailed in Chapter 1. They were deformed at room temperature using a DY 35 ADAMEL testing machine equipped with a 20 kN cell force. The tensile direction was parallel to the building direction and the tests were carried out at a constant strain rate of 3.10^{-3} s^{-1}. The strain was measured by digital image correlation (ARAMIS software). The gauge length of the samples was preliminary recovered with a speckle made of black and white paintings. Images were recorded during the tensile tests at a frequency of 1 Hz.

2.3   How to define the tensile stress of EBM as-built and post-treated thin samples

As can be seen in Figure 2.1, the EBM process produces irregular cross sections along the gauge length in the as-built conditions. To identify the mechanical properties of thin parts manufactured by EBM and in particular to estimate the tensile stress, one has to take into account those section changes inherited from the EBM process. For example, Suard et al. introduced the concept of "mechanically efficient material" and used it in order to determine with a relatively good accuracy the stiffness properties of thin parts similar to those of our study [SUA 15a]. Despite its efficiency, it was decided not to apply this model requiring time consuming numerical calculations. We rather focused on *simpler* approaches which could enable us to compare the tensile properties of as-built and etched thin parts to those of machined samples from the literature.

Three different approaches for defining the sections to further estimate the tensile stress are suggested, two of them being based on 3D X-ray microtomography characterization. The three corresponding sections, represented in Figure 2.1, are:

- S_{CAD}, the CAD section alongside the gauge length, i.e. a perfectly circular section with a diameter of 2 mm. This definition does not work for chemically etched samples. In this case, the volumes of the samples gauge length before ($V_{AsBuilt}$) and after chemical etching (V_{ChEt}) were measured based on X-ray tomographic images. The relative volume reduction (ΔV_{red}) induced by chemical dissolution was calculated as follows: $\Delta V_{red} = (V_{AsBuilt} - V_{ChEt})/V_{AsBuilt}$. This relative volume reduction was then applied to the CAD nominal volume, V_{CAD} (volume of a perfect cylinder having a diameter equal to 2 mm) in order to compute the "CAD volume" of a chemically etched sample: $V_{ChEt\ CAD} = V_{CAD} * (1 - \Delta V_{red})$. As a result, the corresponding circular section, denoted $S_{ChEt\ CAD}$ was defined as the CAD section of the chemically etched samples: $S_{ChEt\ CAD} = V_{ChEt\ CAD}/L_0$, where L_0 is the gauge length.

- S_{min}, the minimum cross section within the gauge length (obtained from X-ray tomographic images);

- $S_{average}$, the average cross section of the sample within the gauge length determined from the X-ray tomographic images of the samples.

The tensile stresses measured with these three different sections have to be compared with references in order to determine which section is the most appropriate for defining
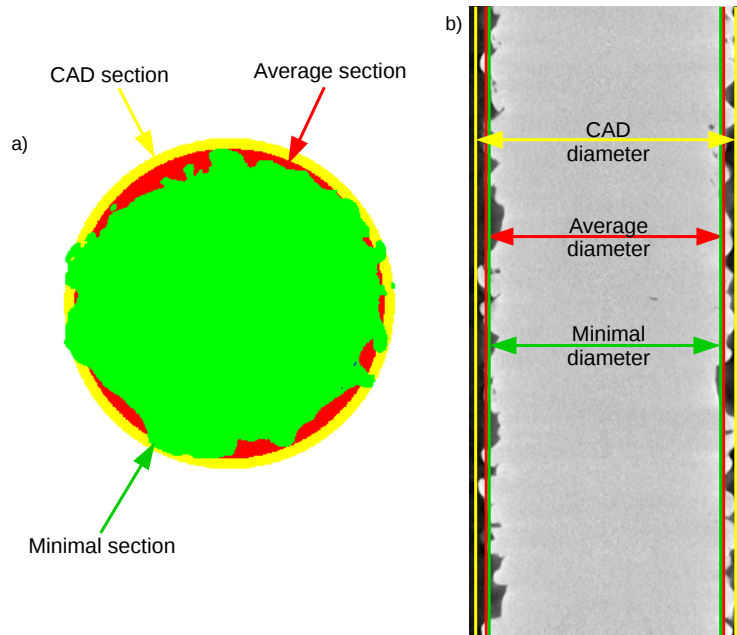
Figure 2.1: a) 2D view of the different sections used to calculate the stresses. The yellow disk represents the CAD section whereas the red one corresponds to a disk equivalent to the average section of the sample gauge length. The green area is the minimum section in the gauge length. b) Radial view of an as-built sample showing the diameters equivalent to the different sections detailed in a).

the tensile stress in as-built and chemically etched samples. Data reported for machined samples will be used as a reference. Several studies showing similar results on machined and "HIP+machined" samples can be used, see amongst others [FAC 09], [FOR 16a], [MUR 09]. For the sake of clarity, the tensile stress-strain curves of only one study carried out by Facchini et al. in [FAC 09] will be used in this work as a reference for machined EBM. The corresponding values reported for the Young modulus (E), the 0.2 offset yield strength ($YS_{0.2}$) taken at 0.2% macroscopic plastic strain and the ultimate tensile strength (UTS) will be also be used for comparison.

In order to have a reliable comparison between the results from the reference and those of the present study, the samples from both studies must be as similar as possible. It has been demonstrated in the previous chapter that the chemically etched samples are more similar to machined samples than as-built samples. Therefore, this analysis will be made by comparing our results obtained on etched samples with those published in [FAC 09] for machined samples. Figure 2.2 shows the corresponding engineering tensile stress-strain curves obtained with the tensile stress calculated using the different sections depicted in Figure 2.1.

The stress levels obtained using S_{CAD} are lower than the reference ones for every sample, whether it underwent post-treatment or not. For example, the 0.2 offset $YS_{0.2}$ values obtained for etched samples are 12% lower than the reference one. As a result, using the CAD section leads to an underestimation of the values of the mechanical properties in comparison with the reference values, see e.g. [FAC 09]. This is due to the obvious
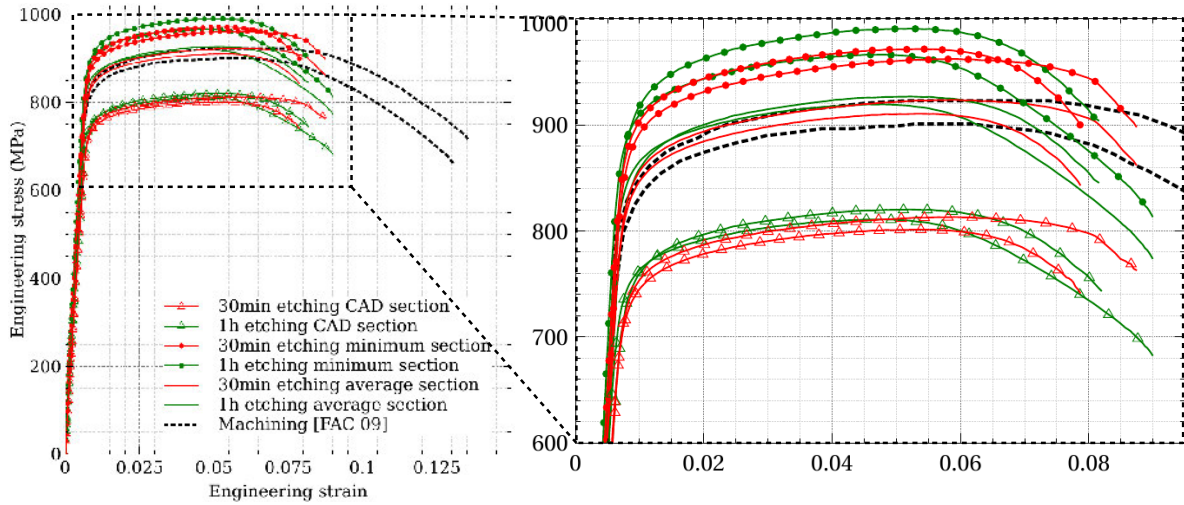
Figure 2.2: Engineering tensile stress-strain curves for samples fabricated by EBM after 30 (in red) and 60 minutes (in green) of chemical etching. The stresses are calculated with the CAD section (triangles symbols) or with the minimum section (dotted curves) or with the average section (continuous line). The black dashed curves correspond to data from Facchini et al. [FAC 09].

mismatch between the CAD section and the true cross sections of the manufactured samples. An example of the variations of the section along the gauge length of one sample in different conditions, namely as-built and after 1 hour of chemical etching, is shown in Figure 2.3. For comparison, the values of the CAD section before (in blue) and after 1 hour of chemical etching (in red) are also shown. In that figure, it can be seen that there is a significant difference between the CAD section and the sections of the built sample. For instance, the difference between the CAD and the average section represents 13% of the CAD section for an as-built sample and 12% after chemical etching. This can account for the underestimation of the tensile stresses observed in Figure 2.2.

A "weak link" type approach may also be considered: the sample mechanical behavior was assumed to be governed by the minimum section within the gauge length, S_{min}. The corresponding engineering tensile stress-strain curves for the etched samples are plotted in Figure 2.2 (continuous lines with circles). With this definition of section, the $YS_{0.2}$ and UTS of the etched samples are now clearly overestimated in comparison with the reference.

The tomographic scans acquired on fractured specimens reveal that the failure does not always occur at the overall minimum section. This is further illustrated with two examples in Figure 2.4. In Figure 2.4b, the overall minimum section is located exactly within the failure area whereas it is not the case for the sample shown in Figure 2.4a. Both cases are samples which have been etched for 30 minutes. The minimum section was found to be located in the failure zone for only 50% of the etched samples while for samples with as-built surfaces (as-built and HIP samples), the failure *never* occurred at or near the minimum section. **This means that, for an as-built surface state, the failure is more likely to be driven by the morphology and aspect ratio of the surface defects rather than by the minimum section.**

Finally, the stresses have been calculated based on the average section of the sample
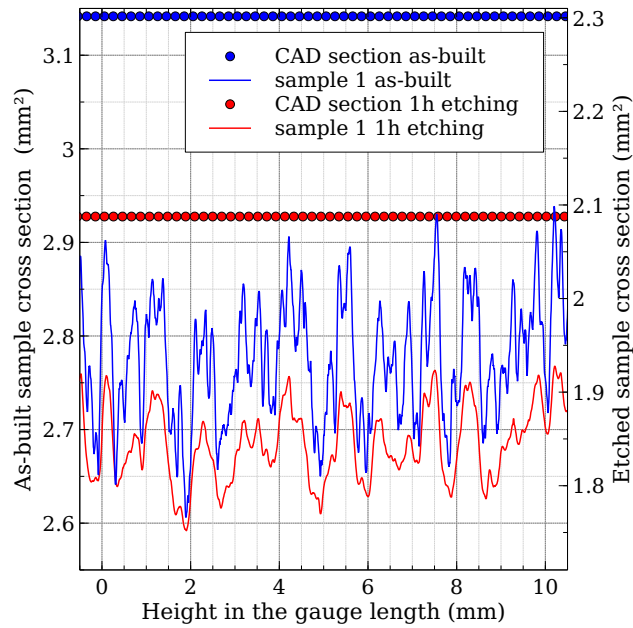
Figure 2.3: Example of variations of the cross section along the gauge length for one sample before (in blue) and after 1h of chemical etching (in red). The corresponding standard deviations are respectively 0.063 (blue curve) and 0.038 mm^2 (red curve). The dotted lines represent the corresponding CAD sections. The volume reduction induced by the chemical dissolution was taken into account to calculate the CAD section of the chemically etched samples as explained in section 3.1.
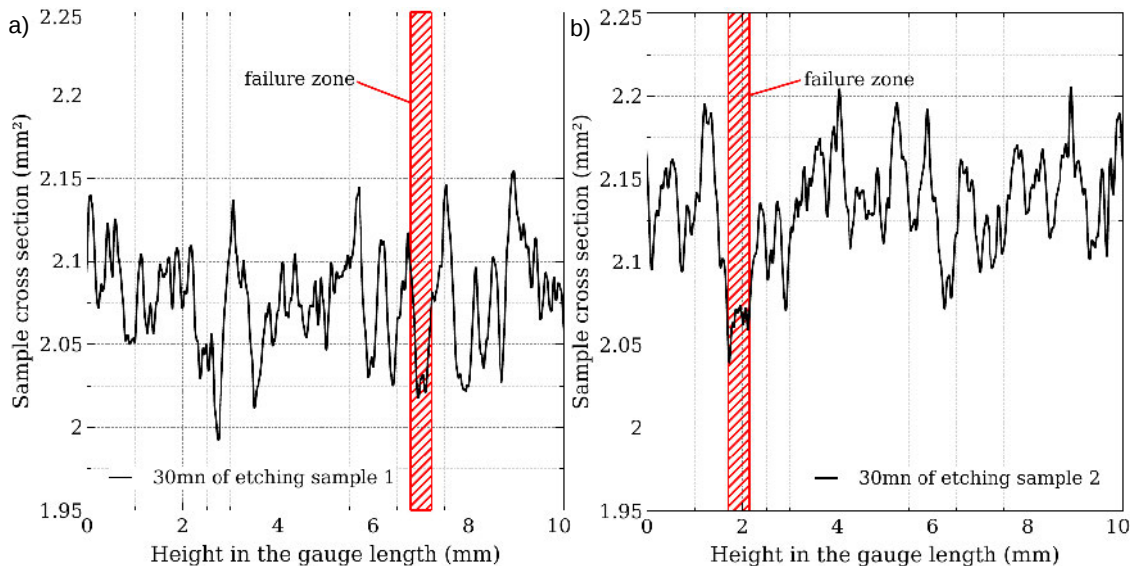
Figure 2.4: Example of variations of the cross section along the gauge length for two samples chemically etched for 30 minutes. The region highlighted in red represents the height at which failure occured. For sample 2 shown in b), the minimum section is located inside the failure zone whereas this is not the case for sample 2 shown in a).

within the gauge length $S_{average}$ which is represented in Figure 2.1. As shown in Figure 2.2, the corresponding engineering stress-strain curves (continuous lines without symbols) are in relatively good agreement with the curves reported in [FAC 09] for machined samples. This is confirmed by the data summarized in Table 2.1 where the standard tensile properties determined based on the average section $S_{average}$ are reported for the as-built conditions and after different post-treatments. Indeed, the $YS_{0.2}$ and UTS of the etched samples appear to be very similar to those reported by Facchini et al. [FAC 09] for machined samples. As a conclusion, it seems that **the average section approach enables us to correctly estimate the tensile properties of the chemically etched samples**, at least for the $YS_{0.2}$ and the UTS. In what follows, the mechanical properties of the as-built samples as well as the effect of the post-treatments will be analyzed based on the stress levels calculated with the *average section $S_{average}$*.

Table 2.1: Average tensile properties (Young's modulus (E), Yield Strength ($YS_{0.2}$) taken at 0.2% macroscopic plastic strain, Ultimate Tensile Strength (UTS) and elongation to failure (A%)) for Ti-6Al-4V samples fabricated by EBM in the as-built conditions and after different post-processing operations: HIP, chemical etching, machining and some of their combination. The values of the mechanical properties reported here are calculated based on the average section ($S_{average}$) in the gauge length. The symbol $^{+y}_{-x}$ gives an idea of the scatter of the results by providing respectively the minimum and maximum values of the investigated property. The symbol $\pm z$ represents the standard deviation of the measured values reported in the litterature.

Sample state	E (GPa)	$YS_{0.2}$ (MPa)	UTS (MPa)	A%
As-built	108^{+1}_{-2}	753^{+4}_{-3}	824^{+4}_{-6}	$6.1^{+0.7}_{-0.8}$
Etched (30 min)	118^{+3}_{-3}	842^{+8}_{-8}	918^{+6}_{-7}	$8.3^{+0.4}_{-0.4}$
Etched (1 h)	119^{+6}_{-5}	854^{+1}_{-1}	923^{+4}_{-4}	$8.6^{+0.4}_{-0.4}$
Machined [FAC 09]	118 ± 5	830 ± 5	915 ± 10	13.1 ± 0.4
HIP	111^{+3}_{-3}	697^{+0}_{-0}	777^{+4}_{-5}	$8.8^{+0.7}_{-0.8}$
HIP + Etched (30 min)	117^{+1}_{-1}	757^{+4}_{-4}	841^{+5}_{-4}	$7.3^{+0.1}_{-0.2}$
HIP + Etched (1 h)	117^{+1}_{-1}	763^{+1}_{-2}	844^{+1}_{-0}	$9.1^{+1.4}_{-1.4}$
HIP + Machined [FAC 09]	117 ± 4	795 ± 10	870 ± 10	13.7 ± 1.0

2.4   Tensile properties of thin parts

2.4.1   As-built properties

Figure 2.5 shows the stress-strain curves obtained for as-built and chemical etched samples and compares them to the tensile responses reported by Facchini et al. for machined samples [FAC 09]. **The tensile properties ($YS_{0.2}$, UTS and A%) of samples with the as-built surfaces are *lower* than the ones reported for machined samples** (see Table 2.1 and Figure 2.5). A limited and scattered ductility is measured (average value of elongation to failure: $6.1 \pm 0.8\%$). It is likely that the notch-like defects observed at the surface of the as-built samples act as stress raisers sites which promote crack initiation leading to a reduced ductility when compared to the reference one ($\geq 10\%$). Chao et al. [CHA 01] on Fe-40Al alloys and De Formanoir et al. [FOR 16a] on the Ti-6Al-4V alloy

made similar observations showing that the presence of surface defects always led to a ductility drop. These local stress concentrations can also explain the rather low values of UTS and $YS_{0.2}$.


Figure 2.5: Engineering tensile stress-strain responses of samples fabricated by EBM in the as-built conditions (in blue) and after 30 (in red) and 60 minutes (in green) of chemical etching. Black dashed curves were obtained on machined samples from [FAC 09]. The stresses are calculated based on the average section $S_{average}$ determined from the X-ray tomography analysis.

2.4.2 Effect of chemical etching: mechanical properties enhancement

Smoothing the surface irregularities leads to an enhancement of the mechanical properties of the chemically etched samples when compared to those of as-built samples. The $YS_{0.2}$ and UTS are both improved by $\sim 12\%$ after chemical etching, regardless of the etching duration (Table 2.1). This results in $YS_{0.2}$ and UTS values that are equal to the reference values of machined samples as can be seen on Figure 2.5 and Table 2.1. No improvement of the $YS_{0.2}$ and UTS was observed between 30 and 60 minutes of chemical etching. This means that **30 minutes of chemical etching seem sufficient to recover intrinsic properties similar to those of machined samples** and that the roughness improvement between 30 and 60 minutes of etching has no effect on the mechanical properties.

If compared with the elongation to failure measured on as-built samples, the ones obtained after 30 minutes and 60 minutes of chemical etching are respectively 36% and 41% higher. Etching also helps to reduce the scatter of the data: the standard deviation is divided by a factor 2 when compared to the one of as-built samples (Standard deviation (SD) = 0.4% for both etching durations *v.s.* SD = 0.8% for as-built samples). This im-

provement of ductility can be related to the removal of the sub-surface ring of internal defects (see Figure 1.30 in Chapter 1) as well as to the improvement of the surface condition after chemical etching. Both were discussed in the previous chapter. The reduction of the roughness and of the criticality of the surface defects is likely to reduce the stress concentrations and to delay crack initiation. Early failure is then avoided and the ductility improved. However, after chemical etching, some surface defects are still present and the roughness is still larger than after machining, see Figure 1.31 and Table 1.7 in Chapter 1. This can account for the systematic lower elongation to failure in comparison with machined samples (reference value of 13.8%). **A linear trend can be observed between the ductility and the maximum roughness Rt** (correlation coefficient R=0.87), see Figure 2.6.
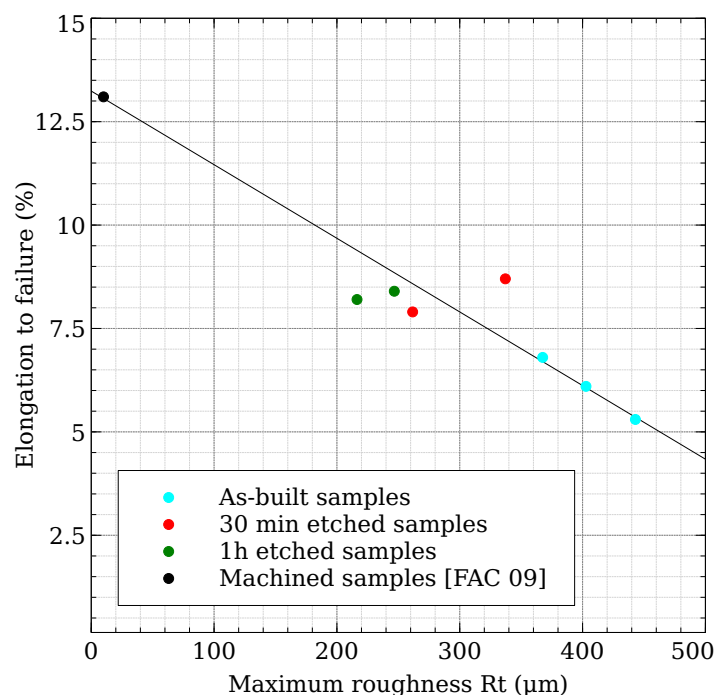
Figure 2.6: Elongation to failure of as-built, etched and machined [FAC 09] samples as a function of the maximum roughness of the samples. A linear trend can be observed.

2.4.3 Effect of HIP

The tensile tests indicate that the HIP post-treatment decreases the $YS_{0.2}$ and UTS of Ti-6Al-4V samples obtained by EBM, see Figure 2.7 and Table 2.1. For the as-built samples, **the HIP treatment reduces the $YS_{0.2}$ by roughly $\sim$ 50 MPa.** The same trend was reported in the literature [FAC 09] and also for grade 5 Ti-6Al-4V which differs from the material of this study only by its oxygen content ($\geq 0.15\%$) [ALB 10]. In both cases, the reduction of $YS_{0.2}$ and UTS reported is similar to the one observed in our study for the as-built samples.

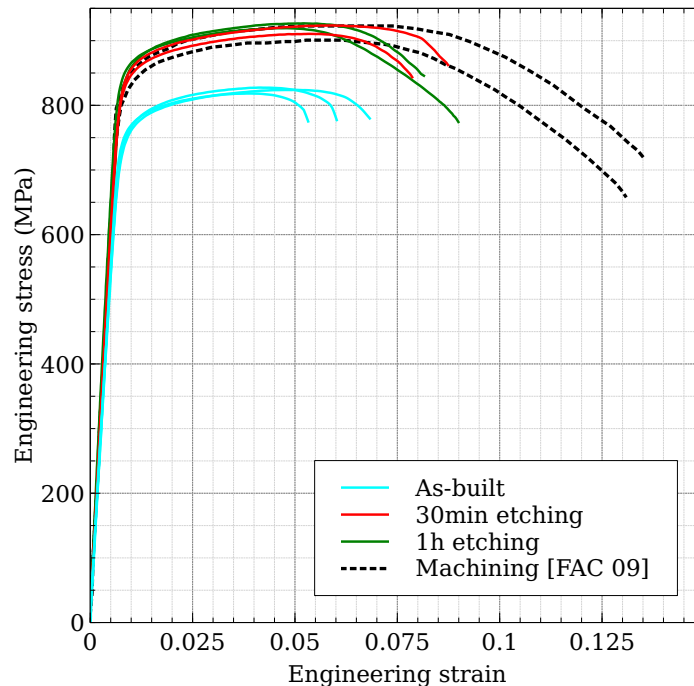Both Facchini [FAC 09] and Al-Bermani [ALB 10] have attributed the decrease of $YS_{0.2}$
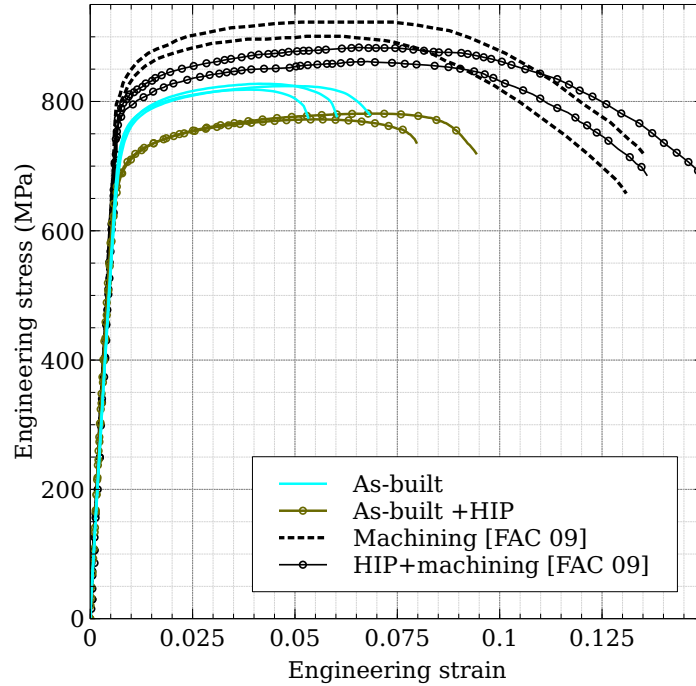
Figure 2.7: Engineering tensile stress-strain responses of samples fabricated by EBM in the as-built conditions (in blue) and after HIP treatment. Black dashed and dotted curves were obtained on respectively machined and "HIP+machined" samples from [FAC 09]. The stresses are calculated based on the average section $S_{average}$ determined from the X-ray tomography analysis.

and UTS after HIP to its effect on the microstructure, the α laths being coarser than in the as-built conditions. The coarsening of the microstructure leads to an increase in the effective slip length and thus causes the decrease of $YS_{0.2}$ and UTS. A similar coarsening is observed in our samples (Figure 1.23 in Chapter 1) and the same conclusions can then be drawn here.

HIP has also a beneficial effect on the ductility since the elongation to failure of as-built samples is increased by 44% after HIP. However, for machined samples, the increase of the ductility after HIP was rather limited with only a 5 to 10% increase, see amongst others [ALB 10], [FAC 09]. Since the HIP treatment has no impact on the surface state of the samples, this ductility enhancement can be attributed to the coarsening of the microstructure as well as to the internal pores removal.

Regarding the pores, their spatial distribution is heterogeneous in the as-built conditions with the presence of the sub-surface ring with a higher density of internal defects. As explained in details in the previous chapter, this ring is likely to be related to the melting strategy. It perfectly superimposes itself with the sub-surface ring generated by the surface irregularities (stacking defects, notch-like defects, ...), as shown in Figure 1.20 in Chapter 1. In order to obtain a defect-free surface, all surface irregularities must be removed through a machining process, meaning that the layer removed during this step is always thicker than both rings. As a result, whether the samples to be machined are fabricated near net shape or in cylindrical rods, this ring which is around $\sim 300\ \mu m$ thick

is always removed by the machining step. Consequently, the as-built geometry of the samples to be machined only affects the quantity of material that needs to be trimmed away during machining operations [YAD 17]. This explains why no such ring was reported in [ALB 10] or [FAC 09]. This also indicates that the benificial impact of HIP on the ductility of machined samples is not due to the closure of the pores contained in this ring. On the contrary, **when applied to as-built samples, the HIP post-treatment does provoke the closure of the pores contained in the sub-surface ring which can partly explain the better improvement of the ductility.**

The beneficial effect of microstructure coarsening on the ductility has been reported by several authors, see e.g. [MUR 09], [ALG 16], [ZHA 16b], [GAL 16], [LU 15]. However, in those studies, it was not decoupled from the beneficial effect of the internal pores closure. This means that the effect of microstructure coarsening on the ductility was therefore not clearly identified. In order to decorrelate the effect of microstructure coarsening from the one of internal defects closure, tensile tests should be conducted on samples which underwent the same heat treatment (2 h at 920°C and furnace cooling) without pressure.

Such tests were performed by Shui et al. on Ti-6Al-4V EBM samples [SHU 17]. They have divided cylindrical rods vertically manufactured in the same batch into three groups: the samples from the first group were directly machined whereas the samples from the second and third groups were respectively submitted to HIP and to the aforementioned heat treatment prior to machining. The authors report that both the heat treated and HIP treated samples share the same microstructure.

Regarding the tensile properties, when compared to HIP, the heat treatment leads to similar values of elongation to failure. This means that the internal pores closure induced by HIP did not impact the ductility. Therefore, these identical values of elongation to failure tend to show that the microstructural effect induced by HIP does affect the ductility of EBM Ti-6Al-4V alloy. Shui et al. attribute without confirmation this effect to the decrease of the dislocation density that the HIP treatment provokes rather than to the α-plate coarsening. Nonetheless, they confirm the beneficial impact of the microstructural change caused by the HIP process on the ductility.

2.4.4   Effect of the combination of HIP and chemical etching

As mentioned before, chemical etching has a beneficial effect on the tensile mechanical properties thanks to its positive impact on the surface defects severity. Nevertheless, the associated volume reduction may lead to the emergence of internal defects at the surface (Figure 1.31 in Chapter 1). To overcome this problem, some samples were first submitted to HIP and then to chemical etching (30 or 60 minutes). With this sequence of post-processing treatments, the residual internal pores have been closed or at least significantly reduced by HIP, and the severity of the plate-pile like stacking defects has been reduced by chemical etching. The effect on the mechanical properties is quantified in Table 2.1 and Figure 2.8.

Regarding the ductility, when chemical etching is applied for 30 minutes on HIP treated samples, the elongation to failure tends to decrease whereas after 60 minutes of etching time, the elongation to failure is equivalent or higher than the one obtained for HIP treated
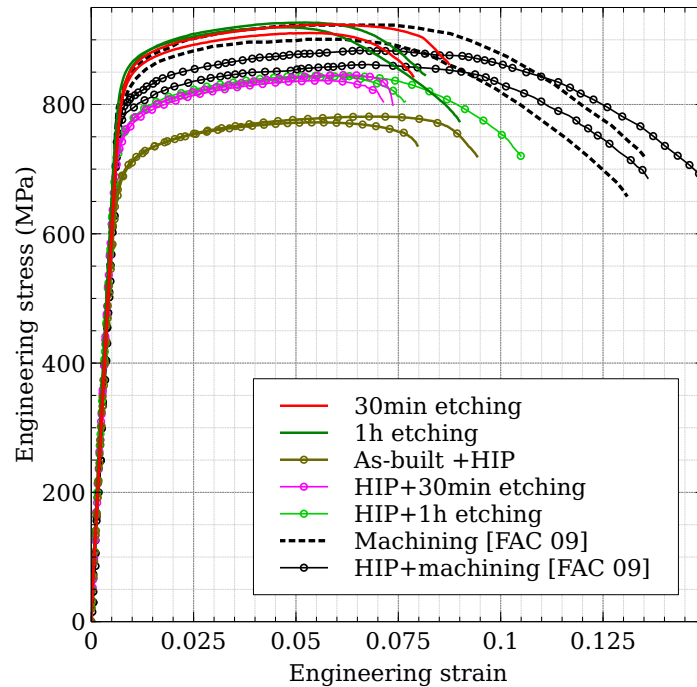
Figure 2.8: Engineering tensile stress-strain responses of samples fabricated by EBM after different post-processing operations. Black dashed and dotted curves were obtained respectively on machined and "HIP+machined" samples from [FAC 09]. The stresses are calculated based on the average section $S_{average}$ determined from the X-ray tomography analysis.

samples. As a result, it seems that depending on the treatment duration, chemical etching can have a slightly detrimental or beneficial effect on the ductility of HIP treated samples. However, considering the important scattering (Standard Deviation = 1.1% and 2.0% for HIP and HIP + 60 minutes of etching respectively) and the limited number of samples tested (2 for each of the three conditions: HIP, HIP + 30 minutes of etching and HIP + 60 minutes of etching), a larger number of specimens would be required to clearly address this point.

For both etching durations, an improvement of both the $YS_{0.2}$ and the UTS of roughly $\sim$ 60-65MPa is observed when compared to the results of HIP treated samples. Nevertheless, the $YS_{0.2}$ and UTS obtained for the "HIP+etched" samples are still slightly lower (30-35 MPa) than the reference values for "HIP+machined" samples (Table 2.1). As the $YS_{0.2}$ and UTS values obtained for etched samples were equal to those of machined samples, this means that the HIP impact on those properties was more important for etched samples than for machined ones. This might be linked to the machining process: the "HIP+machined" samples are likely to have some compressive residual stresses at the surface. This could, at least partly, explain their $YS_{0.2}$ and UTS values which are larger than those of "HIP+etched" samples.

2.4.5 Design rules: definition of down scaling factors

As shown in Figure 2.5 and Table 2.1, the $YS_{0.2}$ and UTS obtained for as-built samples are lower than the reference values of machined samples. This is due to the as-built surface which leads to stress concentrations that are not taken into account into the stress calculation. There is then a need to account for this negative effect of the surface defects and irregularities for the design of as-built thin parts and/or lattice structures.

One way to achieve this is to identify a **down scaling factor (DSF) that quantifies the reduction of tensile properties when considering as-built or post-treated samples** in comparison with the reference values. For instance, in terms of stress level, a simple ratio between the average $YS_{0.2}$ obtained for as-built samples and the targeted $YS_{0.2}$, i.e. the one reported for machined EBM samples, gives a DSF = 0.91. This ratio enables us to correctly assess the stress levels of as-built thin parts. The values of DSFs calculated for the different post-treatments are reported in Table 2.2.

This method can also be used on other mechanical properties such as the elongation to failure. In this case, the impact of roughness is more important as pointed out by Figure 2.6 which shows a linear relationship between the roughness and the elongation to failure. It also leads to a larger scatter of the results (Table 2.1) which means that the DSFs for A% need to be used with caution.

Table 2.2: Summary of the down scaling factors (DSF) necessary to meet the tensile properties of machined EBM samples.

Sample state	Down scaling factors		
	$YS_{0.2}$	UTS	A%
As-built	0.91	0.90	0.47
Etched (30 min)	1	1	0.63
Etched (1 h)	1	1	0.66
HIP	0.88	0.89	0.64
HIP + Etched (30 min)	0.95	0.97	0.53
HIP + Etched (1h)	0.96	0.97	0.66

2.5 Conclusion

When considering complex geometries of additively manufactured parts such as lattices structures, conventional machining techniques are not suitable to remove the surface defects inherited from the EBM process. Therefore, other post-treatments have to be applied. In this study, the impacts of HIP, chemical etching and of their combination on the tensile properties of as-built EBM thin struts have been investigated. The main conclusion can be drawn as follows:

- The average section is the most suitable section to be considered for stress calculation.
- The as-built surface of EBM thin struts has a clear detrimental impact on all the mechanical properties examined in this study (Yield Strength ($YS_{0.2}$), Ultimate Tensile

Strength (UTS) and elongation to failure (A%)).

- After chemical etching, the tensile strength matches the one of machined samples thanks to its impact on the surface defects. This post treatment also increases the samples ductility but the standard values reported for machined bulk samples are not recovered because of the remaining stress concentrations sites.

- HIP also has beneficial impact on the ductility which has been linked to both the internal pores closure and the microstructure coarsening.

- The combination of both post-treatments does not further improve the tensile properties.

- Down scaling factors have been suggested to account for the loss of properties when compared to machined samples.

2.6 Graphical summary

<div align="right">
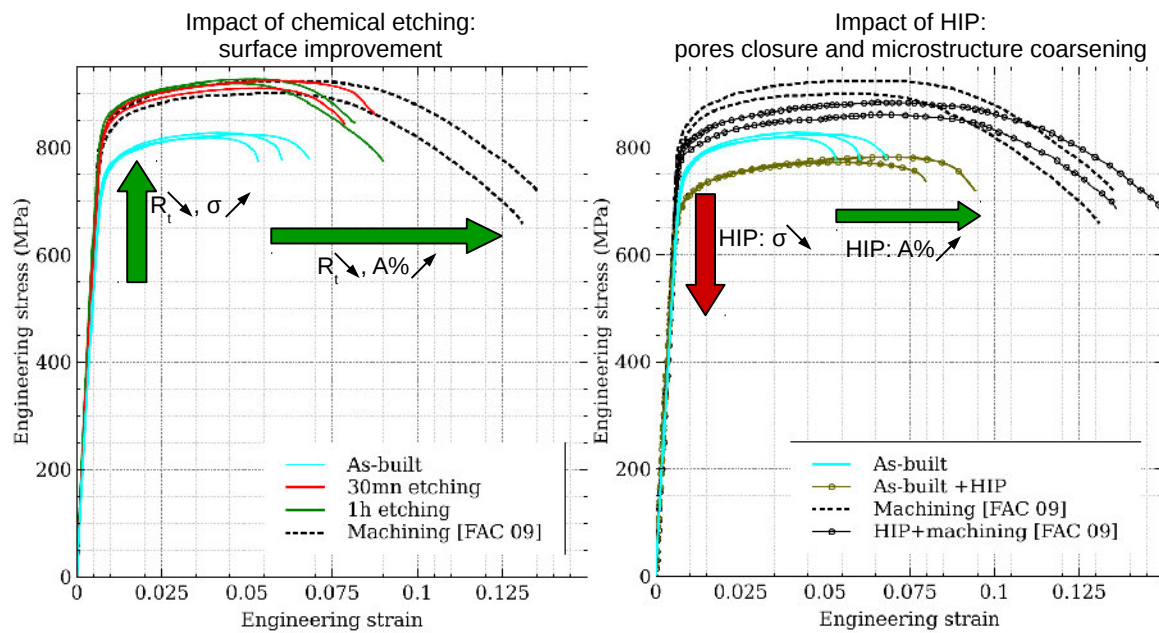
Chapter 3

</div>

<div align="right">

Fatigue properties

</div>

Contents

Because of its good fatigue resistance and its limited density, the Ti-6Al-4V alloy has been widely used in aircraft and biomedical industries for parts mainly designed with respect to cyclic loadings. Such Ti-6Al-4V parts are traditionally manufactured from

cast or wrought material and their fatigue properties are therefore used as references for additively manufactured samples. Those properties are briefly summarized in what follows. For an extensive review on the properties of Ti alloys, the reader is referred for example to [LEY 03].

3.1 Literature review

3.1.1 Fatigue properties of traditionally manufactured Ti-6Al-4V: reference data

The comparison of the fatigue properties obtained with the different manufacturing processes shows that, overall, cast samples lead to worst results than wrought samples. As for most metal alloys, three factors can influence the fatigue properties of Ti-6Al-4V alloys:

- *defects.* Either internal or surface ones, they are inherited from the manufacturing process and can affect the fatigue properties by acting as crack initiation sites or by driving the crack propagation.
- *microstructure.* The type and size of the microstructure can also impact crack initiation and propagation by inhibiting or favoring them. The microstructure varies depending on the thermal history sustained by the material during manufacturing and post-treatments.
- *surface preparation.* This type of post-treatment can be beneficial or detrimental for the fatigue properties depending on the surface finishing process used.

3.1.1.1 Impact of manufacturing defects

The poor fatigue properties of cast Ti-6Al-4V (fatigue limit at 10^7 cycles σ_f ranging between 160 and 380 MPa) are attributed to the presence of internal casting defects such as shrinkage pores [EYL 79b], [LIN 05]. Their range in size is extremely large (from $\sim 20\,\mu m$ to more than 1 mm). Although other factors (proximity to the surface or to other defects, surrounding microstructure favouring crack initiation, ...) are to be considered, the presence of such defects can in itself lead to the reduction of the fatigue properties. To reduce the detrimental effect of those defects, HIP can be used efficiently [EYL 79a], [OH 04]. For wrought samples, fatigue failure is not caused by internal defects but rather by suitably oriented α grains [NII 98], [OGU 10], [NAL 02].

3.1.1.2 Impact of microstructure

The comparison of different studies performed on HIP treated cast samples shows a large scatter in the fatigue properties [EYL 79a], [OH 04], [LI 16]. For HIP treated samples, the fatigue failure always initiates from localized plastic slip bands. The scatter of the fatigue properties is caused by variations at the microstructural level. The microstructure resulting from casting consists in α/β lamellaes; the thickness of the α lamellae within the β matrix depends on the thermal history. It is reported by several authors that a finer α phase leads to better fatigue properties, see e.g. [BAN 10], [LEO 15].

The type of microstructure also appears to impact fatigue properties. For instance, for wrought material, Nalla et al. reported that bimodal ($\alpha + \alpha'$) microstructures lead to better fatigue resistance than lamellar ones for comparable sizes of the α phase [NAL 02]. The better fatigue resistance of the bimodal microstructure in wrought samples was also reported by some authors ($\sigma_f = $ 410-540 MPa), see e.g. [NII 98], [GOL 10], [MOW 14].

3.1.1.3 Impact of surface preparation

Depending on the manufacturing process, a post-processing step might be required (for example, to remove surface roughness). The surface finishing process can lead to improvements or reductions of the fatigue properties. For instance, Electron Discharge Machining (EDM) induces tensile residual stresses and surface roughness which detrimentally affect the fatigue properties [MOW 14] whereas mechanical milling enhances the fatigue properties thanks to compressive residual stresses [GOL 10]. A surface finishing such a electropolishing added to a milled surface in order to reduce surface roughness would then be detrimental as it would remove the compressed layer [GOL 10].

3.1.2 Fatigue properties of AM Ti-6Al-4V: focus on EBM

The literature on fatigue properties of AM Ti-6Al-4V has been exponentially expanding in the last five years. SLM is by far the process with the most published results, see for example Li et al. [LI 16], Beretta et al. [BER 17] or Fotovvati et al. [FOT 19] for recent reviews. Here, we will focus on the fatigue properties reported for EBM samples only.

First, it is necessary to point out that all the results from the literature reported have been obtained for bulk samples, the smallest ones being cylindrical samples with a 6 mm diameter. No results were reported for thin struts with a large surface-to-volume ratio ($\propto \frac{1}{r}$ for cylindrical samples).

3.1.2.1 Fatigue properties of machined samples

No AM process is able to deliver surface conditions that can compete with those of conventionally manufactured and machined samples. In order to compare the mechanical properties of AM samples with those of conventionally manufactured samples, it was therefore admitted that similar surface conditions were needed. That is the reason why most of the published fatigue results on EBM samples are for machined samples. They are reported in Table 3.1.

First, only the results reported for machined samples with no heat treatments are considered. When low fatigue properties are reported ($\sigma_f = $ 200 and 270 MPa in [HRA 17] and [GRE 17] respectively), higher densities of internal voids (*lack-of-fusion defects*) are observed when compared to other studies, see e.g. [ACK 09], [SVE 10]. The authors furthermore determined that these defects were caused by under-melting because of unoptimized melting parameters (for example, low energy density input for high scan lengths for Hrabe et al. [HRA 17]).

For optimized manufacturing conditions, the fatigue limit σ_f at 10^7 cycles ranges between 300 and 460 MPa. These results are similar to those obtained for as-cast samples.

Table 3.1: Fatigue results (fatigue limit σ_f at 10^7 cycles) for machined samples reported in the literature. The results are shown depending on the type of powder and the samples build orientation. Where appropriate, the heat treatments applied to the samples are also indicated. Annealing = 710°C for 2 hours before furnace cooling (FC). SR = stress relief (650°C for 5 hours before FC). HT = 920°C for 2 hours before FC.

Source	Powder	Build orientation	Heat treatment	σ_f (MPa)
[FAC 09]	Grade 23	90°	None	391 ± 21
			HIP	441 ± 42
[SVE 10]	Grade 23	90°	None	407
			HIP	538
		0°	None	441
			HIP	607
[BRA 11]	Grade 23	90°	HIP	600
[BRA 12]	Grade 23	90°	Annealing	395
[ARC 13]	Grade 23	90°	None	400
			HIP	545
		0°	None	400
			HIP	545
[RAF 12]	Grade 23	90°	None	300
		0°		340
[EDW 13]	Grade 23	90°	None	300
		0°		400
[RAF 13]	Grade 5	90°	None	340
[GON 15]	Grade 23	90°	None	400
[ZHA 16b]	Grade 23	90°	None	400
			HIP	550
[CHA 16]	Grade 23	90°	None	320
		0°		320
[GRE 17]	Grade 23	90°	None	270
			HIP	550
[HRA 17]	Grade 5	90°	None	200
			SR	200
			HIP	550
[KAH 17]	Grade 23	90°	HIP	600
[SHU 17]	Grade 23	90°	None	460
			HT	460
			HIP	580
[VAY 18]	Grade 5	90°	None	400

However, they are lower to those of heat treated wrought samples. As no tensile residual stresses are detected with this level of fatigue resistance [HRA 17], this reduction in fatigue properties has been mainly attributed to the defect population [ACK 09], [LI 16].

Indeed, fatal cracks were found to initiate from manufacturing defects (mostly *gas pores*) which were either internal or brought to the surface by the machining step [EDW 13], [RAF 13], [GON 15], [ZHA 16b]. This discrepancy in the critical defect location seems to be the reason for the large scatter of the fatigue lives reported for many studies, see e.g. [EDW 13], [CHA 16], [TAM 17], [CHA 18].

As the internal defects are the main cause of fatigue failure, the impact of those defects on the fatigue properties has received a lot of attention. Brandl et al. deliberatey introduced internal penny-shape defects of three different sizes at the center of fatigue samples by defining non-melted spots in the CAD input [BRA 12]. No data regarding the size of the defects was mentioned. While the smallest defects did not affect the fatigue results, a reduction of the fatigue properties was induced by the largest defects, the fatigue limit being reduced from $\sigma_f = 395$ MPa down to $\sigma_f = 300$ MPa.

Gong et al. altered several process parameters (max current, speed function, line offset, ...) in order to deliberately generate *lack-of-fusion defects* and thus increase the density of internal defects (internal porosity increased up to 5%)[GON 15]. The fatigue properties of these samples were drastically decreased by the large number of these defects ($\sigma_f \sim 50$ MPa), some of which were systematically turned into surface defects by the machining step.

Tammas-Williams et al. [TAM 17] used laboratory X-ray tomography to follow the crack growth from internal defects and from defects brought to the surface by machining and defined several parameters impacting the criticality of defects. They showed that the location (proximity to the surface, to other defects), the shape and the size of a defect impacted its criticality. They found that surface and sub-surface defects were more deleterious than what would indicate the approach of Murakami and therefore considered the distance to the surface as a key parameter. Based on these findings, they used such parameters to rank the defects with respect to their criticality. The defect leading to fatigue failure was always found within the 5% of defects highlighted as the most harmful ones.

Many authors applied HIP in order to remove the internal defects which were identified as the main cause of fatigue failure. After such a treatment, the fatigue results (σ_f=441-607 MPa) were found to match the ones obtained for wrought samples. This fatigue improvement was attributed to the complete closure of the internal defects by many authors, see amongst others [ZHA 16b], [HRA 17]. In this case, as no voids or pores were detected at the crack initiaton sites, localized plastic slip bands seemed to lead to crack initiation and failure [GÜN 17], [KAH 17], [HRA 17].

Contrasted effects of the microstructure coarsening induced by this post-treatment on the fatigue properties are reported. On the one hand, it increases the crack propagation threshold and therefore the fatigue properties [LÜT 98], [FAC 09], [OBE 10], [BER 17], [POL 14], [TAM 17]. On the other hand, microstructure coarsening decreases the resistance to long plastic bands and thus reduces the high cycle fatigue resistance [LÜT 84], [NAL 02], [BRA 11], [BAN 10], [POL 14], [ZHA 16b].

To summarize, as pointed out by the review of Li et al. [LI 16], although the fatigue properties of machined samples are similar to those of cast samples, HIP treatment is needed to match the results obtained for wrought samples.

3.1.2.2 Fatigue properties of samples with as-built surface conditions

Very few studies have focused on the fatigue properties of samples with as-built surface conditions (see Table 3.2). When this is the case, important reductions of the fatigue resistance were observed (σ_f=100-230 MPa) and a surface defect was always reponsible for the fatigue failure. Many studies reported multiple crack initiation sites from the sample surface and related it to the important surface roughness [EDW 13], [CHA 16], [GRE 16], [GRE 17], [KAH 17], [CHA 18]. However, in most cases, no micrographs of the fracture surfaces were shown. Kahlin et al. indicated that the cracks initiated from micro notches ($\sim$150-200 μm deep) caused by the layer stacking [KAH 17]. Such defects have also been reported as the cause of fatigue failure for 3-points bending fatigue by Chan et al. [CHA 13]. A recent study by Vayssette et al. reported crack initiations from extremely deep surface defects ($\sim$ 0.8-1 mm deep) [VAY 18]. The micrographs of the fracture surface showed unmelted powder particles trapped within the defects. The defects strongly looked like *lack-of-fusion defects* that would be connected to the surface by a micro notch.

Table 3.2: Fatigue results for samples with as-built surfaces reported in the literature. The results are shown depending on the type of powder and the samples build orientation. Where appropriate, the heat treatments applied to the samples are also indicated. Annealing = 710°C for 2 hours before furnace cooling.

Source	Powder	Build orientation	Heat treatment	σ_f (MPa)
[RAF 12]	Grade 23	90°	None	150
		0°		230
[EDW 13]	Grade 23	90°	None	100
		0°		150
[CHA 16]	Grade 23	90°	None	150
[GRE 16]	Grade 5	90°	Annealing	150
[GRE 17]	Grade 5	90°	None	150
			HIP	125
[KAH 17]	Grade 23	90°	None	180
			HIP	200
[VAY 18]	Grade 5	90°	HIP	100

Rafi et al. [RAF 12] and Edwards et al. [EDW 13] performed tests on as-built samples built in the horizontal and vertical directions. Both studies showed that better fatigue results were obtained for horizontal samples even if the impact of the build orientation was more limited in [EDW 13]. Rafi et al. related this orientation dependency to the difference in orientation of the surface defects (stacking defects) with respect to the applied load. The surface defects perpendicular to the loading direction in vertical sample produced the largest reduction in fatigue [VIL 11], [RAF 12].

Greitemeier et al. [GRE 17] and Kahlin et al. [KAH 17] applied HIP to as-built samples. No impact on the fatigue properties was reported despite the confirmed closure of internal defects. Both studies concluded that removing the internal porosity does not matter as long as the surface state is not improved.

3.1.2.3 Impact of surface roughness

Some authors have tried to take into account the detrimental effect of surface roughness on the fatigue properties.

Chan et al. found a power relationship between the samples fatigue life and the maximum surface roughness R_t [CHA 13]. They assumed from this relationship that the surface irregularities could be considered as surface micronotches with a depth equivalent to the surface R_t. They showed that such micronotches led to both important stress concentration factors K_t and important stress intensity factor ranges ΔK. They concluded from these results that, because of the surface roughness, fatigue crack initiation could easily occur in as-built samples and that the fatigue crack growth would take place at a higher rate than in machined samples.

Greitemeier et al. considered an experimental crack propagation law and experimental results from fatigue tests (numbers of cycles to failure at different stress levels) to determine an equivalent initial flaw size (EIFS) for both DMLS and EBM samples [GRE 16]. They compared this size to the sample roughness and determined a linear relatonship between EIFS and R_t. With this method, they were able to determine the EIFS corresponding to other surface roughnesses and then estimated fatigue curves for several roughnesses. Finally, they compared these curves with experimental literature data from other sources such as [WYC 14] (stress relieved DMLS samples) and were able to predict rather accurately the fatigue properties.

Kahlin et al. compared the fatigue results of EBM as-built samples to those of machined and polished wrought samples. They determined the fatigue notch factor K_f as the ratio between the two fatigue limits [KAH 17]. They used both K_f and the K_t values determined by Chan et al. [CHA 13] from the surface roughness to determine the notch sensitivy $q = \frac{K_f - 1}{K_t - 1}$. The same q values were obtained for EBM and wrought samples. This means that K_f could be determined from the K_t induced by the surface roughness. Therefore, the fatigue properties of wrought samples could be sufficient to predict the fatigue resistance of an EBM sample based on its roughness. The method was however not tested by the authors.

Vayssette et al. used finite elements simulations to take into account the notch effect of the surface roughness on the fatigue properties [VAY 18]. They meshed volumes obtained from surface scans and conducted elastic computations on them. For each sample, they simulated the number of cycles that it sustained before failure, N_f. To evaluate the fatigue strength, they proposed a fatigue criterion based on the Crossland equivalent stress distribution at the surface and the results from experimental fatigue tests. They applied this method to SLM surfaces and were able to correctly account for the effect of the surface roughness. Indeed, after N_f, the local Crossland equivalent stress induced by the surface roughness and determined from the FE simulations was close to the experimental equivalent stress of the defect free samples. However, although these authors used profilometry measurements to characterize the sample surface, they also showed that the defects leading to fatigue failure of EBM as-built samples could not be detected by profilometry. They were therefore not able to validate this method on EBM samples.

3.1.3 Macroscopic description of the impact of defects on the fatigue properties

Because of the significant and detrimental impact of AM defects on the fatigue properties, several studies were conducted in attempts to quantitatively determine their impact.

Recent literature reviews by Beretta [BER 17] et al. and Cao et al. [CAO 18] used *Kitagawa-Takahashi* diagrams to account for the impact of defects on the fatigue properties, regardless of the defect location (internal or at the surface). Such approaches will be discussed more in details later in this chapter. It sufices to say here that such diagrams determine the maximum stress level that can be applied to a defect without provoking crack growth [KIT 76]. To do so, the stress intensity factor range induced by this defect is compared to the macroscopic material crack propagation threshold. The fatigue limit in the absence of defects and the crack propagation threshold of the material are needed to plot such diagrams.

Beretta et al. gathered extensive data from the literature on these two material parameters to plot *Kitagawa-Takahashi* diagram for Ti and Al alloys [BER 17]. Results from the literature with the size of the defect responsible for failure were reported on those diagrams when available. The stress intensity factor range induced by the defect was determined using Murakami parameter $\sqrt{area}$ which also take into account the location of the defect [MUR 85]). This method was applied to both additively (SLM and EBM mostly) and traditionally manufactured samples [BER 17]. The authors showed that, by considering the defects size and location, such diagrams enable to quantify the impact of defects on the fatigue properties of AM samples.

Leuders et al. used Murakami equation to predict the fatigue properties of SLM samples [LEU 15]. This equation which was determined empirically relates the fatigue limit σ_f to the material hardness and the size $\sqrt{area}$ and location of the defect [MUR 94]. However, when applied to the internal defects from machined samples detected by X-ray tomography, the Murakami equation failed to predict the fatigue limit of these samples. In addition, they found from fracture surface observations that the defects responsible for fatigue failure were not the defects considered as the most critical by Murakami's equation. They were rather small defects close to the surface. They concluded that the impact of the proximity to the surface was underestimated and used the fracture surfaces observations to corrected it based on the method of least squares. Better results were obtained but the scatter remained important.

Cao et al. also found that using the Murakami equation to plot the aforementioned *Kitagawa-Takahashi* diagrams does not describe precisely the experimental data obtained with internal and surface defects [CAO 18]. The authors claimed that the harmfulness of internal defects is clearly overestimated because of the much slower internal crack growth [CAO 17] and proposed a modified *Kitagawa-Takahashi* diagram that takes this phenomenon into account.

To summarize, the key information stemming from this literature review are the followings:

- While the fatigue properties of machined EBM samples have been extensively stud-

ied, the data on as-built samples is very scarce:

- – The reduction of the fatigue properties observed for as-built samples is related to the surface condition. However, the surface defects leading to failure are not precisely characterized. Most of the studies focus on the effect of the surface roughness.
- – All studies on as-built samples were conducted on *bulk* samples. As the crack leading to fatigue failure is always reported to initiate from the surface, the high surface-to-volume ratio of as-built *thin* parts might detrimentally affect their fatigue properties.

- *Kitagawa-Takahashi* diagrams seem to be an efficient tool to predict the impact of internal pores on the fatigue properties of machined samples. Although some authors point out that the impact of the distance between the defect and the surface is underestimated, applying *Kitagawa-Takahashi* diagrams to as-built samples might be interesting.

3.2   Context

In order to determine the fatigue properties of thin struts manufactured by EBM, fatigue tests were performed on as-built and post-treated samples. Their fatigue performance was compared to the one of machined samples. The specimens were first tested in their as-built conditions and the impact of the defects was evaluated[1]. The three post-treatments presented in Chapter 1 (HIP, chemical etching and USP) as well as some of their combinations were applied to as-built samples in order to improve their fatigue resistance. The effects of these post-treatments on the fatigue behavior were linked to their effects on the defects described in Chapter 1.

3.3   Fatigue testing: experimental procedures

As-built fatigue tensile specimens built in three different orientations (0°, 45° and 90° with respect to the build plate) were tested at room temperature using a servo-hydraulic IN-STRON 8516 fatigue testing machine equiped with a 5kN cell force. Constant amplitude stress controlled uni-axial tests were carried out with a frequency of f = 10 Hz (sinusoidal wave form) and a stress ratio R = $\frac{\sigma_{min}}{\sigma_{max}}$ = 0.1 to comply with the aircraft industry requirements [Air01]. All the nomenclature related to fatigue tests (maximum stress σ_{max}, stress range $\Delta\sigma$, stress ratio R, ...) are defined in Figure 3.1.

Based on the results of Chapter 2, the cyclic stress levels were calculated by using the sample average section which is determined from the tomographic scans of the sample gauge length. Fatigue tests were performed until failure or stopped after 10^7 cycles. Since the stress level corresponding to fatigue lives of $\sim 10^5$ cycles is commonly used for fatigue design in aircraft industries [Air01], such fatigue lives were targeted for most of the fatigue tests. The fracture surfaces of the samples were observed using scanning electron

---

[1]The results and the analysis of the as-built properties presented in this chapter have been published in [PER 19]
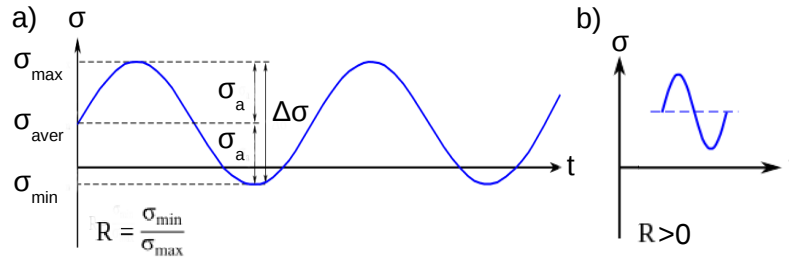
Figure 3.1: Schematic illustration of a sinusoidal fatigue signal. (a) Example of two fatigue cycles used to define the minimum σ_{min}, average σ_{aver} and maximum σ_{max} stresses, the stress range $\Delta\sigma$ and stress amplitude σ_a as well as the stress ratio $R = \frac{\sigma_{min}}{\sigma_{max}}$. (b) Example of a tensile-tensile fatigue cycle with R>0.

microscopy using secondary electron contrast and the broken samples were characterized by X-ray tomography before and after failure.

3.4 As-built samples

3.4.1 Fatigue properties

The S-N curves of the as-built samples are presented in Figure 3.2 where results from ARCAM for machined samples have also been added (hollow symbols) [ARC 13]. The build parameters (powder, machine, build theme, layer thickness, ...) for these machined samples are the same as the ones used in this study except for the sample geometry: ARCAM data were obtained on $\sim$ 5 mm diameter cylindrical tensile specimens that were *machined* from bulk materials. As detailed in the Chapter 2 and as also shown in [YAD 17], it is likely that this machining step has removed sub-surface defects.

For the 90° samples, several stress levels were investigated in order to obtain the full Wöhler curve with fatigue lives ranging between 10^4 and 10^7 cycles. This orientation was chosen as reference as it exhibits the worst surface state as explained in Chapter 1. **A clear reduction of the fatigue properties can be observed for the as-built samples** compared to machined samples. For instance, the fatigue limit σ_f obtained at 10^7 cycles is equal to $\sigma_f = 140$ MPa whereas for machined 90° samples, this value is of the order of $\sigma_f = 400$ MPa [ARC 13].

Figure 3.2 also shows that the build orientation significantly impacts the fatigue properties. The 45° and 0° samples have been tested at a maximum stress level $\sigma_{max} = 290$ MPa corresponding to fatigue lives of about 10^5 cycles. At this stress level, the average fatigue lives of the 90°, 45° and 0° samples are respectively 55 000, 150 000 and 250 000 cycles. This effect of the build orientation was not reported in the literature for machined samples (red and blue hollow symbols in Figure 3.2).

In order to identify the failure mechanisms, the fracture surfaces of samples with different build orientations have been systematically examined by SEM. Three representative fracture surfaces (one for each build orientation) are shown in Figure 3.3. The relatively large flat zones shown in Figure 3.3 and outlined by dashed lines correspond to the stable
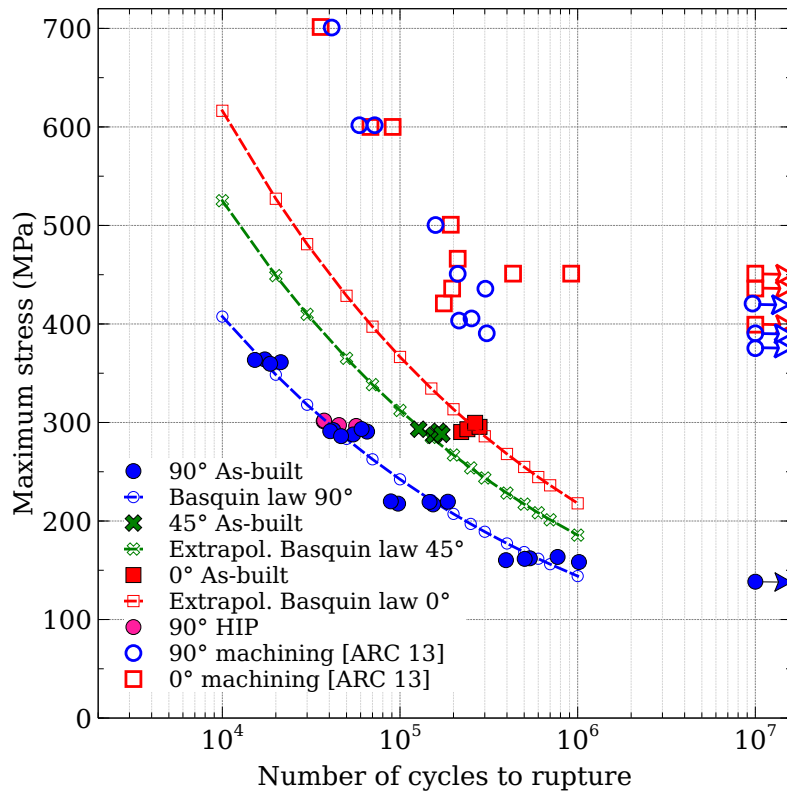
Figure 3.2: S-N curves for as-built fatigue samples fabricated by EBM with 3 different orientations: 0° (red squares), 45° (green crosses) and 90° (blue dots). Hollow symbols correspond to data from ARCAM [ARC 13] on machined samples obtained by EBM. Arrows show run out samples ($N > 10^7$ cycles). The Basquin law of the 90° samples is represented by a blue dashed line with dots and was used to extrapolate the ones of 0° (red dashed line with squares) and 45° samples (green dashed line with crosses). Details regarding the extrapolation are provided in section 3.4.5.2.

crack propagation regime. Their area A_{st} scale with the fatigue lives ($A_{st,90°} < A_{st,45°} < A_{st,0°}$). For the three specimens shown in Figure 3.3, the crack leading to failure initiates from a surface defect. The fracture surfaces of Figure 3.3 are also representative of what was observed at higher and lower stresses for the 90° samples. **Defects at the sample surface are therefore the most critical for the fatigue resistance, as already reported, see e.g. [YAD 17].**

3.4.2 Critical defect identification

In order to identify more precisely the defect that leads to the final failure, systematic tomographic scans were performed before and after failure and compared. This enables to determine at which tomographic slice along the gauge length failure occurs. From this slice and from the SEM image of the fracture surface, the critical defect can be unambiguously identified and one can determine its exact geometry (size and shape) on the tomographic images before the fatigue test. This procedure is illustrated in Figure 3.4. For all investigated samples, and regardless of their build orientation, the crack leading
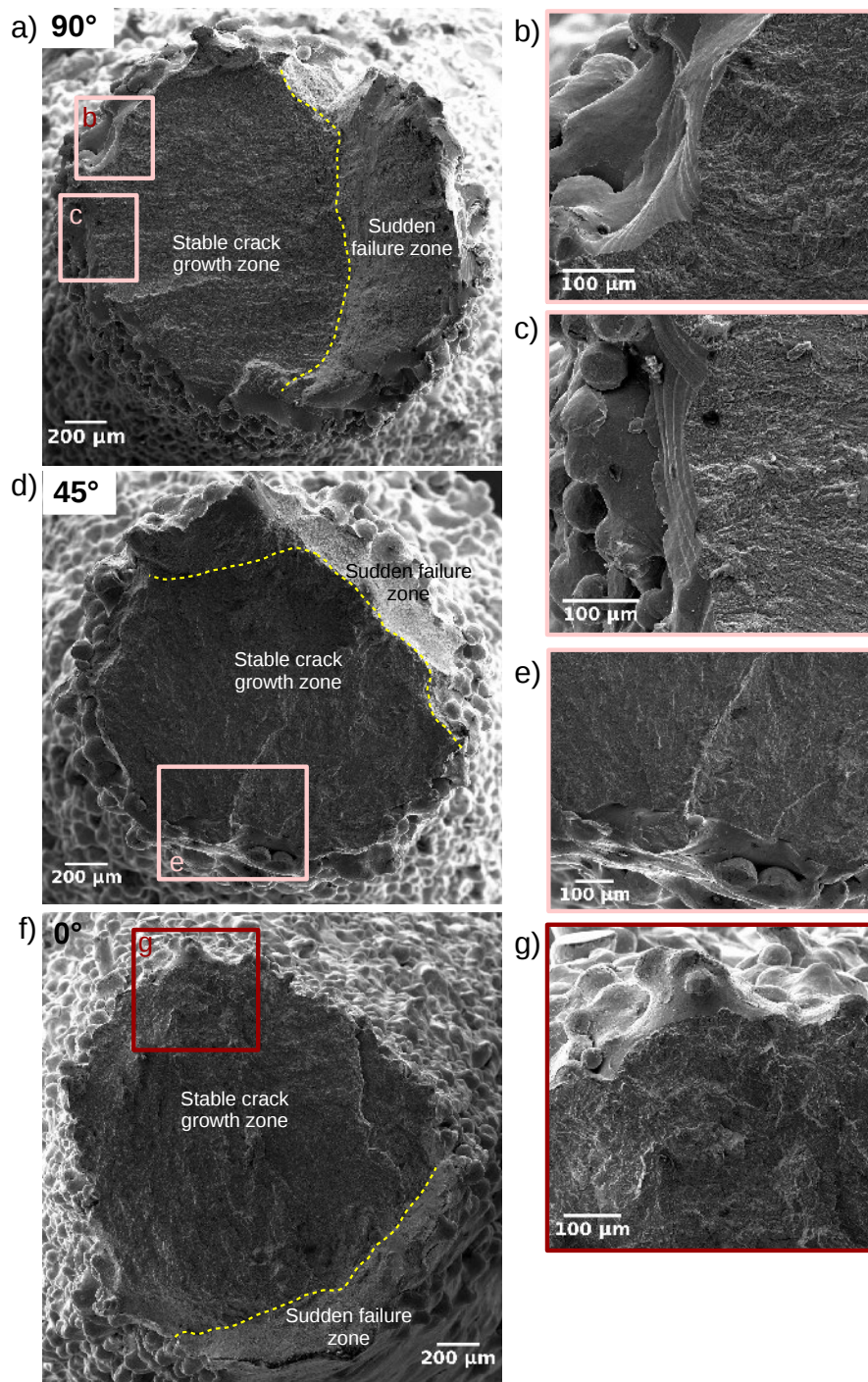
Figure 3.3: SEM-SE micrographs of the fracture surfaces of as-built EBM fatigue samples (σ_{max} = 290 MPa). (a,d,f) Fracture surfaces showing the stable crack growth and sudden failure zones of 90°, 45° and 0° samples respectively. (b,c,e,g) Higher magnification images showing the crack inititiation sites.
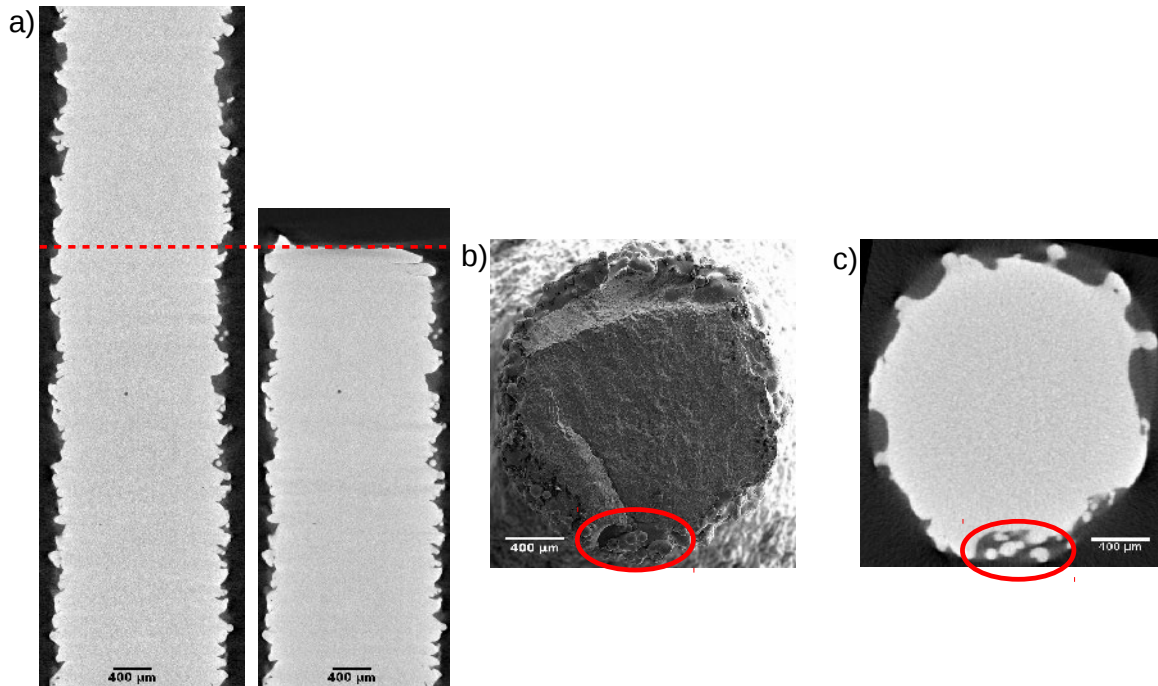
Figure 3.4: Schematic illustration of the methodology used to identify the defect responsible for the fatigue failure. (a) Radial slices obtained by X-ray tomography of a sample before and after fatigue failure. Their comparison enables to identify the critical cross section, i.e. the height within the gauge length at which failure occurred. (b) SEM-SE observation of the fracture surface of the fatigue sample. (c) Tomographic axial view of the sample cross section with the critical defect before fatigue test. Comparison of (b) and (c) leads undoubtedly to the critical defect identification.

to failure was found to initiate from a "plate-pile" like stacking defect. In the case of the 45° and 90° samples, notch-like defects were observed at the root of these "plate-pile" like stacking defects. The cracks were systematically found to initiate at those defects. No notch-like defect was detected for the 0° samples. Example of defects leading to failure are shown in Figure 3.5 for the three build orientations.

3.4.3   Failure mechanisms: multiple crack initiation sites

For several 90° samples, the observation of the tomographic images after failure reveals the presence of long cracks (length over 500 μm) outside the failure area, see Figure 3.6a. A thorough analysis shows that shorter cracks (length $\leq$ 200 μm) can also be identified. These two kinds of cracks were only detected for samples that were submitted to high stress level fatigue tests ($\sigma_{max} \geq$ 290 MPa). The corresponding fatigue lives were always lower than 100 000 cycles (Figure 3.2). For all 45° and 0° samples ($\sigma_{max} =$ 290 MPa) as well as for 90° samples submitted to lower stress levels, no cracks were detected outside the failure zone.

Laboratory X-ray tomography is a limited technique as far as crack observation is concerned [YU 16] because the voxel size (2.5 μm in this case) is not small enough to
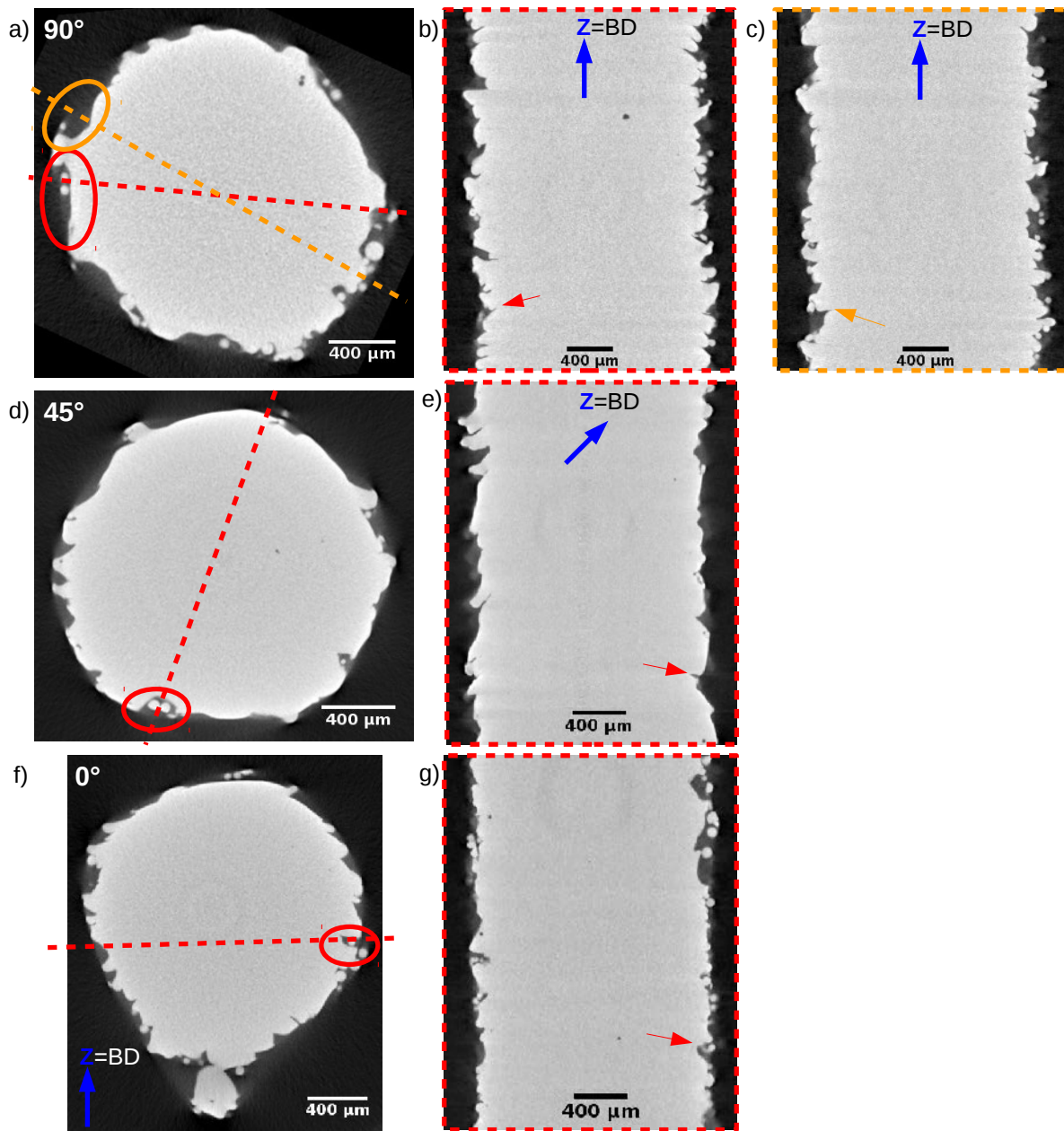
Figure 3.5: Examples of surface defects responsible for the failure of as-built samples (notch-like defects for 90° and 45° samples and a "plate-pile" like stacking defect for the 0° sample). (b,c,e,g) Radial slices of critical defects for respectively 90°, 45° and 0° sample). (a,d,f) Axial slices of critical defects for respectively 90°, 45° and 0° samples. (b,c,e,g) Radial slices of critical defects for respectively 90°, 45° and 0° samples. Arrows and ellipses highlight the critical defects. The dashed lines on the axial slices indicate the location of the corresponding radial slices. For each sample, the building direction is indicated by a blue arrow.

detect cracks with submicron opening. Optical longitudinal micrographs of the gauge length revealed the presence of several cracks that were not detected on the tomographic
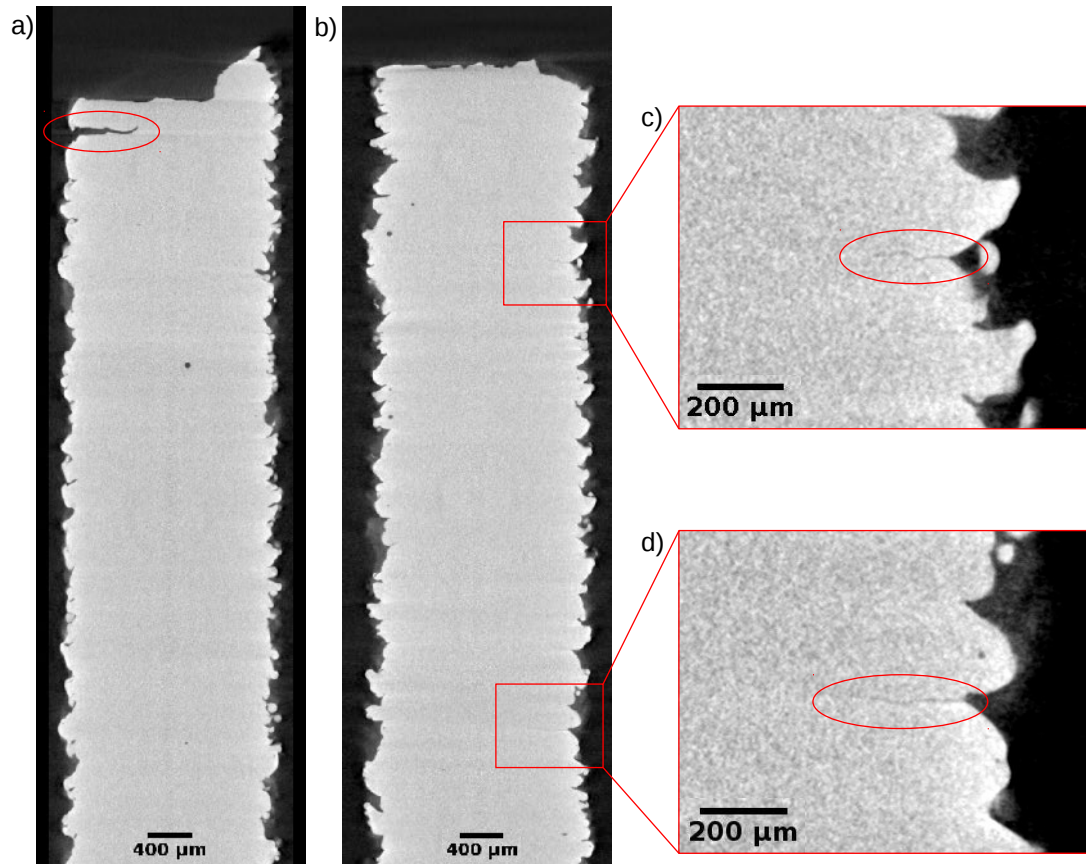
Figure 3.6: Examples of cracks detected outside the failure zone. The cracks are circled in red. (a,b) Radial slices showing a long crack close to the failure zone (a) and shorter cracks that propagated further away from the failure zone (b). (c,d) Enlarged view of the surface defects showing the short cracks. These tomographic slices correspond to samples tested at high stress levels: they lived respectively $\sim 47\,000$ and $\sim 15\,000$ cycles.

images. For example, Figure 3.7 shows the comparison between a tomographic image and an optical micrograph of the same surface defects. The optical micrograph (Figure 3.7b) shows two cracks whereas none appear in the tomographic image (Figure 3.7a). For samples submitted to fatigue stress $\sigma_{max} \geq 290$ MPa, a dozen of those cracks could be identified on a single polished longitudinal cross section. On the contrary, for a sample submitted to a lower stress level ($\sigma_{max} = 220$ MPa and roughly 150 000 cycles to failure), only one crack outside the failure zone was identified.

A thorough characterization of all the cracks that appear in the gauge length of the broken samples by optical microscopy is not possible for obvious practical reasons. Nevertheless, the few micrographs which have been taken confirm the observation made based on tomographic images. Indeed, multiple cracks initiate and grow within the gauge length of specimens submitted to high stress levels during the fatigue tests whereas, when the stress level decreases, the number of initiated cracks is drastically reduced. It is likely that, for a sufficiently low stress level, only the surface defect leading to the failure pro-

vokes crack initiation and crack growth. However, a long and tedious process requiring the observation by optical or scanning electron microscopy of the entire volume of the gauge length would be needed to corroborate this assumption. Besides, the impact of the stress level on the number of propagating cracks is well-known and confirm these observations, see for example [SCH 01a]. The tendency observed for 90° samples is therefore expected to also occur at higher stress levels for 45° and 0° samples.
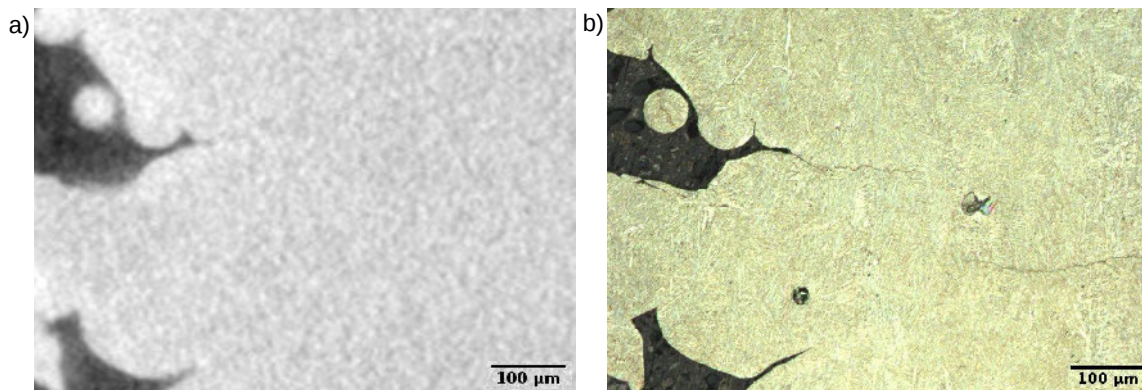
Figure 3.7: Comparison of the imaging of cracks by laboratory X-ray tomography (a) and optical microscopy (b). Two cracks are visible only on the optical micrographs, one initiating from the surface defect and the end of another one. Both images are taken from sligthly different planes which explains why the two internal pores are only visible on the optical micrograph.

If one plans to use tomographic images for defects detection and analysis, the shape and size of every single defect should be captured with enough accuracy. The comparison of the tomographic images with the optical micrographs can also be used to address this issue. Figure 3.7 shows that even though X-ray tomography is not precise enough to detect submicron cracks, the spatial resolution of the tomographic images allows to capture the thinnest surface defects (thin notch-like defects). It can also be seen that the shape of the defects is also well described: only the tip of the thinnest defects is potentially overlooked by the tomographic images (see in Figure 3.7a the defect leading to crack growth in Figure 3.7b). **Consequently, all surface and internal defects are detected by X-ray tomography. The main risk that may be taken when relying on tomographic images to analyze defects is to slightly underestimated the depth and size of the thinnest ones.** The resulting approximation will be measured and commented in details in Chapter 4 where such measurements are extensively used for systematic defect detection.

3.4.4 Fatigue resistance and crack initiation sites of as-built samples

The fatigue results presented in Figure 3.2 show that, for every build orientation considered, the fatigue resistance of as-built samples is considerably lower than that of the machined samples [ARC 13]. This reduction of the fatigue properties is not caused by the microstructure. Indeed, the microstructure of the as-built samples reported in Chapter 1 was found to be relatively similar to the one reported by ARCAM and other literature

references (see for example [ACK 09], [GAL 16] and [FAC 09]) : fine α-laths ($\sim 1\ \mu m$ width) separated by some residual β-rods.

Regarding the crack initiation sites, for both SLM and EBM Ti-6Al-4V *machined* samples, they were either internal, sub-surface or surface defects, see for example [LI 16], [ZHA 16b], [GON 15] or [LEU 14]. Those defects were often gas pores which were contained in the bulk in as-built conditions and brought to the surface or sub-surface during machining ([YAD 17], [GON 15]). Such internal or sub-surface defects were also observed in the as-buit samples of this study (Chapter 1) but they were never found to be responsible for the sample failure. Instead, the crack leading to failure initiated from stacking irregularities (Figure 3.3) which were notch-like defects in the case of 45° and 90° samples (radial slices in Figure 3.5). Similar initiation sites were reported for as-built SLM manufactured samples [KAS 15].

The ability of a defect to initiate a fatigue crack can be assessed through its stress concentration factor K_t [SCH 01b]. A larger local stress results in an increased level of plasticity which leads to crack initiation because of slip irreversibility. In what follows, K_t is used to compare the criticality of pores (internal or sub-surface) to that of "plate-pile" like stacking and notch-like defects. A detailed analysis would theoretically require the calculation of the local plastic strain concentrations induced by the defects. However, such calculations can be time-consuming, especially in the case of cyclic loading. Besides, Tammas-Williams et al. [TAM 17] have shown by FE calculations that, in the neighborhood of a pore, the plastic strain concentrations occur at the same locations that the ones found when performing purely elastic calculations. In what follows, only elastic strain concentrations are considered. Based on this assumption, the stress concentration factor K_t of an internal spherical pore in an infinite elastic material is $K_t = 1.96$ (perfect sphere). If this pore gets closer to the surface, its K_t can reach values of the order of 5 [BOR 02].
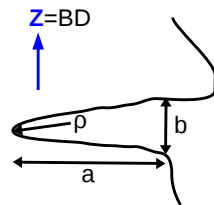
Figure 3.8: Schematic illustration of a notch-like defect with the associated geometrical parameters. a, b and ρ represent respectively the depth, the thickness of the notch and the radius of curvature at its tip.

Notch-like defects (see Figure 3.8) can be considered as semi-elliptical notches at the sample surface with a radius of curvature at the tip ρ and a depth a (Figure 3.8) for which the following classical formula can be used:

$$K_t = 1 + 2\sqrt{a/\rho} \tag{3.1}$$

The radius of curvature ρ at the tip of the elliptical notch is equal to $\rho = b^2/a$ where b is the maximum "thickness" of the notch. From Figure 3.5, typical values of a/b larger

than 10 can be measured, leading to very large values of K_t (for $a/b = 10$, $K_t = 21$). This impact of the aspect ratio of the defect on the K_t values was also reported by Tammas-Williams [TAM 17] using elastic FE calculations. Such large K_t values clearly explain why cracks systematically initiate at notch-like defects and not at internal or sub-surface pores.

In order to confirm that the important loss of fatigue performance observed for the as-built state is not related to the presence of internal or sub-surface pores, a HIP treatment (refer to Chapter 1 for the detailed process parameters) was applied to as-built 90° samples. As aforementioned, the X-ray tomography scans performed before and after the treatment showed that with the voxel size of laboratory tomography (2.5 μm), no internal pore was detected after the HIP treatment. No impact on the fatigue properties was noticed: the HIP treated samples had the same fatigue lives as the as-built samples (pink *v.s.* blue dots in Figure 3.2). **This demonstrates that, as far as as-built samples are concerned, the internal pores (and their closure) have no impact on the fatigue life.** The systematic HIP treatment performed on machined samples (25% improvement of the fatigue limit σ_f, see amongst others [LI 16], [FAC 09]) does not seem necessary for as-built samples.

If notch-like defects are more likely to initiate a crack than internal pores, this does not always mean that such a crack will propagate and lead to the failure of the sample. Consequently, there is a need to consider the ability of such cracks to propagate, which will be the focus of the next section.

3.4.5   Defects and fatigue properties of as-built samples

The comparison of the fatigue lives of as-built samples submitted to medium stress levels ($\sigma_{max} = 290$ MPa) shows an impact of the build orientation (Figure 3.2). If the fatigue lives of 0°, 45° and 90° samples are referred to as $N_{0°}$, $N_{45°}$ and $N_{90°}$ respectively, then, they rank as follows: $N_{90°} < N_{45°} < N_{0°}$. In contrast, no significant difference in fatigue properties can be found between 90° and 0° *machined* samples (Figure 3.2). The relationship between the fatigue properties and the build orientation is likely to be due to the influence of the build orientation on the *surface defects* themselves.

In what follows, we will use a Kitagawa approach to investigate the impact of the surface defects on the fatigue results obtained so far. First, the original version of the *Kitagawa-Takahashi* diagram will be presented. Then, it will be modified to account for the limited number of cycles achieved in our samples. This theoretical framework is then used to discuss the influence of the build orientation on the fatigue resistance of as-built samples.

3.4.5.1   Classical *Kitagawa-Takahashi* diagram

Definition

The *Kitagawa-Takahashi* diagram [KIT 76] can be used to relate the fatigue limit of a sample to the size of the defects that it contains. It considers two thresholds of fatigue, the classical fatigue limit σ_f and the crack growth threshold ΔK_{th} and relies on them to establish the non-propagation condition for cracks. σ_f is determined from the S-N curves

of defect-free samples and is used as the non-propagation condition for small cracks. ΔK_{th} is measured from fatigue crack growth tests performed on notched and pre-cracked samples and represent the stress intensity range below which cracks do not propagate. It is used as the non-propagation condition for long cracks. The curve $\Delta \sigma_{lim}$ representing the non-propagation condition for cracks can therefore be determined as follows:

$$\Delta \sigma_{lim} = \min \left(\Delta \sigma_f, \frac{\Delta K_{th}}{Y * \sqrt{\pi a}} \right) \tag{3.2}$$

where Y depends on the crack location (typically $Y = 0.65$ for a surface crack), $\Delta \sigma_f$ is the stress range at the fatigue limit σ_f and a is the crack length.

With the use of both criteria, two straight lines can be drawn in Figure 3.9 in respectively the short and long cracks regimes. In order to determine a smooth transition between the two regimes, El Haddad et al. [HAD 79] have conducted experimental studies and defined a crack length a_0 below which the fatigue threshold no longer depends on the crack size:

$$a_0 = \frac{1}{\pi} \left(\frac{\Delta K_{th}}{Y * \Delta \sigma_f} \right)^2 \tag{3.3}$$

A single empirical equation is thus sufficient to plot $\Delta \sigma_{lim}$ as a function of crack length, a:

$$\Delta \sigma_{lim\,El\,Haddad} = \frac{\Delta K_{th}}{Y * \sqrt{\pi (a + a_0)}} \tag{3.4}$$

An example of a *Kitagawa-Takahashi* diagram is presented in Figure 3.9. For a given crack length a, if the fatigue stress range $\Delta \sigma \leq \Delta \sigma_{lim\,El\,Haddad}$ (green area), crack growth is not possible and it is assumed that the sample will remain unbroken. Otherwise, fatigue failure is expected (more details can be found in [KRU 06]).

Such diagrams have been used by Wysick et al. [WYC 14] to consider the impact of defects on the fatigue properties of Ti-6Al-4V SLM manufactured samples. Beretta and Romano [BER 17] have shown in a recent review that the *Kitagawa-Takahashi* diagram can reasonably well describe the fatigue properties of Ti and Al alloys fabricated by AM. The defects are considered as cracks and the stress intensity factor range ΔK that they generate is compared to the crack growth threshold ΔK_{th} of the material in order to assess their ability to propagate. This method can be applied in our case since the cracks leading to failure initiate from notch-like surface defects with a crack-like shape. Several approaches can be considered for building the *Kitagawa-Takahashi* diagram (see for example [ROT 17]). The formulation based on the El Haddad's empirical parameter a_0 [HAD 79] presented above will be used in the following sections.

Kitagawa diagram for as-built samples

To construct a *Kitagawa-Takahashi* diagram, the fatigue limit σ_f of defect-free samples is needed. The fatigue failure of as-built samples being always caused by surface defects,
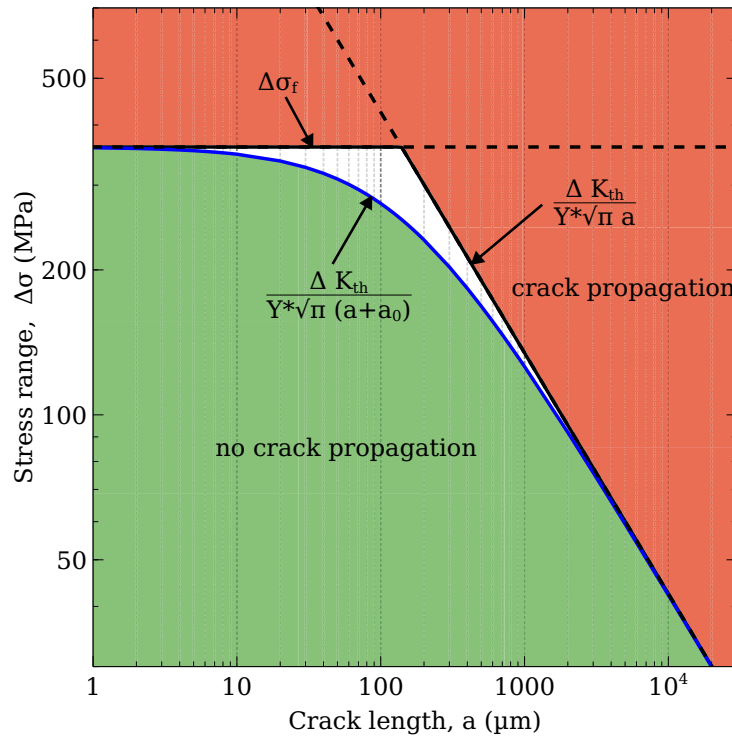
Figure 3.9: Example of a *Kitagawa-Takahashi* diagram for EBM Ti-6Al-4V alloy. The black dotted and continuous lines represent respectively the two threshold of fatigue determined from σ_f and ΔK_{th} and the resulting non-propagation condition $\Delta\sigma_{lim}$. The smooth transition between the short and long cracks regimes computed from El Haddad empirical equation is shown by the continuous blue line. It is assumed that a crack located in the green area will not grow. Otherwise, fatigue failure is expected.

samples without surface defects, i.e. machined samples will be considered as defect-free samples. The fatigue limit σ_f reported by ARCAM [ARC 13] is therefore used.

Published results of standard fatigue crack growth tests on Ti-6Al-4V samples additively manufactured by EBM are used for the ΔK_{th} values. Several studies ([SEI 15], [ZHA 16a], [GRE 16], [SEI 17], [GRE 17]) have been compared and the minimum, average and maximum values obtained from them have been reported in Table 3.3. For EBM machined samples, the ΔK_{th} values provided by these studies were found to depend on the orientation of the notch and thus of the crack propagation with respect to the building direction. Different values are reported for cracks propagating on an horizontal plane (perpendicular to the building direction) and for cracks propagating on a vertical plane parallel to the building direction. Figure 3.10 illustrates the two orientations of crack growth.

This orientation dependency has also been reported for SLM samples (see e.g. [LEU 13]), however, in both cases, it has not been clearly linked to the samples microstructure. Some authors have related it to the anisotropy of microstructural features such as basket-weave and Widmanstätten microstructures and report that they would impact the nucleation and the propagation of short cracks [BER 17], [COL 16]. Nevertheless, the Widmanstätten mi-
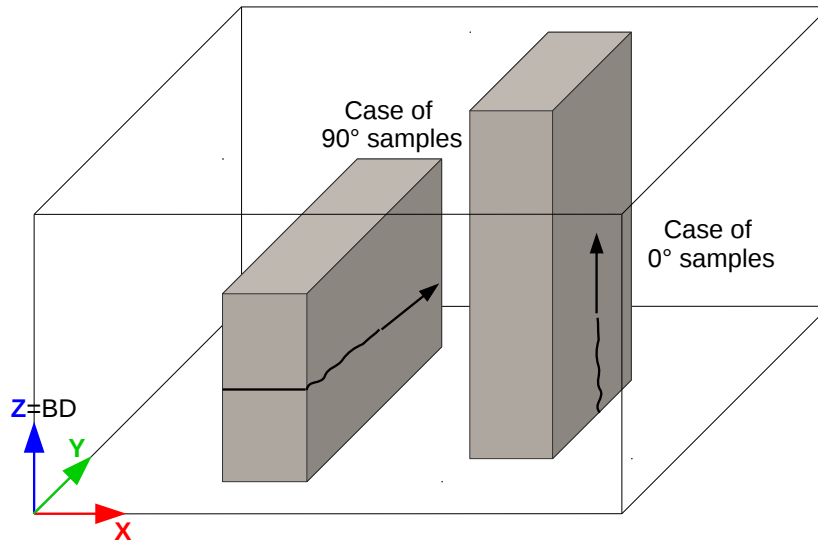
Figure 3.10: Schematic illustration of the orientations of crack growth with respect to the building direction. The cracks are represented by the dark lines and their growth orientation is shown by black arrows. The building direction is indicated by the blue arrow.

crostructure is rather isotropic in Ti-6Al-4V EBM samples. Therefore, the reason for this orientation dependency must be found elsewhere. It may be linked to the anisotropy of the prior columnar β grains but no studies have confirmed this hypothesis.

Based on those values, two non-propagation curves, one for each orientation of crack propagation, can be determined thanks to El-Haddad equation [HAD 79]. The resulting *Kitagawa-Takahashi* diagram is shown in Figure 3.11.

Table 3.3: Literature data for ΔK_{th} and corresponding values of the a_0 parameter of equation 3.3 [SEI 15], [ZHA 16a], [GRE 16], [SEI 17], [GRE 17].

	crack growth perpendicular to the building direction			crack growth parallel to the building direction		
	$\Delta K_{th,min}$	$\Delta K_{th,av}$	$\Delta K_{th,max}$	$\Delta K_{th,min}$	$\Delta K_{th,av}$	$\Delta K_{th,max}$
ΔK_{th} (MPa$\sqrt{m}$)	3.4	3.6	3.8	4.2	4.9	5.7
a_0 (μm)	53	60	66	81	110	149

The fatigue results obtained for some as-built samples have then been reported on the *Kitagawa-Takahashi* diagram (Figure 3.11). The experimental stress range $\Delta\sigma$ was directly used. The defect size a was determined using the approach developed by Murakami [MUR 85] which considers the projected area of the defect perpendicular to the loading axis so that: $a = \sqrt{area}$. The SEM images of the fracture surfaces (Figure 3.3) were used to obtain the projected areas of the defects which lead to failure. The resulting points are represented in blue, green and red symbols for respectively the 90°, 45° and 0° samples. As shown in Figure 3.4, the crack responsible for the sample failure always propagates on a horizontal plane. This plane is parallel, tilted at 45° and perpendicular to the building direction respectively for 0°, 45° and 90° samples. Therefore, the 0° samples must be

compared with the red curves (crack growth parallel to the building direction) and the 90° samples to the blue ones (crack growth perpendicular to the building direction). 45° samples are rather similar to 90° samples (notch-like defects perpendicular to the building direction leading to failure, ...) and no data was reported for this direction of crack growth. It was therefore chosen to compare them with the same curves than 90° samples, the blue ones.
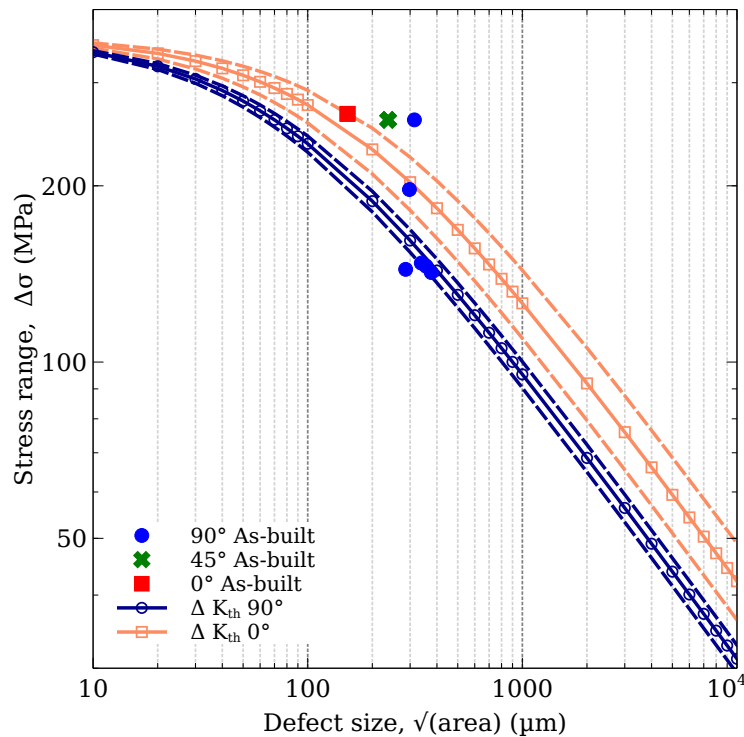
Figure 3.11: Classical *Kitagawa-Takahashi* diagram of as-built EBM Ti-6Al-4V alloy. The blue and red lines correspond respectively to notches perpendicular and parallel to the building direction. The continuous lines were plotted using the average ΔK_{th} value from the literature while minimum and maximum values were considered for the dashed lines. The blue dots, green crosses and red squares correspond respectively to the 90°, 45° and 0° samples. They were plotted using directly the experimental stress range $\Delta\sigma$ and the size $\sqrt{area}$ of the defect responsible for the failure measured on the SEM-SE micrograph of the fracture surface.

Limits of the classical *Kitagawa-Takahashi* diagram

Figure 3.11 shows that **the fatigue failure of as-built EBM Ti-6Al-4V samples is rather well predicted by the classical *Kitagawa-Takahashi* diagram.** Indeed, for almost all samples reported on the diagram, the defect responsible for the failure stands on or over the corresponding non-propagation curve. There is only one defect which is located just below this curve and whose criticality is slightly underestimated.

Nevertheless, to be consistent with the framework of classical *Kitagawa-Takahashi* diagrams, the experimental points taken from fatigue data must correspond to samples tested at low stresses having fatigue lives long enough to be close to the fatigue limit. This value

is generally defined for a given number of cycles to failure (e.g. 10^7). As it is difficult to test samples for a given number of cycles, in the literature, samples which have survived at least until the knee point of the Wöhler curve are considered in the *Kitagawa-Takahashi* diagram. This is because in the flat region of the curve, the error on the load which has to be applied to reach a certain life is reduced. Besides, at the knee point, the crack growth rate is small enough to comply with the crack propagation close to the threshold. For a more detailed discussion on this, see [CIA 06].

Figure 3.2 shows that, for 90° as-built samples, the knee region of the Wöhler curve corresponds to a number of cycles of the order of ~ 4 to 5.10^5 cycles and a stress range of $\Delta\sigma \sim 145$ MPa. Therefore, broken samples with a fatigue life larger than this number of cycles can be placed directly on the *Kitagawa-Takahashi* diagram. For the three build orientations, some points on the Wöhler curve correspond, however, to specimens with fatigue lives of the order of or smaller than 10^5 cycles. Those points cannot therefore be directly inserted on the Kitagawa-Takahashi diagram. Two different approaches have been tested to overcome this issue.

3.4.5.2 Finite lives *Kitagawa-Takahashi* diagram: Beretta approach

The first approach suggested by Beretta and Romano [BER 17] consists in modifying the stress range $\Delta\sigma$ used to plot the experimental dots on the *Kitagawa-Takahashi* diagram. Instead of using the experimental stress ranges leading to fatigue lives of about 10^5 cycles, extrapolated stress ranges leading to longer fatigue lives (in the knee region of the Wöhler curve) are used. This way, the experimental points are consistent with the framework of classical *Kitagawa-Takahashi* diagrams. This has been done for the three orientations and the results are shown on Figure 3.12.

For the 90° samples, a value of $\Delta\sigma = 145$ MPa where the knee point is observed was used for the points corresponding to fatigue lives shorter than 3.10^5 cycles. For the 0° and 45° samples, all fatigue tests were performed at a single stress level, which means that the stress level at which the knee region occurs is not known. The fatigue results of the 90° samples have therefore been used to extrapolate the fatigue behavior of the other two orientations. Two assumptions have been made:

- the slope of the Wöhler curve is the same for the three build orientation;
- the fatigue lives at which the knee region occur are similar for all three orientations: ~ 4 to 5.10^5 cycles.

Given that the samples microstructure and defects are quite similar, these two hypotheses seem reasonable but additional fatigue tests would be needed to further validate this approach. The Basquin law was used to represent the Wöhler curve of 90° samples [BAS 10]:

$$N * \Delta\sigma^k = B \tag{3.5}$$

where k and B are constant parameters. They are determined from the experimental data through a linear regression in a log-log S-N diagram.

This Basquin law was then extrapolated to the other orientations. The resulting curves are shown in Figure 3.2. Stress ranges corresponding to their *assumed* knee region were
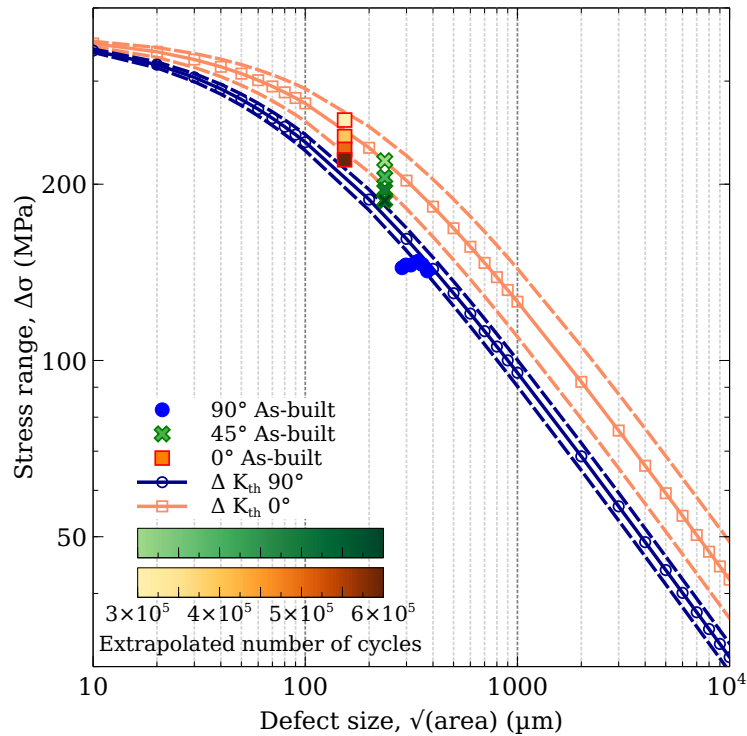
Figure 3.12: Modified *Kitagawa-Takahashi* diagram of as-built EBM Ti-6Al-4V alloy following the method suggested by Beretta and Romano [BER 17]. The blue and red lines correspond respectively to notches perpendicular and parallel to the building direction. The continuous lines were plotted using the average ΔK_{th} value from the literature while minimum and maximum values were considered for the dashed lines. The blue dots, green crosses and red squares correspond respectively to the 90°, 45° and 0° samples for which the size of the defect responsible for the failure was measured on SEM-SE micrographs of the fracture surfaces. Their stress range was extrapolated to larger fatigue lives corresponding to the knee-point of the Wöhler curve.

thus obtained. The modified *Kitagawa-Takahashi* diagram obtained with this first approach is shown in Figure 3.12. The scatter of the data obtained at the knee-point of the Wöhler curve of the 90° samples is taken into account by varying the number of cycles used for extrapolation for 0° and 45° samples from 3 to 6.10^5 cycles. The resulting stress ranges varies as follows: $\Delta\sigma = 220\text{-}257$ MPa and $\Delta\sigma = 188\text{-}219$ MPa for 0° and 45° samples respectively.

Figure 3.12 shows that **once the extrapolation is being carried out on the Wöhler curve, the experimental points fall reasonably well on the Kitagawa-Takahashi curves for the 3 investigated orientations.** As a reminder, the red squares (critical defects in 0° samples) are to be compared with the red curves (crack growth parallel to the building direction) and the green crosses and blue dots (critical defects in 45° and 90° samples respectively) with the blue curves (crack growth perpendicular to the building direction). For 0° samples, when the extrapolated number of cycles used exceeds 4.10^5 cycles, the predictions cease to be conservative (the square stands below the average non-propagation curve). For 45° samples, the predictions are always conservative and

get better when the number of cycles used for extrapolation increases (they are getting closer to the non-propagation curves). This slight discrepancy between the results from the two build orientations (the best fit being obtained for different extrapolated number of cycles) suggests that the hypotheses made to position these points on the diagram may not be completely valid. This emphasizes the need of additional fatigue tests for 0° and 45° samples. For 90° samples, no assumptions were necessary and the experimental points fit well with the modified *Kitagawa-Takahashi* diagram.

3.4.5.3 Finite lives *Kitagawa-Takahashi* diagram: Ciavarella approach

The second approach is based on the work of Ciavarella and Monno. They have proposed a method to extend the *Kitagawa-Takahashi* diagram to a given number of cycles N_{fl}. The procedure can be briefly summarized as follows (for details, see [CIA 06]): when the fatigue resistance at a given N_{fl} is sought, both the left (horizontal) and the right (decreasing) part of the $\Delta\sigma_{lim}$ curve should be modified (Figure 3.9).

For the left part, the fatigue limit is defined as the stress amplitude corresponding to N_{fl} on the Wöhler curve of the machined samples (Figure 3.2). For the right part of the diagram, a propagation law is assumed. For example, a Paris power law can be considered:

$$\frac{da}{dN} = C * \Delta K^m \tag{3.6}$$

where C and m are constant parameters.

This propagation law is integrated for N_{fl} up to the final size of the crack, a_f, which is defined from the fracture toughness of the material, K_{1c}:

$$a_f(N_{fl}) = \frac{1}{\pi}\left[\frac{K_{1c}(1-R)}{\left(\frac{B}{N_{fl}}\right)^{1/k}}\right]^2 \tag{3.7}$$

where k and B are constant parameters from the Basquin law (equation 3.5). As a reminder, R is the stress ratio (R $= \frac{\sigma_{min}}{\sigma_{max}}$).

Therefore, the decreasing part of the new $\Delta\sigma_{lim}$ curve can be determined from both crack propagation and fracture toughness data. In order to ensure a "smooth" transition between the horizontal and decreasing parts of the new $\Delta\sigma_{lim}$ curve, the concept of *intrinsic crack* from El Haddad can be applied. The following equation enables to plot $\Delta\sigma_{lim}$ as a function of the number of cycles N_{fl} and of the crack length a:

$$\Delta\sigma_{lim}(N_{fl}, a) = \frac{2}{2-m}\frac{1}{C\pi^{m/2}N_{fl}}\left[a_f(N_{fl})^{\frac{2-m}{2}} - (a + a_t(N_{fl}))^{\frac{2-m}{2}}\right] \tag{3.8}$$

where a_t, the intrinsic crack, is defined as follows:

$$a_t(N_{fl}) = \left[a_f(N_{fl})^{1-m/2} + C\pi^{m/2}\left(\frac{m-2}{2}\right)B^{m/k}N_{fl}^{k-m/k}\right]^{\frac{2}{2-m}} \tag{3.9}$$

For both orientations of the crack propagation, a propagation law in the Paris regime and a fracture toughness value are needed. Those used here were taken from the work of

Seifi et al. [SEI 17] and reported in Table 3.4. The results of this second approach are shown on Figure 3.13a (90° samples) and Figure 3.13b (0° and 45° samples).

Table 3.4: Literature data for crack propagation (m and C parameters of the Paris law) and fracture toughness K_{1c} [BRA 12], [ZHA 16a], [SEI 17], [GRE 17].

Sources	crack growth perpendicular to the building direction			crack growth parallel to the building direction		
	C	m	K_{1c} (MPa$\sqrt{m}$)	C	m	K_{1c} (MPa$\sqrt{m}$)
[BRA 12]	2.34×10^{-8}	3.01	N/A	N/A	N/A	N/A
[ZHA 16a]	5.16×10^{-8}	2.80	N/A	1.19×10^{-8}	3.30	N/A
[SEI 17]	1.41×10^{-8}	2.66	91	4.92×10^{-9}	2.94	96
[GRE 17]	1.35×10^{-7}	2.44	106.5	N/A	N/A	N/A
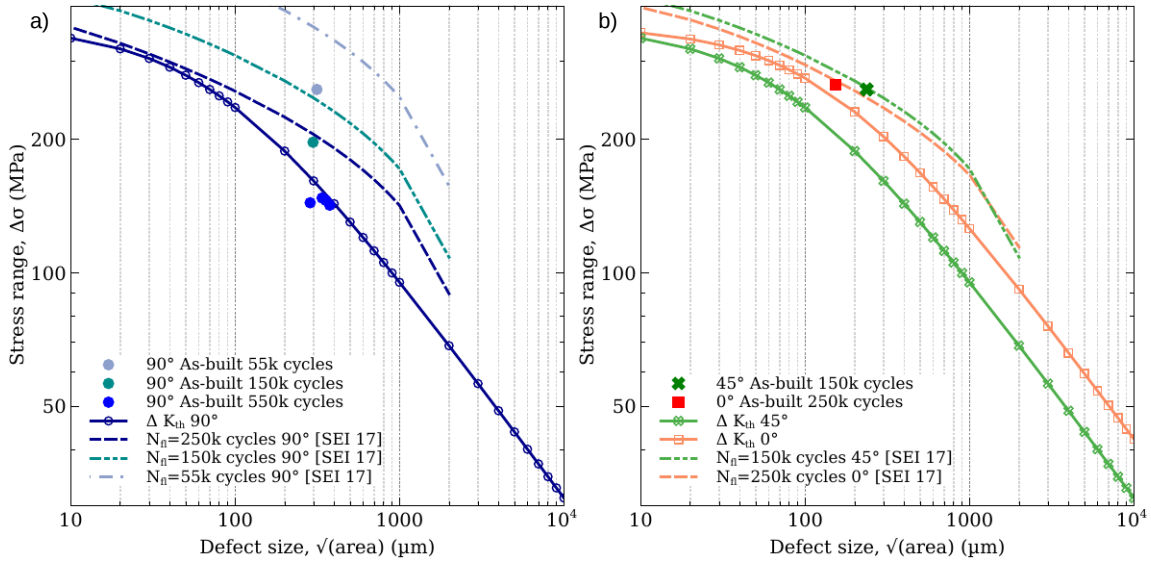
Figure 3.13: Modified *Kitagawa-Takahashi* diagrams of as-built EBM Ti-6Al-4V alloy extended to finite lives following the approach of Ciavarella and Monno [CIA 06]. The continuous dotted lines were plotted using the average ΔK_{th} value from the literature. Each dashed curve corresponds to a given number of cycles N_{fl} and relies on the stress amplitude corresponding to N_{fl} as well as a propagation law and a fracture toughness value K_{1c}. The experimental stress range was directly used for the blue dots, green crosses and red squares. (a) Diagram for 90° samples. (b) Diagram for 0° and 45° samples.

The results from this second approach are contrasted. **Good predictions are obtained for 0° and 45° samples** (with *very limited* data available, see Figure 3.13b). However, **for 90° samples, the fatigue resistance is clearly overestimated** for fatigue lives shorter than the knee point of the Wöhler curve (Figure 3.13a). For example, samples that lived 55 000 and 150 000 cycles respectively are supposed to reach respectively 150 000 and 250 000 cycles according to the diagram.

One reason might be that the cracks initiating from the notch-like defects might have a typical short crack behavior. This would lead to a faster growth rate than the one

predicted by the classical Paris law established for long cracks (as suggested by [CIA 06]). Note that this is also true for 0° and 45° samples.

Another reason for these contrasted results can stem from the literature data used and reported in Table 3.4. Data from the work of Seifi et al. [SEI 17] have been used but other data can be found ([BRA 12], [ZHA 16a], [GRE 17]). A large scatter of the results can be observed between these different studies and it was decided to rely on the data from Seifi et al. [SEI 17] as it is the only study which provides all the data required for this approach.

To summarize, as already shown by Beretta and Romano [BER 17] for machined samples, the *Kitagawa-Takahashi* approach seems to predict reasonably well the fatigue resistance of our as-built samples at finite or infinite lives. Nevertheless, improving the quality of the predictions would require supplementary data (full Wöhler curves for 0° and 45° samples, short crack growth rates, ...) which is out of the scope of this study.

3.4.5.4 Impact of the build orientation

The Kitagawa approach has shown that the critical parameters for assessing the fatigue strength are the crack growth threshold ΔK_{th} and the stress intensity factor range ΔK which has been calculated using the $\sqrt{area}$ parameter (equation 3.2).

As shown in Table 3.3, the ΔK_{th} values found in the literature for a crack growth parallel to the building direction (case of 0° samples) are higher than the ones found for cracks growing perpendicular to it (case of 45° and 90° samples). This means that the microstructure is more resistant to crack growth in 0° samples. Furthermore, Figure 3.11 shows that the build orientation has an effect on the surface defects size: $\sqrt{area}_{90°} > \sqrt{area}_{45°} > \sqrt{area}_{0°}$. Thus, 0° samples contain smaller critical surface defects. Both factors can account for the longer fatigue lives measured for these samples.

In addition, even in the case of similar $\sqrt{area}$ values, some authors have shown that there is an influence of the defect orientation on the fatigue strength. Lorenzino et al. [LOR 15] have studied the fatigue limit of high strength steels using the $\sqrt{area}$ parameter. They showed that when the angle between the loading axis and the defect major axis is decreased, fatigue lives increase for a given stress level. This is consistent with our observations: as shown in Figure 3.14[2], the notch-like defects of 90° and 45° samples are respectively perpendicular and tilted at 45° with respect to the loading axis and experimentally we observe that $N_{90°} < N_{45°}$. **Both effects (defects size and orientation) can therefore account for the observed dependency of the fatigue strength on the build orientation.**

Another factor that can impact the fatigue properties is the number of defects which can initiate a crack. The differences between the density of surface defects within the gauge length of the three types of samples has been reported in Chapter 1 . Hardly any notch-like defects can be identified in the 0° samples whereas many can be observed in the 90° samples, 45° samples being somewhere in between those two cases (Figure 3.14). Even though the fatigue strength should be linked to the largest defects within the defects distribution [ROM 17], **a larger number of defects increases the probability of**

---

[2]For a better reading, this Figure from Chapter 1 has been pasted here.
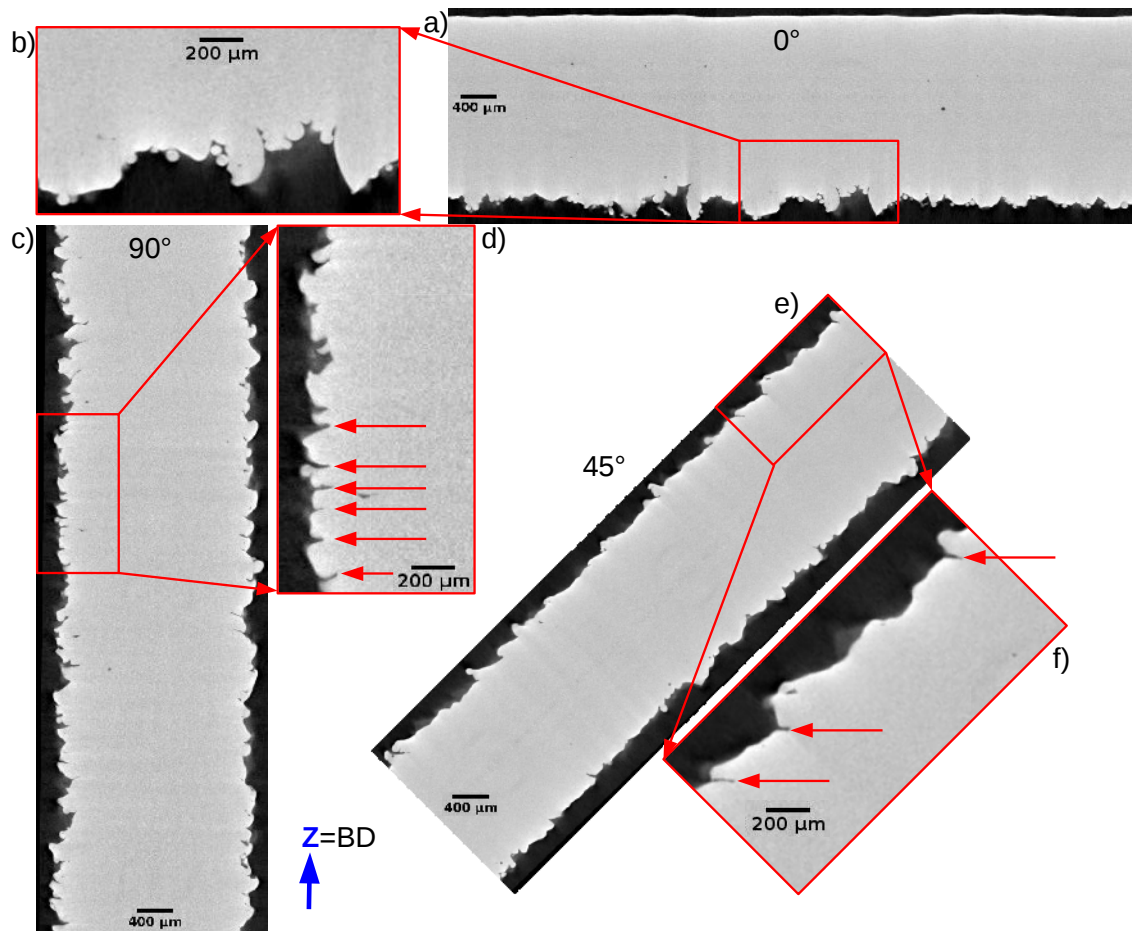
Figure 3.14: Impact of the build orientation on the surface of the samples gauge length. (a,c,e) Radial slices of samples manufactured respectively at 0°, 45° and 90°. (b,d,f) Magnification around surface defects. The slices are oriented in order to mimic the sample orientation in the build chamber, the building direction being vertical (blue arrow).

having one that is critical and could also explain the influence of the build orientation on fatigue lives. A thorough study of the defects distributions for each build orientation would be required in order to confirm this tendency. This point will be adressed in Chapter 4.

3.4.6   Notch-like defects detection and fatigue life prediction: is roughness the appropriate index ?

From an industrial point of view, it might be interesting - or even critical - to be able to detect the presence of the notch-like surface defects responsible for crack initiation by non-destructive tests (NDT) and also to be able to link the fatigue properties to standard and easy to determine parameters such as surface roughness.

On the one hand, the notches leading to failure are clearly visible on the X-ray tomographic images (see for example Figure 3.5) when a small voxel size is used (2.5 μm in this

case). However, with this voxel size, only parts with a size of the order of 1 cm (for Ti alloys) could be imaged by X-ray tomography because of the need to use a small specimen-to-source distance; X-ray attenuation would also limit the size of the samples to ~ 1 cm. This size is likely to be too small for practical application of lattices in macroscopic parts and therefore 3D control of the lattices will not be possible.

On the other hand, the roughness measurements performed on 90° show that the average value of R_a based on tomography scans where crack-like notches are detected is sligthly larger than the average value of R_a obtained by profilometry (44 μm v.s. 36.9 μm). The reason for this discrepancy is than such thin and deep defects are systematically overlooked by classical profilometry. This technique is therefore not suited for the detection of notches and, as a result, only X-ray tomography based roughness measurements should be used for an accurate measurement of the surface defects size and roughness.

Vertically (respectively horizontally) manufactured samples with their large (respectively limited) population of stacking defects (Figure 3.14) exhibit the highest (respectively the lowest) R_a value, see Table 3.5[3]. A correlation seems to appear between the R_a values and the fatigue life, larger R_a values giving shorter fatigue lives (Table 3.5 and Figure 3.2). Nevertheless, fatigue failure is always triggered by notch-like defects (Figure 3.5) which induce very localized variations of the surface height. Their impact on the R_a measurements is thus limited. **This means that, in spite of the apparent correlation reported above, R_a *cannot* be considered as the relevant parameter for predicting the fatigue life in the case of as-built EBM samples.**

Table 3.5: Effect of the build orientation on the as-built EBM samples roughnesses: R_a, R_t and R_v. The average values and the standard deviations are reported. For R_a, the values for the upper and lower surfaces of the samples are also reported.

Material characterization	R_a (μm)			R_t (μm)	R_v (μm)
	Average	Upper surface	Lower surface		
0° samples	30.7 ± 1.5	11.0 ± 2.1	56.9 ± 7.7	494 ± 29	227 ± 39
45° samples	36.4 ± 1.5	32.4 ± 2.9	42.3 ± 6.3	356 ± 34	174 ± 11
90° samples	43.4 ± 2.1	N/A	N/A	379 ± 36	230 ± 27

The R_t and R_v parameters which describe the *local* roughness variations could potentially be more relevant parameters. However, their rankings differ from the fatigue resistance ranking: 0° samples have the longest fatigue lives but also the highest R_t values and 0° and 90° samples show similar R_v values, see Table 3.5. Two facts can explain these observations. First, the method used for the roughnesses calculation (see Chapter 1) extracts surface profiles every 10° along the circumference of the gauge length. Very local surface irregularities such as notch-like defects are thus more likely to be overlooked. Second, the R_t (repectively R_v) value considers the distance between the highest (respectively the mean line along the surface profile) and the lowest point of the surface. None of them describes the shape of the defects responsible for crack initiation. A large R_t or R_v value can thus be caused by a deep stacking defect (45° and 90° samples) with a large radius of curvature which would be the lowest point of the surface. They can also be caused by

---

[3]To facilitate reading, this Table from Chapter 1 has been pasted here.

some large protrusions caused by the thermal process. These protrusions would affect the median line position and thus the R_v value and one of them could represent the highest surface point which would increase the R_t value. This justifies why no straightforward correlation can be made between the R_t or R_v values and the fatigue lives of as-built samples.

3.4.7 Conclusion on as-built samples

For additively manufactured lattice structures, conventional machining cannot be used to improve the surface state. Furthermore, the struts constituting the lattice are built in many different orientations. Determining the impact of the as-built state as well as of the build orientation on the fatigue properties is mandatory and was the aim of the work presented in this section. The main conclusions can be drawn as follows:

- The detrimental effect of the as-built surface state on the fatigue resistance of individual struts have been clearly shown. Designing fatigue-resistant lattice structures using data obtained on machined samples is unsafe and can lead to erroneous conclusions.

- Classical *Kitagawa-Takahashi* diagrams as well as modified approaches to consider limited fatigue lives can predict rather well the impact of surface defects on the fatigue resistance of individual struts.

- The build orientation impacts the fatigue properties of as-built samples because of its influence on the shape, size and number of notch-like defects from which fatal cracks initiate.

- Horizontal and vertical samples are respectively the best and worst samples in terms of fatigue lives.

- Considering the fabrication of lattice structures, it might be interesting to adopt a build orientation which would limit the number of vertically built struts and increase the number of horizontally built struts.

- Using roughness measurements of as-built AM samples to infer information regarding the fatigue properties is unsafe since these measurements do not reveal the thin and deep notch-like defects which are responsible for fatigue crack initiation.

3.5 Post-treated samples

It has been shown in the previous section that the as-built surface of EBM samples leads to a significant reduction of the fatigue resistance of thin parts. The post-treatments described in Chapter 1 have been applied to single struts. The effect of those various post-treatments on the fatigue properties is investigated in what follows.

3.5.1 HIP treatment

HIP has been applied to fatigue specimens and the results are shown in Figure 3.2. The effect of this post-treatment on the fatigue properties of *as-built* samples has already been discussed in section 3.4.4. It has been demonstrated that, despite the internal pores closure and a slight microstructural coarsening, no influence on the fatigue properties was observed. As a result, this point will not be discussed any further.

3.5.2 Chemical etching

The low fatigue properties of as-built samples have been attributed to the presence of surface notch-like and "plate-pile" like stacking defects which were found to be systematically responsible for the crack growth leading to failure. Based on the results presented in Chapter 1, it was therefore decided to apply chemical etching to as-built samples in order to improve their fatigue properties. Chemical etching was applied only to 45° and 90° samples because a limited number of samples were built in the 0° orientation.

3.5.2.1 Effect of chemical etching duration: case study on 90° samples

It has been shown in Chapter 1 that, at least for the conditions used in this study, the "plateau region" of the chemical etching process was reached after approximately 45 minutes as far as roughness is concerned. Two different chemical etching durations were applied to the fatigue specimens in order to observe the possible effect of chemical etching duration on the fatigue properties: 30 minutes (intermediate state) and 45 minutes ("plateau region"). This study was performed on 90° samples as they are the worst case scenario from the point of view of surface defects and fatigue resistance. The results are presented in Figure 3.15.

A clear improvement of the fatigue properties can be observed after chemical etching. Both the fatigue limit at 10^7 cycles and the fatigue stress at 10^5 cycles are enhanced by ~ 75 MPa which correspond to respectively 57% and 32% improvements. Samples etched for 30 and 45 minutes exhibit similar fatigue performances. In comparison with the case of as-built samples, a large scatter of the fatigue lives is observed at low stress ($\sigma_{max} = 220$ MPa) for fatigue specimens etched for 30 minutes. Two of those samples failed around 350 000 cycles while others were run out after 3.10^6 or 4.10^6 cycles. This scatter was not observed for samples chemically etched for 45 minutes: both samples ran out (only two samples were tested).

The notch-like defects have been identified as the critical defects leading to the failure of as-built samples. In addition, it has been shown in Chapter 1 that chemical etching largely
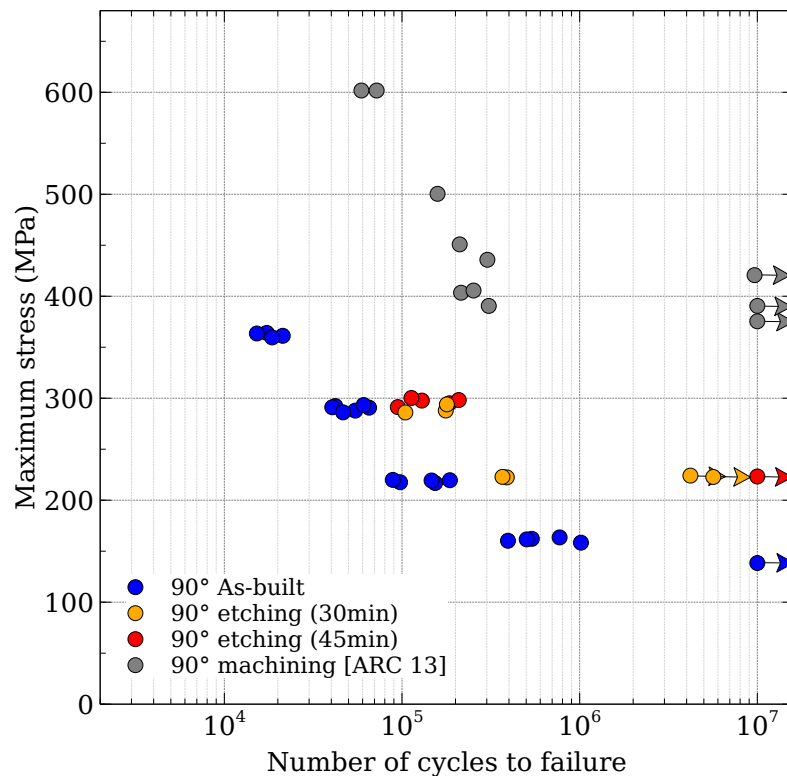
Figure 3.15: S-N curves for EBM 90° fatigue samples in the as-built conditions (blue dots) and after 30 minutes (orange dots) and 45 minutes (red dots) of chemical etching. Grey symbols correspond to data from ARCAM [ARC 13] on 90° machined samples manufactured by EBM.

reduces their criticality: it decreases their depth and increase the radius of curvature at the tip of these defects. Depending on how much the criticality of the notch-like defects is reduced, two scenarii can be assumed regarding the critical defects leading to failure:

- their criticality has been reduced in such a way that they are no longer the most critical defects. In this case, the fatigue failure could be caused by other type of defects: e.g. internal defects whose criticality has been increased since chemical etching brought them closer or even connected them to the surface.

- their criticality has not been reduced sufficiently and they remain the most dangerous defects.

Nevertheless, the analysis of fracture surfaces from chemically etched samples indicates that, for all etched samples, the crack leading to failure still initiates and propagates from surface defects as shown for example in Figure 3.16. This proves that chemical etching was not sufficiently efficient for the first assumption to be validated. Longer etching duration may change this conclusion (it has been shown in Chapter 1 that the notch-like defects of 90° samples can still be improved after 1 h of treatment).

If the critical defect identification method described in section 3.4.2 is now applied to chemically etched samples, it appears that the surface defects leading to failure are still notch-like defects. An example is shown in Figure 3.17.
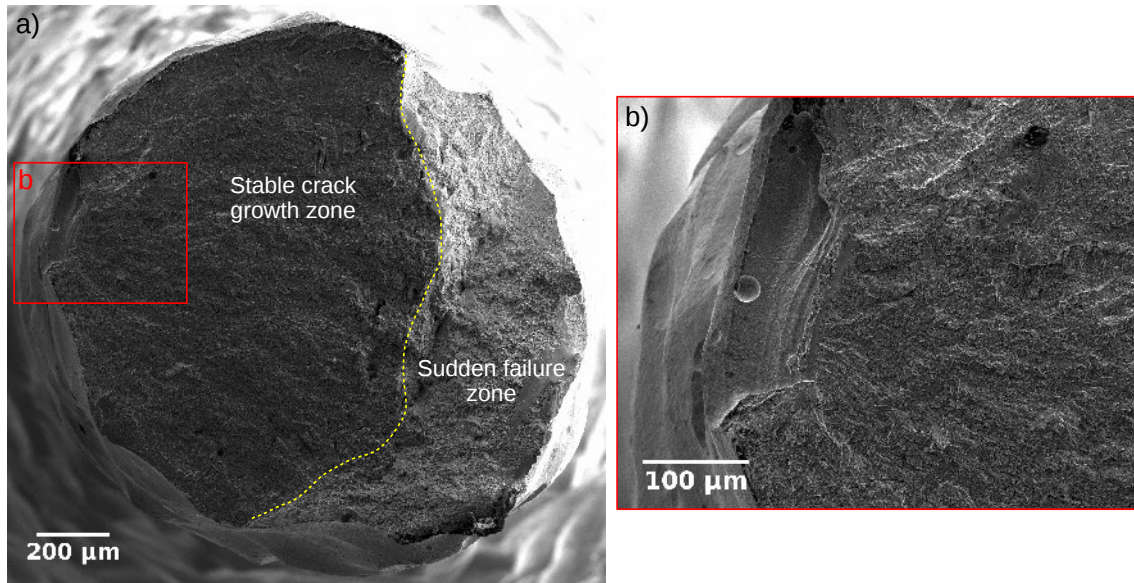
Figure 3.16: SEM-SE micrographs of the fracture surface of a chemically etched 90° EBM fatigue sample. (a) Fracture surface showing the stable crack growth and sudden failure zones. (b) Higher magnification image showing the crack inititiation site.
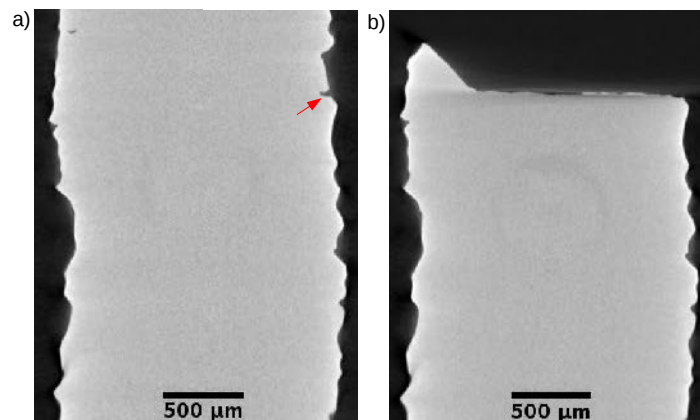
Figure 3.17: Radial slices obtained by X-ray tomography of a sample before (a) and after fatigue failure (b). The defect leading to failure is pointed out by a red arrow.

Tomographic images taken before and after chemical etching can be superimposed in order to observe the evolution of the critical defects. Two examples are shown in Figure 3.18. They confirm that **the remaining surface defects leading to failure were notch-like defects before chemical etching.** The radial slices clearly show that the defect depth has been largely reduced (Figure 3.18d and 3.18h). The depth decrease can be measured on the detailed views (Figure 3.18c and 3.18g); values ranging from 50 to 75% are obtained in that case. The same kind of observation can be made for the $\sqrt{area}$ parameter and thus for the defect size a (a rough approximation of the $\sqrt{area}$ value can be evaluated from the radial slices in Figure 3.18a and 3.18e). The large reduction of

the critical defects size can explain the significant improvement of the fatigue properties reported in Figure 3.15.

Figure 3.18: Effect of chemical etching on two notch-like defects (a-d and e-h) leading to fatigue failure. Dark gray: sample slices in the as-built state. Light gray: sample slices after 45 minutes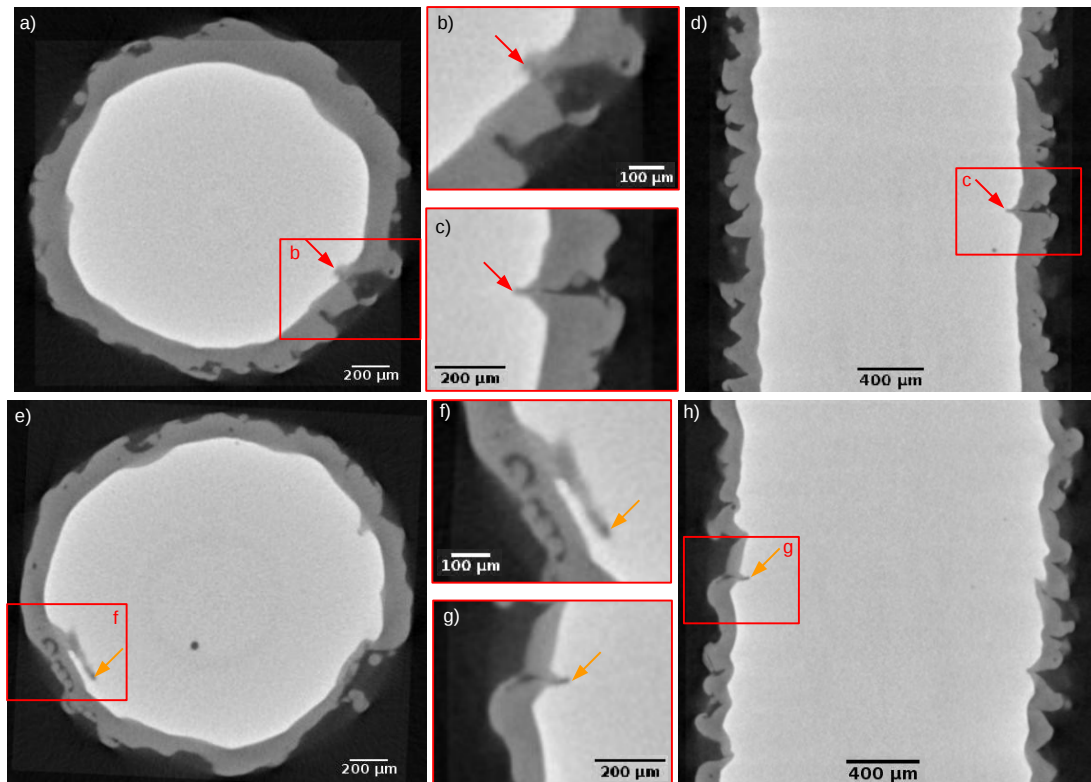 of chemical etching. (a,e) Overlaps of the axial slices showing two critical defects before and after 45 minutes of chemical etching. (d,h) Overlaps of the corresponding radial slices before and after 45 minutes of chemical etching. (b,c,f,g) Detailed views of the defects shown in respectively a, d, e and h. The red and orange arrows point out the root of respectively the first and second notch-like defects.

Figure 3.18 also highlights the etching process that has been described by Lhuissier et al. [LHU 16] and discussed in Chapter 1: after 45 minutes of chemical etching, the tips of the two notch-like defects presented in Figure 3.18 are not affected similarly by the etching process. The tip of the first defect (Figure 3.18a-d) starts to be affected by chemical dissolution: its radius of curvature slightly increases in the etched conditions (red arrow in Figure 3.18c) and its width also starts to increase (red arrow in Figure 3.18b). On the contrary, the tip of the second defect (Figure 3.18e-h) remains unchanged: the as-built and etched slices are perfectly superimposed on one another (red arrow in Figure 3.18f and g). This discrepancy is caused by the difference between the as-built shape of both defects: the tip of the first defect was more favorably exposed to the chemical reagent than the one of the second defect.

Those observations also allow to explain the large scatter in terms of fatigue lives observed at low stress levels. The premature failure of the broken samples is due to the

remaining part of a notch-like defect. This means that some as-built notches were not sufficiently etched and that they remained critical even after etching. The defects shown in Figure 3.18 are examples of such defects. On the contrary, for samples than ran out, it is likely that the 30 minutes of chemical etching were enough to reduce the defects criticality to such an extent that they were no longer able to provoke crack growth. A thorough analysis of all remaining defects in both the samples that failed and the ones that did not is needed to confirm - or infirm - this assumption. This issue is adressed in Chapter 4.

Finally, the main conclusion regarding the fatigue performance of chemically etched 90° samples is that, despite the large improvement of the fatigue lives that was observed, there is still room for more improvement. For example, the stress level corresponding to fatigues lives of about 2.10^5 cycles is $\sigma_{max} = 290$ MPa for chemically etched samples whereas it is around $\sigma_{max} = 425$ MPa for machined samples (Figure 3.15). In order to reduce this difference, an even better surface corresponding to the complete removal of the remaining notch-like defects is required. Longer etching duration are thus required. It has been shown in Chapter 1 that the tips of the deepest notch-like defects can still be observed at the surface of samples that have been etched for 60 minutes meaning that longer etching duration must be used. However, increasing too much the etching duration might be counter-productive: after a given time, the surface is no longer improved whereas the material is still being dissolved resulting in a useless loss of material and in an increase of the criticality of internal defects. Consequently, additional chemical etching tests would be required to determine the optimal etching duration which would be defined as the minimal duration for which these tips could be completely removed.

3.5.2.2 Impact of the build orientation: 90° *v.s.* 45° samples

It has been reported in Chapter 1 that 45 minutes of chemical etching leads to the complete removal of all notch-like defects of 45° samples because they are fewer in number and appear to be less critical. 45° samples etched for such a duration were therefore submitted to fatigue tests whose results (as well as the fatigue results of as-built 45° samples) are reported in Figure 3.19 and compared to the results obtained for 90° samples.

First, it is interesting to point out that the same fatigue results are obtained for as-built 45° samples and chemically etched 90° samples. It means that, for the latter, the chemical etching process enables to counterbalance the impact of the build orientation on the surface defects. Second, after chemical etching, the fatigue properties of 45° samples are further improved: the stress level corresponding to fatigue lives ranging between 1 and 2.10^5 cycles increases from $\sigma_{max} = 290$ MPa to $\sigma_{max} = 360$ MPa (24% improvement). Even though the fatigue properties of machined samples are not reached yet, the 45° samples are getting closer after chemical etching.

An analysis of the fracture surfaces shows that the failure is still caused by surface defects. These defects have been identified on the tomographic images. The radial and axial views of two critical defects are represented before and after chemical etching in Figure 3.20. Both are thin and relatively deep defects but their origin in the corresponding as-built samples differ. On the one hand, the first one (orange arrows in Figure 3.20a-d) is inherited from a notch-like defect (Figure 3.20d). In this case, the chemical dissolution has started to affect the tip of the defect but not sufficiently to smooth it (Figure 3.20c). This
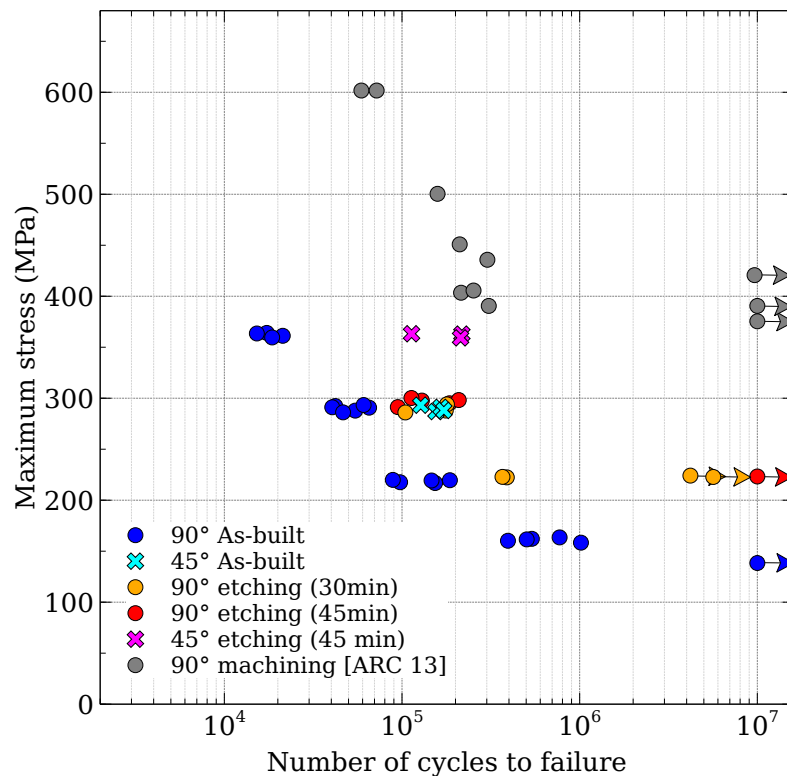
Figure 3.19: S-N curves for EBM 45° and 90° fatigue samples in the as-built conditions and after chemical etching. The dots and crosses correspond respectively to 90° and 45° samples. The blue colors (blue and cyan) depict the as-built conditions and the chemically etched one is represented by the orange (30 minutes), red and pink (both 45 minutes) symbols . Grey symbols correspond to data from ARCAM [ARC 13] measured on 90° machined samples.

is similar to the critical defects observed in several 90° samples, see for example Figure 3.18b and c. On the other hand, the second surface defect (red arrows in Figure 3.20e-h) does not originate from a notch-like defect but rather from an internal one: no link between the defect and the surface is detected on the tomographic images of the as-built conditions [4]. The tomographic images show that it is a lack-of-fusion defect that has been linked to the surface because of chemical etching (Figure 3.20f and g).

All the internal defects within the gauge length of the sample shown in Figure 3.20e-h can be projected on a single plane; the result is shown in Figure 3.21a and 3.21b respectively for the as-built and chemically etched conditions. It turns out that, in the as-built state, the defect responsible for the sample failure (circled in red) is *not* located within the sub-surface ring exhibiting a higher density of internal defects (red dashed circles). Figure 3.21b shows that this ring has been completely dissolved during the 45 minutes of chemical etching (the same observation was made for 90° samples in Chapter 1).

As the internal pores are randomly distributed in the remaining part of the sample, the probability of turning internal defects into surface ones would not change if the etching

---

[4]within the limit of detection of tomographic imaging

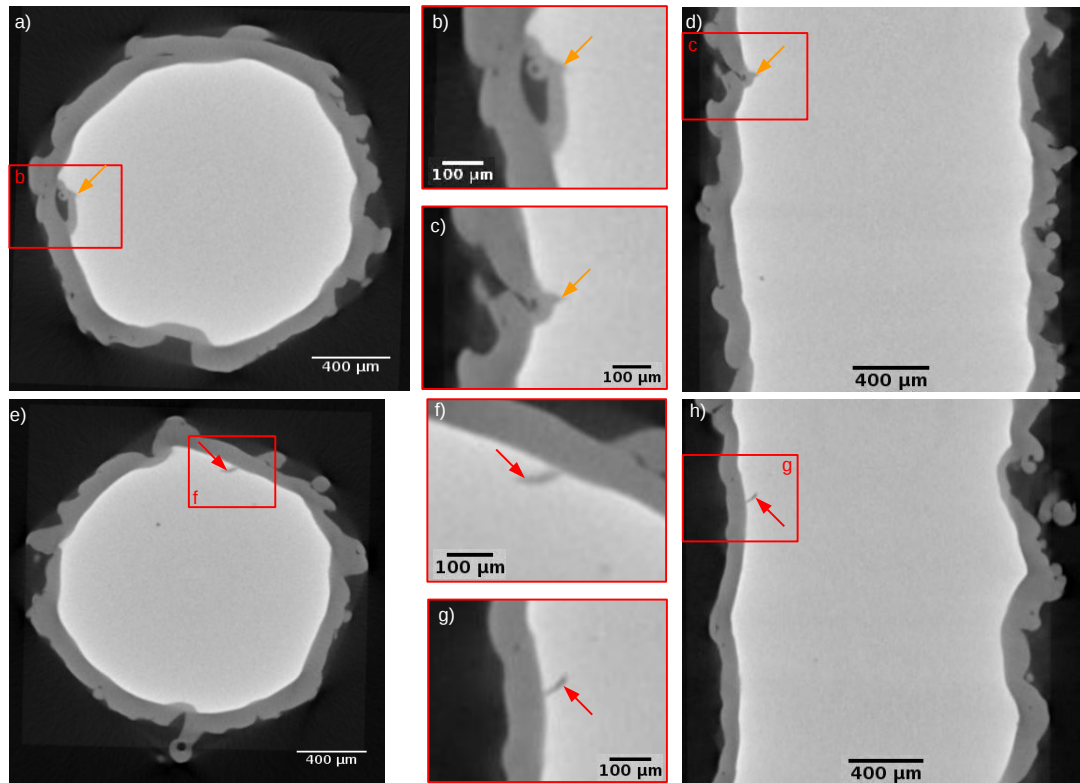*© 2018 – Théo PERSENOT – MATEIS laboratory*

Figure 3.20: Example of two defects leading to the fatigue failure of 45° samples chemically etched for 45 minutes: the remaining part of a notch-like defect (a-d) and an internal lack-of-fusion defect connected to the surface after chemical etching (e-h). Dark gray: sample slices in the as-built state. Light gray: sample slices after 45 minutes of chemical etching. (a,e) Overlaps of the axial slices showing two critical defects before and after 45 minutes of chemical etching. (d,h) Overlaps of the corresponding radial slices before and after 45 minutes of chemical etching. (b,c,f,g) Detailed views of the defects represented in respectively a, d, e and h. The orange and red arrows respectively point out the first and second defects.

duration was increased. In such a case, it seems that 45 minutes is approximatively the optimal duration of chemical etching.

Another interesting result is the link between the fatigue results and the critical defects origin. The two samples whose critical defects are shown in Figure 3.20 respectively failed after roughly 113 000 and 214 000 cycles. This means that the fatigue life of the sample whose failure was caused by an internal defect brought to the surface by chemical etching is roughly twice the fatigue life of the one that failed because of the remaining part of a notch-like defect. This is in agreement with the fact that the projected area of the critical defect leading to failure is much larger in the case of the smaller fatigue life (Figure 3.20a and e). This point is further discussed in Chapter 4.

For both build orientations, large improvements of the fatigue properties have been achieved. Such improvements may still be increased with a longer etching duration as, in many cases, the failure is caused by defects inherited from notch-like defects. This is even more true for 90° samples whose as-built surfaces contain a higher
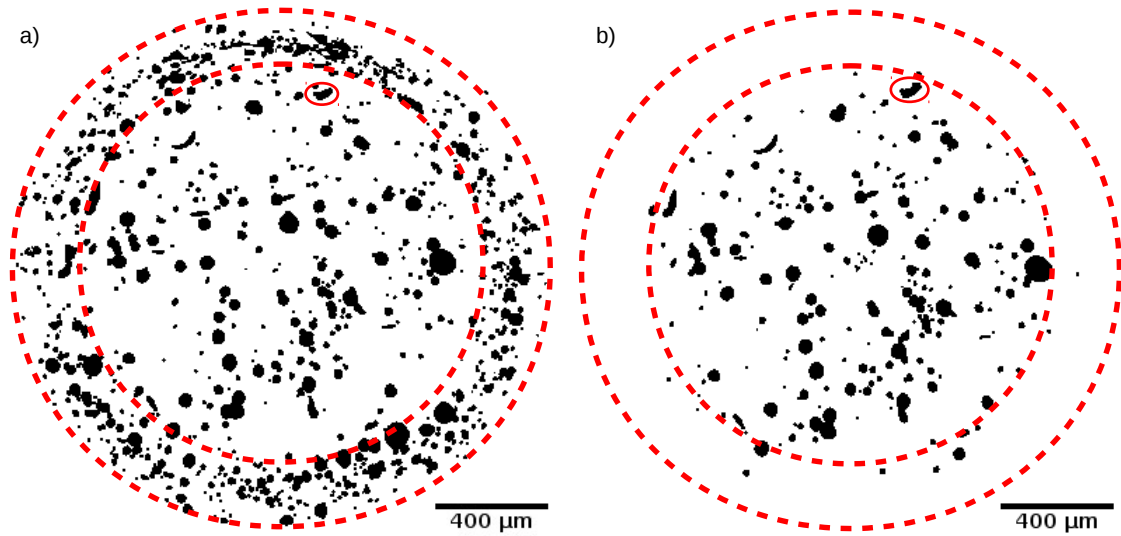
Figure 3.21: Projected view of all the internal defects detected by X-ray lab tomography (2.5 μm voxel size) within the gauge length of the 45° sample presented in Figure 3.20e-h in the as-built (a) and chemically etched (b) conditions. The defect responsible for the sample failure is circled in red and has been added to the projection after chemical etching. The sub-surface ring with a higher density of internal defects is highlighted by the two red dashed circles.

defect density. Fatigue results comparable to the ones of 45° samples can be expected with a longer etching duration. However, the problem of former internal defects that are turned into surface ones observed for 45° samples would remain. This issue can be tackled with the additional use of HIP prior to chemical etching which significantly improves the fatigue properties of machined samples thanks to the internal pores closure, see e.g. [ACK 09], [BRA 11].

3.5.3 HIP followed by chemical etching

3.5.3.1 Experimental results

HIP was applied prior to chemical etching on samples manufactured in the three different orientations and the results are shown in Figure 3.22. **The impact of the build orientation** observed and discussed on as-built samples (section 3.4.5) **remains after successively performing HIP and chemical etching.** The stress level corresponding to fatigue lives around 10^5 cycles is $\sigma_{max} = 500$, 450 and 360 MPa for 0°, 45° and 90° samples respectively. When compared to the experimental fatigue results obtained so far, these fatigue results are better than the ones obtained for as-built samples, HIP treated samples and chemically etched samples.

It also appears that the "HIP + chemical etching" combination does not provide the same fatigue improvement than "HIP + machining". However, after HIP and chemical etching, the 0° samples show fatigue results almost similar to the ones of machined samples (Figure 3.22). For instance, a sample cycled at $\sigma_{max} = 450$ MPa was stopped before failure after $\sim 2.10^6$ cycles which is comparable to the fatigue resistance of machined samples. For
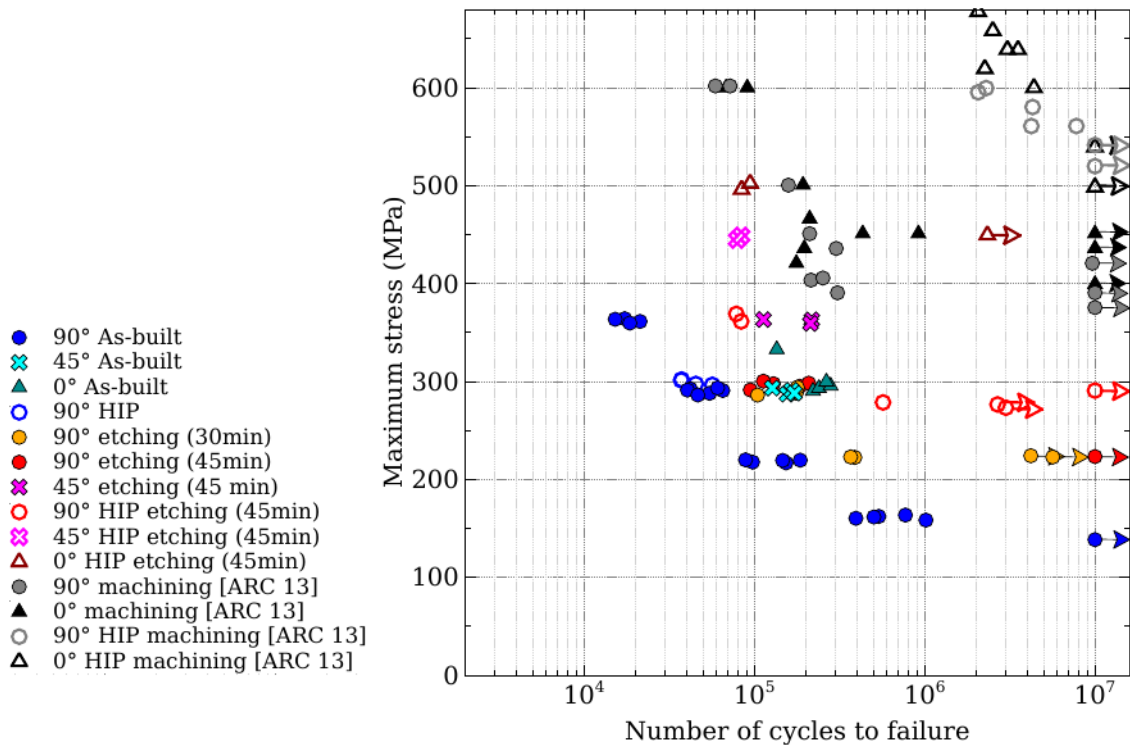
Figure 3.22: S-N curves for EBM 0° (triangles), 45° (crosses) and 90° (dots) fatigue samples. The blue colors (blue, cyan and dark cyan) depict the as-built state. The chemically etched samples are represented by the orange (30 minutes), red, pink and dark red (both 45 minutes) colors. Hollow symbols stand for samples for which HIP was applied. Grey and black symbols correspond to data from ARCAM [ARC 13] on respectively 90° and 0° machined samples obtained by EBM.

a higher stress level ($\sigma_{max} = 500$ MPa), the fatigue lives obtained after HIP and chemical etching are of the same order of magnitude but slightly shorter than the ones reported for machined samples (1 to 2.10^5). This means that, for 0° samples, the detrimental effect of the remaining surface defects after 45 minutes of chemical etching can be almost counterbalanced by the beneficial effect of HIP.

Figure 3.22 shows that **applying HIP prior to chemical etching results in better fatigue performances** for both 45° and 90° samples. This improvement could be due to its effect on the microstructure of Ti-6Al-4V samples: internal pores closure and coarsening of the α-phase laths. The pores closure can affect the crack initiation sites and their criticality whereas the microstructure coarsening can impact the crack initiation and crack growth parameters. Both aspects are discussed in the following sections.

3.5.3.2 Discussions

HIP + chemical etching: influence on crack initiation sites

The fracture surfaces of samples submitted to "HIP + chemical etching" have been characterized.

For all 90° samples, submitted to HIP treatement or not, after chemically etching,

failure occurs from the remaining part of a notch-like defect inherited from the as-built state.

For 45° samples, some samples exhibit the same behavior. However, in some samples, all notch-like defects have been removed by chemical etching. In this case, failure initiates from "plate-pile like" stacking defects remaining at the surface. Figure 3.23 shows the fracture surface of one sample whose fatigue failure was caused by two propagating cracks. Higher magnification micrographs of the two initiation sites are shown in Figure 3.23b and 3.23c. In both cases, it can be observed that the crack initiates from the surface but it is hard to identify any particular defect at the starting point of the crack.
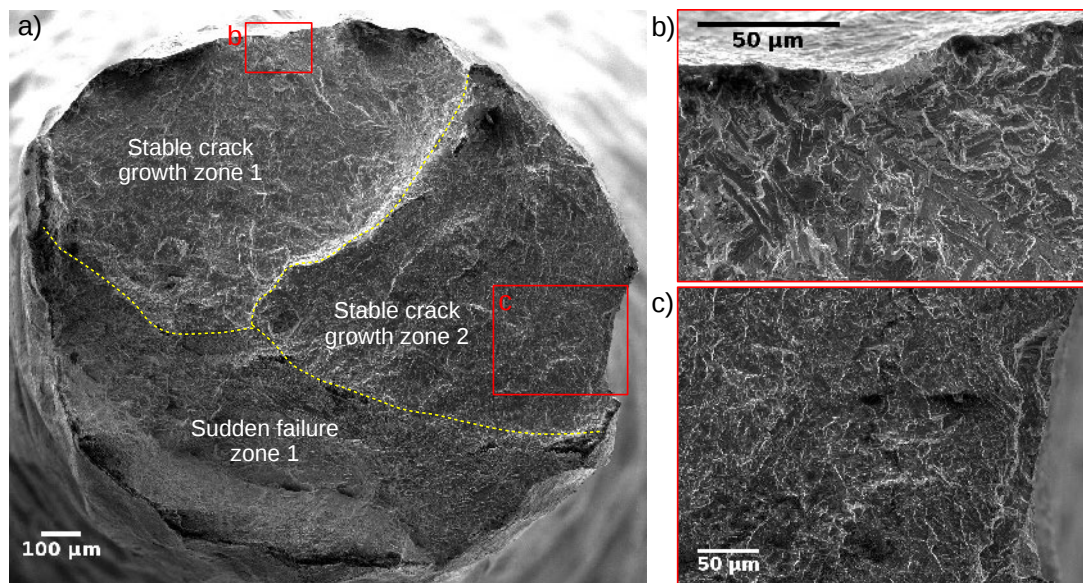

Figure 3.23: SEM-SE micrographs of the fracture surface of one 45° EBM fatigue sample after HIP and chemical etching. (a) Fracture surface showing the stable crack growth and sudden failure zones. (b,c) Higher magnification image showing the crack inititiation sites.

The comparison of the tomographic images before and after failure shows a surface protrusion where the crack initiated but no remaining part of a notch-like defect after chemical etching (Figure 3.24a). It explains why no smooth area - which are typical of surface defects - can be observed in Figure 3.23. The fracture surface shown here represents the bottom part of the broken sample where the protrusion cannot be seen.

The tomographic scans of this sample before and after chemical etching have been compared in order to look at the evolution of this protrusion (Figure 3.24b and c). Before chemical etching (dark gray), a notch-like defect can in fact be observed. Nevertheless, this notch has been completely removed by the chemical etching process and only a small protrusion remained. Its shows that such remaining protrusions can also be detrimental to the fatigue performance.

Besides, it is worth noting that, with respect to the build orientation, this defect is located on the upward facing surface of the sample where the density of such defects is higher in the as-built conditions (Chapter 1). Overall, the fatigue failure of 45° samples after HIP and chemical etching is always caused by surface defects. They can be parts of notch-like
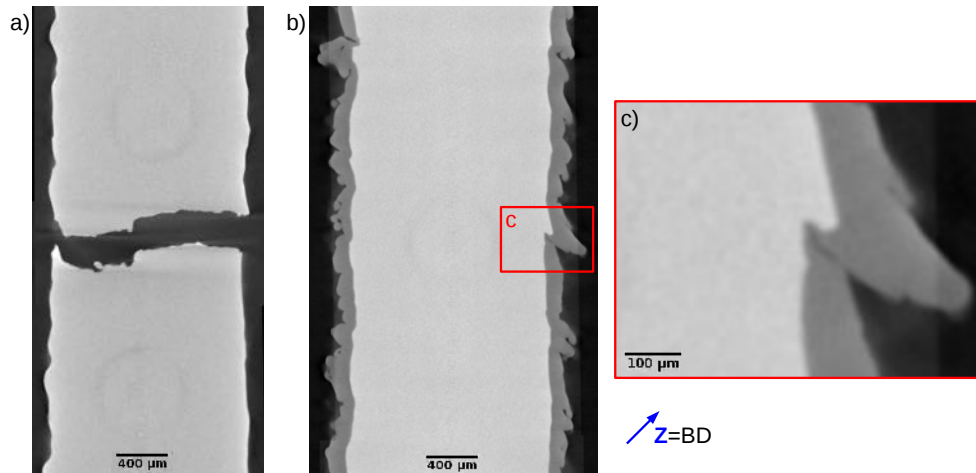
Figure 3.24: Example of one defect leading to the fatigue failure of 45° samples after HIP and chemical etching. (a) Radial slice of the top and bottom parts of the broken sample showing the critical defect. For (b,c), dark gray represents the sample slices after HIP and light gray the sample slices after HIP and 45 minutes of chemical etching. (b) Overlap of the radial slices showing the critical defect before and after 45 minutes of chemical etching. (c) Detailed view of the defect represented in b. The building direction is indicated by the blue arrow.

defects when such defects remain after the post-treatment or stacking irregularities such as protrusions which are less detrimental to the fatigue resistance.

For 0° samples, fatigue failure is always caused by remaining stacking irregularities. An example of critical defect is presented in Figure 3.25. This defect is very thin and mainly elongated on a plane parallel to the build plate (thus parallel to the cylinder axis). It is located on the sample downward facing surface, above a large protrusion (Figure 3.25b). The connection between the root of the defect and the surface is very thin (red arrow in Figure 3.25b). As a result, it is difficult for the chemical reagent to reach the root of the defect whose shape remains unchanged, even after 45 minutes of chemical etching (Figure 3.25b and 3.25c). This is the reason why such large defects persist after 45 minutes of chemical etching and also why the defect leading to fatigue failure is always located at the samples downward facing surface.

To summarize, **for all build orientations,** the fracture surfaces analysis has shown that, in most cases, the defects leading to the failure of "HIP + chemically etched" samples are similar to the ones responsible for the failure of chemically etched samples. In other words, it means that **the pores removal does not impact the crack initiation sites.** Furthermore, when other defects (protrusions) are responsible for the failure, no impact on the fatigue results is observed. Therefore, for all orientations, the improvement of the fatigue properties observed for "HIP + chemically etched" samples over chemically etched samples is not caused by a change in the type of initiation sites or in their criticality.

HIP + chemical etching: effect of the microstructure

If the fatigue performance improvement is not due to a change in the critical defects parameters (type of defect, defect criticality, ...), it must be related to the material prop-
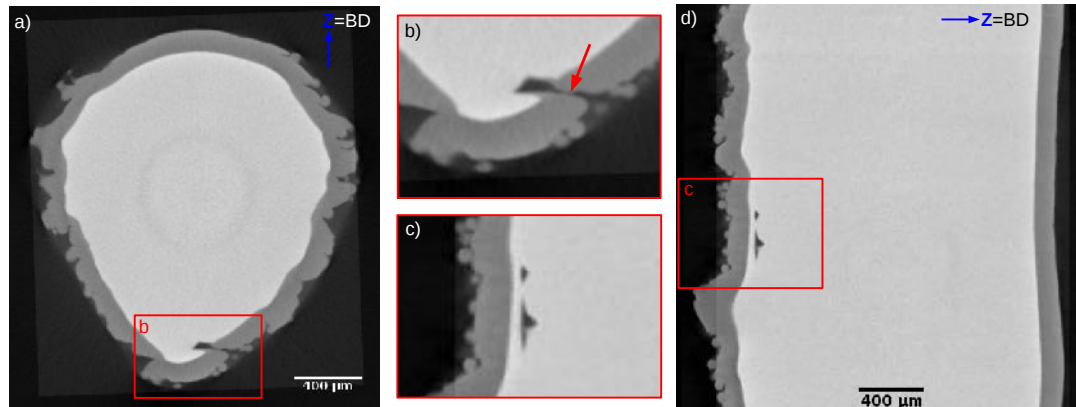
Figure 3.25: Example of one defect leading to the fatigue failure of a 0° samples after HIP and chemical etching for 45 minutes. Dark gray: sample slices after HIP. Light gray: sample slices after HIP and 45 minutes of chemical etching. (a) Overlap of the axial slice showing the critical defect before and after 45 minutes of chemical etching. (d) Overlap of the corresponding radial slice before and after 45 minutes of chemical etching. (b,c) Detailed views of the defect represented in respectively a and d. A red arrow indicates the thin connection between the defect and the surface. The building direction is indicated by the blue arrow.

erties such as crack initiation and crack growth parameters. The crack growth parameters can be determined through standard fatigue crack growth tests. As mentioned earlier, such tests have not been performed in this study and the data from several published studies ([GRE 17], [SEI 17]) have been used to assess how the coarsening of the α-phase laths induced by HIP affects these parameters. Greitemeier et al. [GRE 17] performed fatigue crack growth tests with a stress ratio[5] R = 0.1 on both HIP treated and untreated machined samples (neither the samples build orientation nor the crack growth orientation were reported). Seifi et al. [SEI 17] performed similar tests on HIP treated machined samples but only for a higher stress ratio (R = 0.3) in order to reduce crack closure. These tests were performed on two different build orientations, one of them leading to crack growth perpendicular to the building direction (XY plane) and the other to crack growth in a vertical plane along the X axis (ZX plane).

Regarding the Paris regime, both studies report diverging results. Greitemeier et al. [GRE 17] indicate that HIP does not impact the crack propagation values whereas Seifi et al. report that, after HIP, the slope of the crack growth curves is decreased in the Paris regime. This means that HIP treated and machined samples show the same ([GRE 17]) or better ([SEI 17]) crack growth resistance than machined samples.

The ΔK_{th} values obtained from both studies are reported in Table 3.6. For all crack growth orientations, the ΔK_{th} values of HIP treated samples are higher than the ones obtained for machined samples. Both results (higher ΔK_{th} values and lower Paris slopes) reflect the better crack resistance of the HIP treated samples. Consequently, **the improvement of the fatigue performance when HIP is applied prior to chemical etching is caused by the coarsening of the α-phase laths which make the samples more resistant to crack growth.**

---

[5]Figure 3.1

Table 3.6: Effect of HIP on the ΔK_{th} values of machined samples [GRE 17], [SEI 17]. The results are reported depending on the stress ratio R and the crack growth direction.

Source	State	R ratio	Crack growth orientation	ΔK_{th} (MPa$\sqrt{m}$)
Greitemeier ([GRE 17])	As-built	0.1	unknown	4.2
	HIP	0.1	unknown	4.8
Seifi ([SEI 17])	As-built	0.3	XY plane	4.0
	HIP	0.3	XY plane	5.1
Seifi ([SEI 17])	As-built	0.1	ZX plane	3.8
	As-built	0.3	ZX plane	3.4
	HIP	0.3	ZX plane	4.8

Thanks to the improvement of both the surface state by chemical etching and the sample crack resistance by HIP, a significant improvement of the fatigue properties have been achieved. Nevertheless, they remain lower than those of HIP treated and machined samples regardless of the build orientation because of remaining surface defects. The complete removal of such defects when ultrasonic shot-peening is used as a finishing post-treatment is expected to further improve the fatigue properties of EBM samples. This is the topic of the next section.

3.5.4 Ultrasonic shot peening

3.5.4.1 Experimental results: USP *v.s.* HIP + USP

It has been shown in Chapter 1 that ultrasonic shot peening (USP) leads to a smooth surface geometrically close to what is obtained with machining techniques. A qualitative analysis of the tomographic images showed that no surface defects remain after this post-treatment. The ones from the as-built conditions were either completely "filled" during the process or turned into internal defects, see section 1.4.2.3 in Chapter 1.

For time reasons, USP could only be applied to 90° samples. Both as-built and HIP treated samples were submitted to USP. The corresponding fatigue results are reported in Figure 3.26.

The first result to point out is the **impressive fatigue properties improvement induced by USP when compared to the one induced by chemical etching.** Although, for $\sigma_{max} = 500$ MPa, the fatigue lives of USP samples remain lower than those of machined samples ($N_{USP} \sim 50\,000$ cycles *v.s.* $N_{mach} \sim 160\,000$ cycles), they become similar at low stress levels (unbroken samples after 2.10^6 cycles at $\sigma_{max} = 450$ MPa). Note that these results are similar to the ones obtained for 0° samples after HIP and chemical etching.

A second result is the confirmed positive impact of the HIP process: **the fatigue results of samples submitted to HIP prior to USP are better than the ones of USP only treated samples.** For equivalent fatigue lives of $\sim 50\,000$ cycles, the stress level increases from $\sigma_{max} = 500$ MPa for USP treated samples to $\sigma_{max} = 550$ MPa for
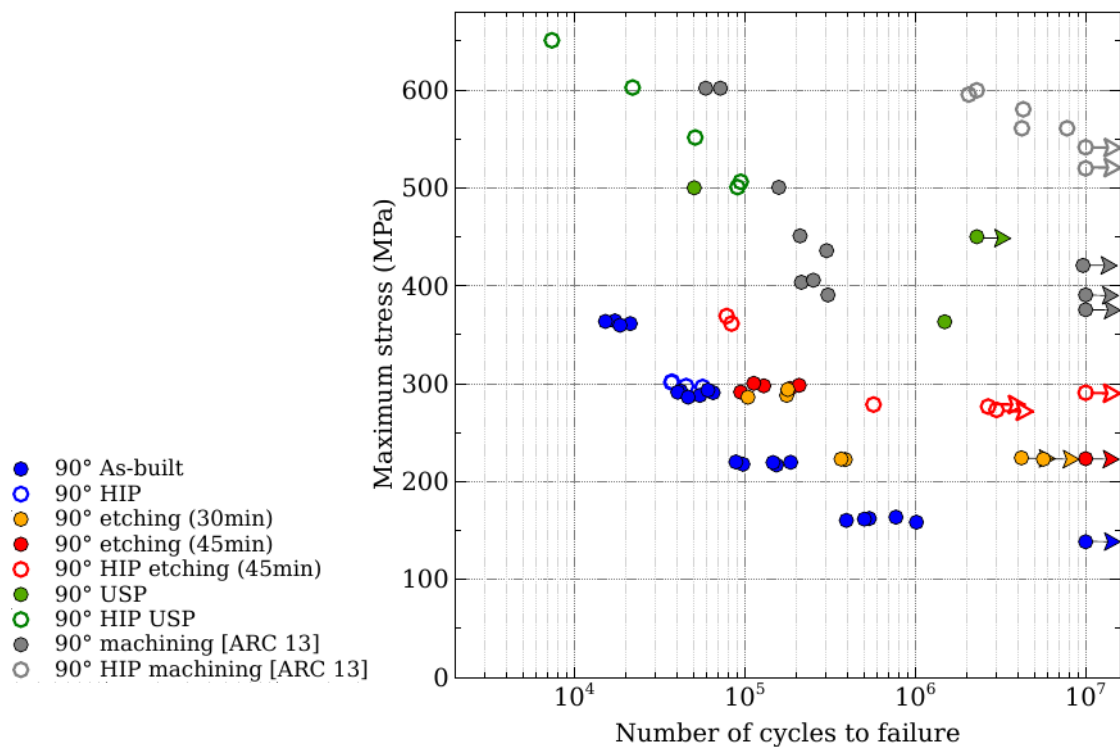
Figure 3.26: S-N curves for EBM 90° fatigue samples in the as-built state (blue dots), after 30 minutes (orange dots) and 45 minutes (red dots) of chemical etching and after 2 hours of USP (green dots). Grey symbols correspond to data from ARCAM [ARC 13] on 90° machined samples obtained by EBM. Hollow symbols represented HIP treated samples.

HIP and USP treated samples. Nevertheless, this improvement (+ 50 MPa for similar fatigue lives) is rather limited when compared to the improvement that HIP generates when applied prior to the machining step: 100-125 MPa and 125-150 MPa improvements are reported by ARCAM [ARC 13] respectively for relatively short fatigue lives ($\sim 25\,000$ cycles) and for the fatigue limit at 10^7 cycles. Therefore, the fatigue results obtained for "HIP + USP treated" samples remain well below the ones of "HIP + machined" samples. For $\sigma_{max} = 600$ MPa, the fatigue lives are 100 times longer for "HIP + machined" samples and a 300 MPa difference is observed between the σ_{max} values corresponding to 25 000 cycles. Note that this comparison was not made at 10^5 cycles because of the lack of data from ARCAM [ARC 13].

This difference in fatigue properties can be linked to the difference between the defects distribution of the samples after "HIP +USP " and "HIP + machining". In the last case, the samples are considered to be free of both internal (gas pores, lack-of-fusion defects, ...) and surface defects (powder particles stuck to the surface, notch-like defects, ...). In the "HIP + USP treated" samples, it has been demonstrated in Chapter 1 that a "ring" of sub-surface defects remains. In order to determine the impact of those defects, the fracture surfaces of USP treated samples have been observed.

3.5.4.2 Critical defects: impact of USP on notch-like defects and limit of X-ray tomography
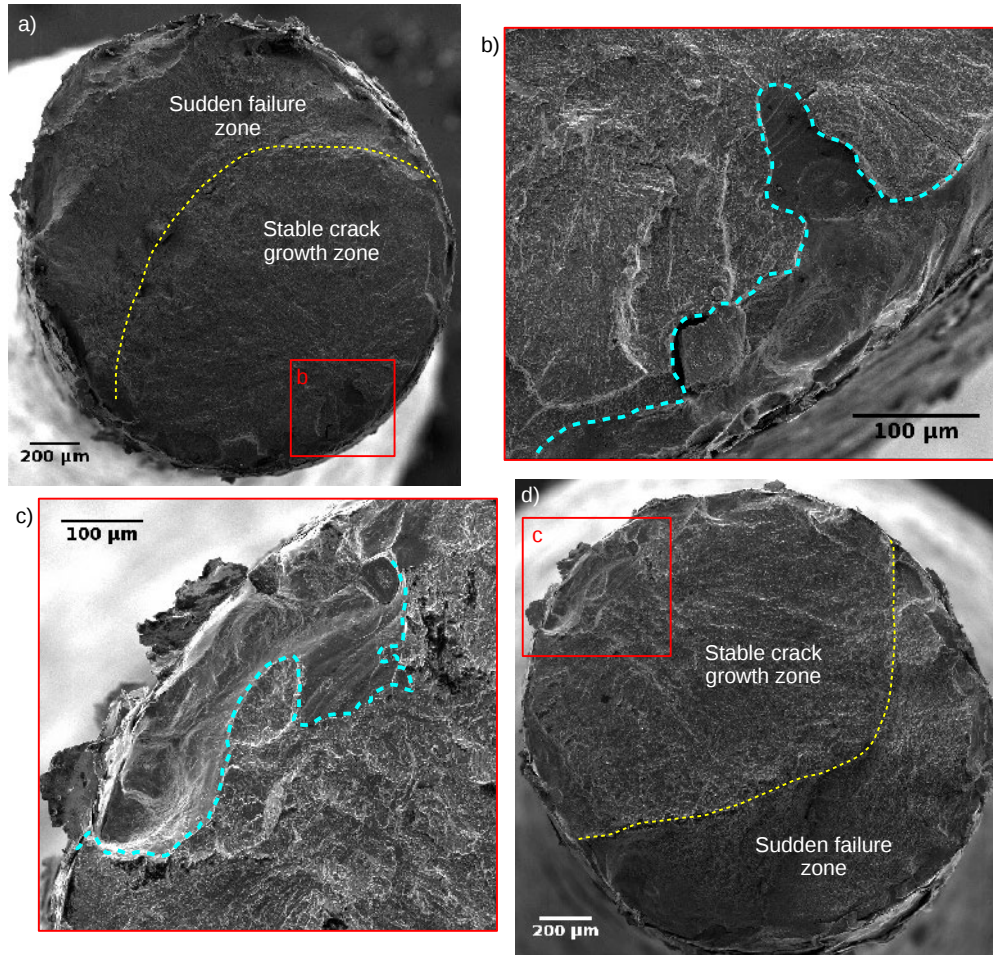
Figure 3.27: SEM-SE micrographs of the fracture surfaces of two 90° EBM fatigue samples: one USP treated (a,b) and one HIP and USP treated (c,d). (a,d) Fracture surface showing the stable crack growth and sudden failure zones. (b,c) Higher magnification image showing the crack inititiation sites. Their inner contour is delineated by a blue dashed line.

Figure 3.27 shows two of those fracture surfaces, one from an USP treated sample and one from a HIP and USP treated sample. Both samples were submitted to the same fatigue stress level ($\sigma_{max} = 500$ MPa) and the corresponding fatigue lives are respectively around 50 000 and 100 000 cycles. For both samples, **the fatal crack initiates from a defect close to the surface** (Figure 3.27a and d). By applying the critical defect identification method presented in section 3.4.2, it turns out that these defects have been detected on the tomographic images and are part of the ring of "new" sub-surface defects presented in Chapter 1. This accounts for the difference in fatigue properties between "HIP+USP" and "HIP+machining" samples being caused by these remaining defects.

Besides, the higher magnification images show that these defects seem to be connected

to the surface which would be contradictory to the observations made only based on the tomographic images in Chapter 1. A higher magnification image of the critical defect for the HIP and USP treated sample is presented in Figure 3.28.

Figure 3.28: Comparison of the high magnification SEM-SE micrograph (a) of the crack initiation site of one HIP and USP treated sample with the corresponding tomographic image (b). (b) Axial view of the critical defect after USP treatment as observed on tomographic images. (c) Overlap of the SEM and tomographic images. The defect detected by tomography is shown in red and the inner contour of the one detected by SEM-SE is delineated by a blue dashed line.

The smooth aspect, typical of surface defects observed in as-built samples, can be recognised for this critical defect which confirms that it originates from a surface defect in the as-built state. It can be clearly differenciated from the rest of the fracture surface where the crack propagates and where microstructural features can be observed. Thanks

to this clear difference, it can be observed that the smooth area which defines the critical defect extends up to the surface (Figure 3.28a). This demonstrates that the critical defect is connected to the sample surface which was not detected on tomographic images[6] as shown in Figure 3.28b.

Figure 3.28c compares the real shape and size of the defect (SEM micrograph) with what was observed on tomographic images (2.5 μm voxel size). It highlights that only the root of the defect is detected. Note that it has been proven in Chapter 1 that lab tomography with a better voxel size (1 μm) gives the same results. This means that the plastic deformation induced by USP is sufficient to "fill in" the surface defects and make them *look like* sub-surface defects. Nevertheless, this deformation is probably not sufficient to induce a cohesive bond between the deformed layer and the preexisting surface. As a result, a weakened area remains between the root of the defect and the surface. It means that those defects must be considered as surface ones. **The real size of the sub-surface defects is therefore much larger than it appears on the tomographic images of USP treated samples.** As these tomographic images cannot be used for the determination of the real material integrity of USP treated samples, the tomographic scans performed prior to this post-treatment have been analyzed and compared with the SEM micrographs, as shown in Figure 3.29.

Radial slices were used to determine the top and bottom of the defect along the Z axis and this part of the sample was separated from the rest of the sample. Within this cropped part, minimum and maximum projection along the Z axis were computed. They reveal respectively the inner and outer limit of the defect. An average computation of both projections finally represents in dark gray the projected area of the defect before USP (Figure 3.29b).

If the inner limit of the surface defect observed on the SEM micrograph (highligthed by the blue dashed line) is reported into the tomographic image, this line matches perfectly with the inner limit of the surface defect in the as-built state (Figure 3.29b). The inner contour of the surface defect does not seem to be impacted by USP in spite of the severe plastic deformation occuring at the surface. Instead, only the outer part of these defects is affected.

To summarize, the tomographic images of "HIP + USP treated" samples show that the surface defects of EBM samples have been either completely "filled" or turned into small subsurface defects by USP. It gives the misleading impression that the resulting samples are almost free of defects. However, the plastic deformation generated by the USP treatment only put in contact the surfaces but never induced a real *cohesion* between them. **Under tensile fatigue stresses, the contact between the surfaces is therefore broken and defects almost identical to the as-built surface defects are finally observed.**

Figure 3.29c depicts the real impact of USP on the defect size: even though it has been reduced when compared to its size in the as-built state, this reduction is rather limited and the defect projected area remains close to that of the as-built state. The defects are thus much bigger that those responsible for the fatigue failure of machined samples. It can explain why, at high stress levels, the fatigue performance of USP treated samples does not match the Arcam results for machined or "HIP + machined" samples (Figure 3.26).
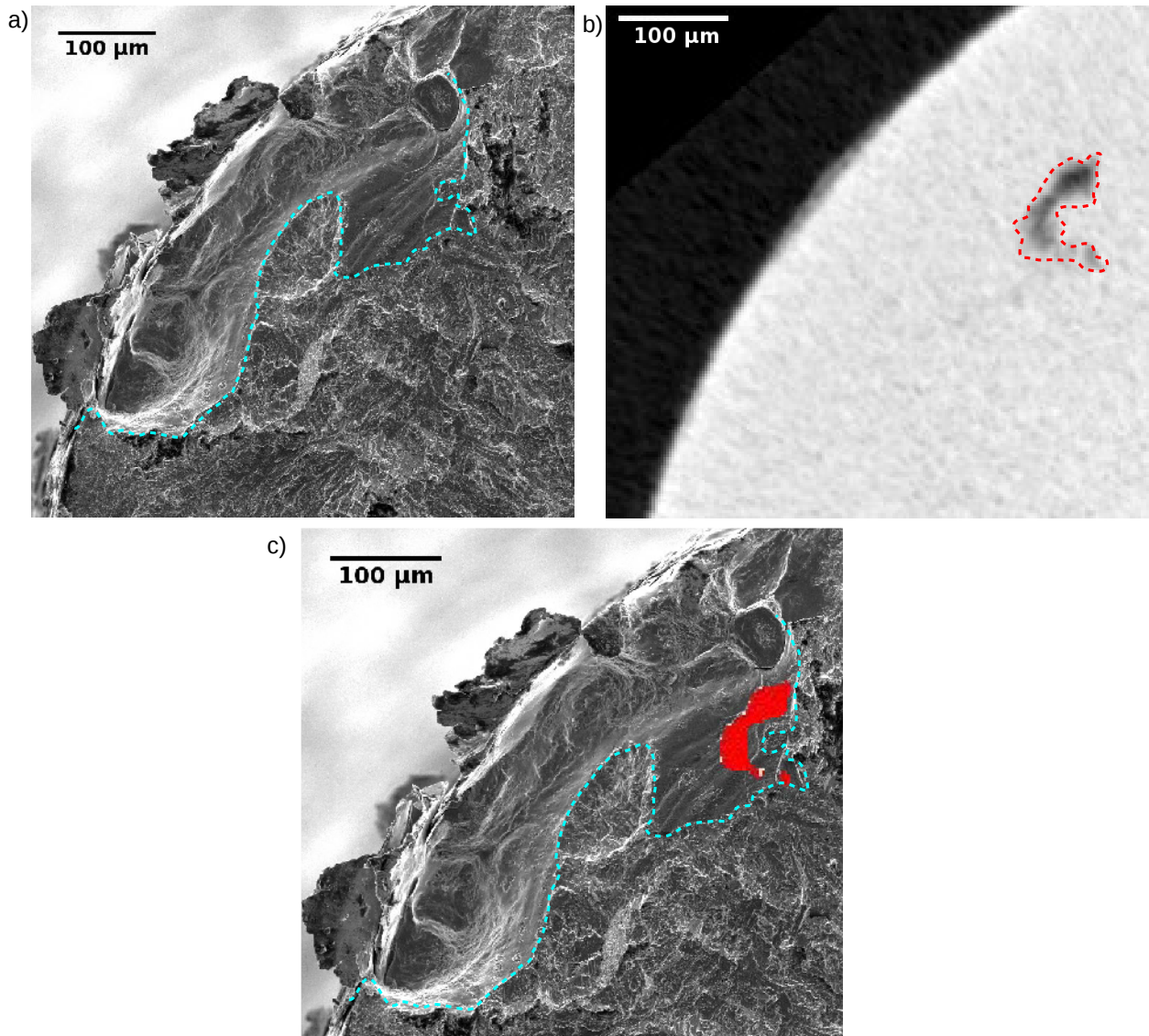
---

[6]with lab X-ray tomography
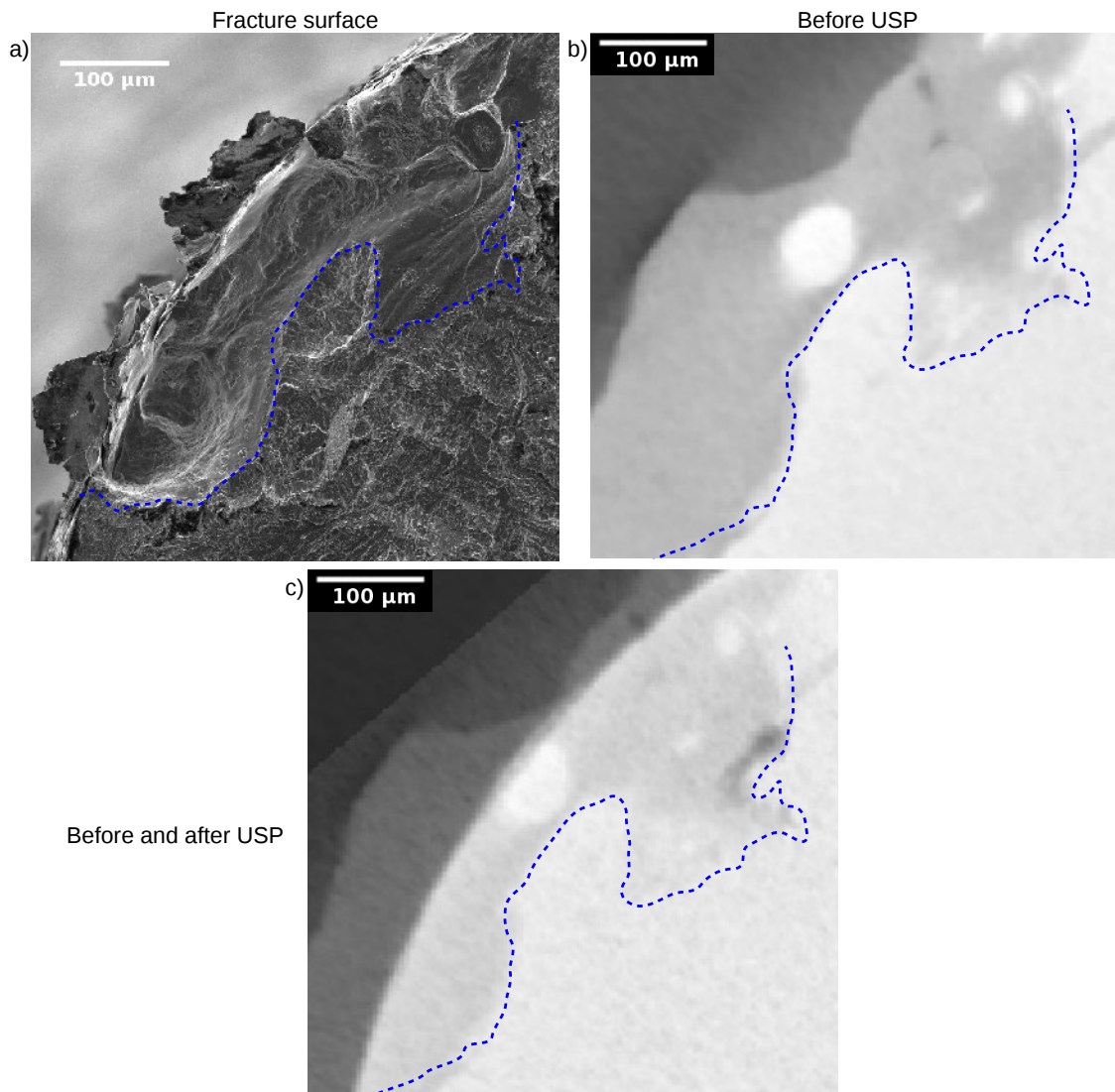
Figure 3.29: Comparison of the high magnification SEM-SE micrograph (a) of the crack initiation site of one HIP and USP treated sample with the corresponding tomographic image in the as-built state (b). The inner contour of the surface defect is highlighted by the blue dashed line. (b) Average computation of the minimum (light gray area) and maximum (combined dark and light gray areas) projections along the loading axis around the critical defect. (c) Average computation of (b) with the tomographic image of the critical defect after USP.

Besides, the comparison of the size of critical defects for 90° as-built (Figure 3.3a), chemically etched (Figure 3.16) and USP treated samples (Figure 3.27) points out that the defects size of the latter ranks between the defects sizes of the two other samples conditions. In a *Kitagawa-Takahashi* diagram, USP treated samples would therefore show worse fatigue properties than the chemically etched samples which contradicts the results presented in Figure 3.26. This discrepancy might come from the compressive residual stresses induced at the surface by USP, see Chapter 1.

3.5.4.3   Towards defect-free samples: HIP + chemical etching + USP

It has been demonstrated in Chapter 1 that several notch-like defects are partially "filled" and turned into sub-surface defects by USP. The analysis of the fracture surfaces discussed in the previous section revealed that these defects are responsible for the fatigue failures. It also showed that their size - and therefore criticality - is greatly underestimated on the tomographic images: they are close to those of notch-like defects in as-built samples. The defects population is thus very different from that of machined samples and this can justify why the fatigue properties of USP treated samples do not match the one of machined samples.
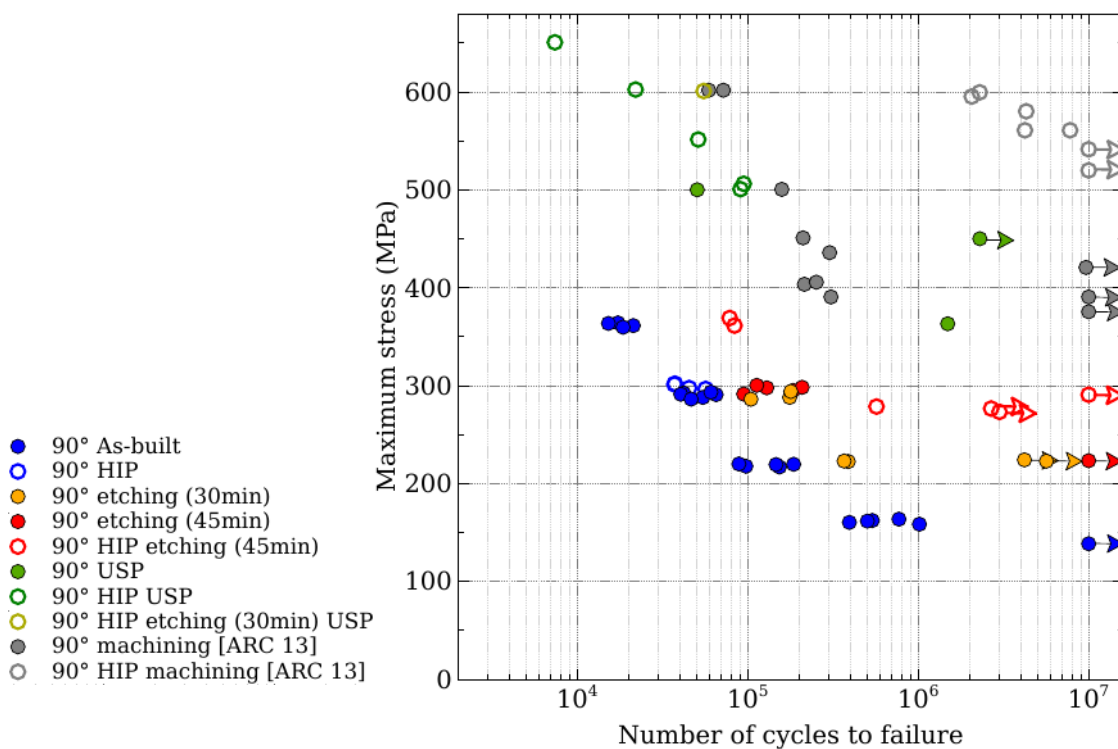
Figure 3.30: S-N curves for EBM 90° fatigue samples in the as-built state (blue dots), after 30 minutes (orange dots) and 45 minutes (red dots) of chemical etching and after 2 hours of USP (green dots). Grey symbols correspond to data from ARCAM [ARC 13] on 90° machined samples obtained by EBM. Hollow symbols represented HIP treated samples. The light green hollow dot represents the sample submitted to HIP + chemical etching + USP.

If one aims at obtaining by post-treatments fatigue performance similar to those of "HIP + machined" samples, as-built notch-like defects must be removed. Such defects can be removed or at least greatly reduced by chemical etching as shown in Chapter 1 with a good impact on the fatigue properties (section 3.5.2). The three post-treatments (HIP, chemical etching and USP) have therefore been applied successively to EBM samples in order to obtain defect-free samples. HIP was first applied so that internal defects are closed. Then, the samples were submitted to 30 minutes of chemical etching for the notch-like defects reduction and finally USP was applied. The tomographic scans performed on

these samples detected only a very limited number of defects. Only one sample could be cycled during the PhD and the corresponding result is reported in Figure 3.30 by a light green hollow dot ($\sigma_{max} = 600$ MPa).
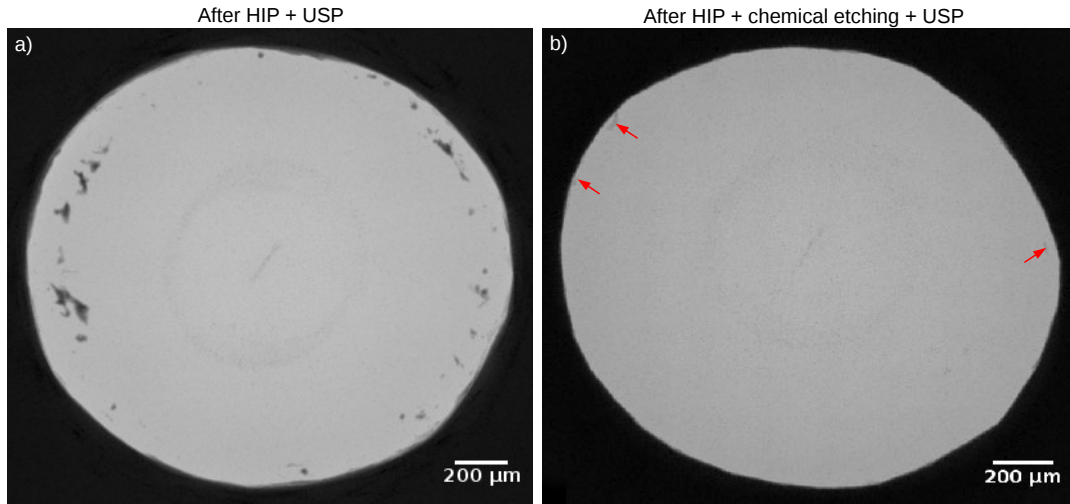
After HIP + USP

After HIP + chemical etching + USP

Figure 3.31: Minimum projections of all the X-ray lab tomographic axial slices (2.5 μm voxel size) within the gauge length of a "HIP + USP treated" sample (a) and a sample that underwent successively HIP, chemical etching and USP post-treatments (b). The detected defects appear in dark gray and are pointed out by red arrows.

For a stress level σ_{max}=600 MPa, the sample sustained $\sim 55\,000$ cycles before fatigue failure. For such fatigue lives, this corresponds to a 50 MPa improvement of the stress level compared to "HIP + USP treated" samples. **It matches the fatigue properties of machined samples but, still, not the fatigue properties of "HIP + machined" samples** which remain far better. As shown by the minimum projection in Figure 3.31b, in the entire gauge length of the sample, only three defects have been detected after the "HIP + chemical etching + USP" combination. This represents a significant improvement when compared to the number of defects remaining in "HIP + USP treated" samples (Figure 3.31a). The comparison of the tomographic images before and after failure indicates that none of these three defects is located within the failure area, meaning that the defect responsible for the sample failure is not clearly detected by laboratory tomography. The corresponding fracture surface is presented in Figure 3.32.

Two different initiation sites can be determined in Figure 3.32, both at the surface of the sample. As illustrated for one of the two defects in Figure 3.33, the comparison of the tomographic scans before and after failure shows that the failure is caused by extremely thin defects. These defects do not appear in Figure 3.31 because of their extremely limited thickness: the difference in gray level between these defects and the rest of the sample is so small that it disappears during the minimum projection. The defects leading to failure can be traced back on to the HIP treated state where it appears that they originate from notch-like defects (Figure 3.33a). The sample was not tomographically scanned after the etching treatment so the defect aspect after chemical etching and before the USP treatment could not be analyzed.
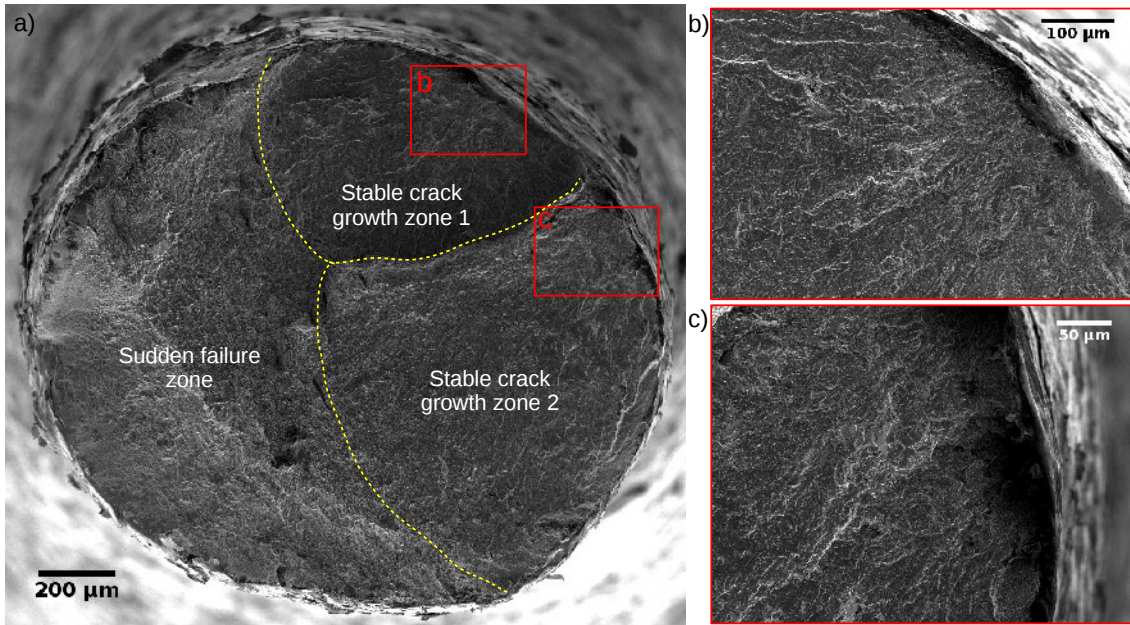
Figure 3.32: SEM-SE micrographs of the fracture surfaces of a 90° EBM fatigue sample HIP treated, chemically etched for 30 minutes and USP treated for 2 hours. (a) Fracture surface showing the stable crack growth and sudden failure zones. (b,c) Higher magnification image showing the two crack inititiation sites.
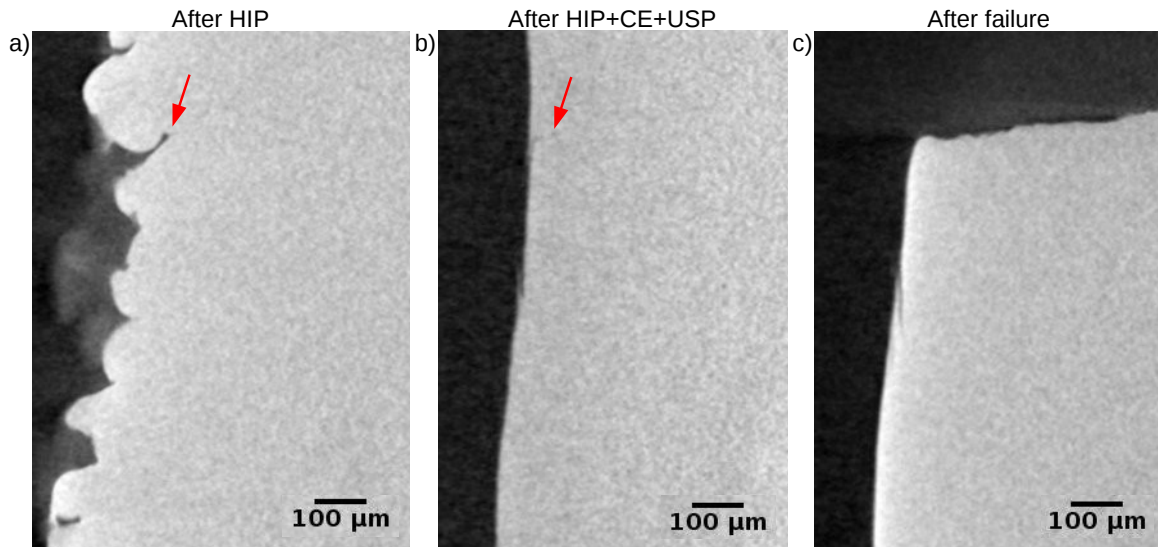
Figure 3.33: Radial slices obtained by X-ray tomography of a 90° EBM fatigue sample HIP treated (a), chemically etched for 30 minutes and USP treated for 2 hours before (b) and after fatigue failure (c). The defect leading to failure is pointed out by a red arrow.

Finally, it can be stated that **30 minutes of chemical etching followed by USP do not represent the perfect combination for achieving defect-free samples.** Besides, it is clear that part of the remaining defects population is not properly detected

by laboratory X-ray tomography which means that this technique is no longer reliable to assess the presence of such defects. This is a critical point since the detected defects are not always the ones causing the fatigue failure (Figure 3.32).

As a result, another method must be applied to determine the right chemical etching duration to obtain defect free samples. In order to avoid an expensive and tedious "trial and error" method, numerical simulations may be considered. Lhuissier et al. [LHU 16] proposed a cellular automaton based model to describe the chemical etching process. This model is based on tomographic images and uses two parameters: a radius R and a critical etchant density ρ_c. For each voxel of the sample, the local density of etchant $\rho_{etchant}$ inside a sphere of radius R is computed and compared to ρ_c. When $\rho_{etchant} > \rho_c$, the voxel is turned into chemical solution; otherwise, it remains bulk material. The model parameters were optimized on one sample by comparing the numerical evolution of the sample with experimental data (tomographic scans performed at several chemical etching intervals). After optimization, it was applied to other struts and a good correlation between the model and the experimental data was reached. For details about this model, see [LHU 16]. Such a model could be directly applied to the thin struts studied in the current work.

In order to determine the optimal chemical etching duration to apply before USP, the quantity of bulk material that needs to be dissolved should be known. It has been shown in Chapter 1 that, after USP, the remaining sub-surface defects are all inherited from notch-like defects which are deep and thin defects: no matter how deep, stacking irregularities are always "filled". Consequently, the thickness at the defects root must be increased by the chemical etching process to enable the material from the surrouding surface peaks to "fill" them. This means that the chemical etching process must access the root of all defects and this corresponds to etching durations longer than 45 minutes. As suggested above, the correct etching duration could be determined using Lhuissier's model [LHU 16]. However, the same authors have reported that the dissolution process is more efficient on convex surfaces such as powder particles stuck to the strut and surface peaks. This implies that after long etching durations the height and number of surface peaks will be largely reduced to such an extent that they can no longer completely "fill" the remaining notch-like defects by plastic deformation. Being able to model the "filling" process induced by USP might therefore be necessary.

However, to the authors knowledge, no model depicting the effect of USP on rough surfaces exists. Many authors focused on the residual stresses generation: Meguid et al. [MEG 99] studied the residual stresses induced by single and twin shots on machined surfaces and Dai et al. [DAI 07] did the same for single and multiple shot peening impacts and analyzed the effect on the hardening process and the nanocrystallized layer which was formed during the peening process. Only one study reports how shot peening affects the surface roughness and it focuses on machined samples: Dai et al. [DAI 04] studied the roughness *induced* by a shot peening process rather than the roughness reduction that optimized parameters can provoke which is what we are interested in. It may be worth applying this finite element model to rough surfaces and compare to results with the tomographic scans performed before and after USP. This has not been performed in the framework of this study.

3.5.5   Conclusion on post-treated samples

The fatigue properties of as-built single struts are limited when compared to the ones of machined samples. As conventional machining cannot be used to improve the surface of additively manufactured lattice structures, other post-treatments must be used. Chemical etching and ultrasonic shot peening were used and their impact on the fatigue properties was investigated. HIP was always combined with these post-treatments. The main conclusions of this study are as follows.

- Chemical etching largely improves the fatigue properties of EBM made samples through a severe reduction of the surface defects criticality.
    - The build orientation impact observed on the fatigue properties of as-built samples remains after chemical etching (longest and shortest fatigue lives for respectively 0° and 90° samples).
    - For 90° samples, the same fatigue properties are obtained for samples etched during 30 and 45 minutes. The root of the deepest notch-like defects remains unaffected by the etchant and these defects are responsible for the failure of all samples.
    - For 45° samples also, the remaining part of notch-like defects can lead to fatigue failure. But in some cases, the fatigue failure is caused by internal defects turned into surface ones because of chemical etching.
    - Longer etching times may improve the fatigue properties of 90° samples (complete removal of all notch-like defects) until they reach the fatigue performance of 45° samples.
- HIP does not affect the fatigue properties of as-built samples but significantly increase the fatigue resistance of post-treated (chemical etching and USP) samples. This has been related to a beneficial impact on the crack growth resistance of EBM Ti-6Al-4V samples.
- Fatigue properties similar to those of machined samples can be obtained thanks to USP, even when applied to the least resistant 90° samples.
    - Fatal cracks always initiate from the remaining part of notch-like defects. The tomographic images show that they have been "filled" and turned into small sub-surface defects during the USP process.
    - The SEM fracture surface observations show that there is no material cohesion where the defects have been "filled". The defects size is larger than it appears on the tomographic images. Tomography is not reliable to assess the material integrity after USP.
    - The criticality of the remaining defects is more important than the one of chemically etched defects and closer to that of as-built samples.
    - The compressive residual stresses at the surface are most likely to play a major role in the impressive fatigue improvement resulting from the USP treatment.
- The three post-treatments (HIP+chemical etching+USP) have been combined to obtain defect-free samples. Although additional tests must be performed, a promising fatigue improvement has already been achieved.

3.6   Graphical summary

Chapter 4

Towards the prediction of EBM samples fatigue properties

Contents

It has been shown in the previous chapter that the fatigue properties of EBM samples are deeply linked to the presence of surface defects and more precisely notch-like defects: for all as-built samples and most of the post-treated ones, the crack leading to failure initiates from such a surface defect. Removing those defects or reducing their criticality by chemical etching leads to an improvement of the fatigue resistance. The objective of this chapter is therefore to describe a method for detecting the notch-like defects and for evaluating their criticality through non-destructive inspections. This should allow to predict the fatigue resistance of one sample based on its surface defects distribution.

4.1   Methodology

4.1.1   Automatic detection of the critical defects

4.1.1.1   Detailed process of the method

The method for detecting automatically the critical defects is first presented step by step based on an example of an as-built sample. The critical notch-like defects can be detected through the important local variations that they induce on the distance between the sample central axis (determined from the tomographic images) and the surface. First, the gray scale tomographic images of the sample gauge length are thresholded in order to obtain binary images. Then, these images are used to detect[1] and remove all internal defects that could skew the distance measurement. This distance is then computed for all voxels belonging to the surface.
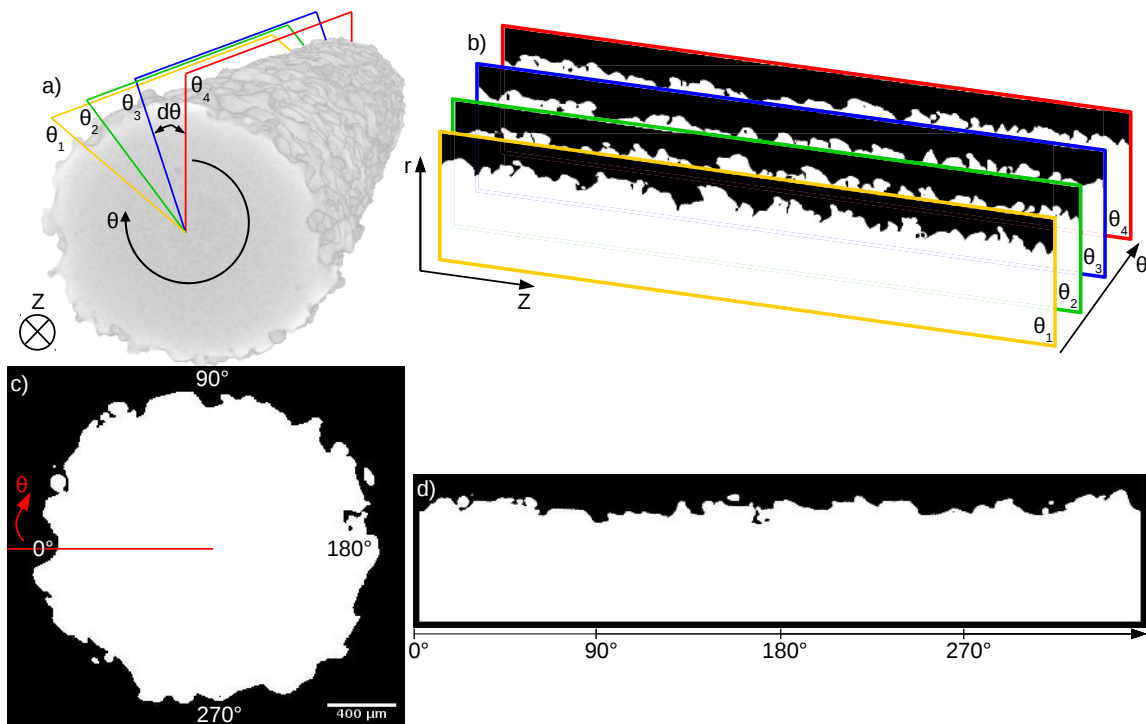
Figure 4.1: (a, b) Schematic illustration of the reslicing process where radial slices are produced from the stack of the sample reconstructed sections. A line starting from the sample central axis and ending at the edge of the tomographic image is rotated around its starting point with a radial step $d\theta$ (in °) (a). For every $d\theta$, the software interpolates the image corresponding to the voxels in the (r,z) plane (b). (c, d) Illustration of this "unfolding" process for one binary slice of an as-built sample. (c) Axial slice of the sample. (d) View of the "unfolded" slice after reslicing. The correspondance between the angular position in (c) and the horizontal one in (d) is shown.

The radial reslice function of the Fiji software is used to produce radial reconstructions of the stack of the sample sections. The "unfolding" of the surface induced by this process

---

[1]through a 3D objects detection method

is shown in Figure 4.1. The radial step $d\theta$ is determined so that the voxels at the surface of the "unfolded" section are not deformed and remain approximately cubic with a 2.5 μm side. As the radial step remains constant along the sample radius, the voxels close to the sample central axis are deformed radially but this drawback is of no concern as the method mainly relies on the voxels surface where the critical defects are located.
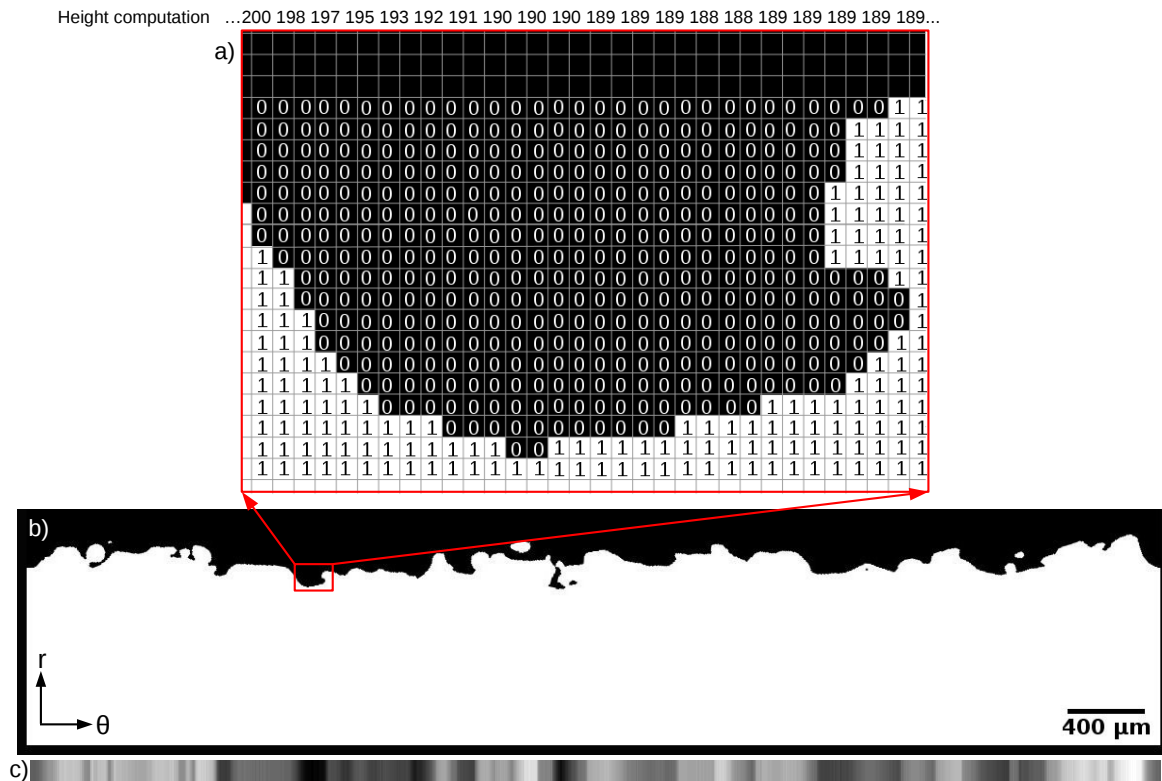
Figure 4.2: Automatic detection of the critical defects: acquisition of the radial distance of all surface points. (a) Illustration of the tomographic images binarization. (b) View of the unfolded slice. (c) Grey scale line obtained from the unfolded slice in (b) (the vertical thickness of the line is arbitrary). The gray colors values (8 bits) correspond to the surface points height.

For each axial slice, an "unfolded" slice is obtained where the distance between the surface and the sample center axis can be measured (see an example in Figure 4.1d). To this end, for each surface voxel, the values of the voxels within the corresponding vertical column are added in order to obtained its height. This protocol is illustrated for one surface profile in Figure 4.2. The height values can then be converted into 8 bits values (Figure 4.2c). By extending this method to all surface voxels, a gray scale map of the surface is obtained. Dark gray areas correspond to small distances and therefore important surface valleys while light gray areas indicate important protrusions. The aim is then to threshold such maps so that only the lowest height values (corresponding to deep surface defects) remain.

An example of such map is shown in Figure 4.3 where the first steps of the detection method are summarized and illustrated for the entire gauge length of an as-built sample. In Figure 4.3c, three vertical light gray bands separated by two darker bands can be seen.
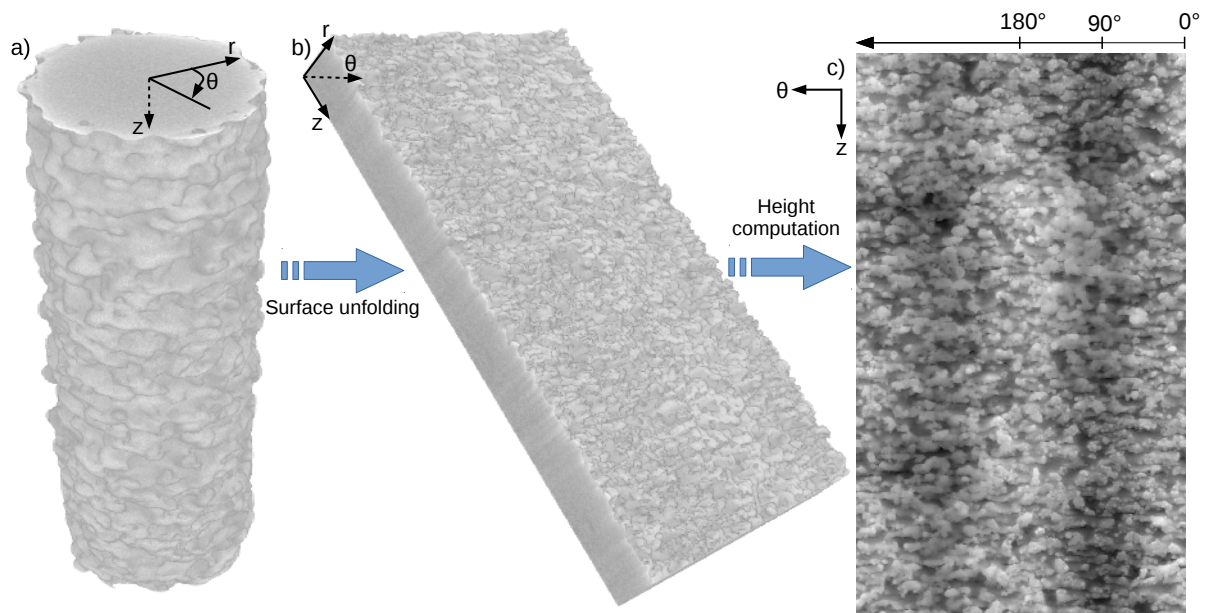
Figure 4.3: Automatic detection of the critical defects: from a 3D volume to a grayscaled surface map. (a) 3D rendering of an a-built sample gauge length. (b) 3D rendering of the same gauge length after unfolding (c) Grey scale surface map. The gray levels correspond to the surface points heights. The angular positions are indicated.

This implies a low frequency macroscopic variation of the sample diameter. This variation is illustrated in Figure 4.4a: the axial cross section is slightly elongated in the left-to-right axis and is closer to an ellipse than to the CAD disk shape. This macroscopic variation of the sample diameter affects the height values and a thresholding of this map would give inconsistent results: harmless defects could be detected as critical in the dark gray bands and, more of an issue, critical notch-like defects within the light gray bands might be overlooked (Figure 4.3). This aspect of the surface maps must be taken into account in order to obtain an accurate depiction of the surface irregularities.

Another factor that needs to be considered is the shape of the surface defects leading to the height variations. Surface maps only show the depth of the surface defects, regardless of their shape. On the slice shown in Figure 4.4b, the deepest measured defect corresponds to a relatively smooth surface variation (large radius of curvature) shown by a letter (A) in the middle of Figure 4.4b. On the sole basis of its depth, this defect would be considered as the most harmful one which is in contradiction with the results presented in the previous chapter.

There is therefore a need to remove such mesoscopic surface height variations so that only the very localised ones remain. For this purpose, a *blurring process* is used, as illustrated in Figure 4.5. A Gaussian blur operation is first applied to the original surface map. This filter uses a Gaussian convolution function for smoothing the gray levels variations in an image. A radius r defines the size of the disc used for the Gaussian function computation. The resulting image (Figure 4.5b) is then substracted to the surface map (Figure 4.5a) so that only the local surface height variations appear (Figure 4.5c). The

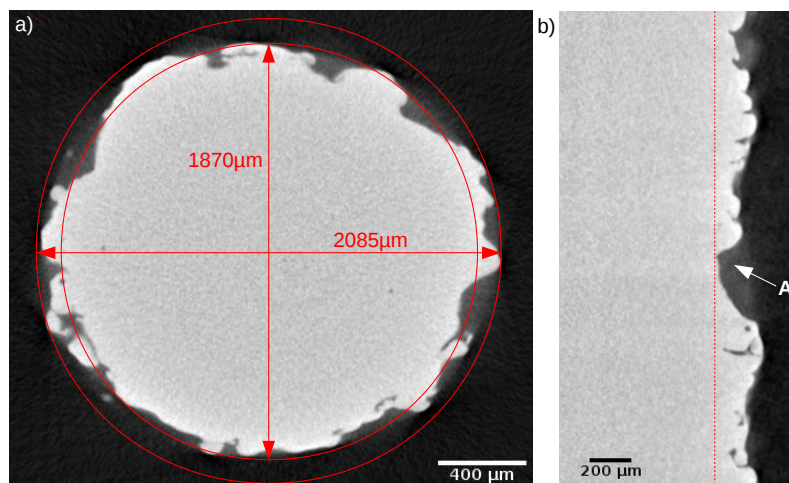**Figure 4.4:** Automatic detection of the critical defects: limits to the surface map of height values. (a) Example of an axial slice showing the elliptical shape of the cross section. (b) Radial slice showing an example of a stacking irregularity (A) deeper than the surrounding notch-like defects.

new surface map obtained after this operation (called "final surface map" in what follows) represents *local* height values i.e. the difference between the absolute height value and the local average one obtained from the blur function. The surface peaks and valleys are respectively represented by positive and negative values and **the lowest values (dark areas) are expected to correspond to notch-like defects.**

It is finally possible to select all the darkest areas (deepest defects) by thresholding this surface map using a threshold value (called *TS* in what follows). The method for selecting the values of the two parameters r and TS is discussed in details in the following section.

4.1.1.2 Optimization of the detection of notch-like defects

For optimizing the process parameters and measuring the defects criticality, a sample chemically etched for 45 minutes with a smoother surface state than that of the as-built conditions is used.

All notch-like defects are first detected and ranked according to their depth. As explained, all surface defects with a footprint on the surface smaller than r (radius of the blur function) are smoothed. For notch-like defects with a thickness b (see Figure 3.8 in Chapter 3), the optimized value of r is the largest b value of all notch-like defects denoted b_{max}. For lower r values, some notch-like defects will not be detected whereas, for higher r values, additional and unrelevant defects will be detected such as the smooth surface variations mentioned before.

Unfortunately, it is not possible to determine b_{max} without entering an endless iterative loop. To compute b_{max}, it is necessary to detect and analyze all notch-like defects, a process which requires to select a value for r, the best one being $r = b_{max}$ and so on and so forth.

As a result, another approach has been considered. A sample chemically etched for 45 minutes has been selected. The tomographic images of its gauge length have been carefully
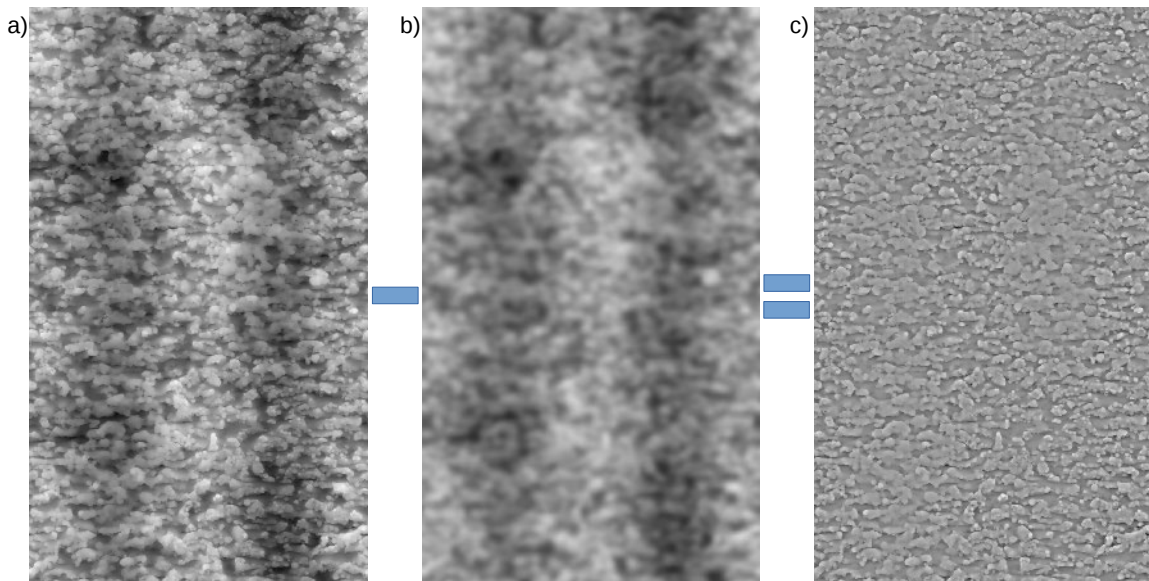
Figure 4.5: Automatic detection of the critical defects: removal of the macroscopic surface height variations. (a) Grey scale surface map. (b) Result of a gaussian blur operation (r=50 μm) on (a). (c) Surface map showing the local variations of height obtained from the mathematical operation (a)-(b). These maps show the entire sample gauge length (∼5.8 mm perimeter and 10mm height).

visually inspected and all potentially harmful surface defects[2] have been identified, their coordinates and depth being measured manually. The critical defect identification method was then applied to that sample using several r values to generate the final surface maps. The defects depth values obtained from these maps were compared with those measured manually. Five values of r have been considered: 25, 50, 75, 100 and 125 μm. For r values lower than 25 μm, the number of defects overlooked became too large (more than 8%).
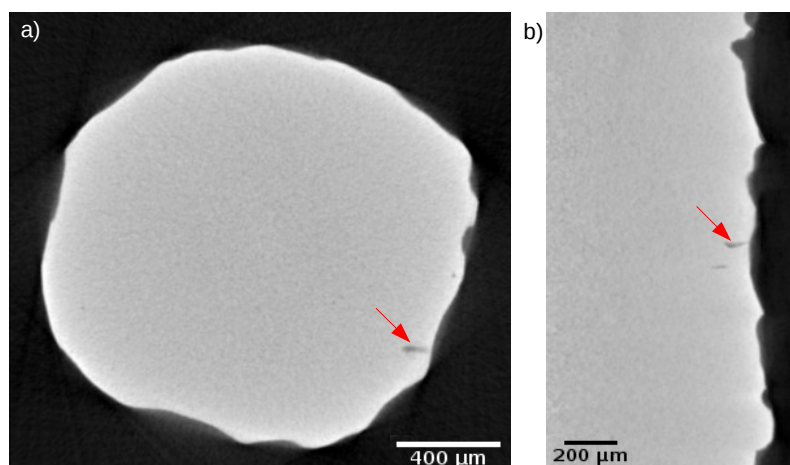
Figure 4.6: Axial (a) and radial (b) local minimum projections of the tomographic images of the undetected defect. Red arrows identify the defect.

---

[2]sharp surface variations which are most likely to originate from notch-like defects in the as-built state

58 defects were identified using the manual procedure. For the different r values considered, **the method succeeds in detecting all potentially harmful surface defects of the analyzed sample** but one. The undetected defect is shown in Figure 4.6 where local minimum projections of the axial (Figure 4.6a) and radial (Figure 4.6b) views are presented. During the visual inspection of the tomographic images, in order to be conservative, this defect was selected as a *surface* defect in spite of the fact that the connection with the surface[3] was not obvious. During the thresholding step preceding the internal pores detection (Section 4.1.1.1), this defect was however identified as internal and removed from the binarized tomographic images. It remained therefore undetected by the automatic procedure.

In order to determine the best value for r, for all detected defects, the local maximum depth values obtained with the 5 different r values have been compared with the ones measured directly on the tomographic images. The results of this comparison are shown in Figure 4.7 which is divided into two subfigures for the sake of clarity. Ellipses have been added to highlight the impact of r on these distributions of depth values.
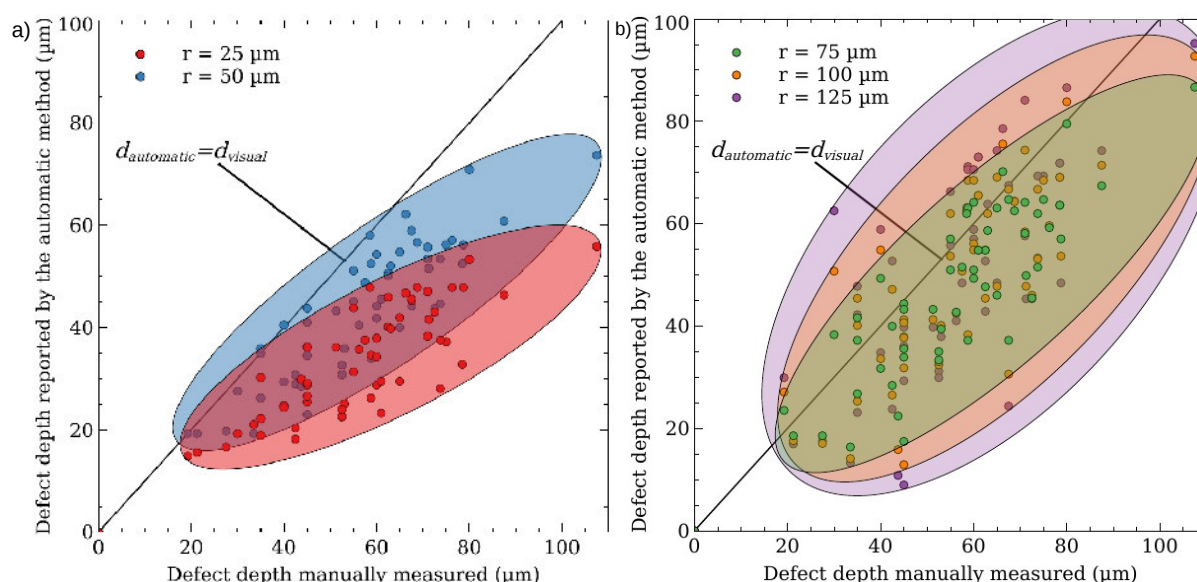
Figure 4.7: Comparison of the depths measurements. Maximum depth values of the detected defects measured by the critical defects identification method for $r = 25$ (red dots) and 50 μm (blue dots) (a) and for $r = 75$, 100 and 125 μm (b) (green, orange and purple dots respectively) as functions of the maximum depth values measured manually on the tomographic images. For each r value, the envelope containing all the defects distribution is represented by a colored ellipse. The egailty between both measurement methods ($d_{automatic} = d_{visual}$) is represented by a black line.

Two distinct subfamilies can be observed:

- one corresponding to $r \leq 50$ μm (Figure 4.7a) for which the defects depth is systematically underestimated by the automatic procedure (points below the black line where $d_{automatic} = d_{visual}$, i.e. both methods of measurement lead to identical results);

---

[3]because of the limited resolution of the images (voxel size $= 2.5$ μm)

- another one for $r \geq 50 \ \mu m$ where the ellipses appear closer to the black line (Figure 4.7b).

The systematic depth underestimation (Figure 4.7a) is explained schematically in Figure 4.8a. It can be seen that if a notch-like defect is located within the disc used for the blur function computation, it will produce a smooth local minimum on the smoothed surface profile and the defect depth will be underestimated. When r increases, this local minimum is reduced and the depth underestimation significantly decreases (see arrows in Figure 4.8a).

However, increasing r can also have a detrimental effect on the depth measurements. Figure 4.7b shows that, for large r values ($r = 100$ or $125 \ \mu m$), the depth values deviate from the black line ($d_{automatic} = d_{visual}$) meaning that large underestimations and overestimations of the defects depth can occur. The reasons for these errors are respectively illustrated in Figure 4.8b and 4.8c.

Defects with large underestimated depths are always close to another notch-like defect; a situation which is illustrated in Figure 4.8b. In this case, the large disc radius takes into account the neighboring defect and lowers too much the surface profile producing significant underestimations of the depth. For some defects, the beneficial impact observed when r is increased is therefore compensated by the detrimental impact of neighboring defects and an optimal value of r can be determined, see the defect on the left of Figure 4.8b. For others, the detrimental impact of the neighboring defect is too important and the lowest values of r give the best depth estimations, see the defect on the right of Figure 4.8b.

Regarding the depth overestimations, in all cases, a protrusion is located close to the defect and the same reasoning can be made: because of the protrusion, the surface profiles obtained for large r values appear higher than the real surface profile and lead to overestimations of the depth (Figure 4.8c).

To summarize, on the one hand, low r values lead to a systematic underestimation of the defects depth which increases when r decreases. On the other hand, large r values produce both large underestimations and overestimations of the depth of defects which are not isolated. Intermediate values of r such as $r = 50$ or $75 \ \mu m$ seem therefore to be a compromise between these two situations (Figure 4.7 and Figure 4.8). Although $r = 75 \ \mu m$ induces slighty smaller depth underestimations for isolated notch-like defects (Figure 4.8a), Figure 4.8b and 4.8c show that it can also lead to important erroneous estimations of the defect depths. Consequently, **$r = 50 \ \mu m$ has been chosen as the best fitting value of r for chemically etched samples.** Interestingly, this value corresponds to the layer thickness used to build the samples by EBM.

The last step is to determine the thresholding value TS to apply to the final surface map. This parameter controls the number of defects that are going to remain after thresholding. The fracture surfaces in Chapter 3 showed that, for all chemically etched 90° samples, the depth of the defect responsible for the sample failure always exceeds $50 \ \mu m$. It was therefore decided to choose $TS = 50 \ \mu m$. For the sample considered here, this leaves 22 defects on the resulting final surface map.
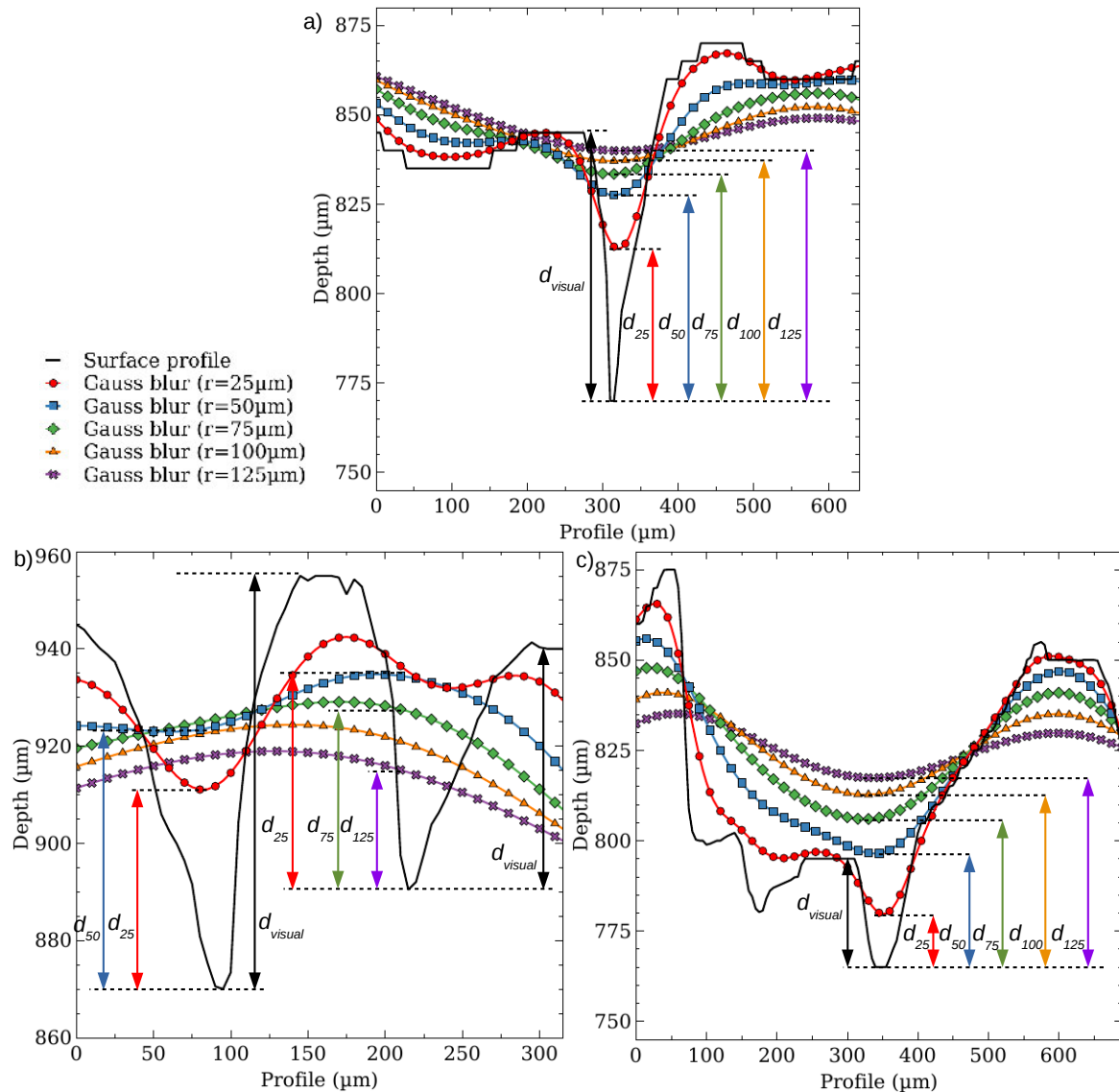
Figure 4.8: Illustration of the gaussian blur impact on the surface profiles of three notch-like defects: an isolated notch-like defect (a), two neighboring notch-like defects (b) and one close to a protrusion. The resulting profiles computed for differents r values (r=25, 50, 75, 100 and 125 μm) are represented by lines with respectively red dots, blue squares, green diamonds, orange triangles and purple crosses. The initial surface profiles are shown by black solid lines. Vertical arrows with different colors represent the visual and automatic depth measurements obtained for the different r values.

4.1.1.3 Validation of the process parameters

Using the method presented in Chapter 3, the defect responsible for the sample fatigue failure is identified and its coordinates on the tomographic images are determined. These coordinates are afterwards used to identify the critical defect on the final surface map. Figure 4.9 shows the final surface map before (Figure 4.9a) and after thresholding where

the 22 remaining defects (blue and yellow circles) can be observed (Figure 4.9b). The critical defect (red circle) can be found amongst these 22 remaining defects. Its shape in the tomographic image (Figure 4.9c) matches perfectly with the SEM observation of the fracture surface (Figure 4.9d). The corresponding maximum local depth on the final surface map is 56 μm which seems to indicate that the value chosen for TS (50 μm) is appropriate. The results obtained with both r and TS set to 50 μm are therefore considered satisfactory and this set of parameters will be applied later on to all chemically etched samples.
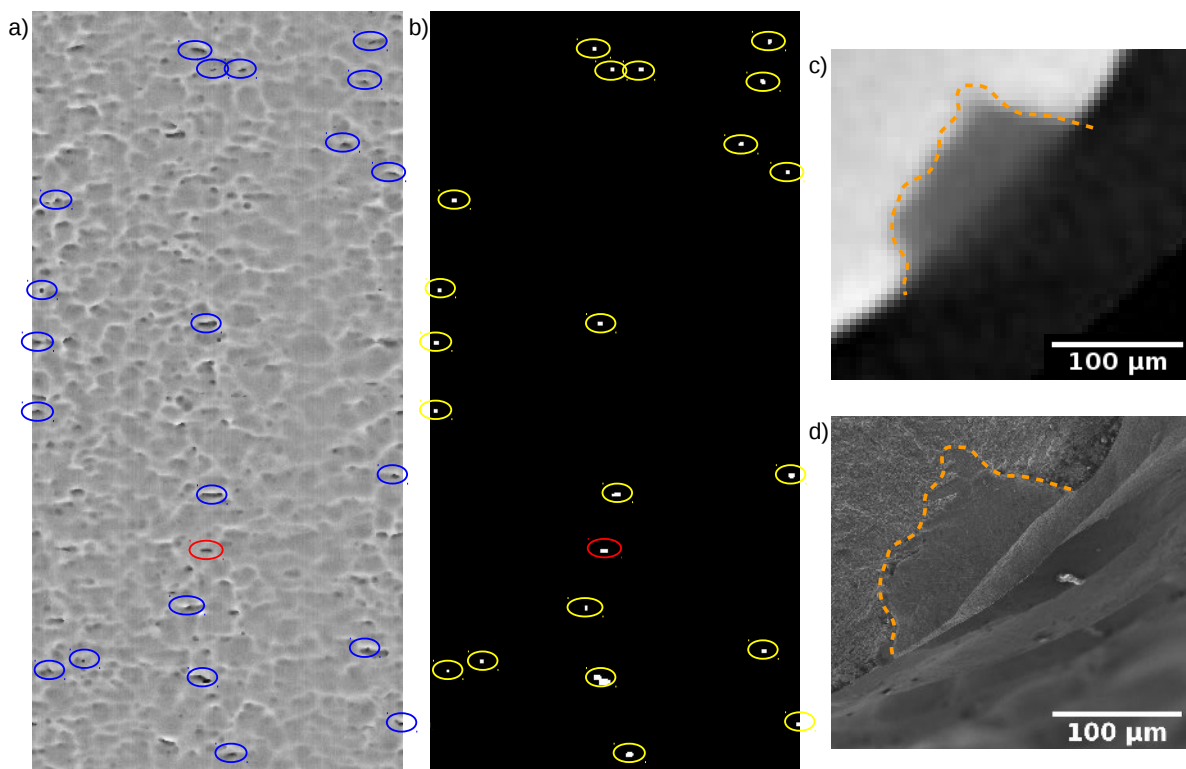
Figure 4.9: Detection of the defect responsible for the sample fatigue failure. Final surface map obtained for $r = 50$ μm before (a) and after depth thresholding (b) ($TS = 50$ μm). The remaining defects after thresholding are circled in blue in (a) and yellow in (b). The defect responsible for the failure is circled in red. Dilatation operations have applied to (b) so that the detected defects could be visualized more clearly. Axial tomographic image (c) and SEM fracture surface micrograph (d) of the defect responsible for the failure.

4.1.2   Measurement of the defects criticality

The method described in the previous section allows to identify the potentially harmful defects from the whole range of surface irregularities. In this work, it was decided to evaluate the criticality of these surface defects through the $\sqrt{area}$ parameter proposed by Murakami et al. [MUR 85]. The previous chapter showed that, based on fracture surface examinations, this parameter gives reliable results for analyzing the fatigue properties of EBM samples.

4.1.2.1 Measurement of the defects projected area

The $\sqrt{area}$ parameter of the thresholded defects can be measured on the tomographic images. As detailed in Chapter 3, local minimum and maximum projections of the tomographic images along the load axis respectively show the inner and outer limits of the defect projected area. When superimposed, the exact projected area of the defect is obtained. This process is illustrated in Figure 4.10: when performed on binarized images, the projected area appears in gray (Figure 4.10d) and its value (in μm^2) can be easily measured. To perform this method automatically imply further development that could not be carried out for time reasons. The measurements were therefore performed manually.
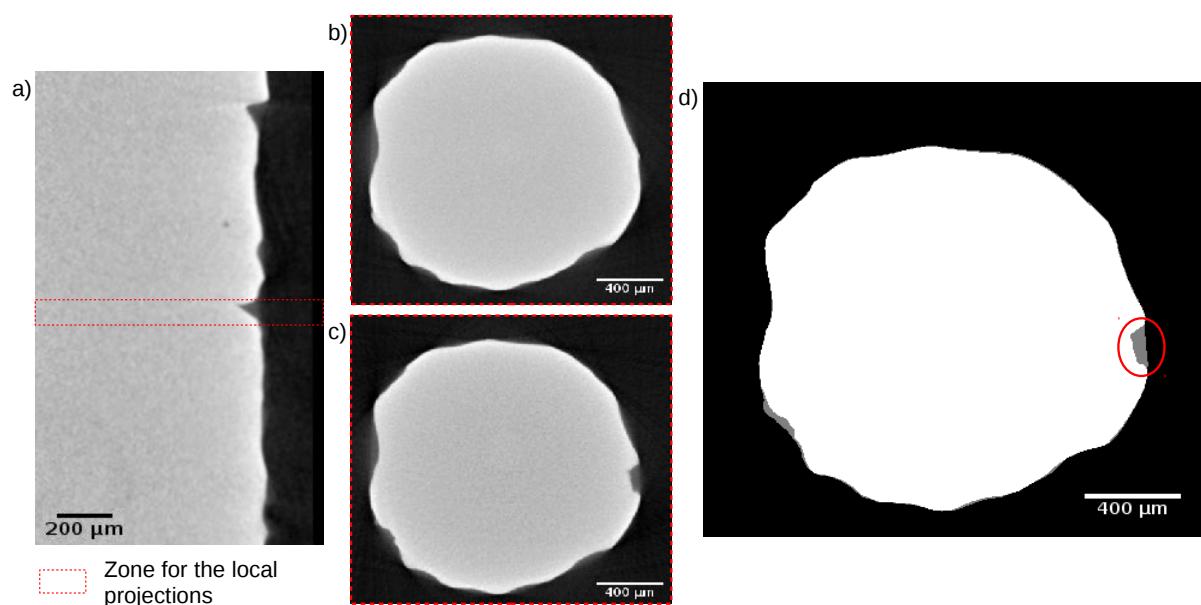
Figure 4.10: Illustration of the process used to measure the projected surface of the defect which has led to failure based on tomographic images. (a) Radial view of the defect which shows by dashed lines the limited zone used for the local projections. Maximum (b) and minimum (c) axial projection around the defect. (d) Average computation of both projections after their binarization. The projected area of the defect (circled in red) appears in gray.

This method can be applied to the thresholded defects which can be ranked according to their projected area.

4.1.2.2 Accuracy of the defects projected area measurements

The values of projected area measurements based on tomographic images have been compared with those obtained by SEM for the defects which have led to failure. Figure 4.11 shows for one critical defect the comparison of the projected areas obtained with the two techniques. When both projected areas are superimposed, it appears that the projected area obtained from the SEM micrograph is sligthly larger than the one obtained from the tomographic images (Figure 4.11e). The main difference comes from the root of the defect which is not detected by lab X-ray tomography (Figure 4.11d and 4.11f). The defect

root shown in Figure 4.11f is hardly visible on the tomographic images (see red arrow on Figure 4.11a). Therefore, the gray level variation is missed out by the thresholding operation (Figure 4.11b). This is due to the very sharp opening at the root of the defect. As shown on the defect radial view (Figure 4.10a), the root of the defect remains thin and sharp even after 45 minutes of chemical etching leading to an underestimation of the real projected area of the defect. However, even in such cases, the error made by using the tomographic images remains limited ($\sim 6\%$). **This indicates that the measurements based on tomographic images can be reasonably used to determine the defects criticality.**
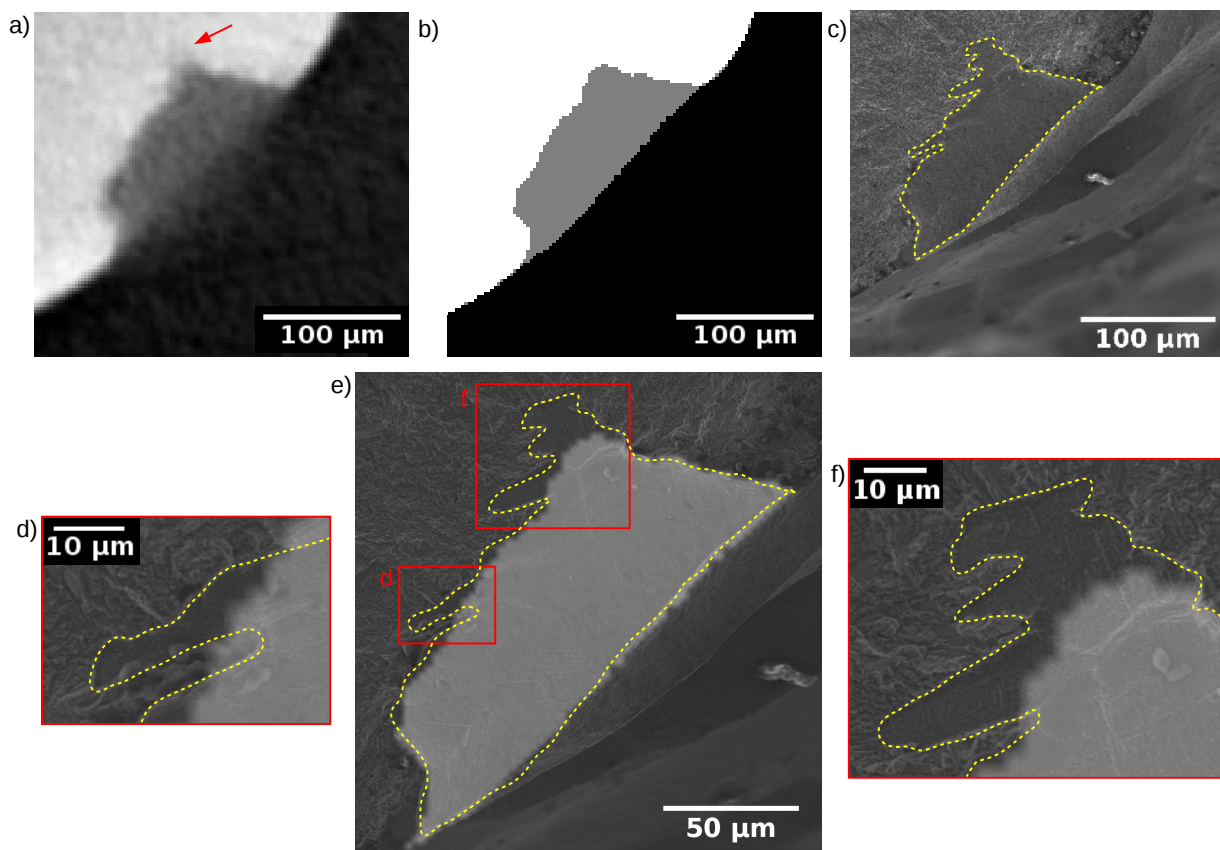
Figure 4.11: Comparison of the projected areas of the same critical defect measured by laboratory X-ray tomography and SEM-SE micrograph. (a) Minimum axial projection around the defect. (b) Average computation of the binarized minimum and maximum projections around the defect. (c) SEM micrograph of the defect on the fracture surface. (e) Overlap of the defect projected area obtained by X-ray tomography and SEM. (d, f) Higher magnification images of the overlap shown in (e). The dashed yellow line highlights the surface defect contour as detected by SEM.

4.1.2.3 *Kitagawa-Takahashi* diagram and fatigue prediction

For all remaining defects on the thresholded final surface map, the value of $\sqrt{area}$ has been estimated and they can be reported on a *Kitagawa-Takahashi* diagram. The fatigue lives of chemically etched 90° samples that broke during the tests range roughly between

100 000 and 400 000 cycles, meaning that most of them have fatigue lives shorter than the knee point of the Wöhler curve (Figure 3.15 in Chapter 3). Therefore, finite lives Kitagawa diagrams based on the two approaches presented and discussed in Chapter 3 could be used. However, because of the lack of fatigue results to determine with accuracy the knee point of the Wöhler curves of 45° and 0° chemically etched samples, the approach suggested by Beretta et al. cannot be used [BER 17]. Regarding the second one proposed by Ciavarella and Monno [CIA 06], the large overestimation of the fatigue lives of as-built 90° samples induced by the method makes it unreliable.

Consequently, it has been chosen to rely on the *classical* Kitagawa curves. The classical curve can be used as a predictive limit: as long as all the points corresponding to the detected defects remain under the propagation curve, it can be considered that the sample will not break and as soon as a defect stands over the curve, then, the sample will fail. The corresponding Kitagawa diagram for all chemically etched 90° samples shown in Figure 4.13 will be presented and discussed in the following section.

4.2 Application of the method to chemically 90° etched samples

4.2.1 *Kitagawa-Takahashi* diagrams and efficiency of the method

The method used to automatically identify critical defects has been applied to all the 90° samples which sustained 30 or 45 minutes of chemical etching prior to fatigue tests whether they were HIP treated or not. The same value of r (50 μm) has been used for all chemically etched samples. Regarding *TS*, in a first approach, the 50 μm value used for the example was applied to all chemically etched samples. The corresponding results are summarized in Table 4.1. **For all broken chemically etched samples,** regardless of the etching time, **the method is able to detect the defect leading to the sample failure** as its depth $d_{crit\ def}$ always meet the $d_{crit\ def} \geq TS$ requirement.

Table 4.1: Results from the application of the critical defects identification method on 90° samples chemically etched for 30 and 45 minutes: number of detected defects per sample after thresholding of the final surface map and depth of the defect responsible for the failure. The minimum, average and maximum values are reported.

Etching duration	TS (μm)	Number of defects			Critical defect depth (μm)		
		Min	Average	Max	Min	Average	Max
30 minutes	50	16	33	64	61	68	76
	60	7	14	34			
45 minutes	50	4	12	22	51	61	73

For samples chemically etched for 45 minutes, only a limited number of thresholded defects is obtained. For example, Figure 4.12 shows the projected areas of all detected defects within a given sample.

However, for samples chemically etched for 30 minutes, the population of thresholded defects are 3 to 4 times larger (Table 4.1). Measuring the projected area for such a large
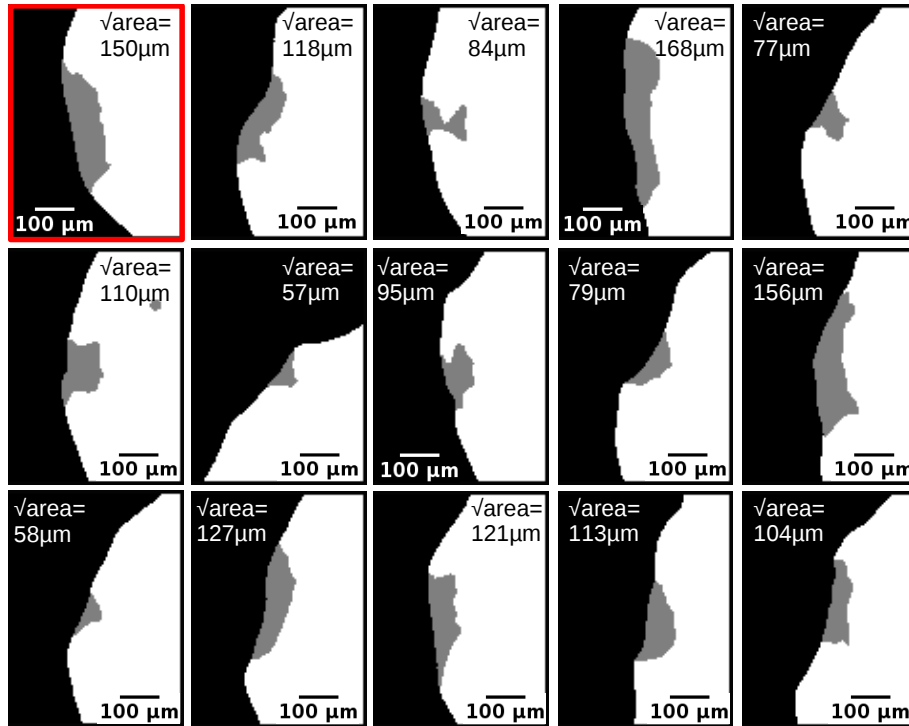
Figure 4.12: llustrations of the projected areas obtained for all detected defects within a 90° sample chemically etched for 45 minutes. The corresponding values of $\sqrt{area}$ are indicated. The defect leading to failure is framed in red.

population of defects is a time consuming process as this step is performed manually. A larger value for TS ($TS = 60 \ \mu m$) significantly reduces the population while keeping the number of defects similar to that of the 45 minutes samples and still detecting the critical defect. This value is used in what follows. The defect projected areas have been manually determined on all chemically etched samples and reported on *Kitagawa-Takahashi* diagrams as shown in Figure 4.13. For the sake of clarity, two diagrams have been plotted in order to differentiate unbroken samples (fatigue lives longer than 3.10^6 cycles) (Figure 4.13a) from the ones that failed (Figure 4.13b).

For all samples in Figure 4.13a, all the thresholded defects remain under the corresponding propagation curve, meaning that none of these defects is supposed to provoke crack growth and lead to the sample failure. As none of these samples failed during the experimental fatigue tests, their fatigue performance is well predicted by the *Kitagawa-Takahashi* diagram.

Regarding the samples that failed during fatigue tests, it appears that for 11 chemically etched samples (out of 13 failed samples), the critical defect (red dots in Figure 4.13b) is located above the propagation curve meaning that the sample failure is correctly predicted. This means that overall, **out of the 19 chemically etched 90° samples considered, the fatigue behaviour of 17 samples is correctly determined by the classical *Kitagawa-Takahashi* diagrams.**

Interestingly, the data of Figure 4.13b shows that out of the 13 broken samples, there
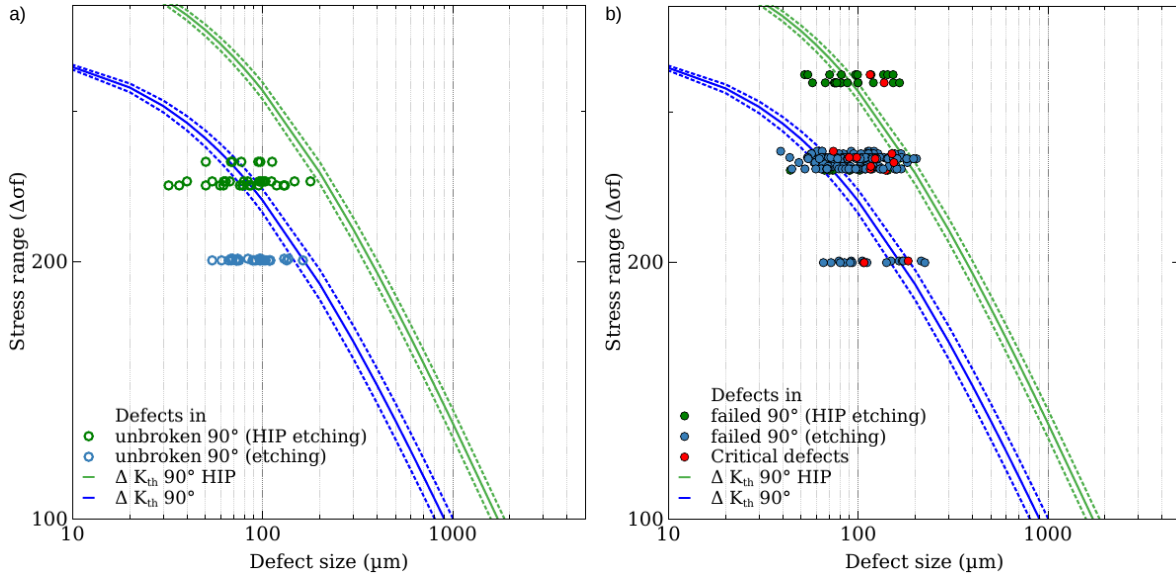
Figure 4.13: *Kitagawa-Takahashi* diagrams of chemically etched 90° samples. The green and blue colors correspond respectively to samples that did and did not undergo a HIP treatment. The continuous lines were plotted using the average ΔK_{th} value from the literature while minimum and maximum values were considered for the dashed lines. The empty dots (a) and filled ones (b) correspond to all remaining defects detected on the thresholded final surface maps of respectively unbroken and failed samples. The red dots represent the critical defects in the failed samples. The defects size was measured on tomographic images. The defects within HIP treated (respectively untreated) samples must be compared with the propagation curves obtained for HIP treated and machined (respectively machined) samples.

is only one sample whose failure is caused by the defect with the largest projected area. This is more clearly illustrated in Figure 4.14 where the detected defects in each broken sample are ranked based on their $\sqrt{area}$ values. The $\sqrt{area}$ parameter is therefore not sufficient to automatically capture the defect that will cause the sample failure. In the following section, the defects leading to failure are going to be compared with the other detected defects to understand why the failure occured from these defects.

4.2.2 Defects criticality and samples failure

4.2.2.1 Impact of the defect shape

The shape of the critical defects has been investigated for all broken samples and compared to the shape of larger defects. An example of such a comparison is shown in Figure 4.15: the defects are shown in both as-built and chemically etched conditions. The axial views showing the projected areas of the two defects (Figure 4.15a and 4.15d) clearly illustrate the size difference between the two defects.

After chemical etching, the root of the defect with the largest value of $\sqrt{area}$ has a relatively large radius of curvature (Figure 4.15b) whereas the root of the critical defect has remained sharp (Figure 4.15a): $\rho_{curv_{largest}} \gg \rho_{curv_{crit}}$ where ρ is the radius of curvature
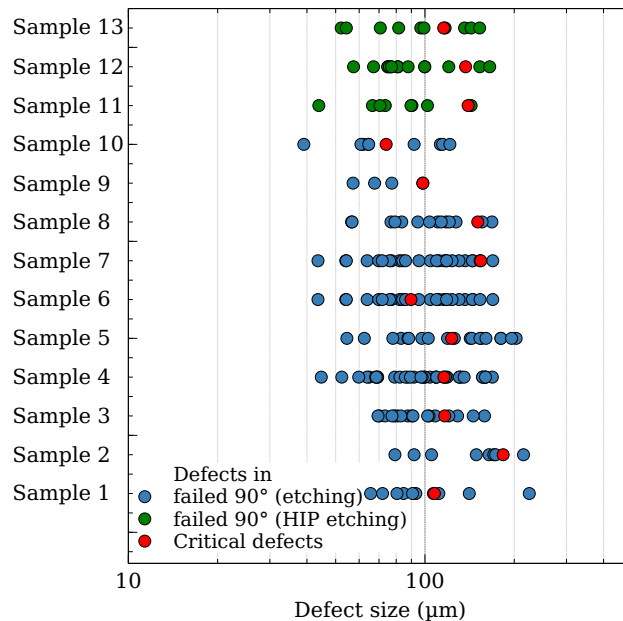
Figure 4.14: Rankings of the detected defects in chemically etched 90° samples based on the $\sqrt{area}$ values. The green and blue dots correspond to the defects detected in samples that respectively did and did not undergo a HIP treatment. The red dots represent the defects leading to failure. The defects size was measured on tomographic images.
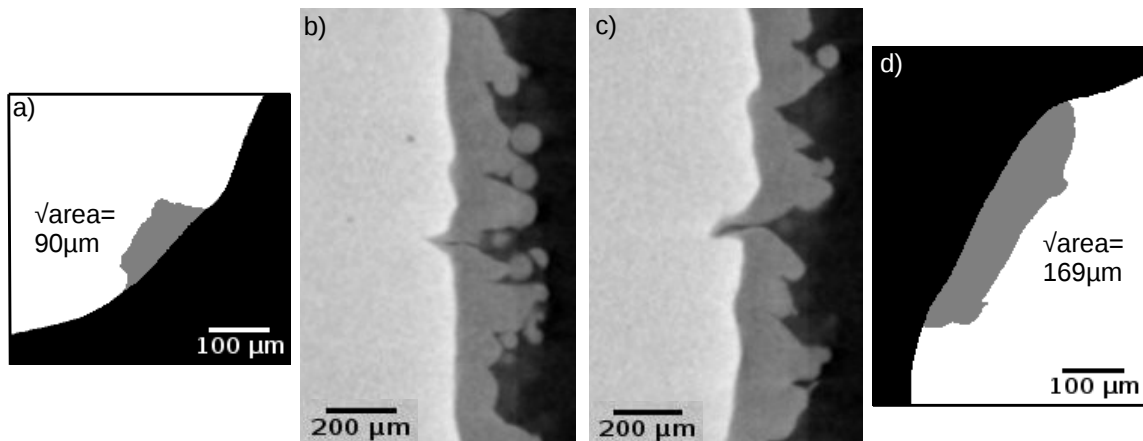
Figure 4.15: Shape comparison of the critical defect (a, b) with the defect with the largest projected area (c, d) for a sample chemically etched for 45 minutes (failure after $\sim 185\,000$ cycles at $\sigma_{max} = 295$ MPa). (a, d) Average computation of the minimum and maximum local projections showing the projected area of the defects in gray. The corresponding values of $\sqrt{area}$ are indicated. (b, c) Radial views of both defects before (dark gray) and after chemical etching (light gray).

estimated at the root of the defect. As $K_t \propto \sqrt{a/\rho}$ (with a being the defect depth), for similar values of a, the critical defect leads to a larger K_t. Consequently, the critical defect is more likely to provoke crack initiation and this might explain why this defect led to failure.

A sharp root was observed for all defects leading to the failure of chemically etched samples (three examples are shown in Figure 4.16). This means that, **the criticality of a defect is affected by both the size of its projected area and the radius of curvature at its root.** Both should therefore be considered. Of course, if the defect with the largest $\sqrt{area}$ value also has a sharp root, it will lead to failure (this is the case for the defect shown in Figure 4.16c).
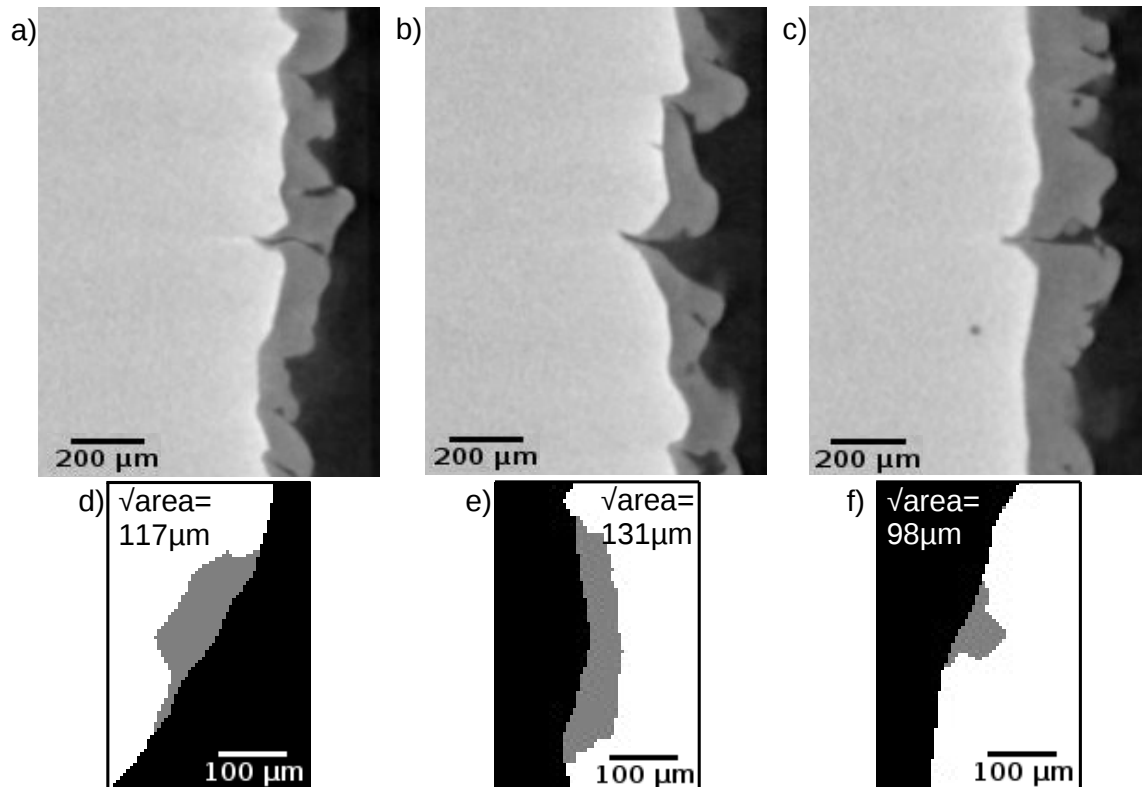
Figure 4.16: Examples of critical defects roots before (dark gray) and after chemical etching (light gray). Overlap of as-built and chemically etched radial views of the defects responsible for the failure of samples chemically etched for 30 (a, b) and 45 minutes (c). (d, e, f) Projected areas of the defects respectively shown in (a, b and c). The corresponding values of $\sqrt{area}$ are indicated.

4.2.2.2 Sharpness of the critical defects: as-built state and chemical etching efficiency

Prior to chemical etching, all detected defects are notch-like defects and have a large $\sqrt{area}$ value and a sharp root (Figure 4.15). They have rather similar shapes, the thickness of the largest defect being only slightly more important. However, after chemical etching, this discrepancy dramatically increases. The thickness at the root of the critical defect (Figure 4.15a) remains almost unchanged whereas the one of the largest defect increases significantly, turning a notch-like defect into one with a larger ρ (Figure 4.15b). This means that the efficiency of the chemical dissolution is not identical for all notch-like defects.

This heterogeneity might be caused by the geometrical shape of the as-built notch-like defects. The slightly more important thickness of the largest defect leads to an increase of the local density of etchant $\rho_{etchant}$. As shown by Lhuissier et al. [LHU 16], this directly impacts the efficiency of the chemical dissolution and may thus explain its heterogeneity.

Therefore, **the sharpness of the defects after chemical etching is logically linked to their shape in the as-built state but also to the local efficiency of chemical etching.** For defects with a limited thickness and an important depth, the chemical reagent can barely reach their root and the efficiency of the chemical etching process decreases drastically. This suggests that the potentially harmful defects in the as-built state may not remain as such after chemical etching.

4.2.3 Failed prediction of the fatigue performance: further analysis

A detailed analysis of the two samples whose fatigue failure was not correctly predicted by the *Kitagawa-Takahashi* diagram has been performed. These samples will be referred to as "failed sample 1" and "failed sample 2".

"Failed sample 1" was HIP treated and then chemically etched for 45 minutes while "failed sample 2" was only chemically etched for 30 minutes. Both samples were cycled at a low stress level and their long fatigue lives ($\sim$ 570 000 cycles at σ_{max} = 285 MPa and $\sim$ 390 000 cycles at σ_{max} = 222 MPa for respectively "failed sample 1" and "failed sample 2") both exceed the knee point of the corresponding Wöhler curve.

Figure 4.17 shows a *Kitagawa-Takahashi* diagram with only the detected defects from the samples cycled at these low stress levels. For the sake of clarity, a magnification of this diagram depicting only "failed sample 1" and "failed sample 2" is also presented (Figure 4.17b).

4.2.3.1 "Failed sample 1": unexpected failure

In the case of "failed sample 1", Figure 4.17b shows that the defect responsible for its failure is the second largest detected defect within the gauge length with a projected area similar to the one of the largest defect ($\sqrt{area}$ = 140 and 143 μm respectively). As shown for the test sample, these tomographic based measurements can slightly underestimate the projected area. Here, the measurement of the projected area based on the SEM micrographs of the fracture surface (Figure 4.19) indicates that the $\sqrt{area}$ of the critical defect is slightly understimated (5%) when measured on tomographic images. Consequently, it can be considered that both defects have the same projected area.

In addition, the radial tomographic image of the critical defect shows that, after chemical etching, this defect is still extremely thin and has a very sharp root (Figure 4.18b). The comparison of the tomographic images before and after chemical etching shows that the defect root remains the same after chemical etching meaning that it has hardly been impacted by the chemical etching process (Figure 4.18a and 4.18b). Both size and shape of the defect can therefore explain why this defect is the one leading to failure but not why its criticality is understimated.
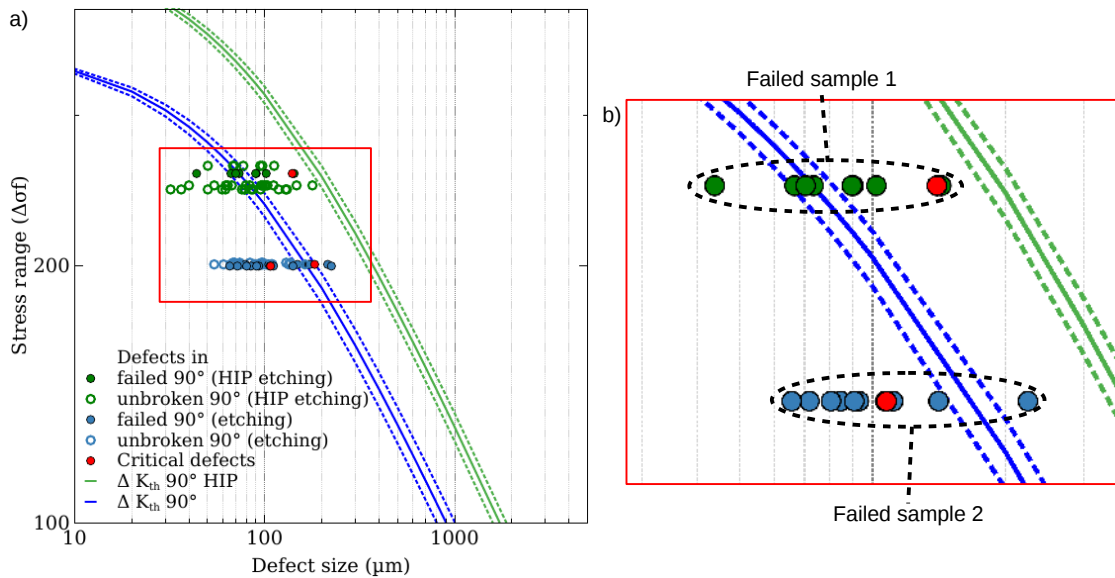
Figure 4.17: *Kitagawa-Takahashi* diagrams of all chemically etched 90° samples cycled at low stress levels. The green and blue colors correspond respectively to samples that did and did not undergo a HIP treatment. The continuous lines were plotted using the average ΔK_{th} value from the literature while minimum and maximum values were considered for the dashed lines. The empty dots and filled ones correspond to all remaining defects detected on the thresholded final surface maps of respectively unbroken and failed samples. The red dots represent the critical defects in the failed samples. The defects size was measured on tomographic images. (a) Diagram for all the samples solicited at low stress levels. (b) Detailed view of the diagram only for the two samples whose failure is not predicted.
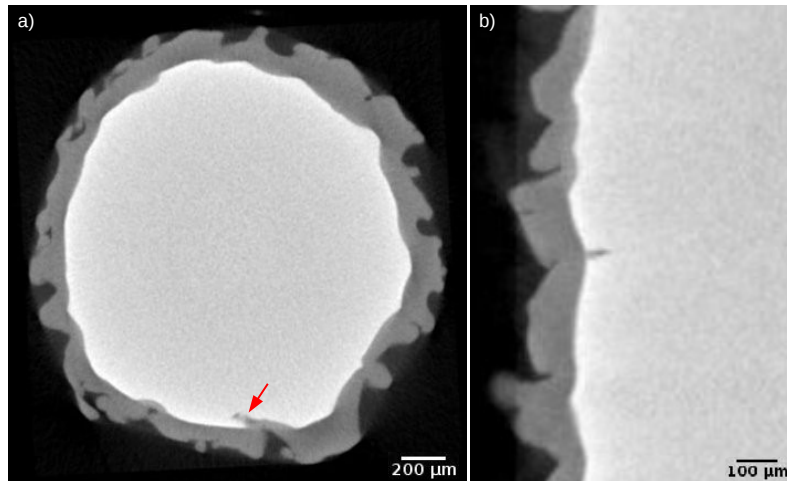
Figure 4.18: Overlay of as-built (dark gray) and chemically etched (light gray) axial (a) and radial (b) views of the defect leading to the unpredicted fatigue failure of "failed sample 1". The defect is pointed out by a red arrow.

A detailed analysis of the critical defect was performed. Figure 4.19b shows a magnification of the fracture surface around it. The impact of the chemical etching process is

visible at the sample surface with "lath pattern" visible on the entire surface. This is the sample microstructure (α laths) that is revealed by the chemical etching reagent. This secondary effect of the chemical etching can be used to determine the areas affected by the post-treatment. No lath can be observed at the root of the critical defect meaning that the chemical etching reagent did not reach this area (red dashed line on Figure 4.19b). **The root of the critical defect remained as in the as-built condition. This may be the reason for the underestimation of the defect criticality and the premature failure of the sample.**
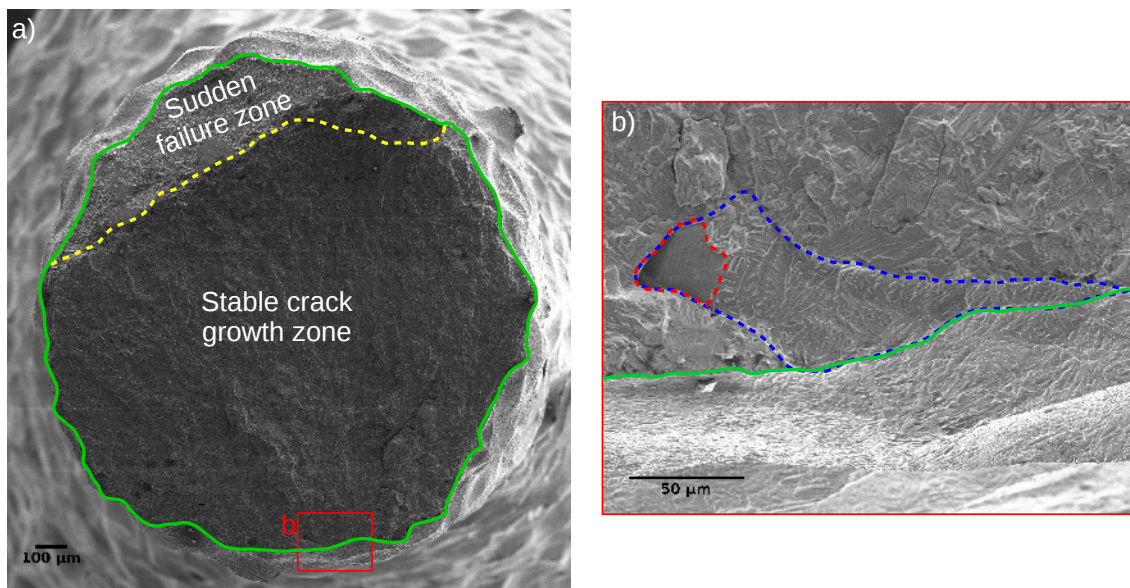
Figure 4.19: SEM-SE micrographs of the fracture surface of "failed sample 1". The HIP treated and chemically etched sample sustained $\sim$ 570 000 cycles at σ_{max} = 285 MPa before failure. (a) Fracture surface showing the stable crack growth and sudden failure zones separated by a yellow dashed line. (b) Higher magnification image showing the crack inititiation site. The green continuous line highlights the edges of the fracture surface. The pattern visible on the surface is created by the topography of the α laths. It can be observed where the chemical reagent has affected the surface. The critical defect and its zone unaffected by the chemical etching process are respectively delineated by blue and red dashed lines.

Another point to raise is that the curves from the *Kitagawa-Takahashi* diagram are plotted based on data from the literature. The validity of these curves is thus not confirmed and their exact position in the diagrams remains uncertain. It is therefore possible that the distance between the critical defect and the propagation curve is not as important as it appears in Figure 4.17.

4.2.3.2 "Failed sample 2": unexpected final crack initiation site

First, the *Kitagawa-Takahashi* diagram (Figure 4.17b) shows that, potentially, a crack could grow from the largest defect within "failed sample 2". The tomographic images of the largest defect after fatigue failure does show a small crack initiating from the tip of the defect (red arrow in Figure 4.20) despite the rather limited spatial resolution ($\sim$ 4 μm).

Higher resolution tomographic images are needed but this seems to confirm the results of the *Kitagawa-Takahashi* diagram.
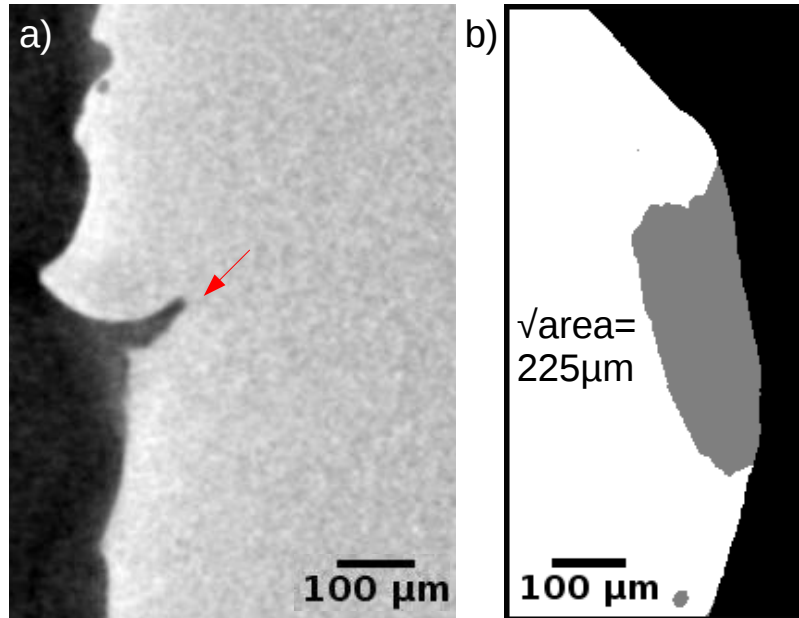
Figure 4.20: Tomographic images of the defect with the largest projected area in "failed sample 2". (a) Radial view of the defect after failure. The red arrow points out the crack that grew from this defect. (b) Average computation of the minimum and maximum local projections showing the projected area of the defect in gray. The corresponding value of $\sqrt{area}$ is indicated.

Second, the defect responsible for the failure of "failed sample 2" is similar to the defects which have led to sample failure in the correctly predicted samples: a relatively sharp defect with its root slightly affected by the chemical etching process. No sound explanation could therefore be found to explain why the failure of this particular sample was not predicted.

4.3 Application to the remaining build orientations

The critical defects identification method has been applied to both other build orientations, namely 0° and 45° samples with a chemically etched surface, whether they were HIP treated or not. The same value of r (50 μm) used for chemically etched 90° samples is used for both build orientations. Figure 4.21 compares the final surface maps obtained before the thresholding step for the three different build orientations.

The influence of the build orientation on the surface geometry can be distinguished on these maps. For example, the vertical gray line in the middle of the 0° sample surface map represents the smooth upper surface of the corresponding sample (Figure 4.21a) whereas the white spots in Figure 4.21a and 4.21b correspond to surface protrusions that have not been erased by the chemical etching process. This analysis can be further developed and this will be addressed later in this chapter (Section 4.4.1).

Chemically etched 0°   Chemically etched 45°   Chemically etched 90°
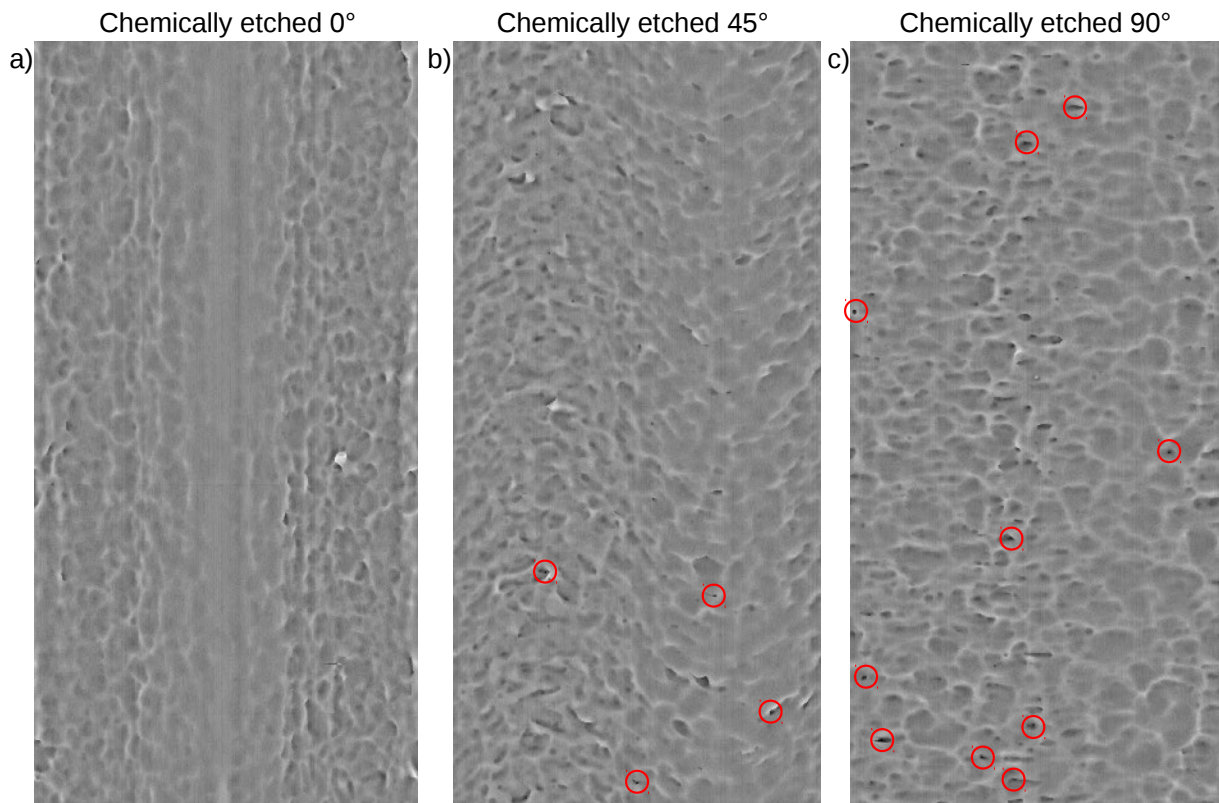
Figure 4.21: Examples of final surface maps obtained by the critical defects identification method for chemically etched 0° (a), 45° (b) and 90° samples (c). The remaining defects after thresholding ($TS = 50\ \mu m$ for the three maps) are circled in red.

Qualitatively, it can be seen in Figure 4.21 that, when the build orientation changes from 0° to 45° and then to 90°, the number of black spots which represent the thin surface valleys of the sample increases. If the same *TS* value (50 μm) is used for all three build orientations, the number of thresholded defects (circled in red in Figure 4.21) also increases. No defect remains for the 0° sample (Figure 4.21a) whereas 4 and 10 defects remains respectively for the 45° and 90° samples (Figure 4.21b and 4.21c respectively). This impact of the build orientation can be extended to all chemically etched samples as shown in Table 4.2.

For all the 45° samples analyzed, the number of remaining defects after thresholding is extremely limited (5 defects at most) whereas, out of the 4 chemically etched 0° samples analyzed, there is only one sample for which the final surface map presents remaining defects after thresholding. This impact of the build orientation is also reflected in the depth values of the deepest defect in each sample (Table 4.2). For instance, for a threshold value $TS = 40\ \mu m$, no defect can be detected on the final surface map of a 0° sample.

The impact of the build orientation on the depth and number of thresholded defects is therefore in good agreement with its impact on the surface defects and roughness reported in chapter 1. This also **correlates well with the fatigue properties of these samples** which, as shown in chapter 3, increases when the number of defects decreases.

Table 4.2: Results from the application of the critical defects identification method on 0°, 45° and 90° samples chemically etched for 45 minutes: number of detected defects per sample after thresholding of the final surface map and depth of the deepest defect on the surface map. The minimum, average and maximum values are reported.

Samples orientation	TS (μm)	Number of defects			Deeper defect depth (μm)		
		Min	Average	Max	Min	Average	Max
0°	50	0	1	4	39	50	73
	30	4	10	15			
45°	50	1	2	5	52	62	82
	40	2	5	10			
90°	50	4	12	23	65	82	109

This is a substantial improvement over the roughness measurements as none of the three measurements performed in this study (R_a, R_t and R_v) were found to describe accurately the impact of the build orientation over the fatigue properties.

4.3.1 Detection of the defect responsible for the failure

The analysis performed on chemically etched 90° samples has shown that, in most cases, the defect responsible for the failure is not the deepest nor the largest defect ($\sqrt{area}$). With the limited population of thresholded defects obtained for $TS = 50$ μm (Table 4.2), it is therefore highly unlikely for the method to always detect the critical defect in 45° and 0° samples. Consequently, it has been decided to lower the threshold value. Several TS (50, 40 and 30 μm) values have been considered. Smaller values of TS were not considered because harmless defects such as smooth surface variations would be thresholded which would reduce the method efficiency. Two conditions have been used to determine the most suitable value for TS:

- if possible, the critical defect must be detected for all broken samples.
- the number of thresholded defects must remain limited so that a manual analysis of those defects is feasible.

Regarding the 45° samples, six samples (three of them were HIP treated beforehand) which underwent 45 minutes of chemical etching were fatigue tested and five of them failed. For both $TS = 40$ and 30 μm, the defect responsible for the failure has been detected for three out of the five samples. $TS = 40$ μm is therefore the most suitable value for TS. Regarding the 0° samples, TS must be lowered down to $TS = 30$ μm in order to detect defects on all surface maps (Table 4.2). The number of thresholded defects with these new values of TS are presented in Table 4.2. The detection of the critical defects on both build orientations will now be addressed separately.

4.3.1.1 45° samples analysis

The method appears to be less efficient for 45° samples than for 90° samples as the critical defect is not detected for two samples over the five samples examined. A thorough analysis

of those two samples will be performed. These samples will be refered to as "45° failed sample 1" and "45° failed sample 2".

"45° failed sample 1": failure at the edge of the gauge length

The location of the failure within the sample is illustrated in Figure 4.22 which shows the variations of the cross-section along the sample gauge length. The area on which the automatic procedure was applied to obtain the surface map is delineated by a blue dashed line (it ranges from 0 to 10 mm on the x-axis). The failure zone (red hatched zone centered around x $\sim$ -0.5mm) is localised outside of it, at the upper edge of the gauge length. This explains why the critical defect was not detected by the automatic procedure. It is worth noting that, in both as-built and chemically etched conditions, the cross-section at the height of the failure is very close to the minimum cross-section of the entire sample.
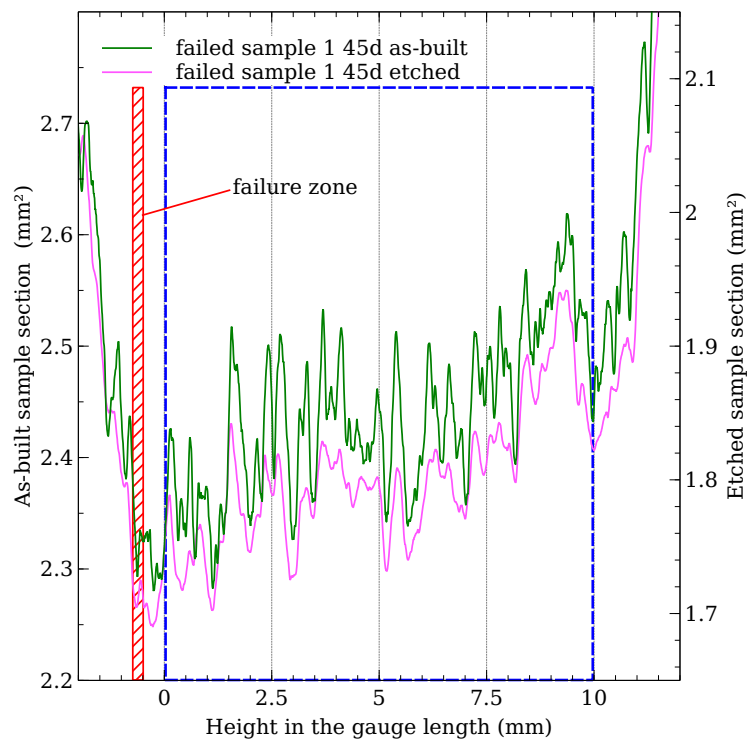
Figure 4.22: Cross section variations along the gauge length of "45° failed sample 1" in as-built (green curve) and chemically etched conditions (pink curve). The red hatched region represents the height at which the failure occured. The area observed on the first surface map is delineated by the blue dashed rectangle.

A new surface map obtained on a larger gauge length is shown in Figure 4.23. The red circles highlight the remaining defects after thresholding ($TS = 40\ \mu m$). Five additional defects are detected on this new surface map amongst which the defect responsible for the failure can be found. It is therefore correctly detected by the method.

"45° failed sample 2": defect orientation and limit of the critical defect identification method
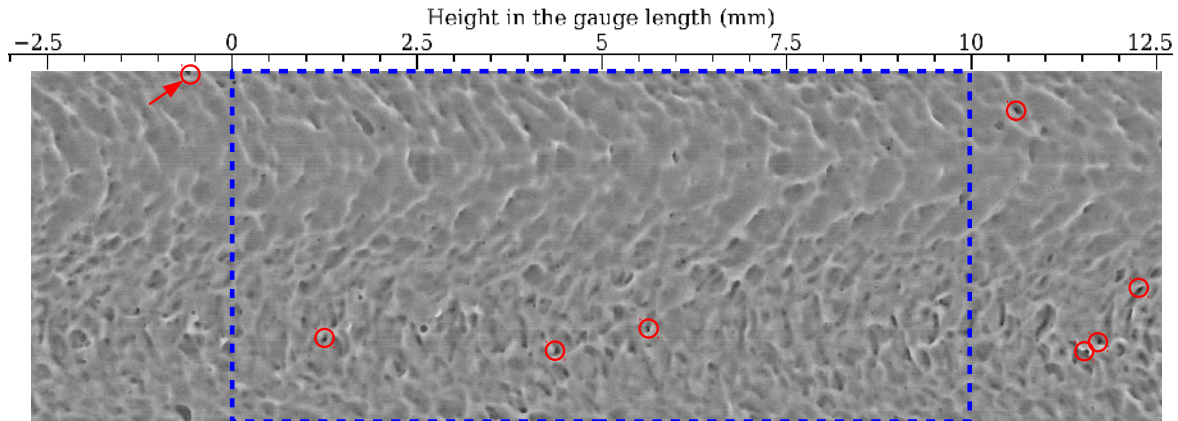
Figure 4.23: Final surface map obtained for "45° failed sample 1" after the application of the critical defects identification method on the entire area scanned by lab X-ray tomography. The part of the surface map corresponding to the gauge area is delineated by the blue dashed line. The remaining defects after thresholding ($TS = 40\ \mu m$) are circled in red and the defect responsible for the failure is pointed out by a red arrow.

In the case of "45° failed sample 2", failure does occur within the gauge length and the corresponding area can be observed on the sample surface map (Figure 4.24). Even though 8 defects (circled in red in Figure 4.24a) remain after the thresholding step ($TS = 40\ \mu m$), the defect responsible for the sample failure (pointed out by a red arrow in Figure 4.24b) is not one of them. It can still be detected in the final surface map and a depth measurement indicates that its maximum depth reported by the method is roughly $\sim 25\ \mu m$ which is *way below* the *TS* value. This means that, for this particular sample, the critical defect would be considered as harmless by our method.

If the threshold value were to be reduced so that the critical defect could be part of the thresholded defects, 64 defects would remain meaning that roughly 60 defects are deeper than the critical one. As mentioned earlier, the projected area measurements become extremely time consuming for such large populations of defects and the method looses its interest as well as its efficiency.

The morphology of the critical defect was analyzed in order to determine why this apparently harmless defect is responsible for the sample failure. Figure 4.25 shows the axial and radial local projected views of the defect. The defect is extremely thin and its main axis is tilted at 45° with respect to the loading axis which impacts the defect depth measurement.

As explained in Section 4.1.1, the measurements of the defects depth are performed on lines *perpendicular* to the load axis as illustrated in Figure 4.26. Because of its orientation, only a small part of the defect will be detected for each horizontal line. This leads to a severe underestimation of the defect depth: the real defect depth measured directly from tomographic images is $\sim 80\ \mu m$ which far exceeds the $\sim 25\ \mu m$ depth obtained with the automatic detection method. This underestimation far exceeds the ones typically reported for other defects, see Section 4.1.2 and was, in fact, only observed for this defect as, after chemical etching, no other thin and tilted defect remains at the surface of any 45° samples.
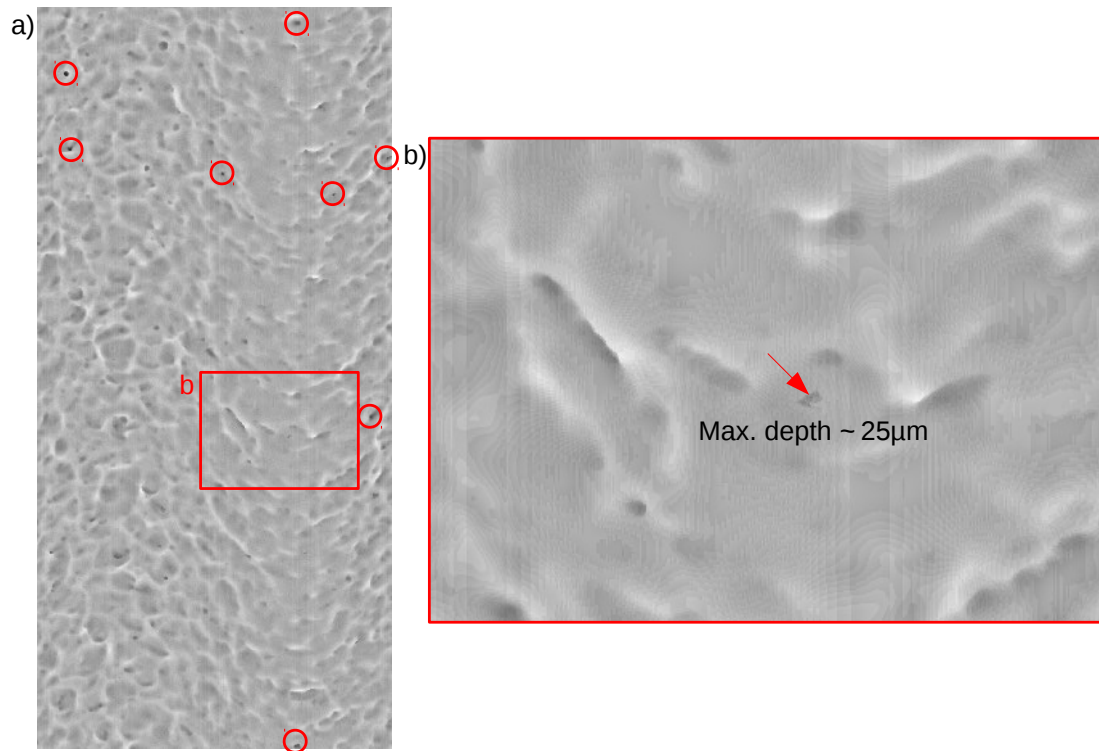
Figure 4.24: Final surface map obtained by the critical defects identification method for "45°" failed sample 2". (a) Map of the entire gauge length. The remaining defects after thresholding ($TS = 40\ \mu m$) are circled in red. (b) Map magnification around the defect responsible for the fatigue failure which is pointed out by a red arrow. Its maximum depth is measured and exhibits a value of roughly $\sim 25\ \mu m$.

Furthermore, this defect was initially an internal defect which was linked to the surface by the chemical etching process. The comparison of the tomographic images before and after chemical etching have already been shown in Figure 3.20e-h in Chapter 3. For a better reading, the detailed views around the defect have been reported in Figure 4.25c and 4.25d. These tomographic images show that the chemical etching duration was long enough for the surface to reach the edge of the defect but not long enough to alter the shape of the defect. Its shape is identical in both as-built and chemically etched conditions. This is the reason why this thin and tilted shape remains even after 45 minutes of chemical etching. Besides, this also explains why this is the only defect for which the depth is largely underestimated by the method. 45 minutes of chemical etching are sufficient to remove or at least significantly change the surface defects with a similar as-built geometry and all the few other internal defects that have been turned into surface ones are round gas pores.

When brought at the surface by chemical etching, the depth of sub-surface lack-of-fusion defects is therefore largely underestimated by the method. Even though they are very few in number, all these defects should thus be identified beforehand on the as-built tomographic images. Otherwise, the fatigue performance of chemically etched 45° samples may be overestimated.
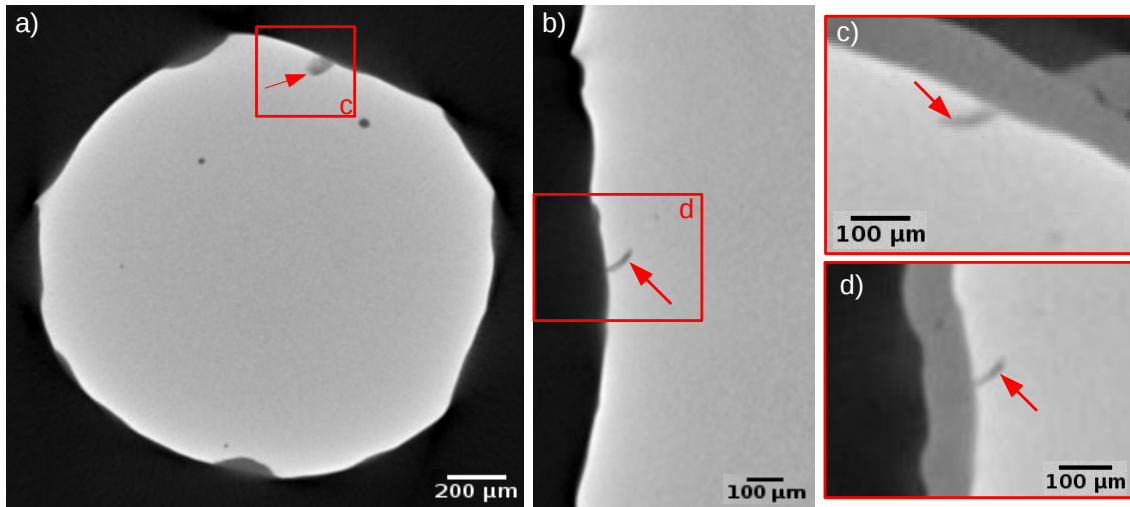
Figure 4.25: Axial (a) and radial (b) local projected views around the defect leading to the fatigue failure of "45° failed sample 2". Axial (c) and radial (d) detailed views of the defect in as-built (dark gray) and chemically etched conditions (light gray).
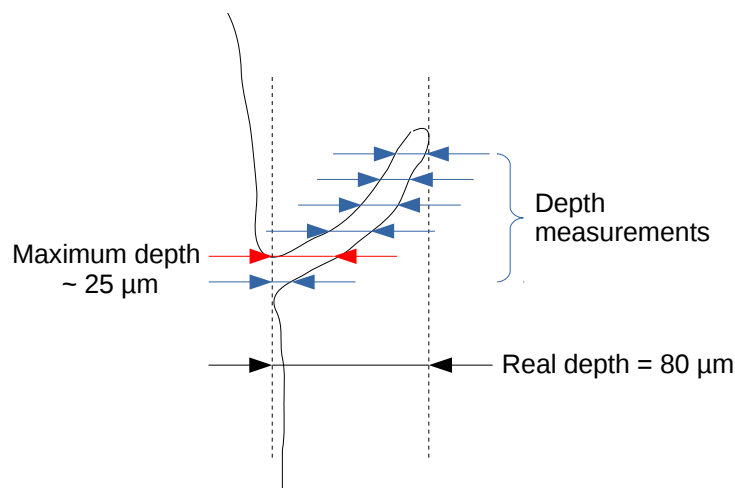
Figure 4.26: Schematic illustration of the depth measurement applied to a tilted defect. The blue, red and black arrows show respectively the depth measurements on horizontal lines, the maximum depth obtained for the defect by the automatic measurements and the real depth of the defect.

4.3.1.2   0° samples analysis

The number of chemically etched 0° samples which were submitted to fatigue tests is more limited: only 3 samples were tested and 2 of them failed. For one sample, failure occured in the gauge length and the defect responsible for the sample failure is detected on the final surface map and remains after thresholding ($TS = 30~\mu m$). For the other sample, failure occured outside the gauge length and even outside the area scanned by tomography. Consequently, the critical defect cannot be observed by tomography and only

SEM micrographs can be used to assess the defect projected area. However, its thickness, depth and the shape of its root cannot be measured. Nevertheless, the method has been applied to the sample gauge length and the defects remaining on the corresponding final surface map have been considered to characterise the sample fatigue resistance.

4.3.2   Prediction of the samples fatigue resistance: 45° and 0° samples

4.3.2.1   Classical *Kitagawa-Takahashi* diagrams

The projected areas of the defects detected in all chemically etched 45° and 0° samples have been reported on classical *Kitagawa-Takahashi* diagrams, see respectively 4.27a and 4.27b.
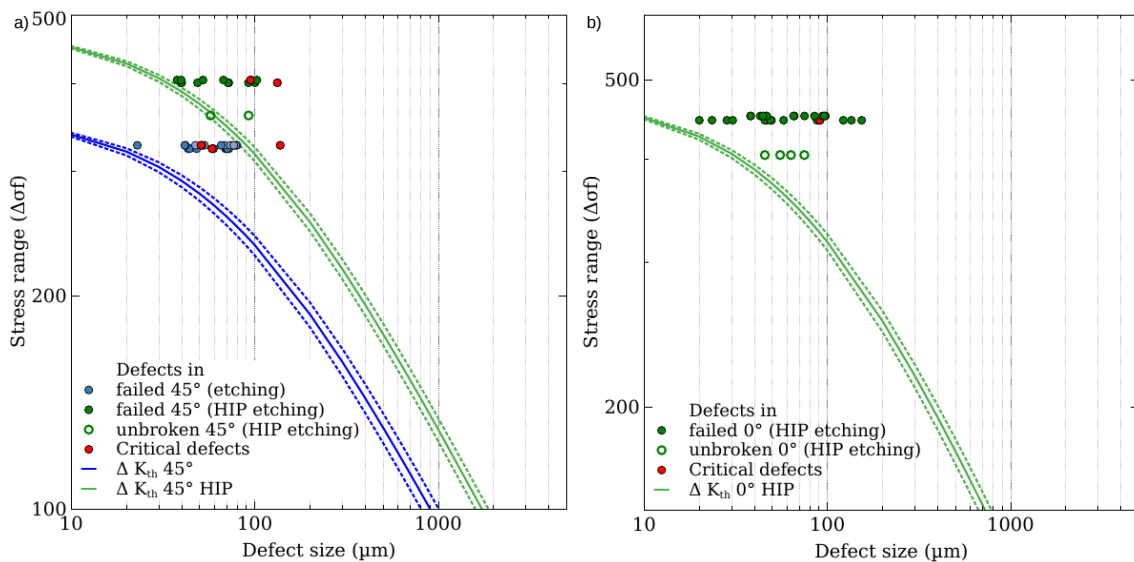
Figure 4.27: *Kitagawa-Takahashi* diagrams of chemically etched 45° (a) and 0° (b) samples. The green and blue colors correspond respectively to samples that did and did not undergo a HIP treatment. The continuous lines were plotted using the average ΔK_{th} value from the literature while minimum and maximum values were considered for the dashed lines. The empty and filled dots (b) correspond to all remaining defects detected on the thresholded final surface maps of respectively unbroken and failed samples. The red dots represent the critical defects in the failed samples. The defects size was measured on tomographic images.

Figure 4.27 shows contrasted results for broken and unbroken samples. **For all 45° and 0° samples, it appears that the failure of the broken samples is correctly predicted by the *Kitagawa-Takahashi* diagram** as the critical defects always stand above the corresponding propagation curves.

However, the fatigue resistance of the unbroken samples is not correctly predicted. Only one sample for each build orientation did not fail during the fatigue tests so the data available are very limited. Nevertheless, in both cases, one or several thresholded defects stand above the propagation curve. This is emphasized for the unbroken 0° sample as all four detected defects should have provoked the sample failure. **Although conservative,**

the fatigue resistance of unbroken samples is therefore largely underestimated in this case.

4.3.2.2 Unbroken samples: underestimation of the fatigue resistance

In order to determine the reason for this underestimation, the defects which should have led to failure according to the *Kitagawa-Takahashi* diagrams have been examined in details. Figure 4.28 shows the radial views of these defects (only three out of the four defects in the 0° sample are shown to limit redundant images). The defect in the 45° sample (Figure 4.28a) does not appear to be less critical than other defects excepted for its rather large depth-over-thickness ratio. However, its projected area may have been overestimated because of the protuberance above the defect which might explain why the sample fatigue resistance was underestimated.

The other three defects which have been detected in the 0° sample illustrate one of the limits of the critical defects identification method. As mentioned previously, for low TS values, smooth surface variations can be thresholded and be misleadingly considered as harmful defects. The thresholded defects in Figure 4.28c and 4.28d show that this is indeed the case for 0° samples when $TS = 30~\mu m$. In this case, the projected area overestimates the criticality. Hence, it is counterproductive to decrease the threshold value to such low values as several detected defects turn out to be smooth surface variations. Higher TS values such as $TS = 40~\mu m$ could be more efficient (critical defects still thresholded) with the drawback of having no thresholded defects for samples such as the one considered here. This means that **the method starts to lose its efficiency when applied to samples whose surface state is free of thin defects and consists only of smooth surface variations**, i.e. samples which look like machined samples.
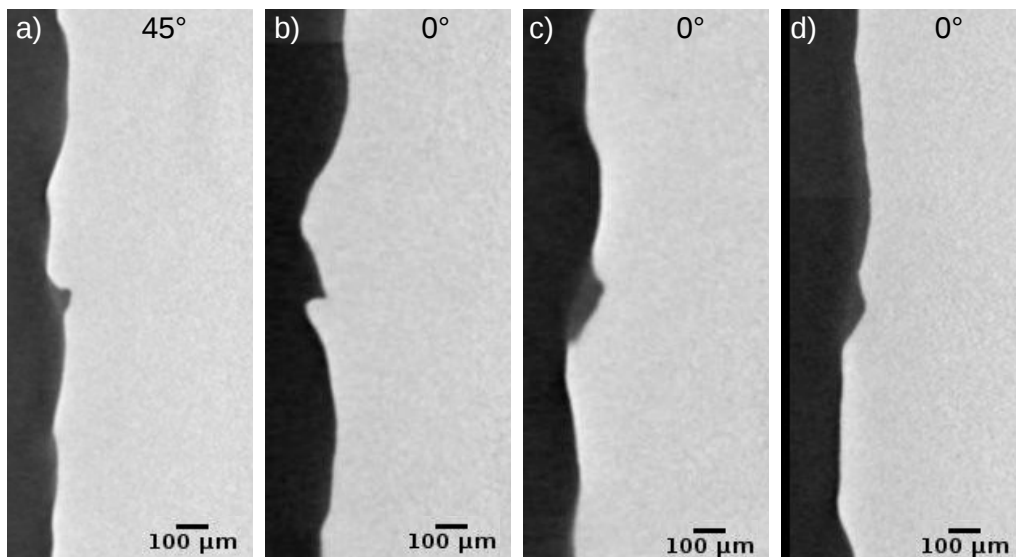
Figure 4.28: Radial views around the largest defects detected in the chemically etched 45° (a) and 0° (b, c and d) samples which did not break during fatigue tests.

4.3.2.3 Broken samples: projected area measurements and defects shape

For each 45° and 0° broken sample, the detected defects were ranked based on their $\sqrt{area}$ values, see Figure 4.29.
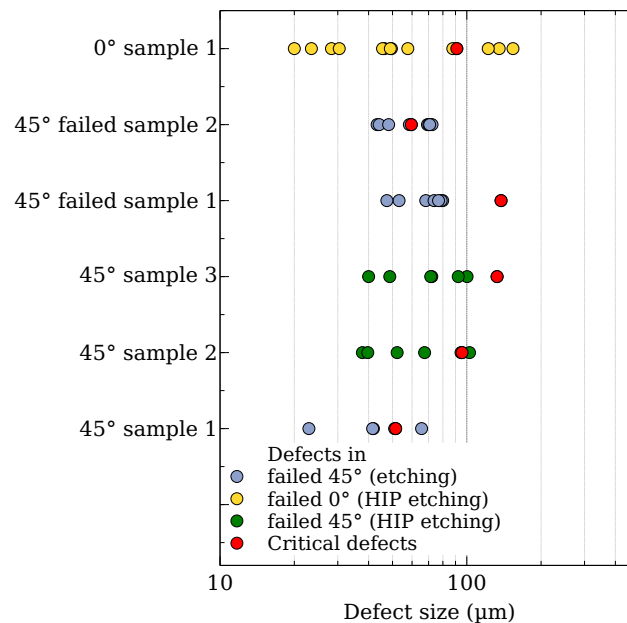
Figure 4.29: Rankings of the detected defects in chemically etched 45° and 0° samples based on the $\sqrt{area}$ values. The dots correspond to the defects detected in samples that did (green and yellow dots for 45° and 0° samples respectively) or did not undergo a HIP treatment (blue dots). The red dots represent the defects leading to failure. The defects size was measured on tomographic images.

For all 45° samples except "failed sample 2", the critical defect is always amongst the two largest thresholded defects (Figure 4.29). For "failed sample 2", the critical defect is ranked lower (5th) because it is a different type of defect (sub-surface *lack-of-fusion* defect that turned into a surface defect) as explained above.

Overall, **the predictions for 45° samples are better than those of 90° samples (Figure 4.14), probably because of the better as-built surface state.** Indeed, after 45 minutes of chemical etching, all the notch-like defects within 45° samples have been smoothed and the radius of curvature at their root increased (see Chapter 1). This means that the projected area can accurately determine the criticality of all remaining defects which is not the case for 90° samples.

Regarding the 0° sample, the critical defect is amongst the defects with the largest projected areas but ranks lower that the ones of 45° samples (Figure 4.29). The final surface map of this sample shows that the critical defect (red arrow) as well as all the largest defects are located on the downward facing surface of the sample (Figure 4.30).

The tomographic images before and after chemical etching have already been shown in Figure 3.25 in Chapter 3. For a better reading, the detailed views around the defect have been reported in Figure 4.30d and 4.30e. They show that the defect originates from
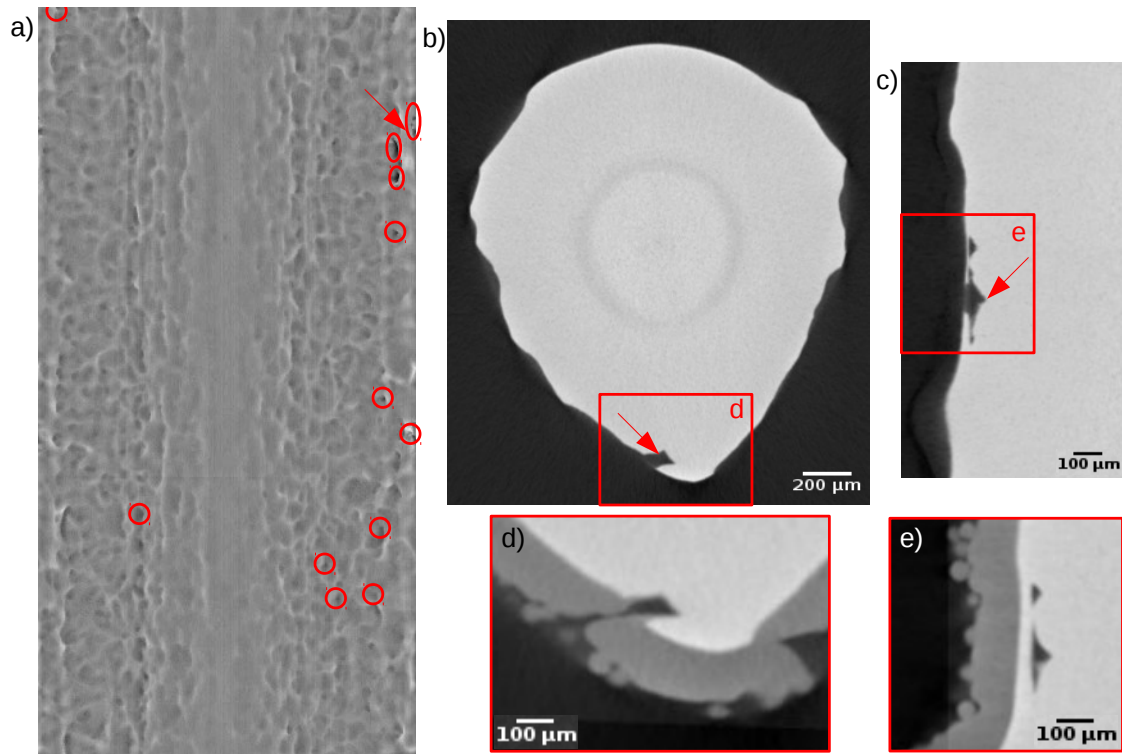
Figure 4.30: Identification of the defect responsible for the failure of a chemically etched 0° sample. (a) Final surface map obtained by the critical defects identification method. The remaining defects after thresholding ($TS = 30 \ \mu m$) are circled in red and the critical defect is pointed out by a red arrow. Axial (b) and radial (c) local projected views of the defect. The sharp root of the defect is pointed out by a red arrow. Axial (d) and radial (e) detailed views of the defect in as-built (dark gray) and chemically etched conditions (light gray).

stacking irregularities and is elongated along the z-axis. The same observations can be made for all the large defects ($\sqrt{area} > 75 \ \mu m$) detected within this sample. An horizontal sharp end that can be observed on the radial view of the critical defect shown in Figure 4.30c (red arrow) is not observed for the other large defects. This relatively sharp root perpendicular to the load axis can also be observed on the axial view (red arrow in Figure 4.30b). As explained for 90° samples (section 4.2.2.1), the radius of curvature at the root of defects appears to increase the criticality of the defects. As this is not taken into account by the $\sqrt{area}$ parameter, it can, in the present case, explain why the critical defect is ranked rather low in terms of projected area.

4.3.2.4   Finite lives *Kitagawa-Takahashi* diagram

In the case of these two build orientations, it has been shown in Chapter 3 that, in spite on the limited number of samples tested, the finite lives diagrams were a relatively efficient way to determine the fatigue performance of as-built Ti-6Al-4V EBM made samples. As fatigue results are lacking to determine the knee point of the Wöhler curves, it was therefore decided to use the finite life approach proposed by Ciavarella and Monno [CIA 06] rather

than the one proposed by Beretta et al. [BER 17]. The resulting diagrams are presented in Figure 4.31a and 4.31b respectively for the 45° and 0° samples.
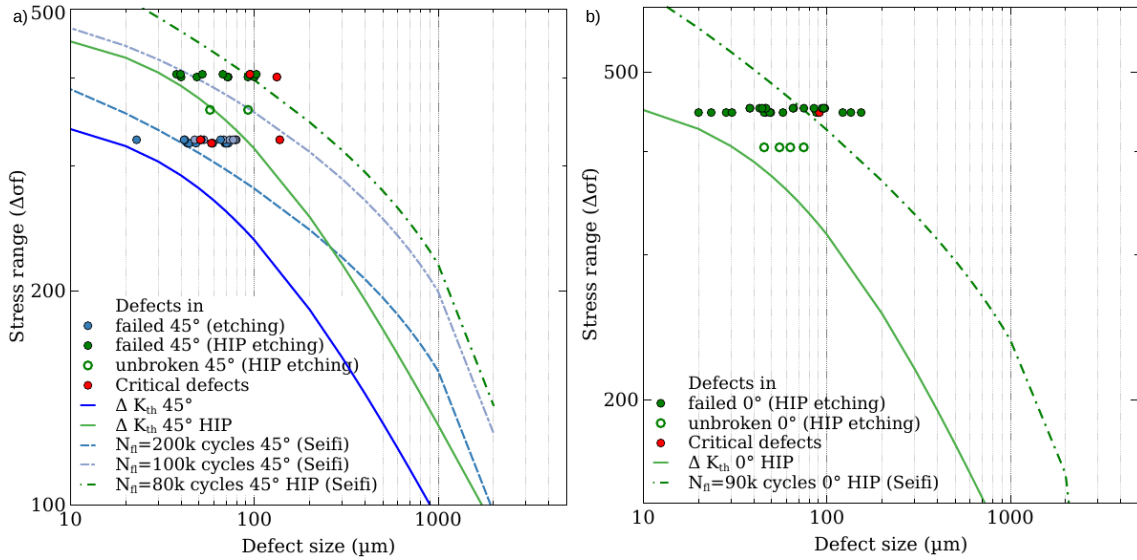
Figure 4.31: *Kitagawa-Takahashi* diagrams of chemically etched 45° (a) and 0° (b) samples. The green and blue colors correspond respectively to samples that did and did not undergo a HIP treatment. The continuous lines were plotted using the average ΔK_{th} value from the literature while the dotted curves were obtained following the Ciavarella and Monno approach [CIA 06]. Each dotted curve corresponds to a given number of cycles N_{fl} and relies on the stress amplitude corresponding to N_{fl} as well as a propagation law. The empty and filled dots (b) correspond to all remaining defects detected on the thresholded final surface maps of respectively unbroken and failed samples. The red dots represent the critical defects in the failed samples. The defects size was measured on tomographic images.

For every broken sample, the red dot representing the critical defect is found close to the dotted curve obtained for the number of cycles that the corresponding sample sustained before failure (Figure 4.31). **Finite lives diagrams are therefore able to correctly predict the fatigue lives of chemically etched 45° and 0° samples.**

To summarize, it has been shown that, regardless of the sample build orientation, the critical defects identification method is able to automatically detect the defect responsible for the failure of chemically etched samples. Furthermore, the $\sqrt{area}$ parameter, which is computed from X-ray tomography measurements is, overall, a good criterion to define the defects criticality and, once combined with *Kitagawa-Takahashi* diagrams, it can be used to predict with a relatively good accuracy the sample fatigue resistance.

Based on the defects distribution of one sample, this method could therefore be used to predict beforehand its fatigue limit. Indeed, thanks to the *Kitagawa-Takahashi* diagram, the stress range $\Delta\sigma_{crit}$ corresponding to the fatigue limit can be determined from the defects size distribution and, more precisely, from the largest defect size. If $\Delta\sigma < \Delta\sigma_{crit}$, with $\Delta\sigma$ being the stress range applied to the sample, no crack growth is supposed to occur and the sample fatigue life can exceed 10^7 cycles (Figure 4.13a). Otherwise, fatigue

failure is expected. However, in many cases, the defect leading to the sample failure is not the one with the largest projected area. Therefore, a conservative fatigue limit would be obtained from the *Kitagawa-Takahashi* diagram.

The method efficiency has therefore been proven for chemically etched samples which show an intermediate surface state between as-built and machined samples. It has also been shown that the method starts to loose its efficiency when applied to samples whose surface state is free of thin defects and consists only in smooth surface variations, i.e. samples which look like machined samples. However, the method efficiency on the other side of the surface state spectrum i.e. as-built samples has yet to be discussed.

4.4   Application of the method to as-built samples

4.4.1   Impact of build orientation

The critical defects identification method was applied to as-built samples fabricated in the three different orientations. In a first approach, the value of the Gaussian blur radius r which was found to be efficient for the defects detection in chemically etched samples ($r = 50 \ \mu m$) was kept for as-built samples. Examples of typical surface maps are shown in Figure 4.32.

The impact of the built orientation seen for chemically etched samples (Figure 4.21) can also be observed for as-built samples before (Figure 4.32) and after thresholding (Figure 4.33) with a few additional observations.

For instance, for 0° samples, the smooth upper surface and the lower surface characterized by large protrusions, which have been shown in Chapter 1, can be observed respectively at the center and on the sides of Figure 4.32a. The same surface map also shows the spatial distribution of stacking defects and notch-like defects (black areas in Figure 4.32a and white ones in Figure 4.33a). They can be found on the entire surface map except in the central part, i.e. the sample upper surface. For θ values between 90° and 135° and between 225° and 270° which correspond to upward facing parts (Figure 4.32d), all the dark areas are elongated in the Z direction and correspond to stacking irregularities. This geometry limits the criticality of those defects. In the downward facing part of the sample, the dark areas do not show a clear preferred orientation (some are elongated in the horizontal direction for example) but they appear darker. They correspond therefore to deeper defects than the defects detected on the rest of the final surface map which makes them potentially more harmful.

Regarding the 45° samples, wavy patterns can be observed on the final surface map (Figure 4.32b and Figure 4.33b). They depict the impact of the layer stacking on the upper and lower surfaces of the sample which are respectively centered around the angular positions 90° and 270°, see Figure 4.32e. These patterns are delimited by a series of white (protrusions) and thin black areas (notch-like defects). The spatial distributions of the latter ones indicate that most of the notch-like defects are located at the center and on the left and right sides of the surface map meaning that these defects are more likely to form on the sample side faces. They also appear to be mostly tilted at 45° with respect to the Z axis (Figure 4.33b).

Figure 4.32: Examples of final surface maps obtained by the critical defects identification method ($r=50\mu m$) for as-built 0° (a), 45° (b) and 90° samples (c). The correspondence between the positions in the surface map and in the sample are illustrated by the cross sections of 0°, 45° and 90° samples shown respectively in (d, e, f).

For the 90° samples, the black areas in Figure 4.32c and the corresponding white ones in Figure 4.33c can be seen between horizontal layers which confirms that they correspond to stacking irregularities and most likely notch-like defects. Although no upper nor lower surface exists in 90° samples, some heterogeneity can be observed in the spatial distributions of both black and white areas. In the central part of the surface map, darker and brighter areas can be observed meaning that larger protrusions and deeper stacking defects are detected (Figure 4.32c). They correspond respectively to powder particles stuck to the strut and to notch-like defects. The same observation can be made for the left and right edges of the final surface map. This signifies that a larger number of powder particles and notch-like defects can be found on both left and right surfaces (respectively centered around 0° and 180° in Figure 4.32f). The notch-like defects are also deeper in

As-built 0°   As-built 45°   As-built 90°

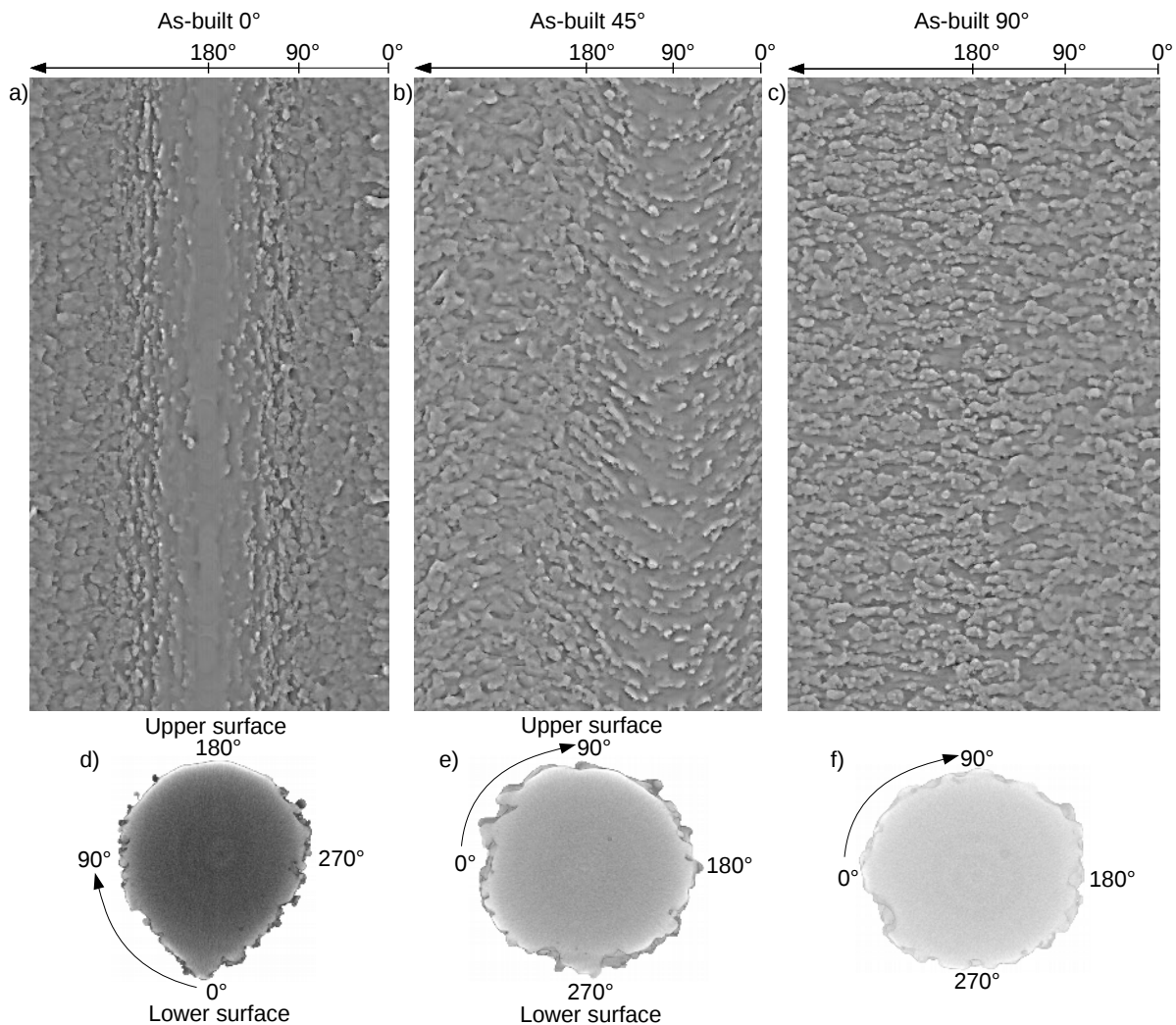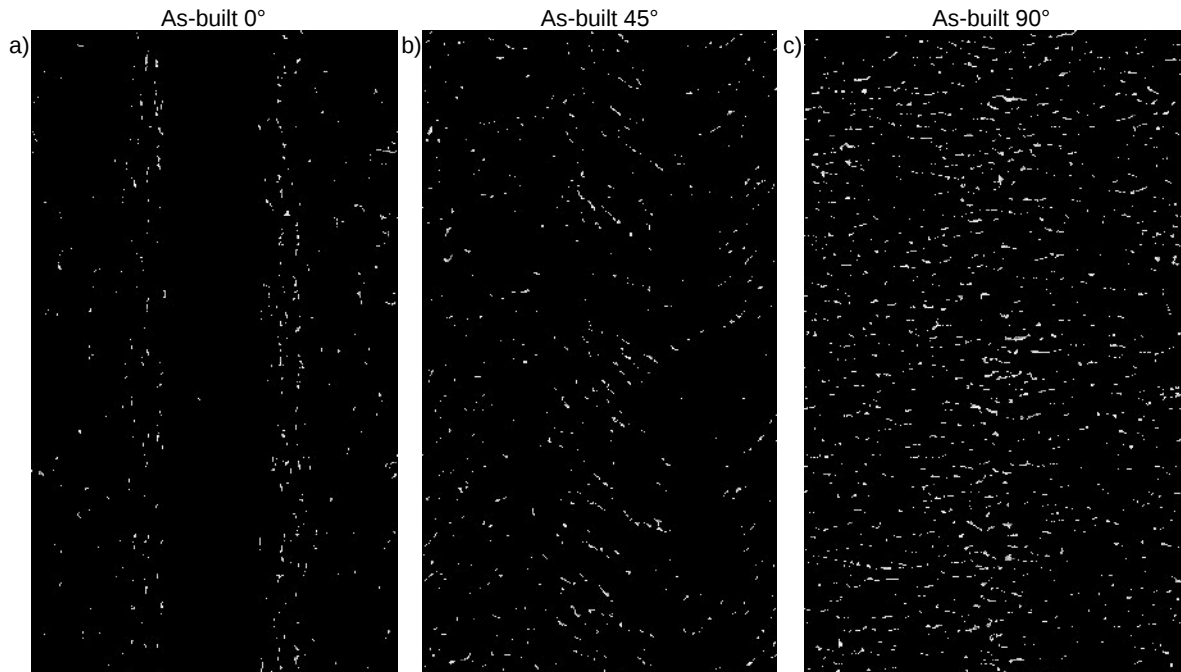**Figure 4.33:** Examples of thresholded final surface maps obtained by the critical defects identification method ($r = 50\ \mu m$) for as-built 0° (a), 45° (b) and 90° samples (c). The anisotropy of the detected defects can clearly be observed.

these areas. Such a spatial distribution was observed on all 90° samples and is most likely linked to the manufacturing process. It can be postulated than this phenomenon is linked to the rake impact on the powder deposition (and therefore the thermal gradient during manufacturing): the rake always move on the 0°-180° axis in Figure 4.32f. This link is yet to be confirmed.

Once thresholded, a clearer view of the defects spatial distributions is obtained **from these surface maps** which makes the comparison between the build orientations easier. For instance, **the impact of the build orientation on the surface defects orientation and density can be observed** (Figure 4.33).

4.4.2   Quantitative analysis

In every broken sample, the defect responsible for failure has been identified and the corresponding area on the final surface map examined to determine if the defect is detected by the method. For all samples, the defect responsible for fatigue failure is always detected as a local depth minimum on the final surface map. The depth values have been computed and the minimum, average and maximum depth values detected for the critical defects are reported in Table 4.3. They can be compared with the maximum depth values detected on the surface maps which confirm that, as in the case of chemically etched samples, the highest depth values are obtained for defects within 90° samples.

For the three build orientations, the measurements of the depth of the critical defects

Table 4.3: Results from the application of the critical defects identification method on all 0°, 45° and 90° samples fatigue tested in as-built conditions: depth and ranking of the defect leading to failure and depth of the deepest defect on the surface map. The minimum, average and maximum values are reported. For the ranking of the critical defect, for the three build orientations, the proportion of samples in which this defect is ranked amongst the 50 deepest defects is reported (in %) with respect to the overall number of samples analyzed.

Samples orientation	Crit. defect depth (μm)			Crit. defect amongst the 50 deepest defects	Deeper defect depth (μm)		
	Min	Average	Max		Min	Average	Max
0°	51	77	106	25%	116	147	177
45°	82	93	115	33%	122	131	137
90°	66	119	180	75%	147	169	188

show a large scatter. In addition, **the critical defect does not always rank amongst the deepest defects.** For instance, for 90° samples which show the best results, it sometimes does not belong to the 50 deepest defects (Table 4.3). This means that, if *TS* were to be lowered so that the critical defect could be thresholded, the number of thresholded defects would be important and the projected areas measurements extremely time consuming. The method would therefore loose its efficiency. Several reasons can be given to explain this lack of efficiency and they will be further discussed in the next section.

4.4.3 Limit of the method

As detailed in Chapter 1, in as-built samples, powder particles are stuck to the strut and, combined with stacking irregularities, they create a rough and geometrically complex surface which make the depth measurements much more difficult. For example, powder particles can be stuck within a notch-like defect (red arrows in Figure 4.34c). In that case, during the height measurement, those powder particles are considered as solid and, as a consequence, the defect depth is underestimated. The same drawback can be caused by not fully melted powder particles that obstructs the defect extremity (green arrows in Figure 4.34b and d).

Another origin of the underestimation of the defects depth is the orientation of their main axis with respect to the gauge length axis. This point has already been discussed for the chemically etched "45° failed sample 2" and it has been shown that, in this case, the defect depth is largely underestimated. However, while the number of such defects is extremely limited in chemically etched samples, this is a recurring phenomenon in as-built 45° samples where several occurrences of this kind of defect can be observed in only one radial view of a small part of the gauge length in one sample (blue arrows in Figure 4.34a).

Both aforementioned issues are overcome in the first minutes of the chemical etching process. Simulating the first stages of this dissolution could therefore enable to "eliminate" these artefacts from the as-built surface. To this end, the cellular automaton based model developed by Lhuissier et al. [LHU 16] could be used. When applied to such artificially "healed" surfaces, the critical identification method can be expected to better evaluate the
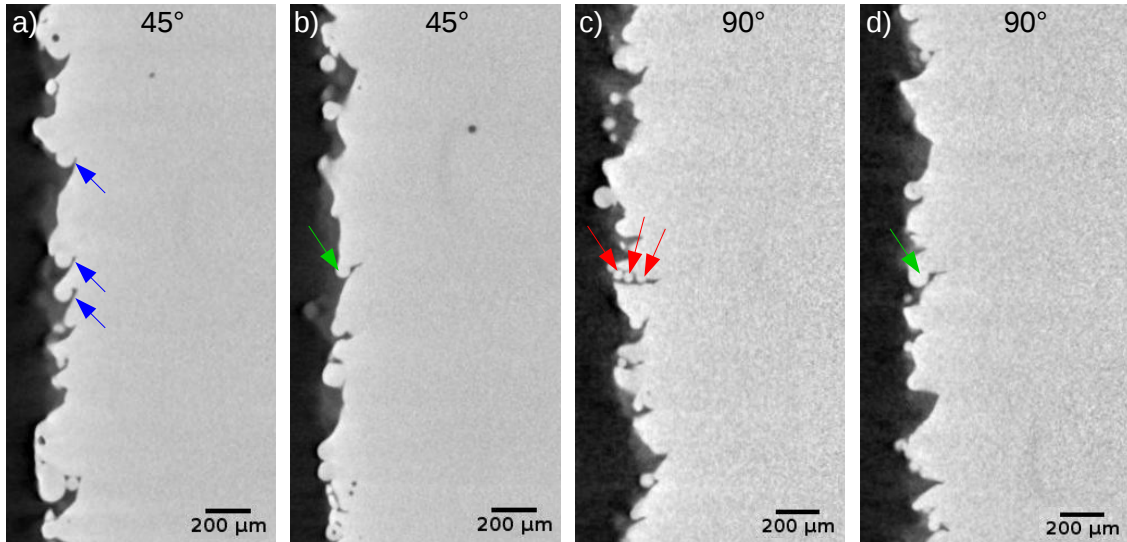
Figure 4.34: Radial views of surface defects detected in as-built 45° (a, b) and 90° (c, d) whose depth is underestimated by the critical defects identification method. The reasons for these underestimations are tilted defects (a) or powder particles not fully melted (b,d) or stuck in notch-like defects (c). They are respectively shown by blue, green and red arrows.

depth of the detected defects. For lack of time, this remains to be done.

4.5 Conclusion

Based on the fact that fatigue cracks always initiate from the sample surface for both as-built and post-treated samples, a method has been proposed and discussed to systematically and automatically extract the most critical surface defects and quantitatively analyze their influence on fatigue life. The results obtained can be summarized as follows:

- The proposed critical defects identification method relies only on X-ray laboratory tomographic images (voxel size = 2.5 μm).
    - The defects responsible for the failure of as-built and chemically etched samples are in a vast majority notch-like defects. They can be distinguished by their peculiar geometrical footprint: important and localized variations of height at the sample surface.
    - Through several image processing operations, final surface maps are obtained and their thresholding enables to differenciate all the notch-like defects on a sample surface from the rest of the surface irregularities.
    - Projected areas measurements of the detected defects are used to determine their criticality. They are then reported on a *Kitagawa-Takahashi* diagram from which the fatigue performance of the corresponding sample can be determined.
- The efficiency of this method has been first assessed with success on chemically etched samples (HIP treated or not).
    - For almost all broken samples, the defect responsible for the fatigue failure

remains on the thresholded final surface map meaning that it is correctly considered as one of the most harmful defects.

– Classical *Kitagawa-Takahashi* diagrams correctly predict the fatigue failure or the infinite fatigue lives ($> 3.10^6$ cycles) of most samples. For 45° and 0° samples, the finite lives diagrams based on the approach proposed by Ciavarella and Monno [CIA 06] are successful in predicting the fatigue lives of the samples.

– In most cases, the defect responsible for failure is not the defect with the largest projected area. This was attributed to the fact that defects with extremely sharp roots inherited from the as-built state and ones with less acute roots are not differentiated by the method. Additional investigations on the impact of the shape of the defect root and the microstructure in its vicinity would be required to correctly predict the defects criticality.

• The method was applied to as-built samples with a geometrically more complex surface.

– The final surface maps are useful to visualize the build orientation impact on the as-built surface and on the surface defects population.

– The as-built surface condition reduces the efficiency of the method. Additional image post-processing operations are needed to overcome this issue.

4.6   Graphical summary

Automatic detection of the harmful notch-like defects

Local height variations

Projected area measurements

Fatigue prediction

Prediction of the sample fatigue resistance

Determination of their criticality
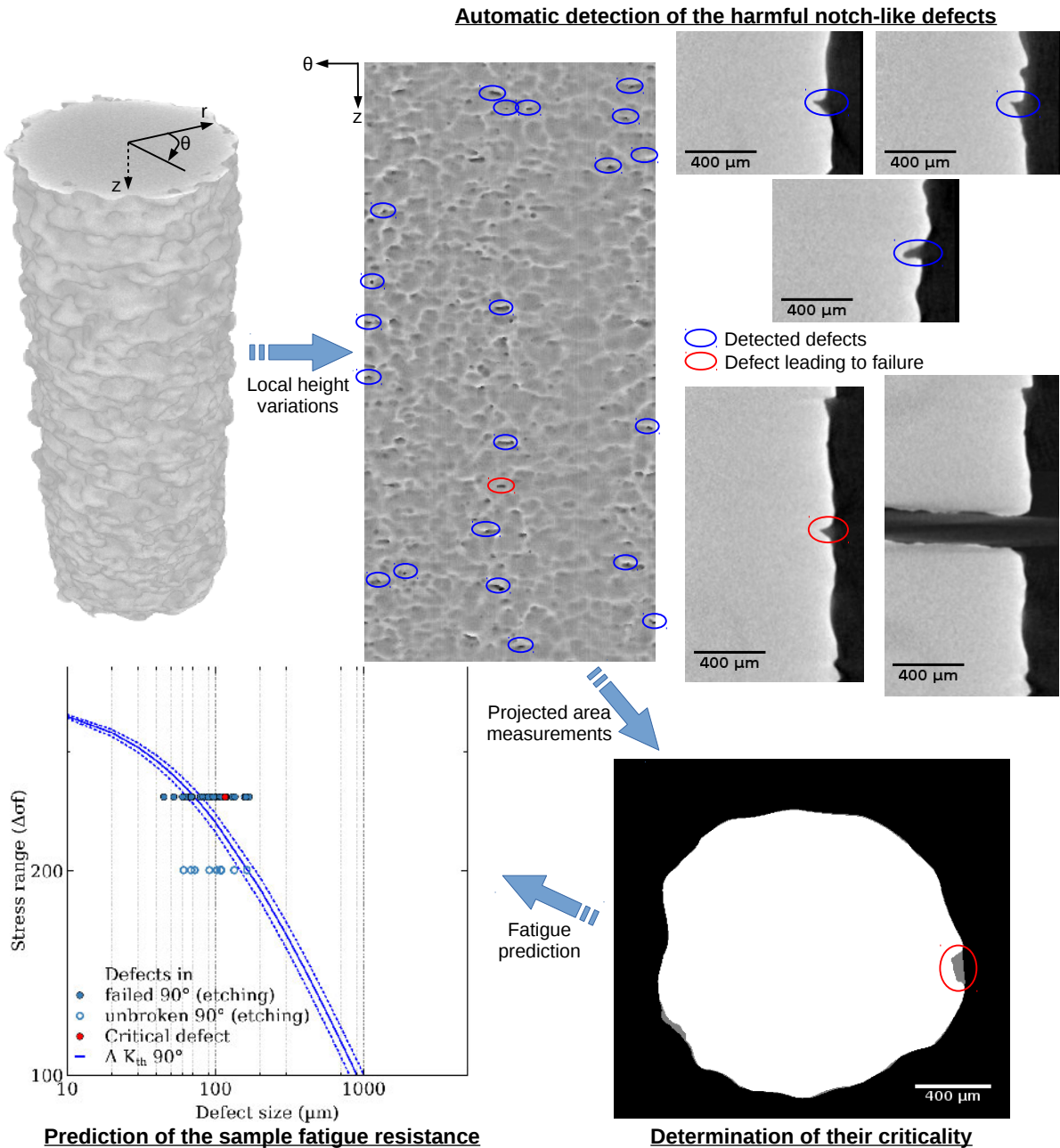
Conclusion and Perspectives

Conclusion

This work was aimed at determining the fatigue properties of as-built and post-treated Ti-6Al-4V thin struts elaborated by Electron Beam Melting. These properties will be later used for fatigue tests performed on lattices structures. The material in as-built conditions and the impact of the post-treatments were characterized in chapter 1. The tensile static and fatigue properties of the samples were determined in chapter 2 and chapter 3 respectively. A method for the detection of the critical defects for fatigue was proposed and used to predict fatigue properties in chapter 4.

Material characterization of as-built and post-treated samples
First, the samples were manufactured in three different build orientations and characterized is as-built conditions in **chapter 1**. A fine and lamellar $\alpha + \beta$ microstructure was observed and the typical defects induced by additive manufacturing were observed:

- *gas pores* (inherited from the powder atomization) and *lack-of-fusion defects* in terms of internal defects;
- powder particles stuck to the surface and "plate-pile" like stacking defects which can lead to notch-like defects in terms of surface defects.

The latter were found to account for the important surface roughness of all samples. This characterization was consistent with the literature.

The build orientation was found to affect the sample geometry and the surface defects distribution. On the one hand, the poor thermal diffusion through unmelted powder particles led to a severe overmelting at the downward facing surfaces. It resulted in large protrusions and a water drop shaped cross section for horizontally built samples. On the other hand, the density of surface defects was related to the layer stacking (highest density of surface defects obtained for vertical samples).

For all build orientations, an heterogeneous spatial distribution of internal defects was observed with the presence of a sub-surface ring with a higher density of defects. This ring can be perfectly superimposed to the ring generated by the surface irregularities. Both rings were found to be linked to the melting strategy: they are most likely caused by a reduced energy density used for the contour melting.

Regarding the impact of post-treatments, Hot Isostatic Pressing (HIP) led to the closure

or shrinkage of all internal defects. It also induced a coarsening of the microstructure (increase of the α-laths thickness from ~ 1 to ~ 3-4 μm).

Chemical etching (CE) improved the surface of EBM samples through dissolution. All powder particles stuck to the surface were dissolved and the "plate-pile" like stacking defects and notch-like defects were positively impacted. Their depth was significantly reduced and the radius of curvature at their root increased. However, the impact of the build orientation on the surface defects (density, orientation and shape) remained. It also brought internal defects closer to or at the surface.

Ultrasonic shot-peening (USP) affected both the surface and the sub-surface layer of as-built samples. The surface condition obtained by this post-treatment was similar to that of machined samples. In addition, the sub-surface ring with a higher density of internal defects detected in as-built samples was also removed. However, the folding process of surface peaks over the neighboring valleys through plastic deformation led to a ring of "new" internal defects underneath the surface. Those defects were identified as partially "filled" notch-like defects. The microstructure was also affected by the plastic deformation down to a ~ 100 μm depth. At the surface, all α-laths were deformed: their width reduced to sub-micron values and the orientation of their major axis became parallel to the surface. This deformed microstructure induced surface hardening and compressive residual stresses.

The effect of the differences in microstructure and type of defects on the tensile properties was studied in **chapter 2** for as-built, post-treated and machined EBM samples.

Tensile properties: down-scaling factors

Because of important cross section variations along the gauge length in both as-built and chemically etched samples, defining the tensile *stress* was not straightforward. Three simple approaches were considered and the average section determined from tomographic images was found to be the most suitable for stress calculations.

The as-built surface of EBM thin struts detrimentally affected all the mechanical properties examined in this study (0.2 offset Yield Strength ($YS_{0.2}$), Ultimate Tensile Strength (UTS) and elongation to failure (A%)). This was related to the presence of surface notch-like defects which acted as stress concentrations sites. After chemical etching, the tensile strength values ($YS_{0.2}$ and UTS) matched the ones of machined samples thanks to its beneficial impact on the surface defects. The ductility was also improved but the standard values reported for machined bulk samples were not recovered because of the remaining stress concentrations sites. A linear relationship between the roughness and the elongation to failure was determined.

HIP led to a slight decrease of both $YS_{0.2}$ and UTS and had a beneficial impact on the ductility. This was linked to the removal of internal defects and the impact of the treatment on the microstructure (coarsening of the α-laths). The combination of both post-treatments did not further improve the tensile properties.

Finally, down scaling factors (DSF) were suggested to account for the loss of properties when compared to machined samples.

With the material being characterized and the tensile properties determined, the fatigue properties of thin struts manufactured by EBM were studied and presented in **chapter**

3. Based on the results from the previous chapter, the average cross section within the samples gauge length was used to compute the fatigue stress levels.

Fatigue properties: influence of manufacturing defects

The as-built conditions provoked a clear reduction of the fatigue properties when compared to the machined ones. This detrimental impact was attributed to the presence of notch-like or "plate-pile" like stacking defects at the surface as they always caused the fatal crack initiation. Classical *Kitagawa-Takahashi* diagrams as well as modified approaches taking into account limited fatigue lives enabled to predict with a relatively good accuracy the impact of such defects on the fatigue resistance of individual struts.

The impact of the build orientation on the fatigue properties of as-built samples was related to its influence on the shape, size and density of surface defects. Horizontal and vertical samples were therefore shown to be respectively the best and worst build orientation in terms of fatigue resistance.

Finally, it was shown that roughness measurements were not significantly impacted by the critical thin and deep notch-like defects showing that roughnesses were not relevant parameters for predicting the fatigue properties of as-built AM samples.

Regarding lattice structures, the design of fatigue-resistant lattice structures cannot be based on data from machined samples which are systematically superior to those of as-built AM samples . Considering their manufacturing, the build orientation impact showed that it would be interesting to adopt a build orientation which would limit the number of vertically built struts and increase the number of horizontally built struts.

A large improvement of the fatigue properties was obtained for chemically etched samples thanks to the severe reduction of the surface defects criticality. However, the fatigue failure was still caused by surface defects, mostly remaining part of notch-like defects. Consequently, their complete removal, possibly through a longer etching time, is expected to further improve the samples fatigue resistance.

Thanks to USP, the fatigue properties of machined samples were matched at low stress levels, even when applied to the least resistant vertical samples. The fatal cracks always initiated from the remaining part of a "filled" notch-like defect. However, SEM fracture surface observations showed that no material cohesion had been induced by the "filling" process. The real defect size remained therefore almost the same that in as-built conditions. The impressive fatigue improvement resulting from the USP treatment was thus attributed to the compressive residual stresses at the surface. Besides, it was shown that X-ray tomography largely underestimated the defects size of USP treated samples.

The impact of HIP on the fatigue properties was found to depend on the sample surface conditions. On the one hand, no impact was observed for as-built samples. On the other hand, HIP significantly increased the fatigue resistance of post-treated (chemical etching and USP) samples despite the absence of internal crack initiation sites. This was related to the coarsening of the microstructure induced by HIP which was reported to have a beneficial impact on the crack growth resistance of EBM Ti-6Al-4V samples.

The three post-treatments (HIP + chemical etching + USP) were combined in an attempt to obtain defect-free samples. Although some defects remained, the fatigue prop-

erties were further improved.

As the fatigue properties of EBM samples were deeply linked to the presence of surface defects and more precisely to notch-like defects, a method for detecting them and for evaluating their criticality through non-destructive inspections was proposed and described in **chapter 4**.

Detection of the critical defects and fatigue resistance prediction

The proposed critical defects identification method relied only on X-ray laboratory tomographic images. After several image processing operations, surface maps were obtained where all severe notch-like defects could be distinguished from the other surface variations thanks to their peculiar geometrical footprint. The defects criticality was then assessed from projected areas measurements using Murakami's parameter $\sqrt{area}$. *Kitagawa-Takahashi* diagrams were finally used to determine the fatigue performance of one sample based on its defects distribution.

This method was successfully applied to all chemically etched samples. First, for the vast majority of the broken samples, the defect leading to fatigue failure was correctly identified as one of the most harmful defects. Second, classical *Kitagawa-Takahashi* diagrams correctly predicted the fatigue failure or the infinite fatigue lives ($> 3.10^6$ cycles) of most samples. Furthermore, finite lives diagrams were successful in predicting the fatigue lives of 45° and 0° samples.

However, in most cases, the method failed to detect *the* defect responsible for failure as the most critical one. The radius of curvature at the defect root which was reported to affect crack initiation was found to impact the criticality of the defects. Adding this parameter to the criticality measurements may improve their efficiency.

Besides, the impact of chemical etching on the root of the notch-like defects was found to depend on the initial defect geometry. Additional investigations on the link between the defect shape and the etching efficiency are required to better understand this point.

The final surface maps were useful to visualize the build orientation impact on the *as-built* surface state and on the surface defects population. Nevertheless, erroneous values were obtained for the depth measurements of as-built surface defects because of powder particles stuck to the surface or because of the inclination of those defects with respect to the surface. The method could not be used for as-built samples.

Perspectives

The results obtained during this work open at least two directions of future research. One is to further improve both the fatigue properties of thin struts and their prediction. The other is the application of the results obtained on struts to lattice structures.

Improving the fatigue properties of EBM thin struts

Tayloring of the process parameters

The optimization of process parameters did not fall within the scope of this study but the material characterization showed that future work was needed in this field. Some potential improvements are developped below.

During this study, it was postulated that the sub-surface ring of defects was caused by the contour step and the low energy density applied during this melting step. In order to confirm this hypothesis, the area melted only by the contours must be modified for instance by adding contours. A corresponding increase of the width of the rings would confirm our assumtion. More drastic changes such as the complete removal of the contour step or the hatching step can also be considered.

The next step would be to try to remove this ring while keeping an optimized surface roughness. In this regard, subtle changes can be applied to the contours: increasing the energy density of only the inner contour may for example reduce the density of internal defects. Preliminary tests have been performed but the limited number of samples manufactured did not allow to determine a new set of optimized parameters.

Another impact of the manufacturing process was observed in 90° samples. Both the cross sections and the ring of surface irregularities were elongated in the raking direction, making them more elliptical than circular. In addition, the critical defects identification method showed that the vast majority of the detected notch-like defects were located on the surfaces perpendicular to this direction. This implies that the melting conditions were not identical in the raking direction and in the direction perpendicular to it. One way to confirm this hypothesis would be to stop the 90° rotation of the scanning direction. By building samples using a constant scanning direction (along the x axis for some and along y for others), this hypothesis could be confirmed and the better scanning direction identified.

Optimisation of the post-treatments

Despite the significant beneficial impact induced by the post-treatments on the material and fatigue properties, the results reported for "HIP + machined" samples are yet to be achieved. One way of exploration is the optimization of the post-treatments discussed during this study.

Regarding chemical etching, increasing the etching time is likely to further improve the surface state and thus the fatigue properties of 90° samples. Nevertheless, the room for improvement is rather limited as the "ceiling" of the fatigue properties seems to be already

defined as the ones obtained for 0° samples. In addition, increasing too much the etching duration would result in very thin struts ($\sim$ 2 mm diameter in as-built conditions).

As for USP, the limiting factor is the remaining parts of the notch-like defects. The combination of "HIP + CE + USP" seems very promising in this regard and the optimisation of the etching duration to apply before USP is key. As mentioned previously, simulating the chemical etching step (for example with the model proposed by Lhuissier et al. [LHU 16]) could give an insight on which duration could allow to obtain defect-free samples. The expectations regarding the fatigue properties of such samples are rather high considering the important compressive residual stresses measured at the samples surface.

Better prediction of the fatigue properties

The method developed was successful in detecting all harmful defects and in predicting their criticality. However, the critical defect was not always correctly identified. The radius of curvature at the defects root appears to affect their criticality. Futur works would therefore be focused on integrating this parameter in the criticality measurements.

Another direction to explore is the modification of the detection method in order to apply it successfully to as-built samples. As previously mentioned in Chapter 4, simulating the first stages of the chemical dissolution might be a way to "remove" the sources of erroneous depth measurements (powder particles, ...). If successful, the method could be then applied to as-built samples and its efficiency evaluated.

Finally, applying the detection method to USP treated samples remains to be done. First, the samples could be analyzed *before* USP in order to determine which defects are more likely to remain "unfilled" by the process. Second, in order to predict the fatigue properties of such samples, it would be first necessary to determine accurately the beneficial impact that the compressive residual stresses have on the fatigue properties.

Application to lattices structures

The primary goal of this work was to study EBM thin struts in order to gather data for future works on lattice structures. Applying the results presented in this manuscript to lattice structures is therefore the other logical perspective of this work. The first tested approaches and preliminary results that have been obtained will be discussed below.

Sample geometry

The lattice structures considered here are periodical and can be described by the unit cell which is going to be repeated within the entire structure. Several unit cells are commonly used in the literature (tetrahedron, diamond, cubic, rhombic dodecahedron, ...) but most of them are bending-dominated structures. In our case, we chose to focus on the stretching dominated octet-truss cell because of their higher Young's modulus and yield strength [GIB 82]. All struts within the lattice structures will therefore be deformed in tension or compression which means that the results obtained from the fatigue tests on the single struts can be transferred to the lattice structure.

Regarding the sample geometry, the number of unit cells is of utmost importance. Suard showed that, for the Young modulus of lattices, the representative volume element

(RVE) was a cube with 5 cells on each side [SUA 15b]. For smaller samples, boundary effects were observed.

In our case, being able to follow how fatigue failure occurs during the fatigue test of a lattice is key. A compromise between a RVE and a limited number of unit cells so that the evolution of each strut could be assessed with the naked eye or with high resolution pictures was therefore chosen. In order to confirm its representativeness, the results obtained with the chosen geometry will have to be confirmed on lattice structures with higher number of unit cells. The actual geometry is shown in Figure 4.35.
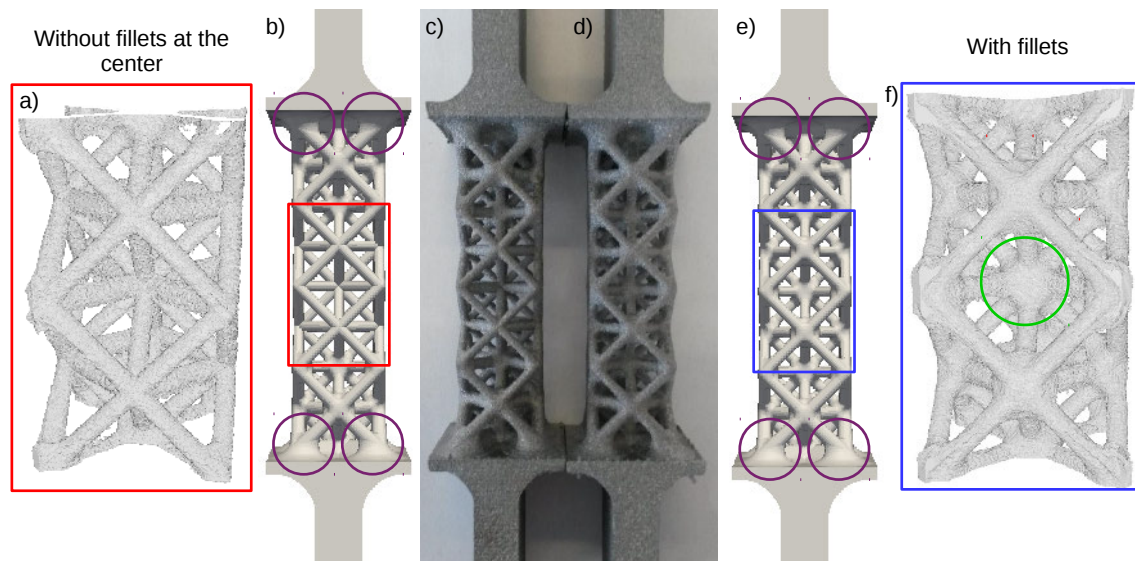

Figure 4.35: Geometry of the lattice samples without fillets at their center (a, b, c) and with fillets on all nodes (d, e, f). (a, f) 3D renderings of the tomographic images of the two center cells (voxel size: 18 μm). A fillet is circled in green in (f). (b, e) CAD inputs of the two geometries. (c,d) Photographs of the manufactured samples. Large fillets (purple circles) have been added at the interface between the bulk heads and the lattice structure.

It consists in one column of 4 stacked octet-truss cells between two heads that will be clamped in the grips of the fatigue machine. The risk with such geometries is to fail at the interface between the bulk part and the struts. Indeed, important stress concentrations occur because of the sudden change of density/stiffness at those interfaces [ALS 16]. To reduce this effect, important fillets were added to smooth the geometrical variations and the diameter of the struts in contact with the heads were significantly increased.

The unit cells are composed of cylindrical struts with a 2 mm diameter and a 10 mm length. This corresponds exactly to the geometry of the single strut samples used during this PhD work. In order to localize the failure at the center of the sample, a porosity gradient was introduced in the lattices. In both the upper and the lower cells, the cylindrical struts with a 2 mm diameter were replaced by conical struts. The diameter of the struts near the heads was set to 3 mm and it was linearly decreased to reach 2.5 mm at the middle of these unit cells and then 2 mm at their end. 4 cells were stacked as it was the minimum requirement to have a central node where only cylindrical struts are connected (node at the center of the sample).

Preliminary numerical simulations showed that severe stress concentrations occured at the nodes of the cells (Figure 4.36a). In order to avoid a systematic failure at the nodes, two sample geometries were manufactured: with fillets at all nodes and with fillets only at the nodes of the upper and lower unit cells. With the addition of fillets, the stress concentrations are moved towards the struts edges (Figure 4.36b).
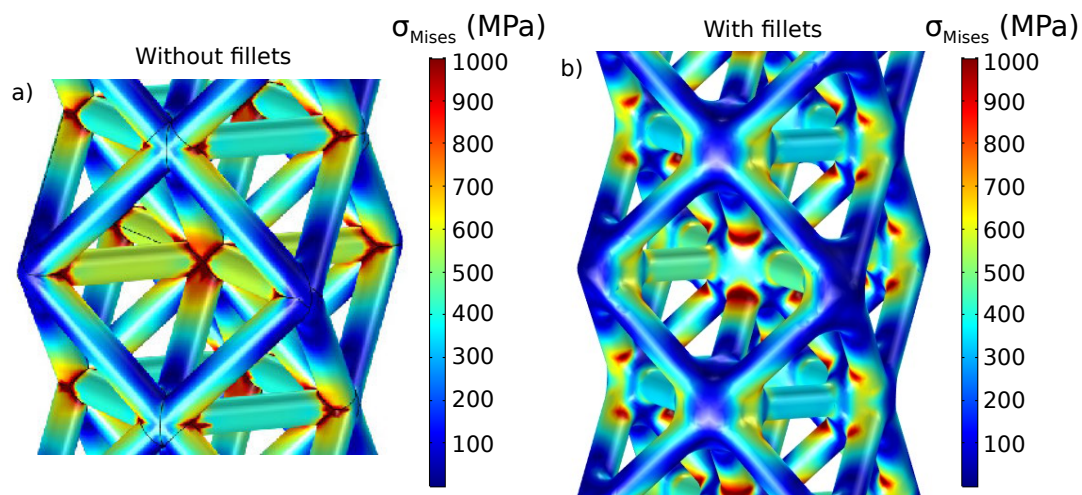
Figure 4.36: Elastic finite element simulations performed on the lattice samples without fillets at their center (a) and with fillets on all nodes (b). Under tensile loading (10 kN), the stress concentrations (in red) are shift from the nodes towards the struts edges with the addition of fillets.

Sample manufacturing

The results obtained on as-built single struts have been used to determine the manufacturing orientation of the lattice samples. As 90° struts must be avoided (worst surface condition and fatigue resistance), the samples were manufactured vertically. With this building orientation, the struts were either built in the 0° direction or in 45° and -45° directions. The two latter orientations depict the same manufacturing conditions and will be refered to as 45° struts.

Regarding the differences with the CAD input and between the cross section of the two build orientations observed in chapter 1, it was chosen not to counterbalance them. This way, the fatigue properties reported in 3 can be directly used. Consequently, all struts will be thinner than the CAD input and the 45° struts will be thinner than the 0° ones.

Fatigue tests

The first fatigue tests (f = 5 Hz, R = 0.1) performed on these lattice samples are rather promising. The sample geometry was validated as the failure always occured within the center part of the samples, i.e. within the two unit cells composed exclusively of 2 mm struts.

Regarding the failure mechanisms, for both sample geometries, the samples failure started by the failure of a strut which was then followed by the successive failures of

several struts until the catastrophic failure of the sample. Even in the absence of fillets, no failure at the nodes was observed. The struts always failed at their edges near the fillets or nodes meaning that the stress concentrations observed on the numerical simuations did impact the failure location.

The visual inspection of the samples during fatigue tests enabled to define a rather precise scenario of the lattice samples failure. A dozen of samples have been fatigue tested until failure at three differents stress levels and they all comply with the scenario described below. For a better understanding, the two unit cell at the center of the lattice sample will be called upper and lower cell. The nodes inside the lattice column will refered to as *internal nodes* while the ones located on the sides will be called *surface nodes.* Similarly, *internal struts* and *surface struts* will be mentioned. *Upper* (respectively *lower*) struts will refer to struts in the upper (respectively lower) half of the unit cell. For instance, a 45° *upper internal strut* will refer to a strut starting from a *surface node* and going up towards an *internal node.* The failure scenario is described in what follows.

1. After N cycles, a 45° *internal strut* fails. This strut is either an *upper internal strut* of the upper cell or a *lower internal strut* from the lower cell. This means that the first strut to fail is one of the eight 45° *internal struts* not connected to the center *internal node.* The failure randomly occur at either end of the strut.

2. Other 45° *internal struts* fail. Most of the time, the next two to five struts to fail are also amongst the eight 45° *internal struts* not connected to the center *internal node.* However, the location of the first strut to fail does not seem to affect the locations of these new failures: the new failed struts are randomly located in both cells. From these successive failures, one of the two cells is more damaged.

3. A *surface strut* located within the most damaged cell fails. The structure starts to bend during the fatigue test. This also significantly decreases the lattice stiffness and increases the stresses within the remaining struts. A cascade effect occurs leading to a quick catastrophic failure of the sample.

The scenario described above shows that the failure can be concentrated on a single cell or extended to the two center cells. It was considered that the steps of failure aforementioned corresponded to the "failure propagation" within the lattice sample and that "failure initiation" occured before at the scale of the lattice sample. The number of cycles corresponding to each regime will be refered to as N_{propa} and N_{ini} respectively, so that the total number of cycles before failure $N_f = N_{ini} + N_{propa}$.

During N_{propa}, 5 to 10 struts fail before the catastrophic failure of the sample. For all tested samples, the "failure propagation" is rather slow and this regime represent a non-negligible part of the total life of the sample: $N_{propa} \sim 0.25 \, N_f$. Note that the scatter of the N_{propa} values for samples submitted to the same stress level is extremely limited.

These preliminary results are very promising for future applications of lattice structures. For instance, in the case of aircraft parts which are submitted to visual inspections between flights, such a progressive failure could be used to assess the damage sustained by the part. Once a failed strut is identified, the remaining fatigue life of the part could be determined with a good accuracy and the replacement of the part planned.

Post-treatments

The three post-treatments studied during this work were applied to lattice structures in order to assess their efficiency.

The efficiency of HIP on lattice structures was already reported by Wauthle et al. [WAU 15] for SLM samples. Its efficiency for EBM lattice structures was confirmed here as no remaining internal defects were detected by X-ray tomography afterwards.

The effect of chemical etching on lattice structures has already been studied by several authors. Pyka et al. [PYK 12] and Van Hooreweder et al. [HOO 17] reported an impressive improvement of the surface of SLM lattices by chemical etching but did not comment on the homogeneity of the process. Suard et al. [SUA 15b] and de Formanoir et al. [FOR 16b] compared the effect of etching on struts located at the center and on the edges of 5×5×5 lattices manufactured by EBM. Both reported a good homogeneity of the process.

In order to confirm these observations, lattice samples were scanned before and after chemical etching. Contrary to what was done for single struts samples, a magnetic stirrer was used here with the aim of having an homogeneous treatment. This also led to an increase in the kinetic of the reaction. Figure 4.37 illustrates the impact of 30 minutes of chemical etching (with stirring) on a lattice sample.
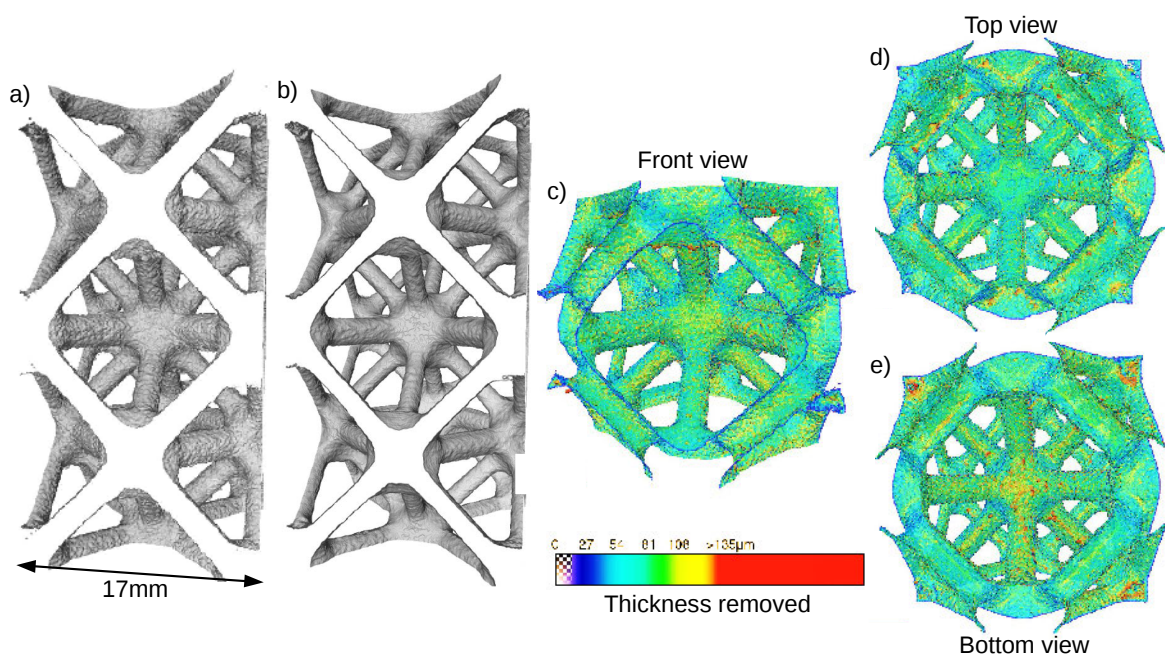
Figure 4.37: Impact of chemical etching on lattice samples. 3D renderings of the two center cells of a lattice sample before (a) and after 30 minutes (b) of chemical etching. Front (c), top (d) and bottom views (e) of the 3D rendering of the dissolved material. The local thickness of the material removed is indicated by a color code. Cold and warm colors correspond respectively to small and high values of the thickness removed. The heterogeneity of the process is highlighted. The tomographic scans were performed with a 18 μm voxel size.

As expected, a clear improvement of the surface state is obtained. Furthermore, the struts are equally etched whatever their position in the lattice and the same observation can be made for the nodes. If the local thickness of the removed material is considered, heterogeneities do appear at a more local level. They were already reported in Chapter 1 and are rather beneficial as the roughest surfaces (downward facing surfaces) are more impacted by the post-treatment.

Ultrasonic shot peening was also applied to lattice structures. The main concern was the capability for the steel balls to reach all surfaces. Tests were therefore performed on the worst geometry in this regard i.e. lattice structure without fillets at the nodes. The result of USP on a lattice structure is shown in Figure 4.38.
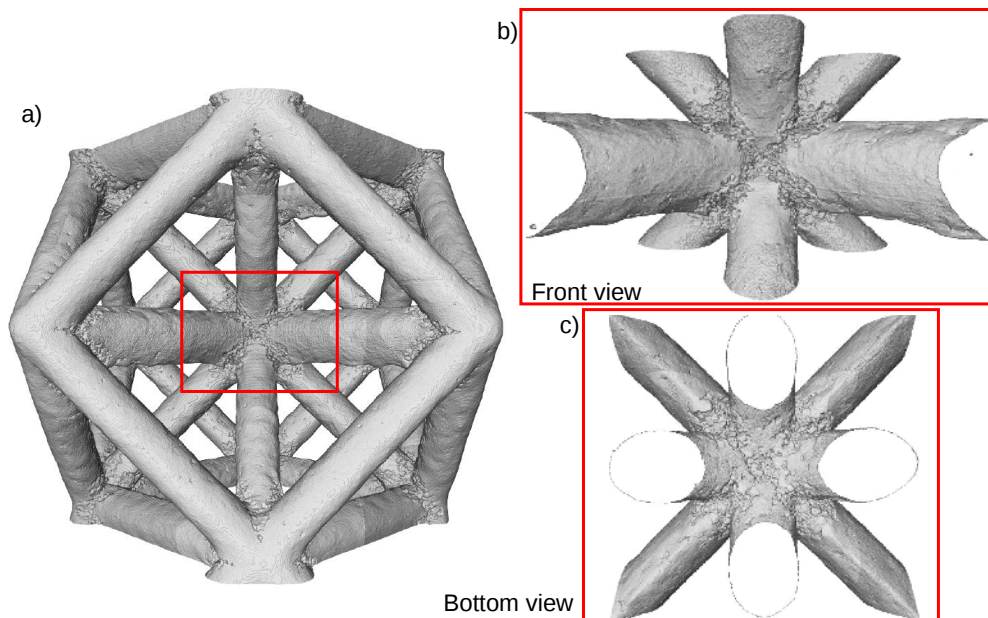
Figure 4.38: Impact of USP on lattice samples. 3D renderings of the two half-cells around the center node of a lattice sample without fillets after USP (a). Detailed front (b) and bottom views (c) of the 3D rendering of the node. The tomographic scans were performed with 13 μm and 8 μm voxel sizes repectively for the global view and the detailed views. The remaining roughness around the node shows the limits of USP for complex shapes.

Although USP seems to be slightly more efficient at the surface of the lattice, all struts have been significantly impacted by the process. They all show surface conditions close to that of machined samples, apart from the downward facing surfaces of the 0° struts where a remaining wavy pattern can be observed. However, the impact on the nodes is extremely limited. The surfaces remain rough and their poor aspect is emphasized by the smooth surface of the struts near the nodes (Figure 4.38).

In addition, this inefficiency of USP does not seem related to the location of the nodes as both *internal* and *surface nodes* share this poor surface condition. It is therefore the geometry at the nodes that is responsible: the angles between connecting struts are too acute for enabling the 1 mm diameter steel balls to reach the nodes.

One way to solve this issue is to remove such acute angles by adding fillets to all nodes for example. The smooth surface variations of the fillets might be sufficient for the steel balls to reach the entire surface. Such lattice structures have been manufactured and are currently being studied. If as-built surfaces were to remain with the fillets, another option to consider is the use of a smaller peening medium, for instance, steel balls with a 0.7 mm diameter. Indeed, their smaller size enable them to affect surface locations unreachable for larger spheres. Resolving this issue would considerably improve the fatigue properties of lattice structures.

Finally, if the study to achieve defect-free single struts samples were to succeed, applying the corresponding combination of post-treatments with success to the lattice samples seems highly plausible given the aforementioned results.

In the near future, the final goal of this work will be to use lattice structures for the design of industrial parts. A first application would be to use the lattice structures as a damage probe. For example, the parts could be designed so that, once the lattice failed, the rest of the part can sustain a certain number of cycles before failure. The complete failure of the lattice structure could be the controlling factor of damage but the first results obtained on lattice samples showed that the failure of the first strut could also play this role. Only the inspection method differs between the two cases. Work focusing on this application is already ongoing.

Another application, but more on a longer term, is the complete replacement of current aeronautical parts by hybrid parts (combination of lattices structures and bulk areas). This would enable considerable weight - and therefore cost - savings. Thanks to the design freedom allowed by AM, parts with complex loadings are more likely to be concerned by such replacements.

References

[ACK 09] ACKELID U., SVENSSON M.
Additive manufacturing of dense metal parts by electron beam melting. *Proceedings of the Materials Science and Technology Conference, Pittsburgh, PA, USA*, vol. 2529, 2009.

[AFN 09] AFNOR, 138 C.
Non-destructive Testing - Test Method for Residual Stress analysis by X-ray Diffraction. rapport, 2009, Association Française de normalisation.

[AHM 98] AHMED T., RACK H.
Phase transformations during cooling in $\alpha + a\beta$ titanium alloys. *Materials Science and Engineering: A*, vol. 243, n° 1, 1998, p. 206 - 211.

[Air01] *Airbus Industrie Test Method standards*, Appendix AITM 1-0011 Constant amplitude fatigue testing of metallic material, p. 1-24. AIRBUS INDUSTRIE, editor, Airbus Industrie, Engineering Directorate, Blagnac cedex, France, 2001.

[ALB 10] AL-BERMANI S. S., BLACKMORE M. L., ZHANG W., TODD I.
The Origin of Microstructural Diversity, Texture, and Mechanical Properties in Electron Beam Melted Ti-6Al-4V. *Metallurgical and Materials Transactions A*, vol. 41, n° 13, 2010, p. 3422–3434.

[ALG 16] ALGARDH J. K., HORN T., WEST H., AMAN R., SNIS A., ENGQVIST H., LAUSMAA J., HARRYSSON O.
Thickness dependency of mechanical properties for thin-walled titanium parts manufactured by Electron Beam Melting (EBM)®. *Additive Manufacturing*, vol. 12, 2016, p. 45–50, Elsevier B.V.

[ALS 16] ALSALLA H., HAO L., SMITH C.
Fracture toughness and tensile strength of 316L stainless steel cellular lattice structures manufactured using the selective laser melting technique. *Materials Science and Engineering: A*, vol. 669, 2016, p. 1 - 6.

[ANT 13] ANTONYSAMY A., MEYER J., PRANGNELL P.
Effect of build geometry on the β-grain structure and texture in additive manufacture of Ti6Al4V by selective electron beam melting. *Materials Characterization*, vol. 84, 2013, p. 153 - 168.

[ARC 13] ARCAM
Documentation from Arcam training level 2. 2013.

[ATK 00] Atkinson H. V., Davies S.
Fundamental aspects of hot isostatic pressing: An overview. *Metallurgical and Materials Transactions A*, vol. 31, n⁰ 12, 2000, p. 2981–3000.

[ATT 11] Attar E.
Simulation of selective electron beam melting processes. , 2011.

[B60 94] B600-11(2017) A.
Standard Guide for Descaling and Cleaning Titanium and Titanium Alloy Surfaces. rapport, 1994, ASTM International, West Conshohocken, PA.

[BAN 10] Bantounas I., Dye D., Lindley T. C.
The role of microtexture on the faceted fracture morphology in Ti-6Al-4V subjected to high-cycle fatigue. *Acta Materialia*, vol. 58, n⁰ 11, 2010, p. 3908 - 3918.

[BAS 10] Basquin O.
The exponential law of endurance tests. *Proc Am Soc Test Mater*, vol. 10, 1910, p. 625–630.

[BEN 17] Benedetti M., Torresani E., Leoni M., Fontanari V., Bandini M., Pederzolli C., Potrich C.
The effect of post-sintering treatments on the fatigue and biological behavior of Ti-6Al-4V ELI parts made by selective laser melting. *Journal of the Mechanical Behavior of Biomedical Materials*, vol. 71, 2017, p. 295 - 306.

[BER 17] Beretta S., Romano S.
A comparison of fatigue strength sensitivity to defects for materials manufactured by AM or traditional processes. *International Journal of Fatigue*, vol. 94, 2017, p. 178 - 191. Fatigue and Fracture Behavior of Additive Manufactured Parts.

[BOR 02] Borbély A., Mughrabi H., Eisenmeier G., Höppel H.
A finite element modelling study of strain localization in the vicinity of near-surface cavities as a cause of subsurface fatigue crack initiation. *International Journal of Fracture*, vol. 115, n⁰ 3, 2002, p. 227–232.

[BRA 11] Brandl E., Leyens C., Palm F.
Mechanical Properties of Additive Manufactured Ti-6Al-4V Using Wire and Powder Based Processes. *IOP Conference Series: Materials Science and Engineering*, vol. 26, 2011, Page 012004.

[BRA 12] Brandl E., Greitemeier D., Maier H. J., Syassen F.
High Cycle Fatigue Properties Of Electron Beam Melted TI-6AL-4V Samples Without And With Integrated Defects ("Effects Of Defects"). *12th European Conference on Spacecraft Structures, Materials and Environmental Testing*, vol. 691, 2012, Page 16.

[CAO 17] Cao F., Chandran K. R.
The role of crack origin size and early stage crack growth on high cycle fatigue of powder metallurgy Ti-6Al-4V alloy. *International Journal of Fatigue*, vol. 102, 2017, p. 48 - 58.

[CAO 18] Cao F., Zhang T., Ryder M. A., Lados D. A.
A Review of the Fatigue Properties of Additively Manufactured Ti-6Al-4V. *JOM*, vol. 70, n⁰ 3, 2018, p. 349–357.

[CHA 01] Chao J., Morris D., Muñoz-Morris M., Gonzalez-Carrasco J.
The influence of some microstructural and test parameters on the tensile behaviour and the ductility of a mechanically-alloyed Fe-40Al alloy. *Intermetallics*, vol. 9, n° 4, 2001, p. 299 - 308.

[CHA 13] Chan K. S., Koike M., Mason R. L., Okabe T.
Fatigue Life of Titanium Alloys Fabricated by Additive Layer Manufacturing Techniques for Dental Implants. *Metallurgical and Materials Transactions A*, vol. 44, n° 2, 2013, p. 1010–1022.

[CHA 16] Chastand V.
Studying the mechanical behaviour and the damaging mechanisms of metallic parts produced by additive manufacturing. Theses, Ecole Centrale de Lille, 2016.

[CHA 18] Charkaluk E., Chastand V.
Fatigue of Additive Manufacturing Specimens: A Comparison with Casting Processes. *Proceedings*, vol. 2, n° 8, 2018.

[CHE 14] Chen G.-q., Yan J., Tian T.-y., Zhang X.-h., Li Z.-q., Zhou W.-l.
Effect of wet shot peening on Ti-6Al-4V alloy treated by ceramic beads. *Transactions of Nonferrous Metals Society of China*, vol. 24, n° 3, 2014, p. 690–696, Elsevier.

[CIA 06] Ciavarella M., Monno F.
On the possible generalizations of the Kitagawa-Takahashi diagram and of the El Haddad equation to finite life. *International Journal of Fatigue*, vol. 28, n° 12, 2006, p. 1826 - 1837.

[COL 16] Collins P., Brice D., Samimi P., Ghamarian I., Fraser H.
Microstructural control of additively manufactured metallic materials. *Annual Review of Materials Research*, vol. 46, 2016, p. 63–91, Annual Reviews.

[DAI 04] Dai K., Villegas J., Stone Z., Shaw L.
Finite element modeling of the surface roughness of 5052 Al alloy subjected to a surface severe plastic deformation process. *Acta Materialia*, vol. 52, n° 20, 2004, p. 5771 - 5782.

[DAI 07] Dai K., Shaw L.
Comparison between shot peening and surface nanocrystallization and hardening processes. *Materials Science and Engineering: A*, vol. 463, n° 1, 2007, p. 46 - 53. TMS 2006, Mukherjee Symposium.

[EDW 13] Edwards P., O'Conner A., Ramulu M.
Electron Beam Additive Manufacturing of Titanium Components: Properties and Performance. *Journal of Manufacturing Science and Engineering*, vol. 135, n° 6, 2013, Page 061016.

[EYL 79a] Eylon D.
Fatigue crack initiation in hot isostatically pressed Ti-6Al-4V castings. *Journal of Materials Science*, vol. 14, n° 8, 1979, p. 1914–1922.

[EYL 79b] Eylon D., Strope B.
Fatigue crack initiation in Ti-6wt % Al-4 wt % V castings. *Journal of Materials Science*, vol. 14, n° 2, 1979, p. 345–353.

[F11 14] F1108-14 A.
Standard Specification for Titanium-6Aluminum-4Vanadium Alloy Castings for Surgical Implants (UNS R56406). rapport, 2014, ASTM International, West Conshohocken, PA.

[F13 13] F136-13 A.
Standard Specification for Wrought Titanium-6Aluminum-4Vanadium ELI (Extra Low Interstitial) Alloy for Surgical Implant Applications (UNS R56401). rapport, 2013, ASTM International, West Conshohocken, PA.

[FAC 09] Facchini L., Magalini E., Robotti P., Molinari A.
Microstructure and mechanical properties of Ti-6Al-4V produced by electron beam melting of pre-alloyed powders. *Rapid Prototyping Journal*, vol. 15, nᵒ 3, 2009, p. 171-178.

[FAC 10] Facchini L., Magalini E., Robotti P., Molinari A., Höges S., Wissenbach K.
Ductility of a Ti-6Al-4V alloy produced by selective laser melting of prealloyed powders. *Rapid Prototyping Journal*, vol. 16, nᵒ 6, 2010, p. 450-459.

[FOR 16a] de Formanoir C., Michotte S., Rigo O., Germain L., Godet S.
Electron beam melted Ti-6Al-4V: Microstructure, texture and mechanical behavior of the as-built and heat-treated material. *Materials Science and Engineering: A*, vol. 652, 2016, p. 105 - 119.

[FOR 16b] de Formanoir C., Suard M., Dendievel R., Martin G., Godet S.
Improving the mechanical efficiency of electron beam melted titanium lattice structures by chemical etching. *Additive Manufacturing*, vol. 11, 2016, p. 71–76, Elsevier B.V.

[FOR 19] de Formanoir C., Martin G., Prima F., Allain S. Y., Dessolier T., Sun F., Vivès S., Hary B., Bréchet Y., Godet S.
Micromechanical behavior and thermal stability of a dual-phase $\alpha+\alpha'$ titanium alloy produced by additive manufacturing. *Acta Materialia*, vol. 162, 2019, p. 149 - 162.

[FOT 19] Fotovvati B., Namdari N., Dehghanghadikolaei A.
Fatigue performance of selective laser melted Ti6Al4V components: state of the art. *Materials Research Express*, vol. 6, nᵒ 1, 2019, Page 012002.

[FRA 14] Frazier W. E.
Metal Additive Manufacturing: A Review. *Journal of Materials Engineering and Performance*, vol. 23, nᵒ 6, 2014, p. 1917–1928.

[GAL 16] Galarraga H., Lados D. A., Dehoff R. R., Kirka M. M., Nandwana P.
Effects of the microstructure and porosity on properties of Ti-6Al-4V ELI alloy fabricated by electron beam melting (EBM). *Additive Manufacturing*, vol. 10, 2016, p. 47–57, Elsevier B.V.

[GIB 82] Gibson I., Ashby M. F.
The mechanics of three-dimensional cellular materials. *Proc. R. Soc. Lond. A*, vol. 382, nᵒ 1782, 1982, p. 43–59, The Royal Society.

[GOL 10] Golden P. J., John R., Porter W. J.
Investigation of variability in fatigue crack nucleation and propagation in alpha+beta Ti-6Al-4V. *Procedia Engineering*, vol. 2, nᵒ 1, 2010, p. 1839 - 1847. Fatigue 2010.

[GON 15] Gong H., Rafi K., Gu H., Ram G. J., Starr T., Stucker B.
Influence of defects on mechanical properties of Ti-6Al-4V components produced by selective laser melting and electron beam melting. *Materials & Design*, vol. 86, 2015, p. 545 - 554.

[GRE 16] Greitemeier D., Dalle Donne C., Syassen F., Eufinger J., Melz T.
Effect of surface roughness on fatigue performance of additive manufactured Ti–6Al–4V. *Materials Science and Technology*, vol. 32, nº 7, 2016, p. 629–634, Taylor & Francis.

[GRE 17] Greitemeier D., Palm F., Syassen F., Melz T.
Fatigue performance of additive manufactured TiAl6V4 using electron and laser beam melting. *International Journal of Fatigue*, vol. 94, 2017, p. 211 - 217. Fatigue and Fracture Behavior of Additive Manufactured Parts.

[GÜN 17] Günther J., Krewerth D., Lippmann T., Leuders S., Tröster T., Weidner A., Biermann H., Niendorf T.
Fatigue life of additively manufactured Ti-6Al-4V in the very high cycle fatigue regime. *International Journal of Fatigue*, vol. 94, 2017, p. 236 - 245. Fatigue and Fracture Behavior of Additive Manufactured Parts.

[HAD 79] Haddad M. E., Topper T., Smith K.
Prediction of non propagating cracks. *Engineering Fracture Mechanics*, vol. 11, nº 3, 1979, p. 573 - 584.

[HOO 17] Hooreweder B. V., Apers Y., Lietaert K., Kruth J.-P.
Improving the fatigue performance of porous metallic biomaterials produced by Selective Laser Melting. *Acta Biomaterialia*, vol. 47, 2017, p. 193 - 202.

[HRA 13] Hrabe N., Quinn T.
Effects of processing on microstructure and mechanical properties of a titanium alloy (Ti-6Al-4V) fabricated using electron beam melting (EBM), Part 2: Energy input, orientation, and location. *Materials Science and Engineering: A*, vol. 573, 2013, p. 271 - 277.

[HRA 17] Hrabe N., Gnäupel-Herold T., Quinn T.
Fatigue properties of a titanium alloy (Ti-6Al-4V) fabricated via electron beam melting (EBM): Effects of internal defects and residual stress. *International Journal of Fatigue*, vol. 94, 2017, p. 202 - 210. Fatigue and Fracture Behavior of Additive Manufactured Parts.

[ISO 96] ISO, 57 I., 3 I., 10 I., 5 S.
Geometrical Product Specifications (GPS). Surface texture : profile method. Rules and procedures for the assessment of surface texture. rapport, 1996, International Organization for Standardization.

[JAI 00] Jain V., Adsul S.
Experimental investigations into abrasive flow machining (AFM). *International Journal of Machine Tools and Manufacture*, vol. 40, nº 7, 2000, p. 1003 - 1021.

[JIA 07] Jiang X., Man C.-S., Shepard M., Zhai T.
Effects of shot-peening and re-shot-peening on four-point bend fatigue behavior of Ti-6Al-4V. *Materials Science and Engineering: A*, vol. 468-470, 2007, p. 137 - 143. The

McEvily Symposium: Fatigue and Fracture of Traditional and Advanced Materials, TMS 2006.

[JUE 14] Juechter V., Scharowsky T., Singer R., Körner C.
Processing window and evaporation phenomena for Ti-6Al-4V produced by selective electron beam melting. *Acta Materialia*, vol. 76, 2014, p. 252 - 258.

[KAH 17] Kahlin M., Ansell H., Moverare J.
Fatigue behaviour of notched additive manufactured Ti6Al4V with as-built surfaces. *International Journal of Fatigue*, vol. 101, 2017, p. 51 - 60.

[KAS 15] Kasperovich G., Hausmann J.
Improvement of fatigue resistance and ductility of TiAl6V4 processed by selective laser melting. *Journal of Materials Processing Technology*, vol. 220, 2015, p. 202 - 214.

[KIT 76] Kitagawa H., Takahashi S.
Applicability of fracture mechanics to very small cracks or the cracks in the early stage. *Second International Conference on Mechanical Behavior of Materials. ASM, Metals Park, Ohio. 1976, 627-631*, 1976.

[KOB 98] Kobayashi M., Matsui T., Murakami Y.
Mechanism of creation of compressive residual stress by shot peening. *International Journal of Fatigue*, vol. 20, n° 5, 1998, p. 351 - 357.

[KOB 03] Kobryn P., Semiatin S.
Microstructure and texture evolution during solidification processing of Ti-6Al-4V. *Journal of Materials Processing Technology*, vol. 135, n° 2, 2003, p. 330 - 339. Special Issue containing paper from the conference Research and Development in Net shape Manufactureing.

[KOH 88] Kohut T.
Surface finishing with abrasive flow machining. *Vol. 2, Proc. of the Fourth Int'l. Aluminum Extrusion Technology Seminar, Washington, DC, April*, 1988.

[KÖR 13] Körner C., Bauereiss A., Attar E.
Fundamental consolidation mechanisms during selective beam melting of powders. *Modelling and Simulation in Materials Science and Engineering*, vol. 21, n° 8, 2013, Page 085011.

[KRU 06] Kruzic J., Ritchie R.
Kitagawa-Takahashi diagrams define the limiting conditions for cyclic fatigue failure in human dentin. *Journal of Biomedical Materials Research Part A*, vol. 79, n° 3, 2006, p. 747–751, Wiley Online Library.

[KUH 04] Kuhn A.
The electropolishing of titanium and its alloys. *Metal Finishing*, vol. 102, n° 6, 2004, p. 80 - 86.

[LEO 15] Leopold G., Nadot Y., Billaudeau T., Mendez J.
Influence of artificial and casting defects on fatigue strength of moulded components in Ti-6Al-4V alloy. *Fatigue & Fracture of Engineering Materials & Structures*, vol. 38, n° 9, 2015, p. 1026-1041.

[LEU 13] Leuders S., Thöne M., Riemer A., Niendorf T., Tröster T., Richard H., Maier H.

On the mechanical behaviour of titanium alloy TiAl6V4 manufactured by selective laser melting: Fatigue resistance and crack growth performance. *International Journal of Fatigue*, vol. 48, 2013, p. 300 - 307.

[LEU 14] LEUDERS S., LIENEKE T., LAMMERS S., TRÖSTER T., NIENDORF T.
On the fatigue properties of metals manufactured by selective laser melting - The role of ductility. *Journal of Materials Research*, vol. 29, n° 17, 2014, p. 1911-1919, Cambridge University Press.

[LEU 15] LEUDERS S., VOLLMER M., BRENNE F., TRÖSTER T., NIENDORF T.
Fatigue Strength Prediction for Titanium Alloy TiAl6V4 Manufactured by Selective Laser Melting. *Metallurgical and Materials Transactions A*, vol. 46, n° 9, 2015, p. 3816–3823.

[LEY 03] LEYENS C., PETERS M.
Titanium and titanium alloys: fundamentals and applications, Appendix 5, p. 153-187. John Wiley & Sons, 2003.

[LHU 16] LHUISSIER P., DE FORMANOIR C., MARTIN G., DENDIEVEL R., GODET S.
Geometrical control of lattice structures produced by EBM through chemical etching: Investigations at the scale of individual struts. *Materials and Design*, vol. 110, 2016, p. 485 - 493.

[LI 16] LI P., WARNER D., FATEMI A., PHAN N.
Critical assessment of the fatigue performance of additively manufactured Ti-6Al-4V and perspective for future research. *International Journal of Fatigue*, vol. 85, 2016, p. 130 - 143.

[LIN 05] LIN C.-W., JU C.-P., LIN J.-H. C.
A comparison of the fatigue behavior of cast Ti-7.5Mo with c.p. titanium, Ti-6Al-4V and Ti-13Nb-13Zr alloys. *Biomaterials*, vol. 26, n° 16, 2005, p. 2899 - 2907.

[LIU 04] LIU X., CHU P. K., DING C.
Surface modification of titanium, titanium alloys, and related materials for biomedical applications. *Materials Science and Engineering: R: Reports*, vol. 47, n° 3, 2004, p. 49 - 121.

[LIU 09] LIU K. K., HILL M. R.
The effects of laser peening and shot peening on fretting fatigue in Ti-6Al-4V coupons. *Tribology International*, vol. 42, n° 9, 2009, p. 1250 - 1262. Special Issue: Fifth International Symposium on Fretting Fatigue.

[LOR 15] LORENZINO P., OKAZAKI S., MATSUNAGA H., MURAKAMI Y.
Effect of small defect orientation on fatigue limit of carbon steels. *Fatigue & Fracture of Engineering Materials & Structures*, vol. 38, n° 9, 2015, p. 1076–1086, Wiley Online Library.

[LU 15] LU S. L., TANG H. P., NING Y. P., LIU N., STJOHN D. H., QIAN M.
Microstructure and Mechanical Properties of Long Ti-6Al-4V Rods Additively Manufactured by Selective Electron Beam Melting Out of a Deep Powder Bed and the Effect of Subsequent Hot Isostatic Pressing. *Metallurgical and Materials Transactions A: Physical Metallurgy and Materials Science*, vol. 46, n° 9, 2015, p. 3824–3834.

[LÜT 84] LÜTJERING G., GYSLER A.
Fatigue–a Critical Review. *Titanium–Science and Technology.*, vol. 4, 1984, p. 2065–2083.

[LÜT 98] LÜTJERING G.
Influence of processing on microstructure and mechanical properties of (Îś+Îš) titanium alloys. *Materials Science and Engineering: A*, vol. 243, nᵒ 1, 1998, p. 32 - 45.

[MEG 99] MEGUID S., SHAGAL G., STRANART J., DALY J.
Three-dimensional dynamic finite element analysis of shot-peening induced residual stresses. *Finite Elements in Analysis and Design*, vol. 31, nᵒ 3, 1999, p. 179 - 191.

[MEY 08] MEYER L. W., KRÜGER L., SOMMER K., HALLE T., HOCKAUF M.
Dynamic strength and failure behavior of titanium alloy Ti-6Al-4V for a variation of heat treatments. *Mechanics of Time-Dependent Materials*, vol. 12, nᵒ 3, 2008, p. 237–247.

[MOH 18] MOHAMMADIAN N., TURENNE S., BRAILOVSKI V.
Surface finish control of additively-manufactured Inconel 625 components using combined chemical-abrasive flow polishing. *Journal of Materials Processing Technology*, vol. 252, 2018, p. 728 - 738.

[MOW 14] MOWER T. M.
Degradation of titanium 6Al-4V fatigue strength due to electrical discharge machining. *International Journal of Fatigue*, vol. 64, 2014, p. 84 - 96.

[MUR 85] MURAKAMI Y.
Analysis of stress intensity factors of modes I, II and III for inclined surface cracks of arbitrary shape. *Engineering Fracture Mechanics*, vol. 22, nᵒ 1, 1985, p. 101 - 114.

[MUR 94] MURAKAMI Y., ENDO M.
Effects of defects, inclusions and inhomogeneities on fatigue strength. *International Journal of Fatigue*, vol. 16, nᵒ 3, 1994, p. 163 - 182.

[MUR 09] MURR L., ESQUIVEL E., QUINONES S., GAYTAN S., LOPEZ M., MARTINEZ E., MEDINA F., HERNANDEZ D., MARTINEZ E., MARTINEZ J., STAFFORD S., BROWN D., HOPPE T., MEYERS W., LINDHE U., WICKER R.
Microstructures and mechanical properties of electron beam-rapid manufactured Ti-6Al-4V biomedical prototypes compared to wrought Ti-6Al-4V. *Materials Characterization*, vol. 60, nᵒ 2, 2009, p. 96 - 105.

[MUR 10] MURR L. E., GAYTAN S. M., MEDINA F., LOPEZ H., MARTINEZ E., MACHADO B. I., HERNANDEZ D. H., MARTINEZ L., LOPEZ M. I., WICKER R. B., BRACKE J.
Next-generation biomedical implants using additive manufacturing of complex, cellular and functional mesh arrays. *Philosophical Transactions of the Royal Society of London A: Mathematical, Physical and Engineering Sciences*, vol. 368, nᵒ 1917, 2010, p. 1999–2032, The Royal Society.

[NAL 02] NALLA R. K., RITCHIE R. O., BOYCE B. L., CAMPBELL J. P., PETERS J. O.
Influence of microstructure on high-cycle fatigue of Ti-6Al-4V: Bimodal vs. lamellar structures. *Metallurgical and Materials Transactions A*, vol. 33, nᵒ 3, 2002, p. 899–918.

[NII 98] NIINOMI M.
Mechanical properties of biomedical titanium alloys. *Materials Science and Engineering: A*, vol. 243, n° 1, 1998, p. 231 - 236.

[OBE 10] OBERWINKLER B., RIEDLER M., EICHLSEDER W.
Importance of local microstructure for damage tolerant light weight design of Ti-6Al-4V forgings. *International Journal of Fatigue*, vol. 32, n° 5, 2010, p. 808 - 814. Papers from the 2009 TMS Annual Meeting Symposium on Mechanisms, theory, experiments and industrial practice in fatigue.

[OGU 10] OGUMA H., NAKAMURA T.
The effect of microstructure on very high cycle fatigue properties in Ti-6Al-4V. *Scripta Materialia*, vol. 63, n° 1, 2010, p. 32 - 34.

[OH 04] OH J., LEE J. G., KIM N. J., LEE S., LEE E. W.
Effects of thickness on fatigue properties of investment cast Ti-6Al-4V alloy plates. *Journal of Materials Science*, vol. 39, n° 2, 2004, p. 587–591.

[PER 18] PERSENOT T., MARTIN G., DENDIEVEL R., BUFFIERE J.-Y., MAIRE E.
Enhancing the tensile properties of EBM as-built thin parts: Effect of HIP and chemical etching. *Materials Characterization*, , 2018.

[PER 19] PERSENOT T., BURR A., MARTIN G., BUFFIERE J.-Y., DENDIEVEL R., MAIRE E.
Effect of build orientation on the fatigue properties of as-built Electron Beam Melted Ti-6Al-4V alloy. *International Journal of Fatigue*, vol. 118, 2019, p. 65 - 76.

[POL 14] POLASIK A. K.
The Role of Microstructure on High Cycle Fatigue Lifetime Variability in Ti-6Al-4V. Thèse de doctorat, The Ohio State University, 2014.

[PYK 12] PYKA G., BURAKOWSKI A., KERCKHOFS G., MOESEN M., VAN BAEL S., SCHROOTEN J., WEVERS M.
Surface Modification of Ti6Al4V Open Porous Structures Produced by Additive Manufacturing. *Advanced Engineering Materials*, vol. 14, n° 6, 2012, p. 363–370, WILEY-VCH Verlag.

[RAF 12] RAFI H. K., KARTHIK N., STARR T. L., STUCKER B. E.
Mechanical property evaluation of Ti-6Al-4V parts made using electron beam melting. *Proceedings of the Solid Freeform Fabrication Symposium*, 2012, p. 526–535.

[RAF 13] RAFI H. K., KARTHIK N. V., GONG H., STARR T. L., STUCKER B. E.
Microstructures and Mechanical Properties of Ti6Al4V Parts Fabricated by Selective Laser Melting and Electron Beam Melting. *Journal of Materials Engineering and Performance*, vol. 22, n° 12, 2013, p. 3872–3883.

[RAK 13] RAKITA M., WANG M., HAN Q., LIU Y., YIN F.
Ultrasonic shot peening. *International Journal of Computational Materials Science and Surface Engineering*, vol. 5, n° 3, 2013, p. 189-209. PMID: 56948.

[ROM 17] ROMANO S., BRANDÃO A., GUMPINGER J., GSCHWEITL M., BERETTA S.
Qualification of AM parts: Extreme value statistics applied to tomographic measurements. *Materials & Design*, vol. 131, 2017, p. 32 - 48.

[ROT 17] Rotella A., Nadot Y., Piellard M., Augustin R.
Influence of natural defects on the fatigue limit of a cast Al-Si alloy. *Procedia Structural Integrity*, vol. 7, 2017, p. 513 - 520. 3rd International Symposium on Fatigue Design and Material Defects, FDMD 2017.

[SAF 12] Safdar A., Wei L.-Y., Snis A., Lai Z.
Evaluation of microstructural development in electron beam melted Ti-6Al-4V. *Materials Characterization*, vol. 65, 2012, p. 8 - 15.

[SCH 01a] Schijve J.
Fatigue of structures and materials, Appendix 2, p. 23-25. Springer Science & Business Media, 2001.

[SCH 01b] Schijve J.
Fatigue of structures and materials, Appendix 3, p. 45-48. Springer Science & Business Media, 2001.

[SEI 15] Seifi M., Dahar M., Aman R., Harrysson O., Beuth J., Lewandowski J. J.
Evaluation of Orientation Dependence of Fracture Toughness and Fatigue Crack Propagation Behavior of As-Deposited ARCAM EBM Ti-6Al-4V. *JOM*, vol. 67, nº 3, 2015, p. 597–607.

[SEI 17] Seifi M., Salem A., Satko D., Shaffer J., Lewandowski J. J.
Defect distribution and microstructure heterogeneity effects on fracture resistance and fatigue behavior of EBM Ti-6Al-4V. *International Journal of Fatigue*, vol. 94, 2017, p. 263 - 287. Fatigue and Fracture Behavior of Additive Manufactured Parts.

[SHU 17] Shui X., Yamanaka K., Mori M., Nagata Y., Kurita K., Chiba A.
Effects of post-processing on cyclic fatigue response of a titanium alloy additively manufactured by electron beam melting. *Materials Science and Engineering: A*, vol. 680, nº Supplement C, 2017, p. 239 - 248.

[SUA 15a] Suard M., Martin G., Lhuissier P., Dendievel R., Vignat F., Blandin J.-J., Villeneuve F.
Mechanical equivalent diameter of single struts for the stiffness prediction of lattice structures produced by Electron Beam Melting. *Additive Manufacturing*, vol. 8, 2015, p. 124 - 131.

[SUA 15b] Suard M.
Characterization and optimization of lattice structures made by Electron Beam Melting. Theses, Université Grenoble Alpes, 2015.

[SUN 16] Sun Y. Y., Gulizia S., Oh C. H., Fraser D., Leary M., Yang Y. F., Qian M.
The Influence of As-Built Surface Conditions on Mechanical Properties of Ti-6Al-4V Additively Manufactured by Selective Electron Beam Melting. *JOM*, vol. 68, nº 3, 2016, p. 791–798.

[SVE 10] Svensson M., Ackelid U.
Titanium alloys manufactured with electron beam melting mechanical and chemical properties. 2010.

[TAJ 08] Tajima K., Hironaka M., Chen K.-K., Nagamatsu Y., Kakigawa H., Kozono Y.
Electropolishing of CP Titanium and Its Alloys in an Alcoholic Solution-based Electrolyte. *Dental Materials Journal*, vol. 27, nº 2, 2008, p. 258-265.

[TAK 03] Takeuchi M., Abe Y., Yoshida Y., Nakayama Y., Okazaki M., Akagawa Y.
Acid pretreatment of titanium implants. *Biomaterials*, vol. 24, nº 10, 2003, p. 1821 - 1827.

[TAM 15] Tammas-Williams S., Zhao H., Lãeonard F., Derguti F., Todd I., Prangnell P.
XCT analysis of the influence of melt strategies on defect population in Ti-6Al-4V components manufactured by Selective Electron Beam Melting. *Materials Characterization*, vol. 102, 2015, p. 47 - 61.

[TAM 16a] Tammas-Williams S., Withers P., Todd I., Prangnell P.
Porosity regrowth during heat treatment of hot isostatically pressed additively manufactured titanium components. *Scripta Materialia*, vol. 122, 2016, p. 72 - 76.

[TAM 16b] Tammas-Williams S., Withers P. J., Todd I., Prangnell P. B.
The Effectiveness of Hot Isostatic Pressing for Closing Porosity in Titanium Parts Manufactured by Selective Electron Beam Melting. *Metallurgical and Materials Transactions A: Physical Metallurgy and Materials Science*, vol. 47, nº 5, 2016, p. 1939–1946, Springer US.

[TAM 17] Tammas-Williams S., Withers P., Todd I., Prangnell P.
The influence of porosity on fatigue crack initiation in additively manufactured titanium components. *Scientific reports*, vol. 7, nº 1, 2017, Page 7308, Nature Publishing Group.

[TAO 02] Tao N., Wang Z., Tong W., Sui M., Lu J., Lu K.
An investigation of surface nanocrystallization mechanism in Fe induced by surface mechanical attrition treatment. *Acta Materialia*, vol. 50, nº 18, 2002, p. 4603 - 4616.

[TOD 04a] Todaka Y., Umemoto M., Tsuchiya K.
Comparison of Nanocrystalline Surface Layer in Steels Formed by Air Blast and Ultrasonic Shot Peening. *MATERIALS TRANSACTIONS*, vol. 45, nº 2, 2004, p. 376-379.

[TOD 04b] Todaka Y., Umemoto M., Watanabe Y., Tsuchiya K.
Formation of Nanocrystalline Structure in Steels by Air Blast Shot Peening and Particle Impact Processing. *Designing, Processing and Properties of Advanced Engineering Materials*, vol. 449 de *Materials Science Forum* Trans Tech Publications, 4 2004, p. 1149–1152.

[TOR 02] Torres M., Voorwald H.
An evaluation of shot peening, residual stress and stress relaxation on the fatigue life of AISI 4340 steel. *International Journal of Fatigue*, vol. 24, nº 8, 2002, p. 877 - 886.

[TSU 09] Tsuji N., Tanaka S., Takasugi T.
Effects of combined plasma-carburizing and shot-peening on fatigue and wear properties of Ti-6Al-4V alloy. *Surface and Coatings Technology*, vol. 203, nº 10, 2009, p. 1400 - 1405.

[UHL 13] Uhlmann E., Doits M., Schmiedel C.
Development of a Material Model for Visco-elastic Abrasive Medium in Abrasive Flow Machining. *Procedia CIRP*, vol. 8, 2013, p. 351 - 356. 14th CIRP Conference on Modeling of Machining Operations (CIRP CMMO).

[URL 17] Urlea V., Brailovski V.
Electropolishing and electropolishing-related allowances for powder bed selectively laser-melted Ti-6Al-4V alloy components. *Journal of Materials Processing Technology*, vol. 242, 2017, p. 1 - 11.

[VAY 18] Vayssette B., Saintier N., Brugger C., Elmay M., Pessard E.
Surface roughness of Ti-6Al-4V parts obtained by SLM and EBM: Effect on the High Cycle Fatigue life. *Procedia Engineering*, vol. 213, 2018, p. 89 - 97. 7th International Conference on Fatigue Design, Fatigue Design 2017, 29-30 November 2017, Senlis, France.

[VIL 11] Vilaro T., Colin C., Bartout J. D.
As-Fabricated and Heat-Treated Microstructures of the Ti-6Al-4V Alloy Processed by Selective Laser Melting. *Metallurgical and Materials Transactions A*, vol. 42, n° 10, 2011, p. 3190–3199.

[WAT 02] Watanabe T., Hattori K., Handa M., Hasegawa N., Tokaji K., Ikeda M., Duchazeaubeneix J. M.
Effect of ultrasonic shot peening on fatigue strength of high strength steel. *Proc. ICSP8, Garmisch-Partenkirchen, Germany, Ed. L. Wagner, pg*, 2002, p. 305–310.

[WAU 15] Wauthle R., Vrancken B., Beynaerts B., Jorissen K., Schrooten J., Kruth J.-P., Humbeeck J. V.
Effects of build orientation and heat treatment on the microstructure and mechanical properties of selective laser melted Ti6Al4V lattice structures. *Additive Manufacturing*, vol. 5, 2015, p. 77 - 84.

[WEL 93] Welsch G., Boyer R., Collings E.
Materials properties handbook: titanium alloys, Page 488. ASM international, 1993.

[WYC 14] Wycisk E., Solbach A., Siddique S., Herzog D., Walther F., Emmelmann C.
Effects of Defects in Laser Additive Manufactured Ti-6Al-4V on Fatigue Properties. *Physics Procedia*, vol. 56, 2014, p. 371 - 378. 8th International Conference on Laser Assisted Net Shape Engineering LANE 2014.

[YAD 17] Yadollahi A., Shamsaei N.
Additive manufacturing of fatigue resistant materials: Challenges and opportunities. *International Journal of Fatigue*, vol. 98, 2017, p. 14 - 31.

[YAN 16] Yang L., Wu Y., Lassell A., Zhou B.
Electropolishing of Ti6Al4V parts fabricated by electron beam melting. *Proceedings of the International Solid Freeform Fabrication (SFF) Symposium, Austin, TX*, 2016.

[YU 16] Yu B., Bradley R. S., Soutis C., Withers P. J.
A comparison of different approaches for imaging cracks in composites by X-ray microtomography. *Philosophical Transactions of the Royal Society of London A: Mathematical, Physical and Engineering Sciences*, vol. 374, n° 2071, 2016, The Royal Society.

[ZHA 16a] Zhai Y., Galarraga H., Lados D. A.
Microstructure, static properties, and fatigue crack growth mechanisms in Ti-6Al-4V fabricated by additive manufacturing: LENS and EBM. *Engineering Failure Analysis*, vol. 69, 2016, p. 3 - 14. Special issue on the International Conference on Structural Integrity.

[ZHA 16b] Zhao X., Li S., Zhang M., Liu Y., Sercombe T. B., Wang S., Hao Y., Yang R., Murr L. E.
Comparison of the microstructures and mechanical properties of Ti-6Al-4V fabricated by selective laser melting and electron beam melting. *Materials & Design*, vol. 95, 2016, p. 21 - 31.

[ZIN 06] Zinn W., Schulz J., Kopp R., Scholtes B.
The Influence of the Velocity of a Peening Medium on the Almen Intensities and Residual Stress States of Shot Peened Specimens, p. 161-166. Wiley-Blackwell, 2006.

FOLIO ADMINISTRATIF

THESE DE L'UNIVERSITE DE LYON OPEREE AU SEIN DE L'INSA LYON

NOM : PERSENOT

DATE de SOUTENANCE : 11 décembre 2018

Prénoms : Théo

TITRE : Fatigue of Ti-6Al-4V thin parts made by Electron Beam Melting

NATURE : Doctorat

Numéro d'ordre : 2018LYSEI117

Ecole doctorale : ED 34 Matériaux de Lyon

Spécialité : Matériaux

RESUME :

Nowadays, reducing the energy consumption is crucial for most of the industries. For transportation industries, it can be achieved through weight reduction. In this context, cellular structures turn out to be one of the most efficient solution. Thanks to the development of additive manufacturing, producing such complex geometries is no longer an issue. However, their use will remain limited as long as their fatigue performances are not known.

This PhD work aimed at understanding the mechanisms that govern the fatigue behaviour of such cellular structures. It was first decided to focus on their unitary element, i.e. a single strut. Single struts samples were manufactured by Electron Beam Melting and then characterized in as-built conditions using different experimental techniques (X-ray tomography, optical and electron microscopy, etc.). Their static and cyclic tensile properties were then evaluated. The rough surface and in particular notch-like defects were found to be responsible for the knockdown of the mechanical properties. Regarding the fatigue resistance, their detrimental impact was predicted using Kitagawa diagrams. It also enabled to explain the impact of the build orientation.

Different post-treatments were used in order to improve these mechanical properties. Chemical etching and ultrasonic shot peening (USP) significantly reduced the severity of surface defects of as-built thin struts and thus increased their mechanical properties. After USP, the fatigue properties of machined samples were almost matched. Hot Isostatic Pressing lead to the closure of all internal defects and to the coarsening of the microstructure. When combined with one of the surface treatments, the fatigue properties were further improved.

Finally, a method enabling to systematically and automatically extract from the surface the most critical defects and quantitatively analyze their influence on fatigue life was proposed and discussed. It was successfully applied to chemical etched samples but improvements are mandatory for other surface conditions.

MOTS-CLÉS : Additive manufacturing, cellular structures, fatigue properties, HIP, chemical etching, Ultrasonic shot peening,

Laboratoire (s) de recherche : MATEIS – UMR 5510
INSA de Lyon
25 avenue Jean Capelle
69621 Villeurbanne CEDEX

Directeurs de thèse: Jean-Yves BUFFIERE (Professeur) et Rémy DENDIEVEL (Professeur)

Président de jury :

Composition du jury : Eric CHARKALUK   (Directeur de recherche)
Véronique AUBIN   (Professeur)
Nicolas SAINTIER   (Professeur)
Guilhem MARTIN   (Maître de conférence)
Philippe EMILE   (Docteur)